

**ÉCOLE DOCTORALE de Physique et Chimie Physique**  
**Institut de Physique et Chimie des Matériaux de Strasbourg**

## THÈSE

présentée par :

**Suvidyakumar HOMKAR**

Soutenance le : 15 Décembre 2020

Pour obtenir le grade de : **Docteur de l'Université de Strasbourg**

Discipline/ Spécialité : Science des Matériaux

### **Ultra-thin multifunctional oxide layers for spintronics applications**

#### THÈSE dirigée par :

**Mme VIART Nathalie**

Professeure, Université de Strasbourg, France

#### RAPPORTEURS :

**Mme DÖRR Kathrin**

Professeure, Martin-Luther-Universität Halle-Wittenberg, Allemagne

**M. PRELLIER Wilfrid**

Directeur de recherche, CRISMAT Caen, France

---

#### EXAMINATEURS :

**M. VIRET Michel**

Chercheur, CEA Gif sur Yvette, France

**M. TRASSIN Morgan**

Lecturer and group leader, ETH Zürich, Switzerland

**M. ROJAS-SANCHEZ Carlos**

Chargé de recherche, IJL Nancy, France

**M. COLIS Silviu**

Professeur, Université de Strasbourg, France

**M. PREZIOSI Daniele**

Chargé de recherche, IPCMS Strasbourg, France



*माझ्या आई – बाबांना समर्पित*

*Dedicated to my parents*



# General Introduction

## Context

During the last few decades, the discovery of giant magnetoresistance whose most emblematic devices are spin valves has allowed a wide range of applications that has opened the path to the new field of spintronics. A typical magneto-resistive device consists of two magnetic layers separated by a non-magnetic spacer. Its electric resistance depends upon the relative orientation of the two magnetic layers. It will be low for parallel arrangement and high for antiparallel arrangement. Operating spintronic devices, therefore, relies on the possibility to modify the relative orientation of the two magnetic layers. The research in this field is currently aimed at lowering the energy needed to operate these devices due to increasing demand for power consumption. In this context, there are great expectations from the next generation of spintronics-based data storage, such as magnetic random-access memories (M-RAMs) to provide these low power consuming devices.

## Motivation

The contemporary focus for M-RAM devices has been on spin-current-based techniques like spin-transfer torque (STT) and spin-orbit torque (SOT). Particularly, SOT-based devices are much sought after due to their low energy requirements and high endurance. In SOT-based devices, a ferromagnet (FM)/heavy metal (HM) heterostructure is used. The current ( $J_c$ ) passed through the heavy metal generates a perpendicular spin current ( $J_s$ ) due to the spin Hall effect (SHE). This spin current is then transferred to the ferromagnetic layer through the interface, which leads to a torque that can effectively be used to manipulate its magnetization. The effects are still relatively low for the moment and exploration of new materials with greater efficiency, endurance, and entangled functionalities are highly sought after. Tremendous importance is given to the quality of the heterostructures, especially at interfaces such as the above-mentioned FM/HM. The loss of spin current due to surface degradation at interfaces is indeed a major inhibitor for large-scale industrial adoption of the SOT effect.

Another area of focus for research in low power memory devices has been the use of magnetoelectric (ME) multiferroic materials, in which the electric and magnetic orders are coupled. It has recently been considered with great enthusiasm as a path for a low power switching of the magnetization. In this concept, the magnetization is modulated through the reversal of its coupled electric polarization under the application of an almost cost-free electric field (when compared to a magnetic field). The efficiency of this magnetoelectric control of magnetization is however still questionable when considering the reliability, speed and production of practical devices.

The inconveniences presented by both ME and SOT techniques can be mitigated by considering a hybrid magnetoelectric-spin orbit torque (ME-SOT) device that reduces the magnetic anisotropy by a cost-effective gate voltage which can then be switched with a low-power  $J_c$  current by SOT.

The goal of this thesis work, as part of the larger ANR project [MISSION ANR-2018], is to introduce in the panorama of SOT-based MRAM a single-phased ME material whose intrinsic electric-field control over the magnetic order degree could offer a new playground to attempt a reduction of  $J_c$  in SHE-based SOT architectures, while adding extra functionalities.

In this thesis, we focus on the potential offered by the orthorhombic gallium ferrite  $Ga_{2-x}Fe_xO_3$  (GFO  $x$ ) for new multilayer spin-current based devices designed for applications in spintronics. GFO is, for  $x=1.4$ , a room temperature multiferroic {ferromagnetic (FM) and ferroelectric (FE)} as well as a magnetoelectric (ME) material, where both FM and FE order parameters are coupled. These highly sought functionalities existing in a single material at ambient conditions is quite rare, which makes this material very interesting for multifunctional devices.

## Organization

My thesis manuscript is organized in six chapters. Each chapter includes its own separate introduction and methods part.

The first chapter introduces the societal motivation for efficient spintronics that has led to the conception of this thesis and gives an in-depth background to the topic. It depicts examples of functional oxides used in the frame of spintronics. It also introduces contemporary background research on the central material of this thesis, GFO, and states our vision to further advance this knowledge towards devices.

The second chapter introduces the methods and instruments for the growth of GFO thin films and structural, surface, and microscopic characterization. This chapter primarily focuses on the

growth-related issues and helps the reader understand the novelty of our films. The samples resulting from this growth forms the base for the study of the next chapters.

The third chapter presents an exhaustive magnetic investigation of our thin films. It brings to light the effects of dimensionality on magnetic properties. It also focuses heavily on the understanding of the highly anisotropic character of magnetization in our thin film *via* macroscopic and microscopic measurement techniques.

The fourth chapter exposes the properties of the electrical polarization of GFO films using *ex situ* and *in situ* optical characterization techniques that probe the ferroic state due to symmetry breaking. The state-of-the-art *in situ* technique reveals ferroic and other symmetry related phenomenon starting from few unit cells at ultra-thin regimes.

The fifth chapter is dedicated towards the exploration of magneto-transport properties of GFO/Pt heterostructures. It helps the reader realize the relevance of GFO in spintronics devices. This chapter serves as a first step toward establishing GFO in practical multifunctional devices.

Finally, a general conclusion will be presented summarizing the significant results of this work, and a list of prospects on the future studies to further optimize applicability of this material.



# Contents

<b>General Introduction</b>	<b>5</b>
Context.....	5
Motivations.....	5
Organization.....	6
<b>1. Introduction</b>	<b>13</b>
1.1 Spin-electronics.....	14
1.1.1 Giant magnetoresistance.....	15
1.1.2 Tunnel magnetoresistance.....	16
1.1.3 The issue of the power consumption.....	17
1.1.4 Magnetic random-access memories (MRAM).....	18
1.1.5 Spin-orbit torque (SOT).....	20
1.1.6 Rashba-Edelstein effect.....	21
1.1.7 The issue of interfaces.....	22
1.1.8 Magnetoelectric-based switching.....	23
1.1.9 Limitations of SOT and ME-based magnetization switching.....	23
1.1.10 Magnetoelectric-aided spin orbit torque.....	24
1.2 Functional oxides as materials of choice for spintronics.....	25
1.2.1 Dielectric and diamagnetic oxides.....	25
1.2.2 Ferro- or Ferri-magnetic oxides.....	26
1.2.3 Ferroelectric oxides.....	28
1.2.4 Multiferroic and magnetoelectric oxides.....	29
1.2.5 Magnetoelectric Spin-orbit (MESO) logic.....	31
1.3 Introduction to $\text{Ga}_{2-x}\text{Fe}_x\text{O}_3$ (GFO x).....	33
1.3.1 Structure of GFO.....	33
1.3.2 Review of GFO thin film growth.....	35

1.3.3	Magnetic properties.....	36
1.3.4	Electrical properties.....	38
1.3.5	Magneto-electric properties.....	40
1.4	Scope of the thesis .....	43
1.5	References.....	44
<b>2.</b>	<b>Ga<sub>0.6</sub>Fe<sub>1.4</sub>O<sub>3</sub> thin films : growth issues</b>	<b>51</b>
2.1	Methods.....	52
2.1.1	Pulsed Laser Deposition (PLD).....	52
2.1.2	In situ RHEED.....	54
2.1.3	X-Ray characterization techniques.....	56
2.1.4	Atomic Force Microscopy (AFM).....	60
2.1.5	Scanning electron microscopy (SEM).....	61
2.1.6	Transmission electron microscopy (TEM).....	61
2.2	Elaboration of Ga <sub>0.6</sub> Fe <sub>1.4</sub> O <sub>3</sub> (GFO) thin films on SrTiO <sub>3</sub> (STO) substrates.....	64
2.2.1	Why STO substrates?.....	64
2.2.2	Growth and structural characterization of GFO films.....	64
2.2.3	Effect of a buffered hydrofluoric acid pre-treatment of the STO (111) substrates...	70
2.2.4	Transmission electron microscopy study.....	72
2.3	Transposition of the growth conditions to another PLD chamber.....	78
2.4	Elaboration of Ga <sub>0.6</sub> Fe <sub>1.4</sub> O <sub>3</sub> thin films on SrRuO <sub>3</sub> (SRO) buffered STO substrates.....	80
2.4.1	Why an SRO buffer layer?.....	80
2.4.2	Growth of GFO/SRO//STO heterostructures.....	80
2.4.3	Conclusions.....	83
2.5	References.....	84
<b>3.</b>	<b>Ga<sub>0.6</sub>Fe<sub>1.4</sub>O<sub>3</sub> thin films : Magnetic properties</b>	<b>89</b>
3.1	Macroscopic magnetic characterizations of Ga <sub>0.6</sub> Fe <sub>1.4</sub> O <sub>3</sub> (GFO) thin films.....	90
3.1.1	Methods.....	90
3.1.1.1	Superconducting Quantum Interference Device – Vibrating Sample Magnetometer	

(SQUID-VSM).....	90
3.1.1.2 Experimental corrections.....	92
3.1.2 Magnetic characterization of the GFO thin films.....	92
3.2 Magnetic Anisotropy.....	96
3.2.1 Types of Anisotropies.....	97
3.2.1.1 Magneto-crystalline Anisotropy.....	97
3.2.1.2 Shape Anisotropy.....	98
3.2.1.3 Surface Anisotropy.....	98
3.2.1.4 Strain Anisotropy.....	100
3.2.1.5 Growth induced Anisotropy.....	100
3.2.1.6 Exchange anisotropy.....	101
3.2.2 Determination of the magnetic anisotropy in GFO thin films.....	101
3.2.3 Conclusions for magnetic properties measured using SQUID-VSM.....	106
3.3 Microscopic magnetic characterizations of Ga <sub>0.6</sub> Fe <sub>1.4</sub> O <sub>3</sub> (GFO) thin films.....	107
3.3.1 An introduction to X-ray magnetic circular dichroism (XMCD) - a powerful characterization tool for magnetism.....	107
3.3.2 XMCD for GFO – pre-existing works.....	115
3.3.3 XMCD for GFO – Our work.....	120
3.3.3.1 Experimental.....	120
3.3.3.2 Contamination issues – Wide range spectra.....	122
3.3.3.3 Elemental Hysteresis.....	124
3.3.3.4 Evidence of a non-zero orbital moment.....	125
3.3.3.5 Thickness dependence of the spin and orbital moments in GFO thin films.....	130
3.3.3.6 Temperature evolution of the orbital moment in GFO films.....	133
3.3.4 Conclusions for magnetic properties measured using XAS / XMCD.....	138
3.4 References.....	140
<b>4. Ga<sub>0.6</sub>Fe<sub>1.4</sub>O<sub>3</sub> thin films : Investigation of the electrical polarization</b>	<b>147</b>
4.1 Introduction to the second harmonic generation (SHG) technique.....	148
4.2 Our SHG investigation.....	152

4.2.1	<i>Ex situ</i> SHG measurements.....	152
4.2.1.1	Conclusion on the <i>ex situ</i> measurements.....	159
4.2.2	<i>In situ</i> SHG (ISHG) measurements.....	159
4.2.2.1	Investigating ISHG signal during GFO growth on STO.....	159
4.2.2.2	Evidencing the electrical ordering temperature.....	164
4.2.2.3	Evidencing sub-unit cell symmetry.....	165
4.2.2.4	Insertion of a conducting electrode – Interface-related effects and influence of the depolarizing field.....	170
4.2.2.5	Conclusion on the <i>in situ</i> measurements.....	173
4.3	References.....	175
<b>5.</b>	<b>Functionality of Ga<sub>0.6</sub>Fe<sub>1.4</sub>O<sub>3</sub> thin films in spintronics</b>	<b>179</b>
5.1	FM/HM: Magnetic axis manipulation in GFO/Pt heterostructures via SHE in Pt.....	180
5.1.1	Growth of GFO/Pt heterostructures on STO (111).....	180
5.1.2	Ferromagnetic Resonance (FMR) investigations.....	186
5.1.3	Magneto-transport in Pt/GFO heterostructures.....	189
5.1.4	Differentiating between AMR and SMR.....	199
5.1.5	Conclusion.....	203
5.2	References.....	204
	<b>General Conclusion and Perspectives</b>	<b>209</b>
	Conclusions.....	209
	Perspectives.....	211
	My own contribution to the work.....	212
	<b>Acknowledgements</b>	<b>213</b>
	<b>Résumé étendu de la thèse</b>	<b>215</b>

---

# Chapter 1

## Introduction

---

In this thesis, we have performed a study of the potential offered by a room temperature magnetoelectric multiferroic compound,  $\text{Ga}_{0.6}\text{Fe}_{1.4}\text{O}_3$  (GFO) in the frame of a quest for magnetic-field-free control of spintronic devices. The work comprises structural and compositional surveys of the GFO thin films deposition arcana, macro- and micro-scopic examinations of their magnetic properties, and a magneto-transport investigation of some application-wise interesting GFO/Pt heterostructures.

We will first highlight the motivation that led to this research project and position it within its academic frame by introducing the related fundamental physical concepts. We will hence briefly discuss the field of spintronics, which is the societal motivation for this project, and the critical need for improvements which may come from multi-functional materials. The fundamental concepts of ferromagnetism, ferroelectricity and their simultaneous existence, coupled or not, in multi-functional materials will be reviewed. We will then describe the decisive role multi-functional oxides can play for spintronics devices and look at some illustrative examples. Finally, we will introduce the material onto which this study is focused, the gallium ferrite,  $\text{Ga}_{0.6}\text{Fe}_{1.4}\text{O}_3$  (GFO), present its already known structural and physical properties, and explain how it could meet the challenge.

The electronics-based lifestyle that we experience today was enabled by decades of research into developing devices that exploit the charge degree of freedom of the electron. Among the first revolutionary devices to be developed by this research were the point-contact transistor<sup>[1]</sup> and p-n junction bipolar transistor<sup>[2]</sup>, which after their miniaturization into an integrated circuit (IC)<sup>[3,4]</sup> soon became a matured technology for computation and data storage. In data storage using electronics, metal-oxide-semiconductor field-effect transistor devices (MOSFET) allowed to encode binary data of '0' or '1' states depending on charged or discharged states, modified by controlling electric charges at a gate terminal with electric fields. The discovery of ICs led to a rapid increase of the transistor density in devices, almost doubling every 18-20 months, roughly following the predictions set by Moore's law<sup>[5]</sup>. This resulted in the widespread acceptance of silicon-based technology and ensured continued development and incorporation of this technology into various industrial and household appliances. In the current era of the 21<sup>st</sup> century, however, the rate of transistor density doubling has slowed down due to interference of quantum effects like gate charge leakage by tunnelling and other technical issues of nanofabrication at such small scales of miniaturization. There are also some other issues such as the volatility of the data storage and the higher power consumption in electronics storage devices which need to be tackled. To circumnavigate these issues, a few options have been considered, the "Beyond CMOS" technologies, which seek to use new classes of materials and techniques to complement or replace the contemporary Si-based CMOS devices<sup>[6]</sup>.

## 1.1 Spin-electronics

The field of spin-electronics or spintronics is considered as one of the most promising approaches for beyond CMOS technologies<sup>[7]</sup>. Spintronics aims to employ both the charge and spin degrees of freedom of electrons to develop a new class of multipurpose devices with advanced functionalities, such as non-volatility and reduced power consumption<sup>[8]</sup>. The non-volatility in spintronics comes from the use of the relative magnetization orientations in two ferromagnetic materials, which can be distinctly noted as binary '0' or '1' magnetic bits, for the antiparallel or parallel magnetic states, respectively. These magnetic bits are uniquely identified by the resistance they oppose to the passage of an electrical current through the phenomenon of magnetoresistance (MR).

The dependence of the electrical resistance of a material on the orientation of its magnetization, also called anisotropic magnetoresistance (AMR), was discovered back in 1856. Its amplitude was however too weak for practical use in devices<sup>[9]</sup>, and it was only much later, in 1991, that IBM incorporated an AMR technology as a magneto-resistive read head device in hard-disk drives (HDD) storage media<sup>[10]</sup>. Even though the AMR was only of about a few percent, it was enough to lead to a massive increase in the HDD storage areal density of up to 25 % per year.

### 1.1.1 Giant magnetoresistance

The discovery of the giant magnetoresistance (GMR), with effects of up to 50 % already at its discovery, dethroned the AMR read head and further allowed a rapid expansion in the rate of areal storage density by up to 100 % per year in 1997 and boosted the field of spintronics by making the HDD technology ubiquitous <sup>[11]</sup>. A typical GMR device, also called spin valve, consists of two thin magnetic layers separated by a non-magnetic spacer. Its electric resistance selectively depends upon the two magnetic layers' relative orientation and will be low for parallel arrangement and high for antiparallel arrangement. Therefore, operating spintronics devices rely on modifying the relative orientation of the two magnetic thin layers. Fig. 1.1 shows conventional hard-disk drive storage and a schematic representation of the magneto-resistive read-head technology (here the GMR sensor) to read the storage bits' magnetic state. The read head flies at a constant height above the magnetic bits and senses the relative magnetic orientation by measuring the GMR. A solenoid type coil is also attached, which generates a magnetic field to write information by modifying one of the magnetic layers' magnetization orientation, and hence the bits' value. For their discovery of the GMR, Albert Fert and Peter Grünberg received the Nobel prize in physics in 2007.

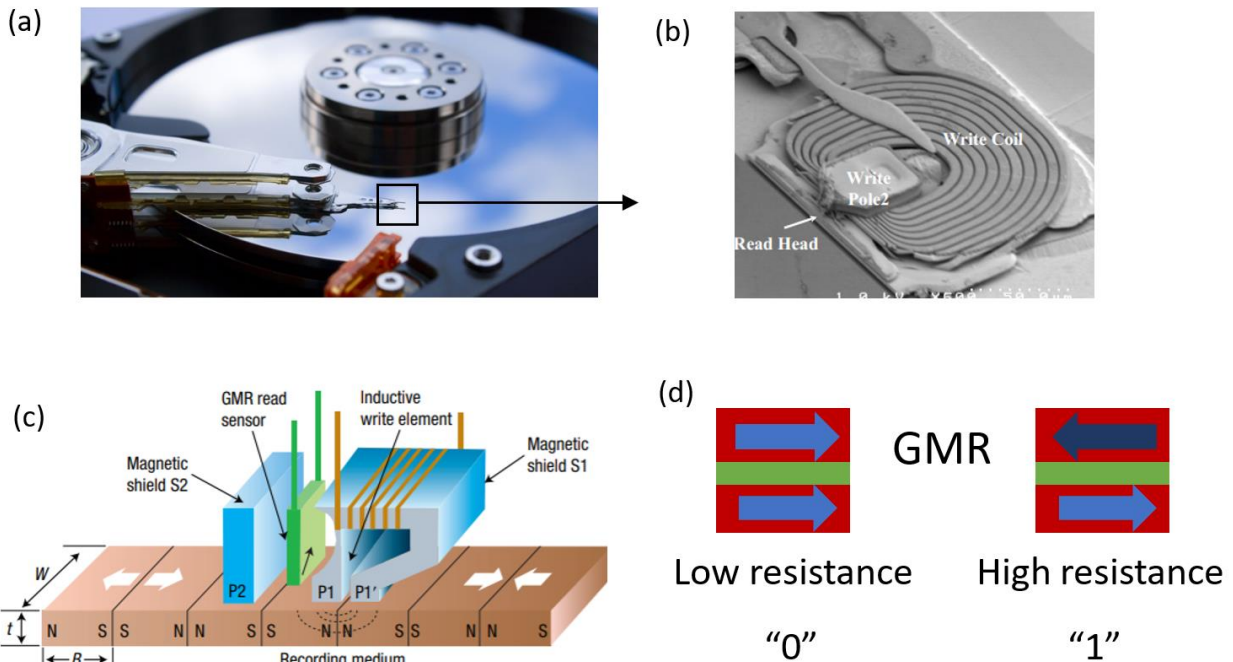


**Fig. 1.1 | Schematic representation of a hard disk drive (HDD).** (a) A close-up image of a conventional HDD. (b) Microscopy image of the magneto-resistive read-write head in an HDD. (c) Diagram of the functioning of the read-write head in an HDD <sup>[12]</sup>. (d) Diagram to describe the two states in a GMR sensor.

### 1.1.2 Tunnel magnetoresistance

Subsequently, the research into this field led to another important discovery of the tunnel magnetoresistance (TMR), where the non-magnetic spacer layer between the two magnetic layers is insulating. In such devices, the passing current is a tunnel current <sup>[13]</sup>. If the two ferromagnetic layers have parallel magnetizations, the electrons, both of spin up and spin down, from one layer will find appropriate available states in the second layer (Figure 1.2 (a)). The density of states for spin-up is high in both ferromagnetic layers, and this allows the passage of spin-up electrons. Conversely, in an antiparallel configuration, the probability that the electrons pass through the barrier decreases. One of the layers has indeed a high spin up density of states while the other does not. This results in an increase of the resistance of the junction (Figure 1.2 (b)).

According to Jullière's model <sup>[14]</sup>, the TMR can be written as a function of the conductance (G), resistance (R), or resistivity ( $\rho$ ), corresponding to the parallel (P) and antiparallel (AP) configurations, as given by Eq. 1.1, and can be reduced to an expression depending only on the spin polarization ( $P'$ ) at the Fermi level of the two electrodes as shown in Eq. 1.2 with  $\rho_{maj}$  the resistivity of majority spin orientation and  $\rho_{min}$  the resistivity of minority spin orientation.

$$TMR = \frac{G_P - G_{AP}}{G_{AP}} = \frac{R_{AP} - R_P}{R_P} = \frac{2P_1 P_2}{1 - P_1 P_2} \quad (1.1)$$

$$P' = \frac{\rho_{maj} - \rho_{min}}{\rho_{maj} + \rho_{min}} \quad (1.2)$$

The discovery of TMR further increased the sensitivity and stability of the read-head device, which contributed to further increase their areal density.

(a) Parallel : large I, low R    (b) Antiparallel : low I, large R

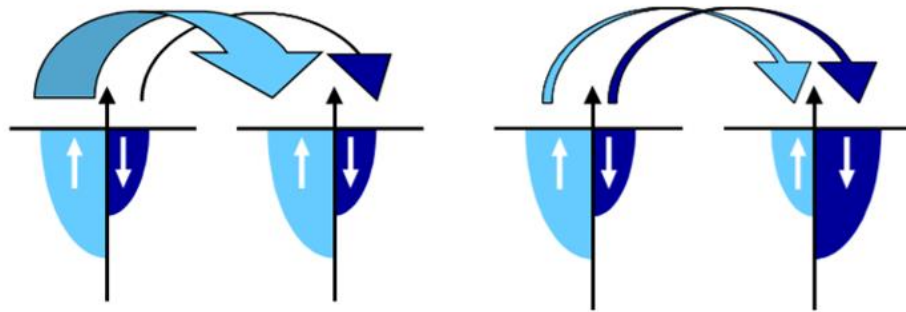


**Fig. 1.2 | A schematic of the Fermi level electronic distributions of a TMR device , and their implications on the possible transport of spins. (a) For parallel configurations. (b) antiparallel configurations.**

Although these spintronics devices based on GMR and TMR have been a considerable improvement relative to the electronic devices based on transistors, their exponential use in current data-driven society has now reached some limitations. This has created the need for an even better new class of devices with increased read/write speed, better endurance, higher life expectancy, absence of moving parts, and, most importantly, lower power consumption.

### 1.1.3 The issue of the power consumption

An estimate of the power consumption by information and communications technologies (ICT) has predicted that a massive amount of energy will be used in data centers in the upcoming decade. In the year 2020, the estimate of ICT's power consumption compared to total global power consumption is 11 % (Fig. 2.1 (a)) <sup>[15]</sup>. Of which these data centers, which form the primary basis for storing the global information and are crucial for sharing information online, were estimated to have consumed 1-1.5 % of the global electricity. It is predicted that they will increase their consumption by up to 3-13 % of the total global electricity by 2030 (See Fig. 1.2 (b)) <sup>[16,17]</sup>. To surmount these power consumption issues, the current research aims to make a collective effort to create energy-efficient spintronics devices to accommodate big data storage. Considerable research has led to a few interesting options, among which the development of magnetic random-access memories (MRAM), which has shown immense potential. MRAM devices are also proposed to solve the other issues of speed, endurance, and moving parts. Such a memory device aims to combine both the capabilities of data storage given by Flash or read-only memory (ROM) and the execution storage of DRAM or SRAM in a single platform <sup>[12]</sup>. Its scalability, endurance, and embedded functionality have been demonstrated on an industrial level with prototypes and, in some cases, full-scale production by many technology-oriented companies such as Everspin, Intel, IBM leading the charge <sup>[18-20]</sup>.

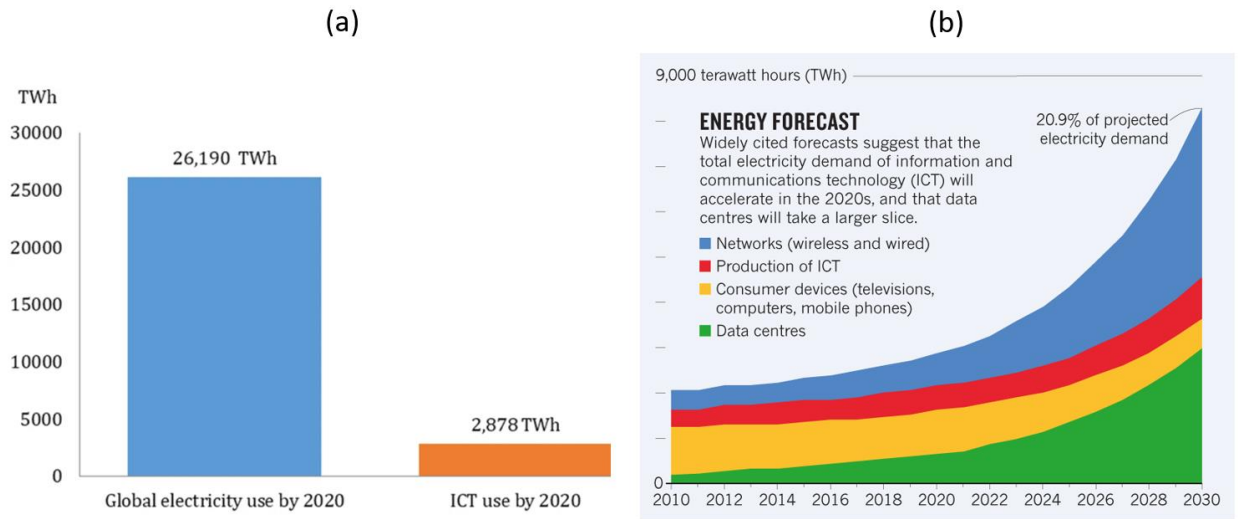


**Fig 1.3 | Graph of power consumption by information and communication technology (ICT).** (a) ICT contributes to a total of 11 % of the global electricity use in 2020. Adapted from ref. <sup>[15]</sup>. (b) Energy forecasts for up to 2030 and the predicted increase of power consumption by data centers. Adapted from ref. <sup>[16]</sup>.

### 1.1.4 Magnetic random-access memories (MRAM)

The MRAM technology mainly consists of 2 sets of parallel conducting lines organized in a perpendicular array with a magnetic tunnel junction (MTJ) device at each cross-point architecture (Fig. 1.4 (a)) <sup>[12]</sup>. The MTJ device is based on a physical structure similar to the one used for TMR read-head devices with some important technical variations, such as the addition of one transistor to make complex 1T/1MTJ devices. This makes them suitable for use as realistic magnetic storage devices compared to TMR's only basic read-head functionality. A bit line in MRAM is used to write the information on the magnetic free layer, whereas the word line is used to access and read the information (Fig. 1.4 (b)). There are a few types of paths envisioned for the magnetization switching and detection in MRAM. Primarily, the current-induced magnetic field switching was used for MRAM devices, but contemporary focus on low energy requirements has shifted it to spin current based techniques like spin-transfer torque (STT) and spin-orbit torque (SOT). Particularly, the SOT based devices are much sought after due to their low energy requirements and higher endurance <sup>[21]</sup>.

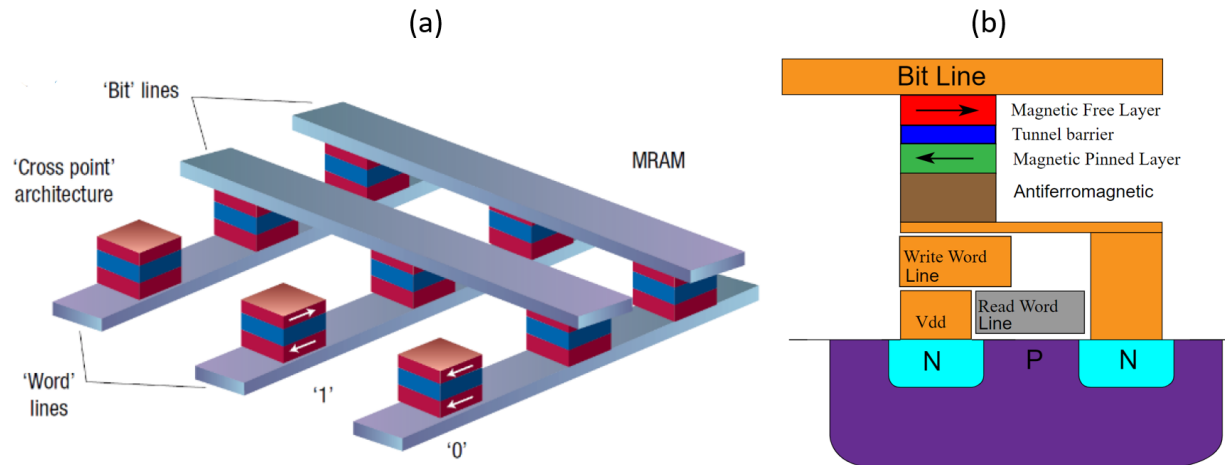


**Fig 1.4 | Schematic of magnetic random-access memory (MRAM).** (a) MRAM 'cross-point' architecture with several MTJs at the cross points of bit and word lines. Adapted from ref. [12]. (b) Components of a single MTJ bit. Adapted from ref. [22].

The current-induced magnetic field devices work by passing a strong current through the word line, which generates a high magnetic field enough to switch the one of the ferromagnetic layers while the other one is pinned (Fig. 1.5) [21,23]. This requires very high energy and is also subject to Joule heating, thus degrading the device's lifetime. To replace this energy-consuming technology, spin-transfer torque employs spin-dependent transfer by passing a current through the device composed of the two ferromagnetic layers. A high-density current from the first encountered ferromagnetic layer creates a spin-polarized current with spins aligned along the direction of this layer's magnetization [21,23]. For an antiparallel state between the two ferromagnetic layers, this spin-polarized current can generate enough torque in the second ferromagnetic layer to switch its magnetization. Changing the direction of the polarized current passing through the device determines the low or high resistance states, allowing them to read the bits. In spin-orbit-torque (SOT)-based devices, a ferromagnet (FM)/heavy metal (HM) heterostructure is used to perform the switching. SOT's microscopic origins are still subject to investigations and highly debated but they are generally acknowledged to be due to spin accumulation at FM/HM interface [8]. The spin accumulation is attributed to two main phenomena caused by the spin-orbit coupling (SOC), the Spin-Hall effect (SHE) and the Rashba-Edelstein effect.

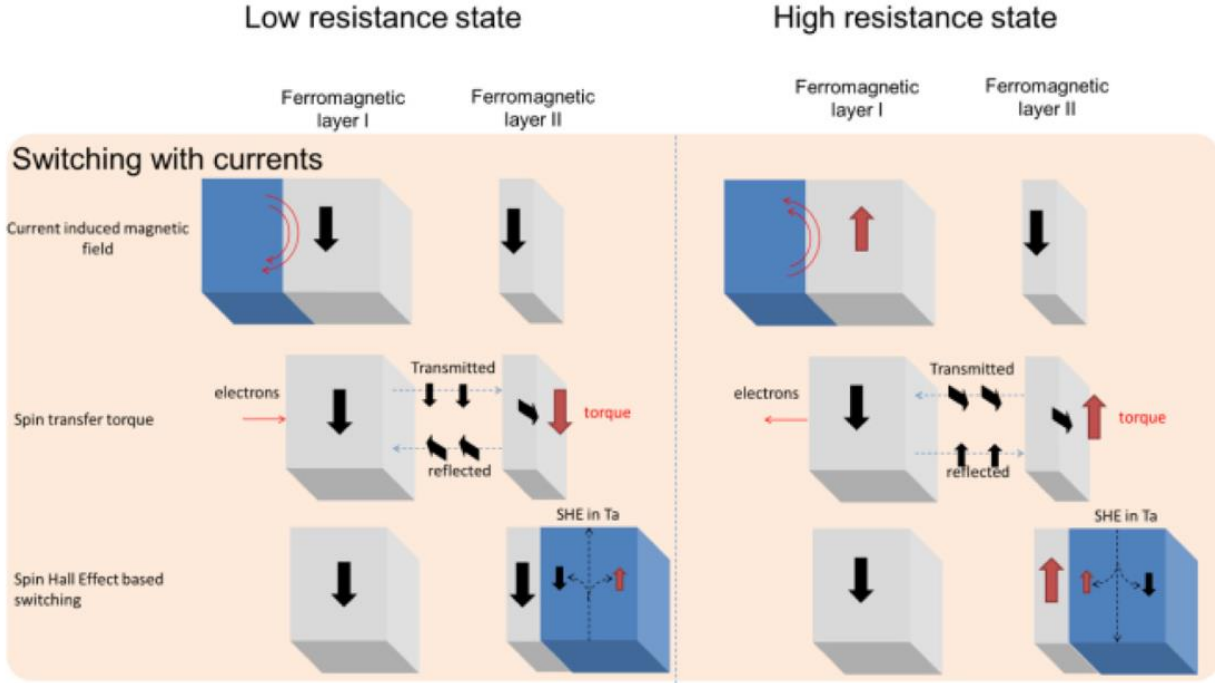


**Fig 1.5 | Different technologies that can be incorporated into MRAM memory architecture.** These technologies are employed to switch the ferromagnetic layer I and create parallel or antiparallel magnetization with respect to the ferromagnetic layer II and thus allowing low or high resistance states, which can be defined as 0 or 1 bits. Adapted from ref. [21].

### 1.1.5 Spin-orbit torque (SOT)

In the SHE-based switching, the current ( $J_e$ ) that is passed through the heavy metal layer with strong spin-orbit coupling (SOC) generates a perpendicular spin current ( $J_s$ ) due to the SHE. This spin current is then transferred to the ferromagnetic layer through the interface, and this leads to a torque that can effectively be used to manipulate the magnetization (Fig. 1.6 (a)) [8,23]. The SHE was first proposed by Hirsch [24] in the 2000s. He claimed that a spin imbalance is created when a current passes through a paramagnetic metal, giving rise to a spin current depicted by Eq. 1.3 :

$$\vec{J}_s = \theta_{SH} (\vec{\sigma} \times \vec{J}_e) \quad (1.3)$$

where  $\theta_{SH}$  is the material or interface dependent spin Hall angle defined as  $|\theta_{SH}| = \left| \frac{J_s}{J_e} \right|$ ,  $\sigma$  is the unit vector of the spin polarization.

The spin imbalance in a HM layer is generated by three types of mechanisms: intrinsic, side-jump, and skew-scattering :

1. The spin velocity distribution associated with the intrinsic mechanism originates from a band structure induced electric field that deflects the spins perpendicularly to the field's direction. This anomalous velocity perpendicular to the electric field is related to their Berry's phase curvature, which depends on the crystal's band structure (Fig. 1.7 (a)) [24,25].

2. The side-jump scattering is the differential deflection of up and down spins due to the opposite electric fields experienced by the respective spins at the impurity site (Fig. 1.7 (b)) [24,25].

3. The spin-dependent skew scattering is related to the asymmetric scattering of spins because of the effective spin-orbit coupling of electron or interaction with impurities (Fig. 1.7 (c)) [24,25].

For heavy metals such as Pt ( $\theta_{SH} = 0.07$ ), W ( $\theta_{SH} = 0.3$ ), and Ta ( $\theta_{SH} = -0.15$ ), the dominating mechanism for SHE is either intrinsic or skew scattering, depending if the conductivity is in moderately dirty or super clean regimes, with respect to the density of impurities, respectively.

Similarly to SHE, there is also an inverse SHE (ISHE), where the flow of spin current in a paramagnetic heavy metal induces a perpendicular charge current. The ISHE is usually used to detect or quantify the SHE induced spin current. A detailed review of the SHE and ISHE effects and the associated effects can be found in Hoffman *et al.* [26] and Sinova *et al.* [27].

### 1.1.6 Rashba-Edelstein effect

In the Rashba-Edelstein effect-based switching, the inversion-symmetry breaking at the interface creates an electric field 'E' along the direction of the symmetry breaking. Due to this electric field 'E', the conduction electrons in the HM moving with a momentum 'p' at the interface are influenced by an effective magnetic field along  $\vec{E} \times \vec{p}$ , which couples with the spin magnetic moment and polarizes it in this direction (Fig. 1.6 (b)) [8,23]. This accumulation of interfacial SOC induced polarized spins then applies a torque to manipulate the FM magnetization. Similarly to the Rashba-Edelstein effect, there is an inverse Rashba-Edelstein effect that leads to a transverse potential due to the accumulation of spins. A detailed description of Rashba-Edelstein, its inverse effects and the associated SOT is well covered by Manchon *et al.* in their review [23].

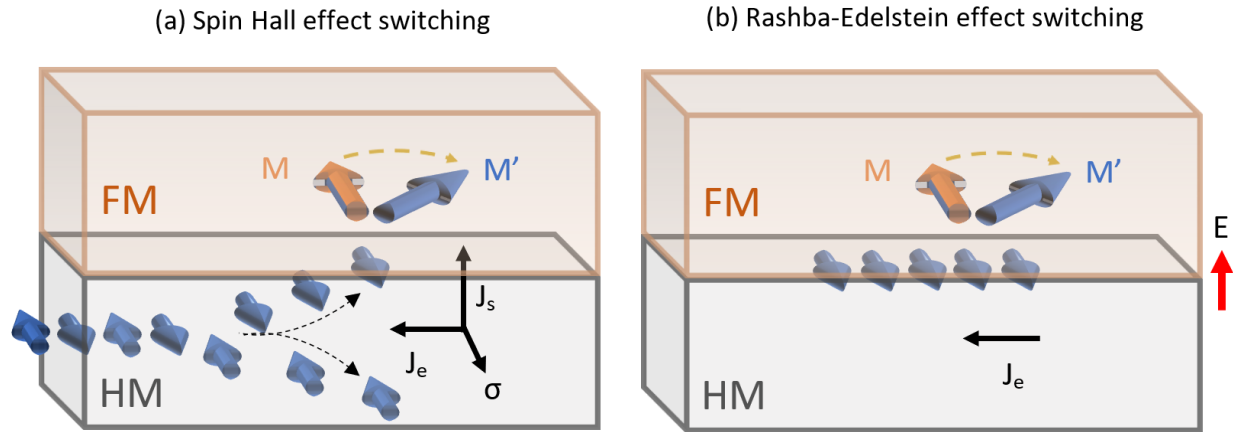


**Fig. 1.6 | Mechanism for functioning of SOT-based switching.** (a) Spin Hall effect-based switching and (b) Rashba-Edelstein effect-based switching of the magnetization in a FM/HM heterostructure.

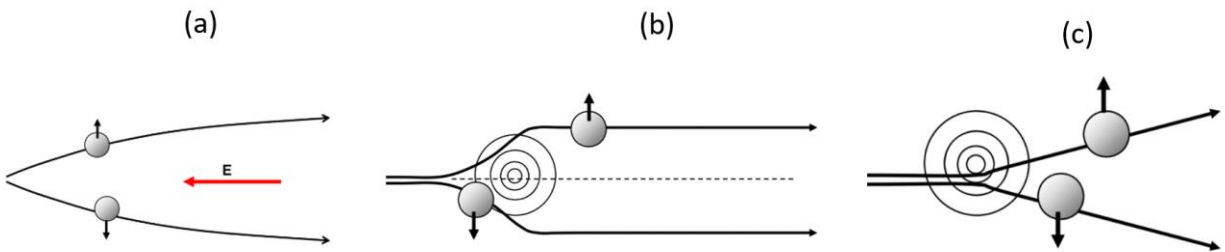


**Fig 1.7 | The various mechanisms responsible for spin Hall effect.** (a) Intrinsic (Band structure related), (b) Side jump scattering, (c) Spin skew scattering. Adapted from ref. [25].

### 1.1.7 The issue of the interfaces

A fundamental pre-requisite in spintronics to avoid a charge/spin transport degradation across the interface due to electrons scattering is the need for atomically smooth thin films [28]. These smooth films allow sharp interfaces, which are mandatory for realizing effects like a spin-orbit torque that depends on the efficiency of spin-current originating from SHE or Rashba-Edelstein effects [29]. A root-mean-square roughness higher than 1-2 nm ruins the reproducibility of spintronics effects, hindering the desired device integration [30].

### 1.1.8 Magnetoelectric-based switching

Apart from the current-induced (magnetic field) and spin-induced (STT and SOT) switching (Fig. 1.5), another important contender for low power switching is the electric field-assisted switching mechanism using the magnetoelectric (ME) effect in a multiferroic magnetoelectric material coupled to a ferromagnetic material. Fig. 1.8 shows an example of a ferroelectric (FE) and antiferromagnetic (AFM) material with magnetoelectric (ME) coupling in proximity to one of the ferromagnetic (FM) layers of an MTJ device. This technique is based on employing the low energy-cost electric field to switch the out-of-plane electric polarization (P) in the material, that also switches the in-plane AFM ordering, thanks to the strong ME coupling. Since the in-plane AFM ordering is coupled to the FM layer *via* exchange bias, the reversal of the AFM ordering results in a reversal of the magnetization of the FM layer <sup>[31]</sup>.

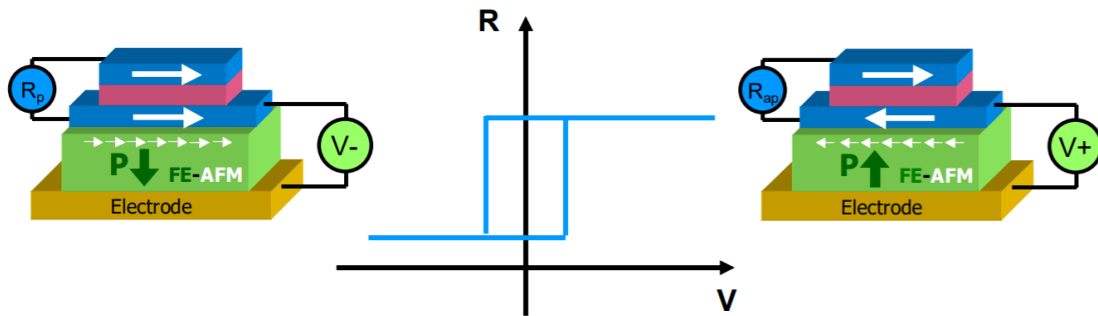


**Fig. 1.8 | Schematic of the electric field-assisted switching in an MTJ device.** A ferroelectric (FE) and antiferromagnetic (AFM) material is magnetically coupled to one of the MTJ's ferromagnetic (FM) layers. Its electrical polarization can be reversed by an electric field. This then reverses the orientation of its AFM order, and subsequently that of the FM layer. Adapted from ref. <sup>[31]</sup>.

### 1.1.9 Limitations of SOT and ME-based magnetization switching

Although, the switching through SOT or magneto-electric coupling based effects are highly desirable, they still have a few shortcomings that can be improved. For the SOT based devices, the critical issue to be solved before incorporation in applications is the dynamic power consumption. The thermal stability of the nanomagnets <sup>[23]</sup> necessitates critical current densities of the order  $10^8$  A/cm<sup>2</sup> for magnetization switching, leading to energy dissipation that remains high, in the range of 1-10 mJ/cm<sup>2</sup> <sup>[32]</sup>. The dissipated power in the current lines is thus a matter of technological concern and leaves a margin for improvement in the SOT-based switching. In this context, search for novel SOT materials is being carried on, for both the HM and FM layers. Concerning the HM, the focus is on finding materials that combine high charge-spin conversion

with low resistivity. Concerning the FM, the focus is on magnetic materials whose properties can be strongly modulated by a low-cost gate voltage.

As far as the magneto-electric (ME) coupling-based devices are concerned, the primary drawback for magnetization switching solely based on the application of an electric voltage is the dearth of single phased magnetoelectric materials with unambiguous ME coupling at room-temperature. Most of the room-temperature ME effects have been observed on composite multiferroics or heterostructure devices <sup>[32]</sup>. Another critical issue is that only a 90° magnetic easy axis reorientation is possible with a single electric pulse as demonstrated by thermodynamic symmetry considerations and some experimental work based on strain-mediated magnetoelectric effect <sup>[33,34]</sup>. The 180° magnetization switching is perhaps only possible with the aid of kinetics or synchronized voltages which will thus reduce the speed of device operation considerably <sup>[32]</sup>.

### **1.1.10 Magnetolectric-aided spin orbit torque**

The inconveniences presented by both the SOT and ME-based techniques can be mitigated by considering a hybrid magnetolectric-spin orbit torque (ME-SOT) system. A perspective on ME-SOT by Meisenheimer *et al.* explores possibilities offered by ME-SOT for reduced threshold switching current and energy dissipation <sup>[32]</sup>. The experimental demonstration of deterministic switching in such an hybrid ME-SOT device is shown in <sup>[35]</sup> and has opened the possibility for novel ME-SOT coupling devices. Although the realization of ME-SOT has been carried out in ferroelectric/ferromagnetic heterostructures, such an observation in a room-temperature single phased multiferroic magnetoelectric material still eludes researchers. It is considered to present important advancements in fundamental understanding of interactions between spin-orbit torque and magnetoelectric effects in a single-phased material by combining high-speed switching with ultra-low power consumption in ME-SOT.

The goal of this thesis, as part of a larger ANR project [MISSION ANR-2018], is to introduce in the panorama of SOT-based MRAM a single-phased ME material whose intrinsic electric-field control over the magnetic order degree could offer a new playground to attempt reducing the critical currents  $J_c$  necessary in the SHE-based SOT architectures, while adding extra functionalities.

The ME material we have chosen is a multifunctional oxide.

## 1.2 Functional oxides as materials of choice for spintronics

In the '80s and '90s, spintronics was mostly carried out with metallic layers. High values of TMR could be achieved with these conventional materials, but the constant need for further miniaturization kept requiring higher TMR values. Julliere's formula (see Eq. 1.1) says that maximum TMR can be obtained for materials that have a single spin polarization, i.e. which are half metals. Since many oxides are half metals, they were considered a good choice for MTJ devices. The multiple degrees of freedom which oxides can present is also an asset for the design of specific devices benefiting from the tuning of their different physical properties. The simultaneous existence of various functional properties in oxides further establishes them as a clear choice for future multi-functional devices, i.e. devices that can perform more than one task<sup>[36]</sup>. Additionally, the advancement in the high-quality growth of oxide films in the ultra-thin regime led researchers to seriously consider the use of oxides in spintronics<sup>[37]</sup>. In this section, we will look at a few examples of functionalities offered by oxides that have found their use in spintronics.

### 1.2.1 Dielectric and diamagnetic oxides

One of the earliest use of oxides in spintronics has been the use of a dielectric and diamagnetic oxide as a thin barrier separating ferromagnetic layers for high TMR in MTJ devices. Notably, MgO has proved to be a great example of a barrier in tunnel junctions, thanks to the symmetry filtering phenomenon in epitaxial films that has been described in a detailed review by Bibes *et al.*<sup>[37]</sup>. A prime example of MgO as an efficient barrier was demonstrated in CoFeB/MgO/CoFeB, where TMR ratios as high as 604 % were recorded at room temperature<sup>[38]</sup>. The adoption of MgO established the relevance of oxides and paved the rather complex way of the use of epitaxial insulating oxides.

Another famous example of the utilization of dielectric and diamagnetic oxides in spintronics is the use of SrTiO<sub>3</sub> (STO) / LaAlO<sub>3</sub> (LAO) perovskites interfaces, as host of an exotic 2-dimensional electron gas (2DEG) (Fig. 1.9 (a))<sup>[39]</sup>. The physics community widely studies the 2DEG phenomenon at the LAO/STO interface due to its rich physics and technological interest as a spin-to-charge converter (Fig. 1.9 (b)) thanks to the inverse Rashba-Edelstein effect<sup>[40]</sup>.

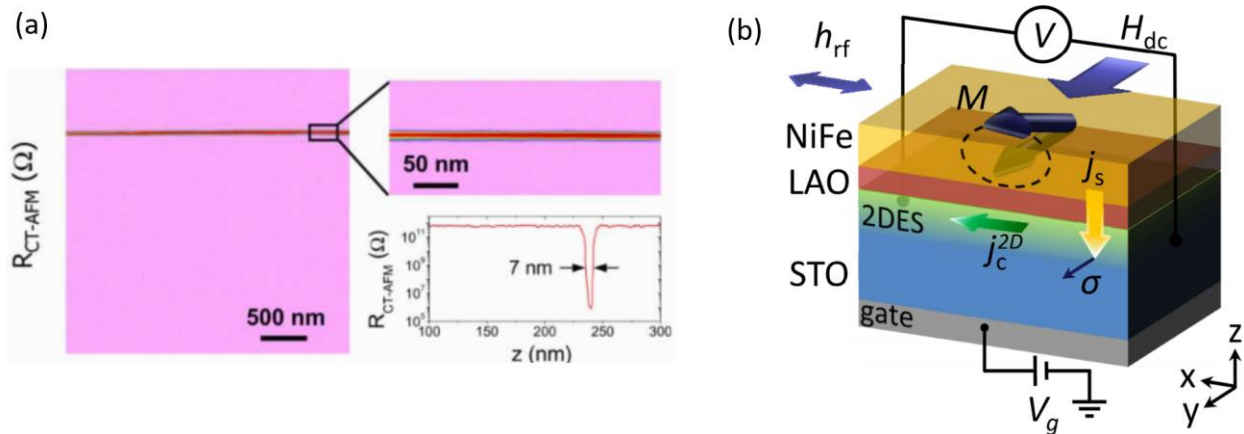


**Fig. 1.9 | Effects of 2D electron gas (2DEG) formed at LAO/STO interface.** (a) Conducting tip AFM mapping of the LAO/STO interface revealing a 7 nm wide, highly conducting metallic interface . Adapted from ref. [39]. (b) Spin ( $j_s$ )-charge ( $j_c$ ) currents interconversion at the interface between a ferromagnet (NiFe) and the 2DEG. Adapted from ref. [40].

### 1.2.2 Ferro- or Ferri-magnetic oxides

The ferromagnetic oxides play a special role in spintronics due to their spin filtering efficiency, leading to high TMR. It has been especially proven for half metals like  $\text{La}_{2/3}\text{Sr}_{1/3}\text{MnO}_3$  (LSMO), which theoretically have single spin polarization. TMR ratios as high as 1850 % have been observed in MTJ's of LSMO/STO/LSMO at temperatures of 4.2 K, thus experimentally showing 95 % spin polarization of LSMO (Fig. 1.10) [41]. This has also shown the validity of all oxide heterostructures in spintronics. Although LSMO proves to be a good example for the concept, the device integration has faced difficulties. This is firstly due to the Curie temperature ( $T_c$ ) of LSMO, which is close to room temperature where the spin polarization and TMR diminish, and secondly, due to the strong dependence of MTJ TMR on the LSMO/STO interface quality [36,42]. It was also shown that the TMR sign changes from positive to negative depending on the interface termination of STO (SrO or  $\text{TiO}_2$ ), which highlights the important role of interface and surface terminations in oxides [43].

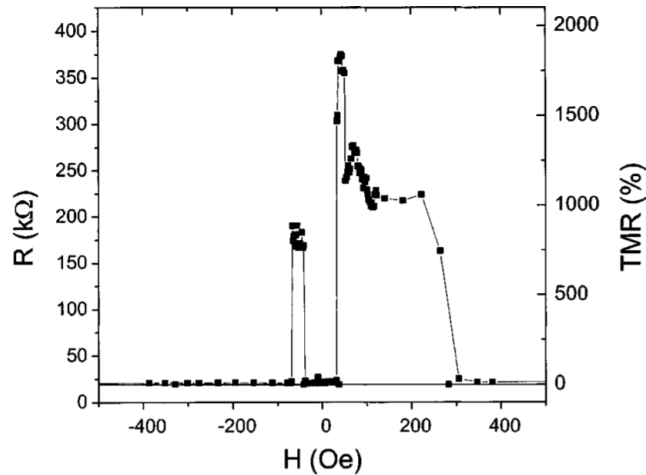


**Fig. 1.10 |** The iconic transport measurement on LSMO/STO/LSMO MTJ junction at 4.2 K, which shows a TMR as high as 1850 %. Adapted from ref. [41].

Apart from metallic ferro- or ferri-magnetic oxides, insulating ferrimagnetic oxides have garnered much attention recently in spintronics. Insulating oxides with a ferromagnetic behavior and high  $T_c$  are rather rare since the dominant mechanism for magnetism in oxides is super-exchange, whose sign depends on the transition metals orbital filling and strength of the orbital overlaps, i.e., on the bonds angles, according to the Goodenough-Kanamori-Anderson rules [37], and which is most often antiferromagnetic. However  $Y_3Fe_5O_{12}$  (YIG) is such a high  $T_c$  (ca. 300 °C) ferromagnetic oxide. It has been the subject of intense investigations due to its high-quality factor (low damping) in microwave frequencies. This has allowed researchers to study and quantify the impact of spin currents from heavy metals like Pt on the magnetic properties of YIG *via* spin-orbit torques (Fig 1.11a) [44–46] or to study the impact of spin currents generated from YIG as a spin source on the non-magnetic (NM) heavy metals (Fig 1.11b) [47–49].

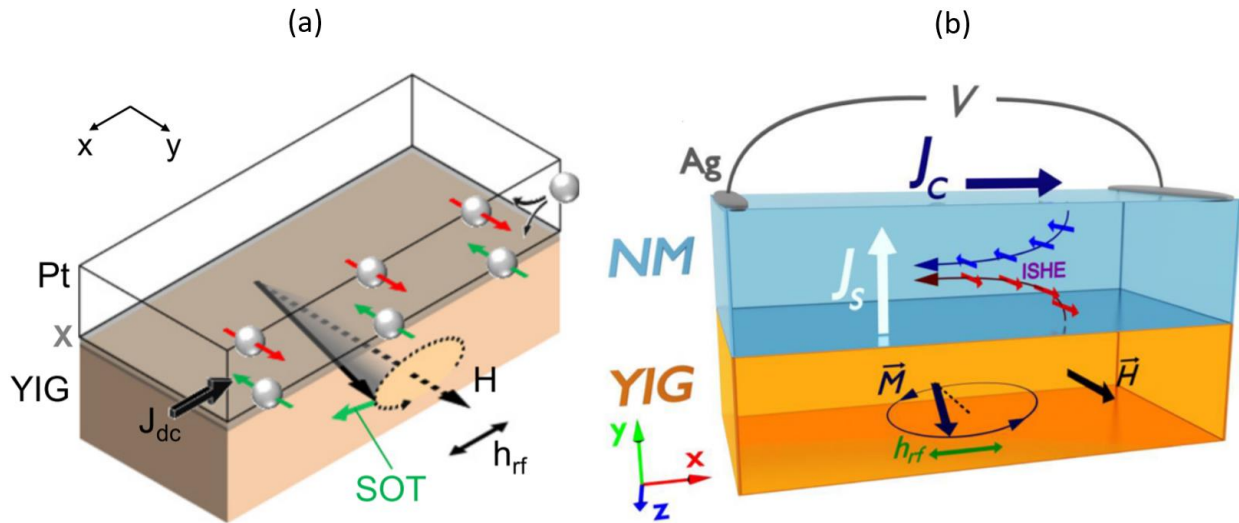


**Fig. 1.11 | Schematic of spin-charge interconversion in YIG/Pt heterostructure.** (a) The spin orbit torque (SOT) due to spin Hall effect (SHE) in Pt modulates the YIG magnetization. Adapted from ref. [46]. (b) The conversion of a spin current from YIG into a charge current in the non-magnetic metal Pt. Adapted from ref. [49].

### 1.2.3 Ferroelectric oxides

One of the prime examples of ferroelectric oxides in spintronics is their use in ferroelectric tunnel junctions (FTJ's). They are considered as advantageous over FeRAM's since their readout mechanism is non-destructive, and unlike for FeRAM's, their initial state does not need to be restored after readout. The FTJ uses an ultra-thin diamagnetic ferroelectric oxide as a tunneling barrier sandwiched between two different metal electrodes. A tunnel electro-resistance (TER) is observed upon switching the polarization orientation of the ferroelectric oxide. One of the main mechanisms for TER suggests that a difference in the Thomas-Fermi screening lengths of the electrodes creates different levels of imperfections in the screening of the ferroelectric charges at the interface between the ferroelectric oxide and the electrode. This leads to a distorted potential profile whose asymmetry changes after flipping the ferroelectric polarization, leading to TER. This mechanism has been depicted in BaTiO<sub>3</sub> (BTO) sandwiched between Pt and Nb:STO, as shown in Fig. 1.12 [50]. Another interesting material widely studied for both FeRAM's and FTJ is Pb(Zr,Ti)O<sub>3</sub> (PZT) due to its large resistance and relative ease in switching by piezo-force microscopy (PFM) methods [37]. Variations of FTJ, such as multiferroic tunnel junctions (MFTJ), also exist, in which the metallic electrode is replaced with magnetic oxide metals such as LSMO or SrRuO<sub>3</sub> (SRO) [50,51]. Since the switching is carried out with only a voltage, the energy required for the memory switching is considerably reduced in an FTJ, making it highly desirable for low power data storage.

A particular challenge while incorporating a ferroelectric oxide as a barrier is to prepare it in ultra-thin regimes to allow the tunneling process to occur. The ultra-thin limit of the ferroelectric material depends on the value of the critical thickness for ferroelectricity to appear in the material. Therefore, much research in FTJ focuses on searching robust materials with a low critical thickness and which can be atomically smooth in ultra-thin regimes.

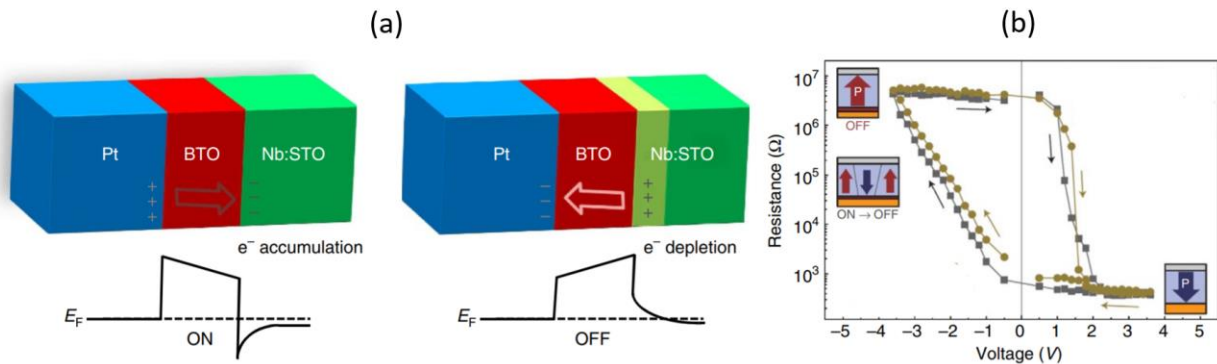


**Fig. 1.12 | Example of a ferroelectric tunnel junction (FTJ) with BTO sandwiched between Nb:STO and Pt electrodes.** (a) Schematic of the functioning of FTJ based on BTO. When the polarization points 'right', the electrons accumulate to screen the positive charges from the BTO polarization and lower the electrostatic potential, thus decreasing the resistance. In contrast, when the polarization points 'left', the electron carriers are depleted, resulting in a Schottky barrier at the BTO/Nb:STO interface, which widens the barrier and increases the resistance. Adapted from ref. [50].

### 1.2.4 Multiferroic and magnetoelectric oxides

Multiferroics are a rare class of materials that simultaneously show two or more ferroic ordering types, such as ferroelectricity, ferromagnetism, or ferroelasticity [52]. Among this rare class of materials, a particularly technologically appealing sub-class has emerged in which there is a coupling between these ferroic order parameters. Particularly in the context of spintronics, the sub-class which couples ferroelectricity and ferromagnetism, giving rise to magnetoelectricity, is extremely desired due to the possibility it gives to control magnetization with an electric field [53,54]. Such magnetoelectric multiferroics are extremely scarce, all the scarcer with room temperature properties, and many of them are oxides.

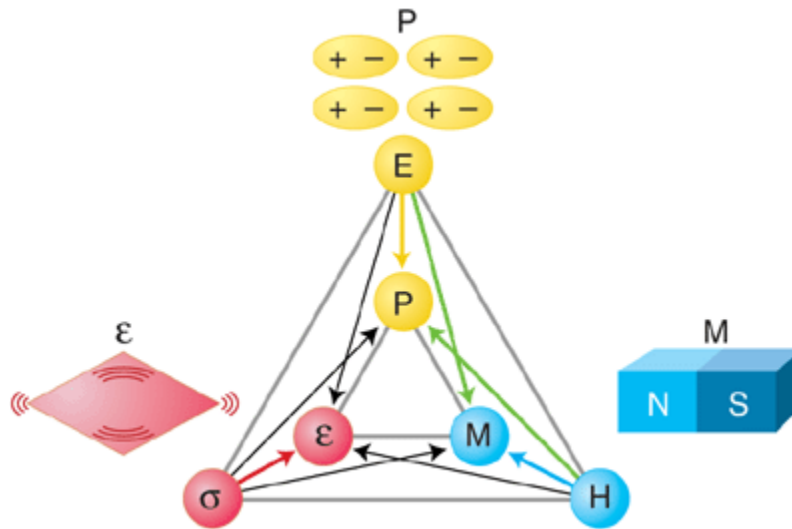


**Fig. 1.13 | The various ferroic orders and their possible interactions.** The electric field (E), magnetic field (H), and stress ( $\sigma$ ) control the electric polarization (P), magnetization (M), and strain ( $\epsilon$ ). Adapted from ref. <sup>[52]</sup>.

The most studied single-phased magnetoelectric multiferroic is the perovskite  $\text{BiFeO}_3$  (BFO). The research in BFO was renewed after the demonstration of epitaxial thin film growth with interesting magnetic and electrical properties, in the early 2000s <sup>[55,56]</sup>. BFO is primarily relevant in spintronics due to its magnetoelectric coupling at room temperature <sup>[31,57]</sup>.

The magnetoelectric functionality of BFO has been demonstrated at room temperature through evidences of the modifications of magnetic domain patterns <sup>[57]</sup> and even magnetization deterministic switching <sup>[58]</sup> in a  $\text{Co}_{0.9}\text{Fe}_{0.1}$  layer, implied by the application of an electric field to a BFO adjacent layer (Fig. 1.14 (a, b)). Evidence of such a phenomenon has wide implications for data storage and has shown the promising potential offered by multi-functional oxide materials.

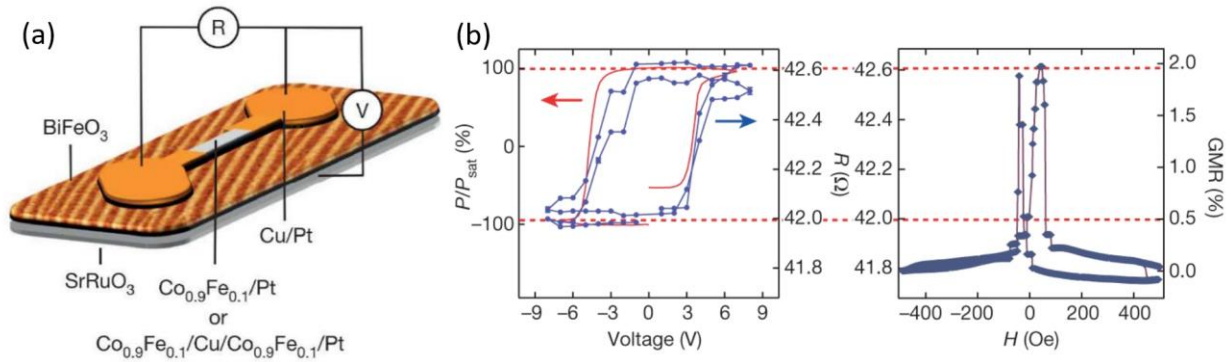


**Fig. 1.14 | Example of magnetoelectric based switching using BFO.** (a) Scheme of a GMR valve activated by the multiferroic magnetoelectric BFO. (b) The hysteresis loops show that the electrical resistance of the Pt/Co<sub>0.9</sub>Fe<sub>0.1</sub>/Cu/Co<sub>0.9</sub>Fe<sub>0.1</sub> valve can be switched by a voltage, through the magnetoelectric coupling present in BFO, and result in an interesting GMR. Adapted from ref. [58].

### 1.2.5 Magnetoelectric Spin-orbit (MESO) logic

The incorporation of BFO into the so called magnetoelectric spin orbit (MESO) logic memory device (Fig. 1.15) developed by teams at both Intel and the University of California, Berkeley, can be evidenced as a good example of far-reaching implications brought upon by the magnetoelectric switching technology. It combines the magnetoelectric exchange bias technique (such as in BFO/Co<sub>0.9</sub>Fe<sub>0.1</sub>) for switching the magnetic orientation, coupled with a strong spin-orbit material (such as a 2DEG at the LAO/STO interface) for a cost effective readout. It demonstrates a drastic reduction in the power consumption for switching and reading the data and is proposed to be ideal for the next-generation non-volatile logic device for computing [59].

The research in this interesting technology is currently only limited by the lack of materials that have multiferroic and magnetoelectric properties at room temperature. Although BFO has been proven to be an excellent material for these techniques, the lack of a finite magnetization in BFO is a limitation for expanding multi-functional usage. This limitation could be overcome using a single phased material that is simultaneously multiferroic with a finite magnetic moment and magnetoelectric at room temperature.

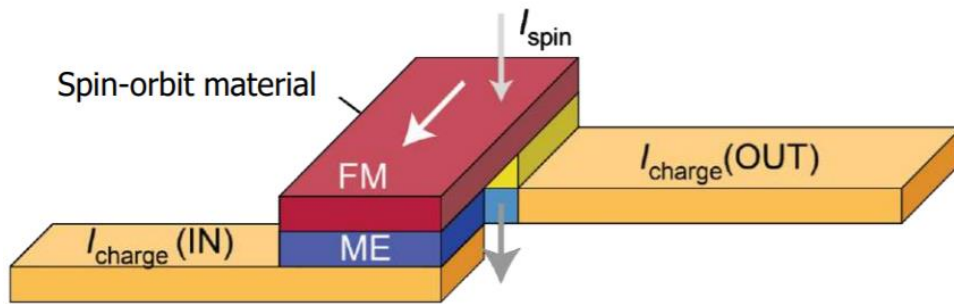


**Fig. 1.15 | Schematic of a MESO logic device.** It combines switching of the FM *via* exchange bias coupling with a magnetoelectric multiferroic and FM orientation readout using a spin-orbit material that converts spin to charge. Adapted from ref. <sup>[59]</sup>.

## 1.3 Introduction to $\text{Ga}_{2-x}\text{Fe}_x\text{O}_3$ (GFO x)

In the previous section, we discussed some of the contemporary multifunctional oxides and their applicability. In this section, we will discuss how  $\text{Ga}_{2-x}\text{Fe}_x\text{O}_3$  (GFO x) fits into these multifunctional oxides and what more it can offer than the already studied systems. We will review the studies already performed on GFO 1.0 and GFO 1.4 in bulk and thin films and describe our ideas for the functionalization of GFO films.

### 1.3.1 Structure of GFO

Gallium Ferrite ( $\text{GaFeO}_3$  or GFO 1.0), synthesized first by Remeika<sup>[60]</sup> in 1960 and later analyzed by Abrahams and Reddy<sup>[61]</sup>, was shown to crystallize in an orthorhombic structure which is different from the usual cubic perovskite structure of the  $\text{ABO}_3$  compounds. GFO crystallizes in the space group number 33 of the International Tables for Crystallography, for which two different settings are commonly used,  $Pc2_1n$  or  $Pna2_1$ . The  $Pc2_1n$  setting (with  $c < a < b$ ) was used historically by Remeika<sup>[60]</sup> and Rado<sup>[62]</sup> in their papers in the 1960s, but  $Pna2_1$  (with  $a < b < c$ ) is a convention used more recently for analytical purposes. The lattice parameters reported by Abrahams and Reddy<sup>[61]</sup> in the  $Pc2_1n$  setting are  $a = 8.7512 \pm 0.0008 \text{ \AA}$ ,  $b = 9.3993 \pm 0.0003 \text{ \AA}$  and  $c = 5.0806 \pm 0.0002 \text{ \AA}$ . One can move from one setting to the other according to a circular permutation exposed in Fig. 1.16<sup>[63]</sup>. We have used the  $Pna2_1$  setting throughout this thesis, but many articles in the literature still use  $Pc2_1n$ .

In the crystallographic structure of GFO 1.0 (shown in Fig. 1.17), the  $\text{O}^{2-}$  anions are arranged in a double hexagonal close-packed ABAC stacking along the 'c' axis. There are four different cationic sites which can be occupied by the  $\text{Ga}^{3+}$  and  $\text{Fe}^{3+}$  cations, named Ga1, Fe1, Ga2, and Fe2. Ga1 is a tetrahedral site, and the Fe1, Ga2, and Fe2 are non-equivalent octahedral sites. Although Fe1 and Fe2 sites are supposed to be occupied by Fe atoms only and Ga1 and Ga2 sites by Ga atoms only, one observes a certain cationic disorder<sup>[64]</sup>. It heavily depends on the growth mode, temperature, and annealing conditions, as shown in Table. 1. It has generally been observed that Ga atoms mostly occupy the Ga1 tetrahedral site, whereas Ga2 and Fe2 sites are mixed. Studies on the effect of the surplus of Fe in  $\text{Ga}_{2-x}\text{Fe}_x\text{O}_3$  stoichiometries with x (Fe) content rising until 1.4 have shown that the Ga1 tetrahedral site, even if it can accommodate some Fe atoms, is mostly occupied by Ga atoms, and Ga2 is preferentially filled with Fe atoms, at about 80%.

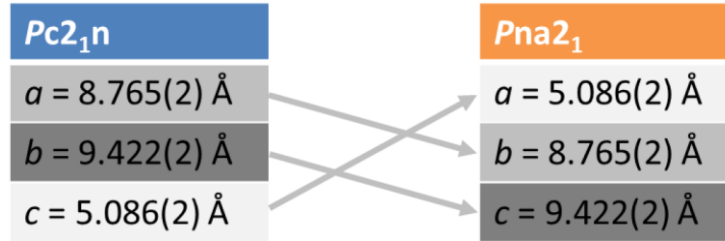


**Fig. 1.16 |** The circular permutations which allow to switch between the  $Pc2_1n$  and  $Pna2_1$  settings. Adapted from ref. [63].

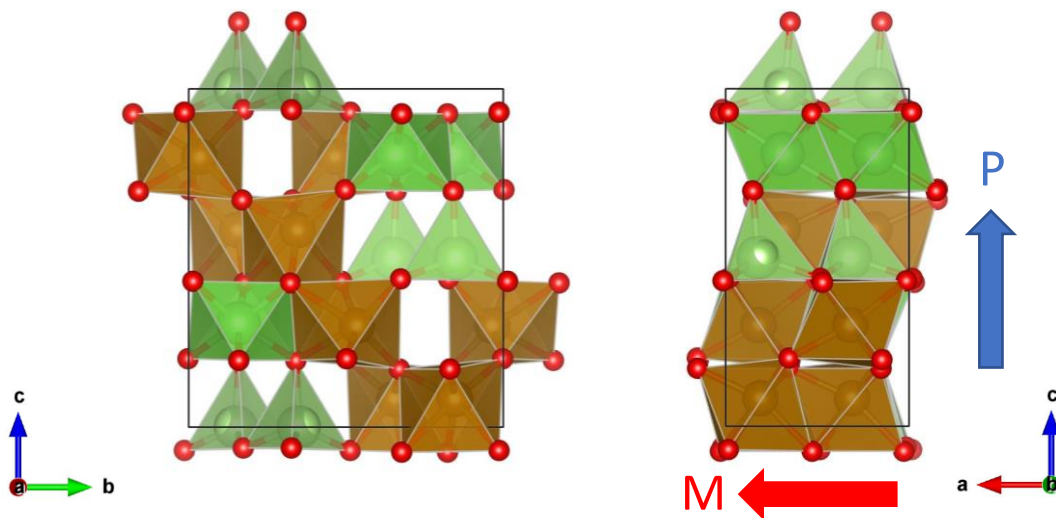


**Fig. 1.17 |** The  $GaFeO_3$  unit cell structure as viewed from the 'a' and 'b' zone axes in the  $Pna2_1$  setting. The markings P and M shows electrical polarization and magnetization easy axis, respectively.

Stoichiometry	Method	Fe/Ga in Ga1	Fe/Ga in Ga2	Fe/Ga in Fe1	Fe/Ga in Fe2
$Fe_{1.0}Ga_{1.0}O_3$ [65]	FZ	10/90	24/76	84/16	83/17
$Fe_{1.0}Ga_{1.0}O_3$ [66]	Flux	0/100	35/65	83/17	83/17
$Fe_{1.0}Ga_{1.0}O_3$ [67]	FZ	0/100	54/64	75/25	73/27
$Fe_{1.0}Ga_{1.0}O_3$ [68]	SSR	12/88	68/32	62/38	58/42
$Fe_{1.2}Ga_{0.8}O_3$ [65]	FZ	26/74	45/55	86/14	85/15
$Fe_{1.4}Ga_{0.6}O_3$ [69]	SSR	33/67	79/21	97/3	82/18

Where FZ stands for floating zone, and SSR for solid-state reaction

**Table 1 |** Fe/Ga occupation in the Ga1, Ga2, Fe1, and Fe2 cationic sites for various stoichiometries and growth methods.

### 1.3.2 Review of GFO thin film growth.

The first GFO 1.0 (001) thin films were grown in 2005 by pulsed laser deposition (PLD) by Kundaliya *et al.*, on yttrium stabilized zirconia (YSZ) (100) and YSZ buffered Si (001) substrates [70]. These studies show the compatibility of GFO 1.0 with the silicon technology. Subsequently, GFO 1.0 films were grown on other substrates such as MgO (001), Al<sub>2</sub>O<sub>3</sub> (0001) [71] and niobium-doped SrTiO<sub>3</sub> (STO:Nb) (111) [72] by Sun *et al.* in 2008. SrTiO<sub>3</sub> (STO) (111) and YSZ (100) were considered as the best substrates since the films were then oriented, with a growth in the [001] direction.

Early works concerning the growth of Ga<sub>(2-x)</sub>Fe<sub>x</sub>O<sub>3</sub> films, with x different from 1, focus on the study the effect of the Fe/Ga ratio on the structure-property characteristics. The first thin film growth of GFO 1.4 was reported on YSZ substrates by Trassin *et al.* in 2009 [73], and the growth was later expanded to STO (111) substrates by Song *et al.* in 2016 [74]. Katayama *et al.* further explored the growth of GFO 1.4 on various substrates like STO (111, 110, 100), (LaAlO<sub>3</sub>)<sub>0.3</sub>(Sr<sub>2</sub>TaAlO<sub>6</sub>)<sub>0.7</sub> (100), and KTaO<sub>3</sub> (100) in 2017 [75], but most studies have predominantly opted for the growth of GFO on YSZ (100) or STO (111).

The growth of GFO 1.0-1.4 (001) on YSZ (100) leads to 6 structural domains (variants) (Fig. 1.18 a), whereas its growth on STO (111) leads to only 3 structural domains (variants) (Fig. 1.18 b) [63,76]. The growth of GFO x as a purely single crystal (with no variants) was not possible until now, given the unfortunately multiple matchings of the GFO orthorhombic cell with the available substrates. If the in-plane mismatch is rather small for a growth on YSZ (100) (about 1 %), it is quite high for a growth on STO (111), at about 5-7 %, as shown in the calculation here below. The epitaxial relationship of GFO (001) with STO (111) is shown in Fig. 1.18 (c), as viewed from their reciprocal lattices point of view. Fig. 1.18 (c) helps understanding why there are 3 types of structural domains for a GFO growth on STO and also allows determining the lattice mismatch [77].

$$\text{mismatch along } a : \frac{\sqrt{2} a_{STO} \sin(60^\circ) - a_{GFO}}{a_{GFO}} = -6.69 \%$$

$$\text{mismatch along } b : \frac{\left(3 \frac{\sqrt{2}}{2} a_{STO}\right) - b_{GFO}}{b_{GFO}} = -5.36 \%$$

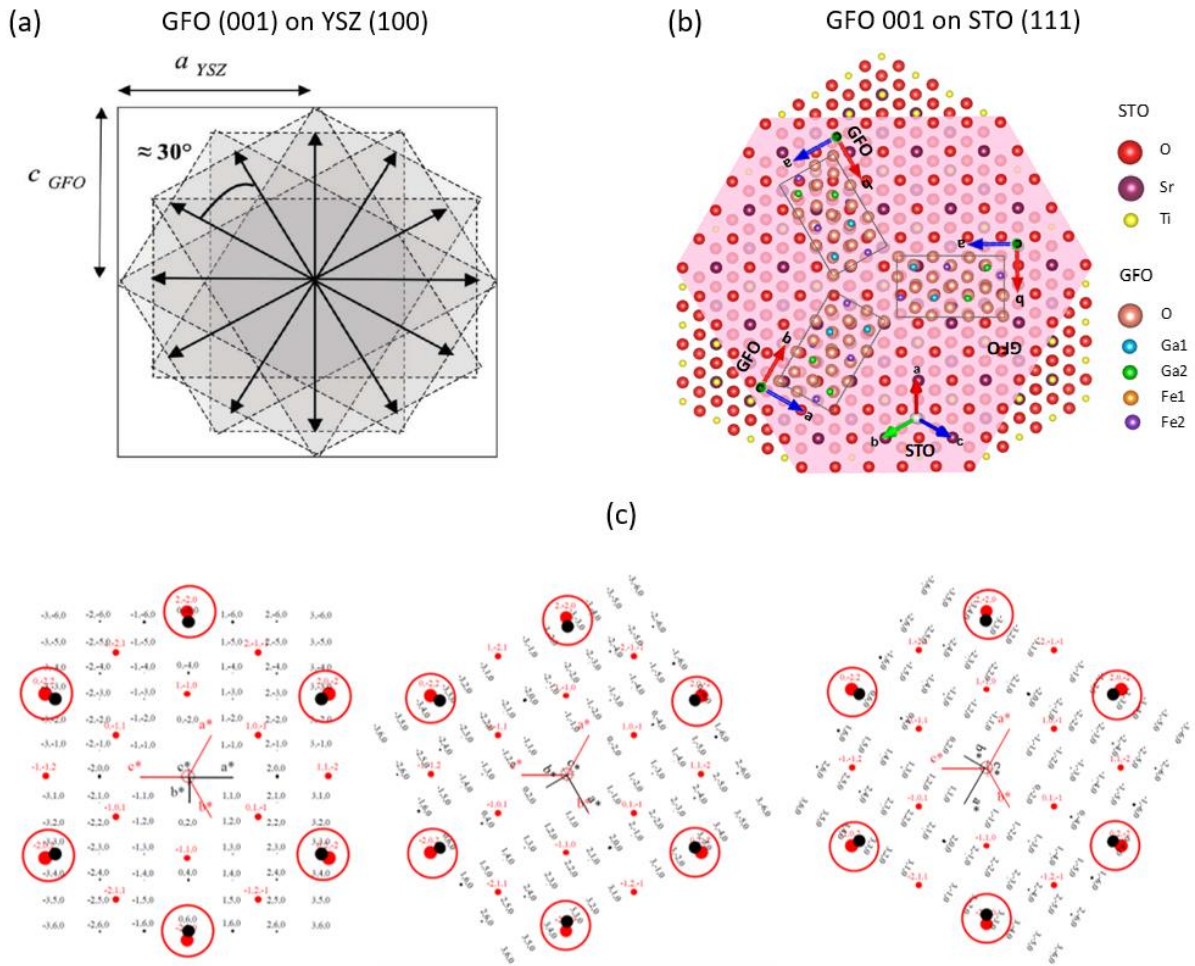


**Fig. 1.18 | Domain and epitaxial relationship of GFO thin film.** (a) The growth of 6 domains of GFO  $x(001)$  separated by  $30^\circ$  on the YSZ (100) substrate. Adapted from ref. [76]. (b) The growth of 3 domains of GFO  $x(001)$  separated by  $60^\circ$  on STO (111) substrate. Adapted from ref. [63]. (c) The three matching possibilities for the growth of GFO  $Pna2_1$  onto STO(111) as viewed from their reciprocal lattice point of view in the GFO ' $c^*$ ' direction (the reciprocal lattice of GFO is in black, that of STO in red). Adapted from ref. [63].

### 1.3.3 Magnetic properties

The magnetic properties of GFO in bulk were first reported by Remeika [60] in 1960. He defined GFO as a ferromagnetic material and demonstrated that the magnetic ordering temperature increases with the Fe content and is above room temperature for GFO 1.4. Bertaut *et al.* [78], in 1966, showed by a neutron diffraction study, that antiferromagnetic coupling exists between the Fe1 and Fe2 sites and the Fe1 and Ga2 sites, with super-exchange interactions. Levine *et al.* [79], Schellang and Rado [80], and Pinto [81] in the 1970s, further studied the magnetic anisotropy properties of GFO in detail and established that the easy magnetic axis was the ' $c$ ' axis ( $Pna2_1$ ).

This material came again into focus when Arima *et al.* studied it in 2004 and reproduced the results by Remeika concerning the increase of  $T_c$  with the Fe content, and those of Bertaut concerning the parallel and antiparallel alignments between the Ga2 and Fe2 sites moments, on the one hand, and of the Ga2 and Fe1 sites moments, on the other hand, respectively. These observations were confirmed for GFO in the form of thin films by Trassin *et al.* [73] in 2009 (Fig. 2.19 (a)). Lefevre *et al.* [69] showed by neutron diffraction on powder samples, in 2013, that the moments of Fe in the Fe1, Fe2, and Ga2 sites were of  $-3.9$ ,  $4.5$ , and  $4.7 \mu_B/\text{Fe}$ , respectively. Katayama *et al.* showed for GFO 1.4 thin films ( $>100 \text{ nm}$ ) that the saturation magnetization value is  $0.6 \mu_B/\text{Fe}$  at  $300 \text{ K}$  (Fig. 2.19 (b)) and  $1.2 \mu_B/\text{Fe}$  at  $5 \text{ K}$  and that it changes with the value of  $x$ , due to a change in cationic site occupancy in thin films [82].

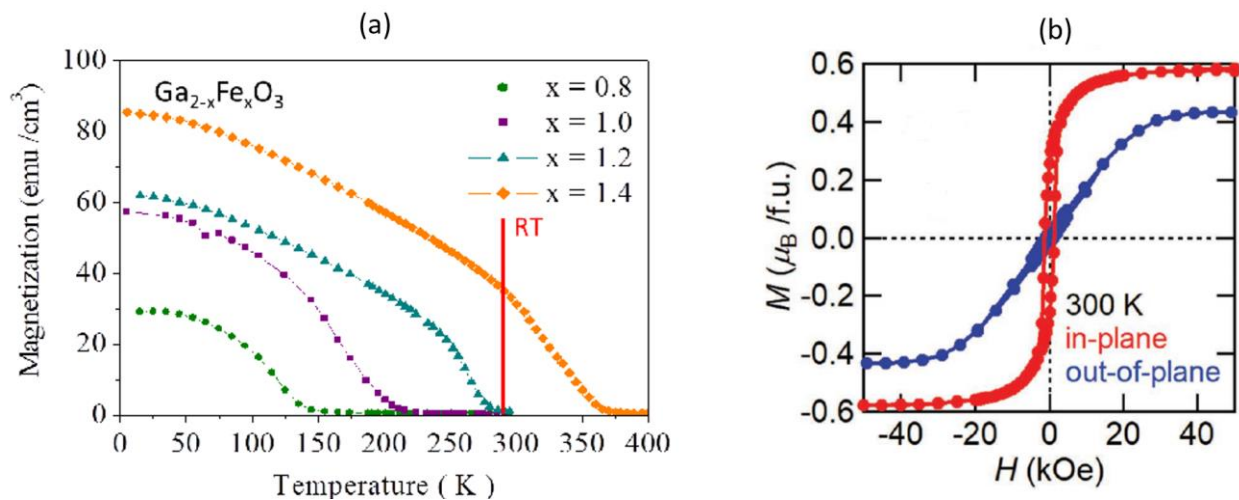


**Fig 1.19 | Magnetic properties of GFO  $x$  thin films.** (a) Curie temperature  $T_c$  for  $\text{Ga}_{2-x}\text{Fe}_x\text{O}_3$  with different  $x$  in thin films. Adapted from ref. [73]. (b) Magnetic hysteresis curves for  $x = 1.4$  at  $300 \text{ K}$  in thin films. Adapted from ref. [82].

The origin of magnetism (existence of a net magnetization) in the GFO  $x=1.0$  compound is related to the disorder in the Fe occupation among the Ga1, Fe1, Fe2, and Ga2 sites, which creates imbalanced antiferromagnetic correlations leading to an uncompensated antiferromagnetism, i.e. ferrimagnetism. Although *ab initio* calculations describe the magnetism as a fully uncompensated antiferromagnet [83,84], one study shows that the alignment is not purely antiferromagnetic and that a canted moment exists, of  $25^\circ$  with respect to the 'c' axis [85]. Recent first-principles Monte-Carlo simulations by Xu *et al.* [86] on the isomorphic compound  $\epsilon\text{-Fe}_2\text{O}_3$  (same structure as GFO, but which only contains Fe, and no Ga) show that the lowest energy state is for collinear spins at three sites and a canted spin perpendicular to each other at the fourth site (Fig. 1.20).

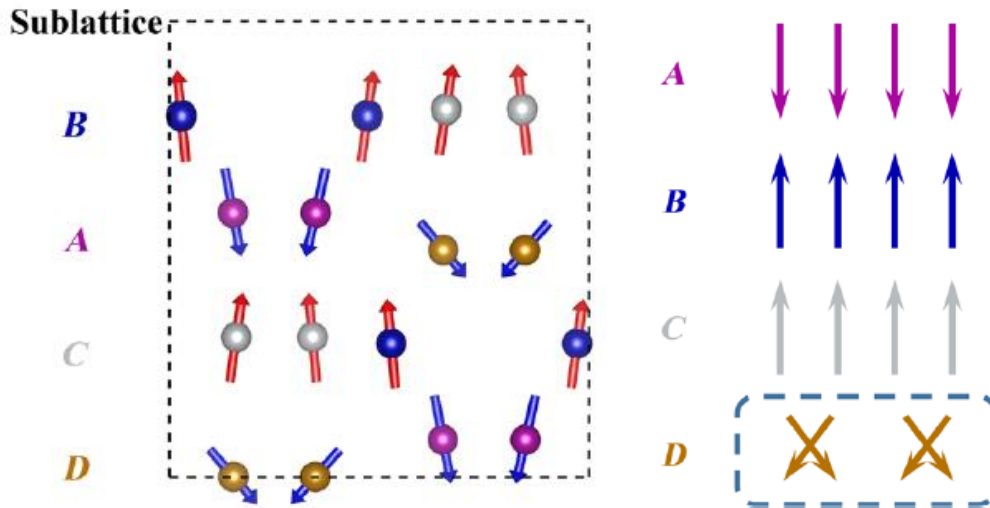


**Fig. 1.20 | Sublattice magnetization of  $\epsilon\text{-Fe}_2\text{O}_3$ .** Here only  $\text{Fe}^{3+}$  occupies A, B, and C sites of octahedral symmetry and D site, which is of tetrahedral symmetry. Adapted from ref. [86].

Regardless of the method used for the synthesis, the low temperatures magnetic hysteresis curves of GFO  $x$  thin films show a "pinch" [87,88], which normally indicates the presence of non-coupled magnetic phases with different coercivities. The studies do not show any correlation between the composition of GFO (the value of  $x$ ) and the existence of the pinch. All hysteresis curves presented in literature do not have this pinch and its origins are still being debated. The observation of a possible spin-glass behavior could explain the presence of pinch [89]. Other studies have tried to explain the phenomenon by the presence of four subnetworks, each having its anisotropy, with that of the tetrahedral site being softer than others [68], probably in a similar fashion as it has recently been calculated for the isomorphic  $\epsilon\text{-Fe}_2\text{O}_3$  (Fig. 1.20) [86]. The existence of ferrimagnetic short-order correlation above the ordering temperature of GFO also shows that perhaps the magnetic structure is more complicated, possibly linked with frustration in the system [90].

### 1.3.4 Electrical properties

The electrical measurements performed on GFO in both bulk and thin-film forms demonstrate a semiconducting behavior [91,92] with a bandgap of 2.28 eV [93]-2.7 eV [94]. Its space group  $Pna2_1$  allows ferroelectricity, but no ferroelectric behavior has been observed for single crystal GFO  $x$ . The GFO  $x$  compound has first been defined as a pyroelectric material and the reversibility of its polarization has not been shown in bulk [60]. The origin of the electric polarization was explained

by Arima *et al.* [65] as the displacement of Fe<sup>3+</sup> ions in their distorted octahedra. The movement of Fe<sup>3+</sup> ions along the 'c' axis, as measured by neutron diffraction, reveals displacements of 0.26 and -0.11 Å for the Fe1 and Fe2 sites, respectively.

The spontaneous polarization of GFO 1.0 was calculated to be 25 μC/cm<sup>2</sup> by Stoeffler using first principles methods and the modern theory of polarization [83]. Lefevre *et al.* [69] established that, in view of the positions of the cations determined by neutron diffraction experiments, the electric polarization will not decrease for an increase of the x Fe content in GFO x.

Some electrical measurements have been performed on sintered pellets of GFO 1.0 by Saha *et al.*, where they show a small polarization of ca. 0.2 μC/cm<sup>2</sup> by detecting a pyrocurrent below 100 K [95]. A study by Kundys *et al.* [96] in 2015 demonstrates a polar state for GFO 1.1 with an ordering temperature of 580 K and a polarization of 33 μC/cm<sup>2</sup>, in very good agreement with the one expected from calculations. In thin films of GFO, the electrical measurements are tricky due to the presence of important leakage currents. In an article which has become very famous [97], Scott warns about the erroneous unsaturated ferroelectric hysteresis loops related to the presence of such leakage currents. Among very few studies reporting the ferroelectric characterization of GFO in thin films, Thomasson *et al.* [98] in 2013 demonstrated a completely saturated and reversible polarization loop at room temperature in 2% Mg-doped-GFO 1.4 films grown on indium tin oxide (ITO) buffered YSZ (100). The 2% Mg doping reduced the leakage currents by four orders of magnitude. The observed polarization of 0.2 μC/cm<sup>2</sup> (Fig. 1.21) is however much lower than the expected one. Interestingly, Song *et al.* [74] in 2016 also showed room temperature ferroelectric behavior in undoped GFO 1.4 thin films grown on both ITO/YSZ (100) and SrRuO<sub>3</sub> (SRO)/STO (111) substrates (Fig. 1.22) with a polarization of 30 μC/cm<sup>2</sup>. This is in close agreement with the expected value of 25 μC/cm<sup>2</sup> from *ab initio* calculations. However, the hysteresis curves which are shown are not saturated. The peaks in the current (I) vs voltage curve (not shown here) still depict ferroelectric characteristics, but with an unusually high coercive field of more than 1100 kV cm<sup>-1</sup>, attributed to a high activation energy of the polarization switching of about 1.05 eV/f.u.. In this paper, the authors also claim the stability of the polar phase up to 1368 K, giving an indication that the ferroelectric T<sub>c</sub> is higher than that originally measured.

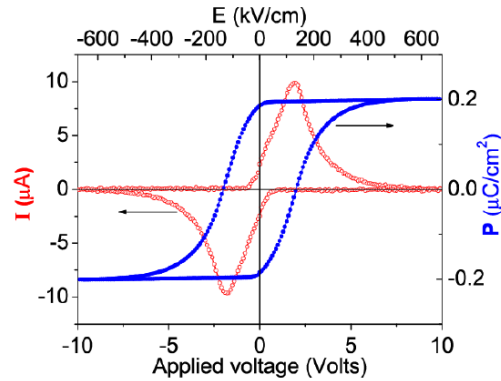


**Fig. 1.21 | Room-temperature ferroelectricity in 2% Mg-doped-GFO 1.4 grown on ITO/YSZ (100).** Adapted from ref. [98].

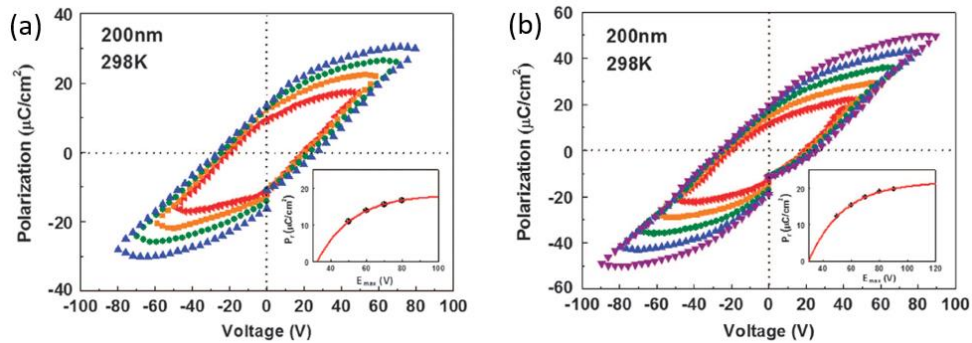


**Fig. 1.22 | Room-temperature ferroelectricity in undoped GFO 1.4 thin films.** (a) Films grown on ITO/YSZ (100). (b) Films grown on SRO/STO (111). Adapted from ref. [74].

### 1.3.5 Magneto-electric properties

The presence of a magneto-electric effect in single crystalline bulk GFO 1.0 was first experimentally demonstrated by Rado [62] in 1964. He showed the temperature evolution of the magneto-electric susceptibility obtained from the change in magnetization along the 'a' axis induced by an applied electric field along the 'c' axis, as well as from the change in polarization along the 'c' axis induced by an applied magnetic field along the 'a' axis (in  $Pna2_1$ ) (Fig. 1.23). Although the magneto-electric susceptibility reduces greatly at temperatures higher than the magnetic Curie temperature  $T_c = 270$  K, it is still present at room temperature. Arima *et al.* again revived the magneto-electric effect in GFO [65] in 2004. They qualitatively measured the magneto-electric coupling term  $\alpha = 2 * 10^{-11}$  s/m, which is one order of magnitude higher than the one observed in the antiferro-magnetic magneto-electric  $Cr_2O_3$  compound, with its  $\alpha = 4 * 10^{-12}$  s/m [62,99]. The magneto-electric coupling was found to be dominant in the tensor component  $\alpha_{ca}$  (in  $Pna2_1$ ) where the modulation of the magnetic field along the 'a' axis leads to a modulation of the

displacement of the Fe atoms at the Fe1 and Fe2 sites along the 'c' axis and hence a change in the polarization (Fig. 1.24 (b)). Several magneto-electric measurements have been performed using optical and X-ray techniques [100,101]. Kim *et al.* [66] suggest that the magneto-electric coupling can be understood by the large magneto-elasticity originating from the bond anisotropy created by the Fe atoms' exotic off-centering. Recently, Dixit *et al.* [102], confirm by *ab initio* calculations that magneto-electricity in GFO could indeed result from such an indirect mechanism. Although the magneto-electric phenomenon has been discovered in GFO x since the '60s, the effect has received relatively little attention, and measurements are limited to bulk samples. The phenomenon has not yet been established in thin films, probably due to difficulties encountered for the direct measurement and manipulation of ferroelectricity. However, with ferroelectricity established in GFO thin films, efforts should now be underway to exploit their magneto-electric properties.

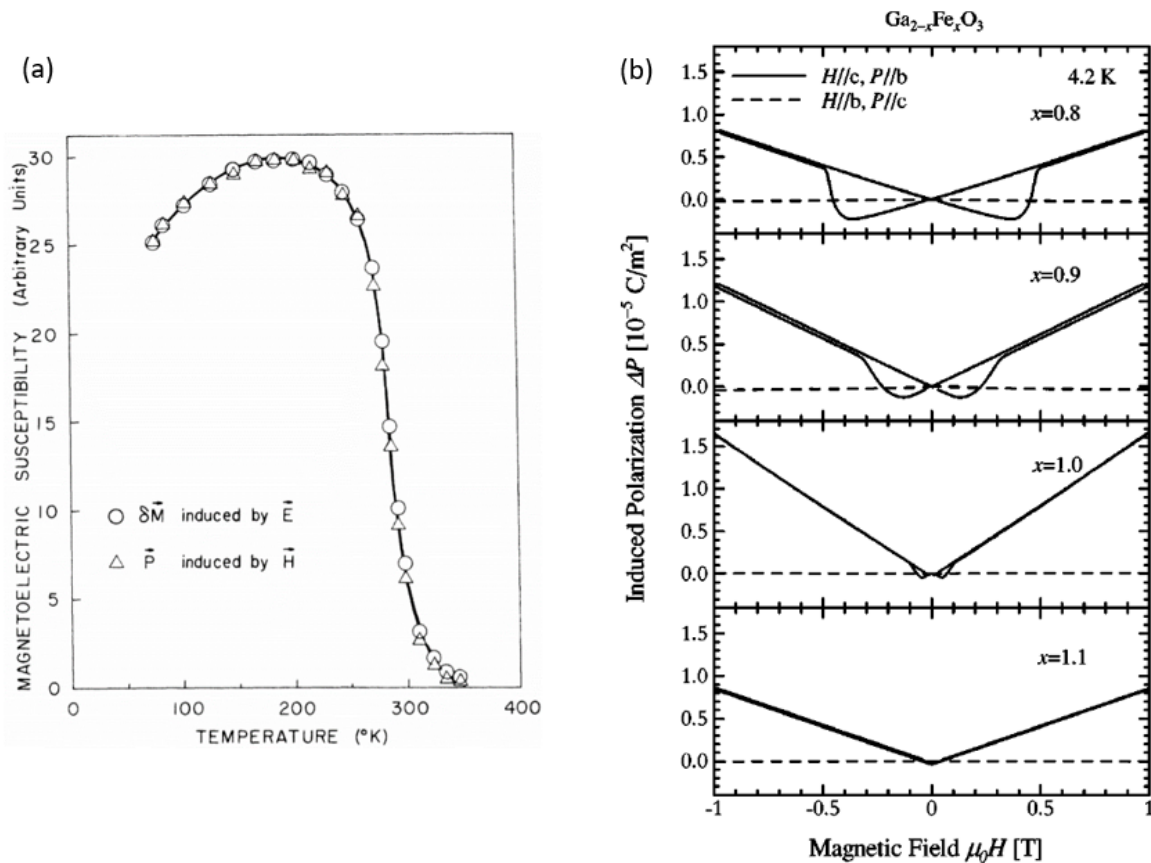


**Fig. 1.23 | Magnetolectric properties of GFO.** (a) Magnetolectric susceptibility as a function of temperature for GFO 1.0. Adapted from ref. [80]. (b) Induced polarization as a function of the applied magnetic field for  $\text{Ga}_{2-x}\text{Fe}_x\text{O}_3$  at different x values. Adapted from ref. [65].

The inorganic oxide GFO 1.4 has thus far demonstrated room-temperature multiferroic (ferrimagnetic and ferroelectric) and magneto-electric properties. These properties in a single-phased material are rare, especially at room temperature, and have thus been considered as a grail in the domain of the correlated electron systems (Fig. 1.24). The use of GFO as a multifunctional material has however been limited until now, and will be the scope of this thesis.

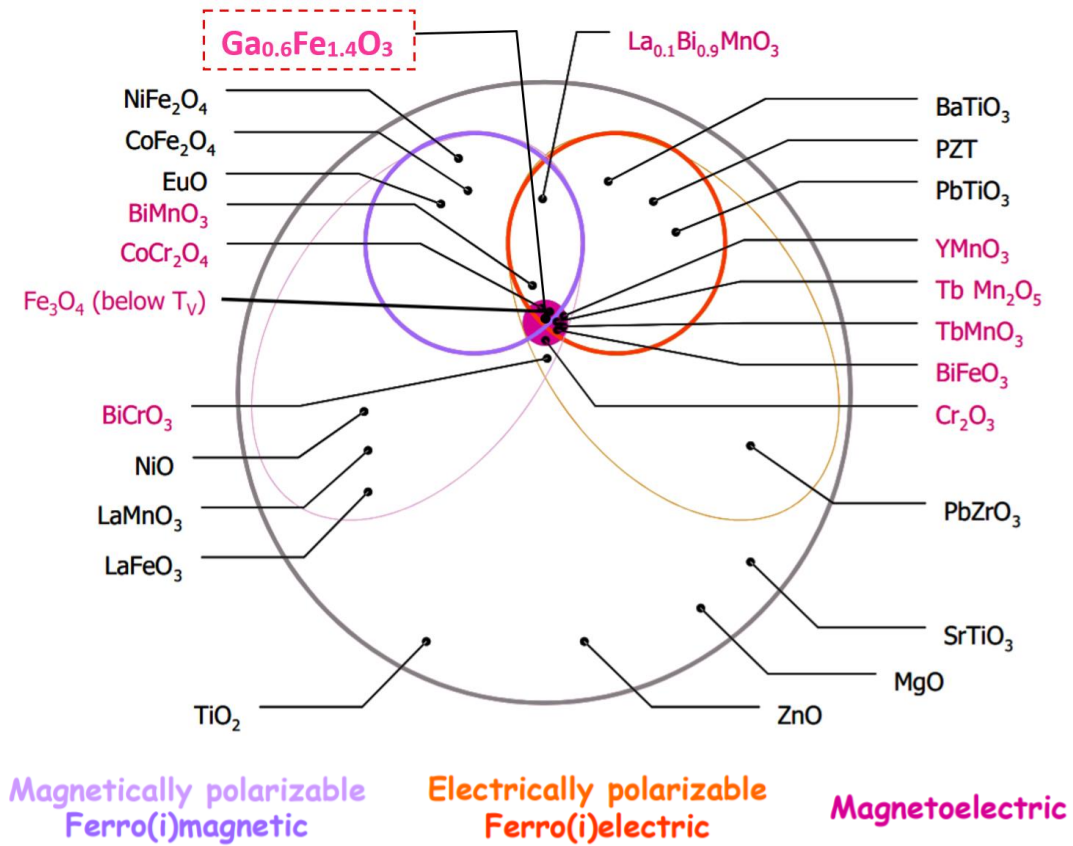


**Fig. 1.24 | A Venn diagram of materials categorized by their magnetic, electric, and magneto-electric properties. Adapted from ref. [103].**

## 1.4 Scope of the thesis

This thesis is positioned within the wider frame of an ANR project [MISSION ANR-2018], whose goal is to explore the possibility to aid the SOT-based magnetization switching possibilities with a ME effect, and thus reduce the necessary critical currents  $J_c$  and introduce new functionalities as well. The chosen ME material for this ANR project is GFO owing to its ferroelectric and ferrimagnetic properties, with a non-zero resulting magnetic moment, at room temperature.

The goal of this thesis was to :

- optimize the growth conditions for GFO 1.4 thin films to obtain an atomically smooth surface, especially at the technologically relevant sub-10 nm regimes, essential in contemporary devices to reduce interface effects after integration into heterostructures. We have performed detailed studies of the early steps of this growth through transmission electron microscopy and second harmonic generation techniques.
- explore the magnetic and ferroelectric properties of these GFO films, at both macro- and microscopic scales, and hence the functionalities they could offer at ultra-thin regimes.
- explore the functional abilities of GFO 1.4 thin films by performing magneto-transport measurements in GFO 1.4/Pt heterostructures envisaged for spin-orbit torque (SOT) memory architecture in MRAM devices (Fig. 1.25 (a)).

The ultimate goal of the ANR project 'MISSION' will be, as a prolongation to this thesis, the search for magneto-electric modulation of this SOT effect (Fig. 1.25 (b)).

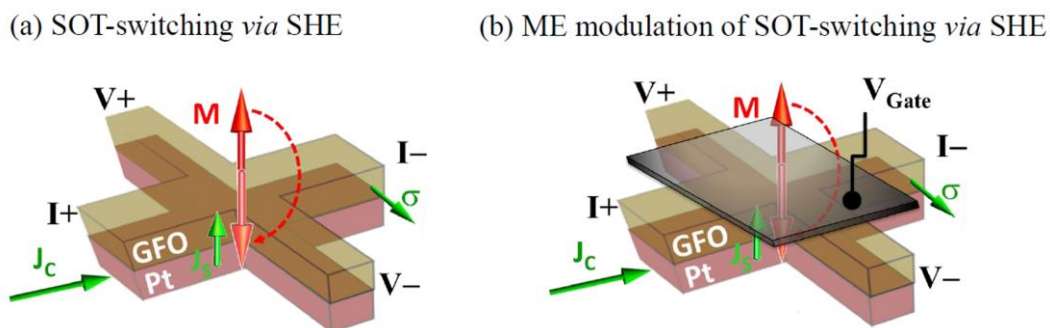


**Fig. 1.25 | Schematic of functionalities envisaged for GFO.** (a) SOT-switching of the GFO magnetization *via* spin Hall effect (SHE) in Pt. (b) Magnetolectric (ME) modulation of the SOT-switching of the GFO magnetization for low-power switching. *Schematics by Carlos-Rojas Sanchez (IJL, Nancy) for the ANR project 'MISSION'.*

## 1.5 References

- (1) Bardeen, J.; Brattain, W. H. The Transistor, a Semi-Conductor Triode. *Physical Review* **1948**, *74* (2), 230.
- (2) Shockley, W. The Theory of P-n Junctions in Semiconductors and P-n Junction Transistors. *Bell System Technical Journal* **1949**, *28* (3), 435–489.
- (3) Kilby, J. S. Miniaturized Electronic Circuits [US Patent No. 3,138, 743]. *IEEE Solid-State Circuits Society Newsletter* **2007**, *12* (2), 44–54.
- (4) Kurt, L. *Multiple Semiconductor Assembly*; Google Patents, **1962**.
- (5) Moore, G. E. *Cramming More Components onto Integrated Circuits*; McGraw-Hill New York, NY, USA, **1965**.
- (6) Association, S. I. International Technology Roadmap for Semiconductors 2005 Edition. <http://www.itrs.net>, **2006**.
- (7) Nikonov, D. E.; Young, I. A. Overview of Beyond-CMOS Devices and a Uniform Methodology for Their Benchmarking. *Proceedings of the IEEE* **2013**, *101* (12), 2498–2533.
- (8) Ramaswamy, R.; Lee, J. M.; Cai, K.; Yang, H. Recent Advances in Spin-Orbit Torques: Moving towards Device Applications. *Applied Physics Reviews* **2018**, *5* (3), 031107.
- (9) Thomson, W. XIX. On the Electro-Dynamic Qualities of Metals:—Effects of Magnetization on the Electric Conductivity of Nickel and of Iron. *Proceedings of the Royal Society of London* **1857**, No. 8, 546–550.
- (10) Moser, A.; Takano, K.; Margulies, D. T.; Albrecht, M.; Sonobe, Y.; Ikeda, Y.; Sun, S.; Fullerton, E. E. Magnetic Recording: Advancing into the Future. *Journal of Physics D: Applied Physics* **2002**, *35* (19), R157.
- (11) Su, L.; Zhang, Y.; Klein, J.-O.; Zhang, Y.; Bournel, A.; Fert, A.; Zhao, W. Current-Limiting Challenges for All-Spin Logic Devices. *Scientific reports* **2015**, *5*, 14905.
- (12) Chappert, C.; Fert, A.; Van Dau, F. N. The Emergence of Spin Electronics in Data Storage. In *Nanoscience And Technology: A Collection of Reviews from Nature Journals*; World Scientific, **2010**; pp 147–157.
- (13) Moodera, J. S.; Kinder, L. R.; Wong, T. M.; Meservey, R. Large Magnetoresistance at Room Temperature in Ferromagnetic Thin Film Tunnel Junctions. *Physical review letters* **1995**, *74* (16), 3273.
- (14) Julliere, M. Tunneling between Ferromagnetic Films. *Physics letters A* **1975**, *54* (3), 225–226.
- (15) Puebla, J.; Kim, J.; Kondou, K.; Otani, Y. Spintronic Devices for Energy-Efficient Data Storage and Energy Harvesting. *Communications Materials* **2020**, *1* (1), 1–9.
- (16) Andrae, A. S.; Edler, T. On Global Electricity Usage of Communication Technology: Trends to 2030. *Challenges* **2015**, *6* (1), 117–157.
- (17) Jones, N. How to Stop Data Centres from Gobbling up the World’s Electricity. *Nature* **2018**, *561* (7722), 163–167.
- (18) Heidecker, J. *MRAM Technology Status*; Pasadena, CA: Jet Propulsion Laboratory, National Aeronautics and Space, **2013**.
- (19) <https://www.mram-info.com/history>. Date of consultation: **29-09-2020**
- (20) Asifuzzaman, K.; Verdejo, R. S.; Radojković, P. Enabling a Reliable STT-MRAM Main Memory Simulation. In *Proceedings of the International Symposium on Memory Systems*; 2017; pp 283–292.
- (21) Trassin, M. Low Energy Consumption Spintronics Using Multiferroic Heterostructures. *Journal of Physics: Condensed Matter* **2016**, *28* (3), 033001.
- (22) Fuxi, G.; Yang, W. *Data Storage at the Nanoscale: Advances and Applications*; CRC Press, **2015**.

- (23) Manchon, A.; Miron, I. M.; Jungwirth, T.; Sinova, J.; Zelezný, J.; Thiaville, A.; Garello, K.; Gambardella, P. Current-Induced Spin-Orbit Torques in Ferromagnetic and Antiferromagnetic Systems. *arXiv:1801.09636 [cond-mat]* **2018**.
- (24) Hirsch, J. E. Spin Hall Effect. *Physical Review Letters* **1999**, *83* (9), 1834–1837.
- (25) Nagaosa, N.; Sinova, J.; Onoda, S.; MacDonald, A. H.; Ong, N. P. Anomalous Hall Effect. *Reviews of modern physics* **2010**, *82* (2), 1539.
- (26) Hoffmann, A. Spin Hall Effects in Metals. *IEEE transactions on magnetics* **2013**, *49* (10), 5172–5193.
- (27) Sinova, J.; Valenzuela, S. O.; Wunderlich, J.; Back, C. H.; Jungwirth, T. Spin Hall Effects. *Reviews of Modern Physics* **2015**, *87* (4), 1213–1260.
- (28) Yuasa, S.; Nagahama, T.; Fukushima, A.; Suzuki, Y.; Ando, K. Giant Room-Temperature Magnetoresistance in Single-Crystal Fe/MgO/Fe Magnetic Tunnel Junctions. *Nature Materials* **2004**, *3* (12), 868–871.
- (29) Trassin, M. Low Energy Consumption Spintronics Using Multiferroic Heterostructures. *J. Phys.: Condens. Matter* **2016**, *28* (3), 033001.
- (30) Borgatti, F.; Bergenti, I.; Bona, F.; Dediu, V.; Fondacaro, A.; Huotari, S.; Monaco, G.; MacLaren, D. A.; Chapman, J. N.; Panaccione, G. Understanding the Role of Tunneling Barriers in Organic Spin Valves by Hard X-Ray Photoelectron Spectroscopy. *Appl. Phys. Lett.* **2010**, *96* (4), 043306.
- (31) Barthélémy, M.; Bibes, A. Multiferroics: Towards a Magnetoelectric Memory. *Nat. Mater* **2008**, *7*, 425–426.
- (32) Meisenheimer, P. B.; Novakov, S.; Vu, N. M.; Heron, J. T. Perspective: Magnetoelectric Switching in Thin Film Multiferroic Heterostructures. *Journal of Applied Physics* **2018**, *123* (24), 240901.
- (33) Wu, T.; Bur, A.; Wong, K.; Leon Hockel, J.; Hsu, C.-J.; Kim, H. K.; Wang, K. L.; Carman, G. P. Electric-Poling-Induced Magnetic Anisotropy and Electric-Field-Induced Magnetization Reorientation in Magnetoelectric Ni/[Pb(Mg<sub>1/3</sub>Nb<sub>2/3</sub>)O<sub>3</sub>]<sub>(1-x)</sub>-[PbTiO<sub>3</sub>]<sub>x</sub> (011) Heterostructure. *Journal of applied physics* **2011**, *109* (7), 07D732.
- (34) Parkes, D. E.; Cavill, S. A.; Hindmarch, A. T.; Wadley, P.; McGee, F.; Staddon, C. R.; Edmonds, K. W.; Champion, R. P.; Gallagher, B. L.; Rushforth, A. W. Non-Volatile Voltage Control of Magnetization and Magnetic Domain Walls in Magnetostrictive Epitaxial Thin Films. *Applied Physics Letters* **2012**, *101* (7), 072402.
- (35) Cai, K.; Yang, M.; Ju, H.; Wang, S.; Ji, Y.; Li, B.; Edmonds, K. W.; Sheng, Y.; Zhang, B.; Zhang, N. Electric Field Control of Deterministic Current-Induced Magnetization Switching in a Hybrid Ferromagnetic/Ferroelectric Structure. *Nature materials* **2017**, *16* (7), 712–716.
- (36) Bibes, M.; Barthelemy, A. Oxide Spintronics. *IEEE Transactions on Electron Devices* **2007**, *54* (5), 1003–1023.
- (37) Bibes, M.; Villegas, J. E.; Barthelemy, A. Ultrathin Oxide Films and Interfaces for Electronics and Spintronics. *Advances in Physics* **2011**, *60* (1), 5–84.
- (38) Ikeda, S.; Hayakawa, J.; Ashizawa, Y.; Lee, Y. M.; Miura, K.; Hasegawa, H.; Tsunoda, M.; Matsukura, F.; Ohno, H. Tunnel Magnetoresistance of 604% at 300 K by Suppression of Ta Diffusion in CoFeB/MgO/CoFeB Pseudo-Spin-Valves Annealed at High Temperature. *Applied Physics Letters* **2008**, *93* (8), 082508.
- (39) Basletic, M.; Maurice, J.-L.; Carrétéro, C.; Herranz, G.; Copie, O.; Bibes, M.; Jacquet, É.; Bouzehouane, K.; Fusil, S.; Barthélémy, A. Mapping the Spatial Distribution of Charge Carriers in LaAlO<sub>3</sub>/SrTiO<sub>3</sub> Heterostructures. *Nature materials* **2008**, *7* (8), 621–625.
- (40) Lesne, E.; Fu, Y.; Oyarzun, S.; Rojas-Sánchez, J. C.; Vaz, D. C.; Naganuma, H.; Sicoli, G.; Attané, J.-P.; Jamet, M.; Jacquet, E. Highly Efficient and Tunable Spin-to-Charge Conversion through Rashba Coupling at Oxide Interfaces. *Nature materials* **2016**, *15* (12), 1261–1266.

- (41) Bowen, M.; Bibes, M.; Barthélémy, A.; Contour, J.-P.; Anane, A.; Lemaitre, Y.; Fert, A. Nearly Total Spin Polarization in  $\text{La}_{2/3}\text{Sr}_{1/3}\text{MnO}_3$  from Tunneling Experiments. *Applied Physics Letters* **2003**, *82* (2), 233–235.
- (42) Gellé, F. Hétérostructures Épitaxiées Avec Des Propriétés Dépendantes de Spin et de Charges Pour Des Applications En Spintronique, Thesis, University of Strasbourg, **2019**.
- (43) Marún, I. V.; Postma, F. M.; Lodder, J. C.; Jansen, R. Tunneling Magnetoresistance with Positive and Negative Sign in  $\text{La}_{0.67}\text{Sr}_{0.33}\text{MnO}_3/\text{SrTiO}_3/\text{Co}$  Junctions. *Physical Review B* **2007**, *76* (6), 064426.
- (44) Hahn, C.; de Loubens, G.; Klein, O.; Viret, M.; Naletov, V. V.; Ben Youssef, J. Comparative Measurements of Inverse Spin Hall Effects and Magnetoresistance in YIG/Pt and YIG/Ta. *Phys. Rev. B* **2013**, *87* (17), 174417.
- (45) Collet, M.; De Milly, X.; Kelly, O. d'Allivy; Naletov, V. V.; Bernard, R.; Bortolotti, P.; Youssef, J. B.; Demidov, V. E.; Demokritov, S. O.; Prieto, J. L. Generation of Coherent Spin-Wave Modes in Yttrium Iron Garnet Microdisks by Spin–Orbit Torque. *Nature communications* **2016**, *7* (1), 1–8.
- (46) Emori, S.; Nan, T.; Belkessam, A. M.; Wang, X.; Matyushov, A. D.; Babroski, C. J.; Gao, Y.; Lin, H.; Sun, N. X. Interfacial Spin-Orbit Torque without Bulk Spin-Orbit Coupling. *Phys. Rev. B* **2016**, *93* (18), 180402.
- (47) Castel, V.; Vlietstra, N.; van Wees, B. J.; Youssef, J. B. Frequency and Power Dependence of Spin-Current Emission by Spin Pumping in a Thin-Film YIG/Pt System. *Physical Review B* **2012**, *86* (13).
- (48) Wang, H. L.; Du, C. H.; Pu, Y.; Adur, R.; Hammel, P. C.; Yang, F. Y. Scaling of Spin Hall Angle in 3d, 4d, and 5d Metals from  $\text{Y}_3\text{Fe}_5\text{O}_{12}$ /Metal Spin Pumping. *Physical review letters* **2014**, *112* (19), 197201.
- (49) Santos, O. A.; Silva, E. F.; Gamino, M.; Mendes, J. B. S.; Rezende, S. M.; Azevedo, A. Investigation of Large Enhancement of Spin Hall Angle in Heterostructures of Ag Nanoparticles Randomly Grown in Pt. *AIP Advances* **2019**, *9* (3), 035025.
- (50) Garcia, V.; Bibes, M. Ferroelectric Tunnel Junctions for Information Storage and Processing. *Nature communications* **2014**, *5* (1), 1–12.
- (51) Velez, J. P.; Duan, C.-G.; Burton, J. D.; Smogunov, A.; Niranjana, M. K.; Tosatti, E.; Jaswal, S. S.; Tsymbal, E. Y. Magnetic Tunnel Junctions with Ferroelectric Barriers: Prediction of Four Resistance States from First Principles. *Nano letters* **2009**, *9* (1), 427–432.
- (52) Spaldin, N. A.; Fiebig, M. The Renaissance of Magnetoelectric Multiferroics. *Science* **2005**, *309* (5733), 391–392.
- (53) Fusil, S.; Garcia, V.; Barthélémy, A.; Bibes, M. Magnetoelectric Devices for Spintronics. *Annual Review of Materials Research* **2014**, *44* (1), 91–116.
- (54) Spaldin, N. A.; Ramesh, R. Advances in Magnetoelectric Multiferroics. *Nature materials* **2019**, *18* (3), 203.
- (55) Wang, J.; Neaton, J. B.; Zheng, H.; Nagarajan, V.; Ogale, S. B.; Liu, B.; Viehland, D.; Vaithyanathan, V.; Schlom, D. G.; Waghmare, U. V. Epitaxial  $\text{BiFeO}_3$  Multiferroic Thin Film Heterostructures. *science* **2003**, *299* (5613), 1719–1722.
- (56) Béa, H.; Bibes, M.; Petit, S.; Kreisel, J.; Barthélémy, A. Structural Distortion and Magnetism of  $\text{BiFeO}_3$  Epitaxial Thin Films: A Raman Spectroscopy and Neutron Diffraction Study. *Philosophical Magazine Letters* **2007**, *87* (3–4), 165–174.
- (57) Chu, Y.-H.; Martin, L. W.; Holcomb, M. B.; Gajek, M.; Han, S.-J.; He, Q.; Balke, N.; Yang, C.-H.; Lee, D.; Hu, W. Electric-Field Control of Local Ferromagnetism Using a Magnetoelectric Multiferroic. *Nature materials* **2008**, *7* (6), 478–482.
- (58) Heron, J. T.; Bosse, J. L.; He, Q.; Gao, Y.; Trassin, M.; Ye, L.; Clarkson, J. D.; Wang, C.; Liu, J.; Salahuddin, S.; Ralph, D. C.; Schlom, D. G.; Íñiguez, J.; Huey, B. D.; Ramesh, R. Deterministic Switching of Ferromagnetism at Room Temperature Using an Electric Field. *Nature* **2014**, *516* (7531), 370–373.

- (59) Manipatruni, S.; Nikonov, D. E.; Lin, C.-C.; Gosavi, T. A.; Liu, H.; Prasad, B.; Huang, Y.-L.; Bonturim, E.; Ramesh, R.; Young, I. A. Scalable Energy-Efficient Magnetoelectric Spin–Orbit Logic. *Nature* **2018**.
- (60) Remeika, J. P. GaFeO<sub>3</sub>: A Ferromagnetic-Piezoelectric Compound. *Journal of Applied Physics* **1960**, *31* (5), S263–S264.
- (61) Abrahams, S. C.; Reddy, J. M. Magnetic, Electric, and Crystallographic Properties of Gallium Iron Oxide. *Physical Review Letters* **1964**, *13* (23), 688.
- (62) Rado, G. T. Observation and Possible Mechanisms of Magnetoelectric Effects in a Ferromagnet. *Physical Review Letters* **1964**, *13* (10), 335.
- (63) Demchenko, A. Investigation of the Potential Offered by Gallium Iron Oxide Thin Films in Terms of Multiferroicity, Thesis, University of Strasbourg, **2015**.
- (64) Thomasson, A.; Ibrahim, F.; Lefevre, C.; Autissier, E.; Roulland, F.; Mény, C.; Leuvrey, C.; Choi, S.; Jo, W.; Crégut, O. Effects of Iron Concentration and Cationic Site Disorder on the Optical Properties of Magnetoelectric Gallium Ferrite Thin Films. *RSC advances* **2013**, *3* (9), 3124–3130.
- (65) Arima, T.; Higashiyama, D.; Kaneko, Y.; He, J. P.; Goto, T.; Miyasaka, S.; Kimura, T.; Oikawa, K.; Kamiyama, T.; Kumai, R. Structural and Magnetoelectric Properties of Ga<sub>2-x</sub>Fe<sub>x</sub>O<sub>3</sub> Single Crystals Grown by a Floating-Zone Method. *Physical Review B* **2004**, *70* (6), 064426.
- (66) Kim, J.-Y.; Koo, T. Y.; Park, J.-H. Orbital and Bonding Anisotropy in a Half-Filled GaFeO<sub>3</sub> Magnetoelectric Ferrimagnet. *Phys. Rev. Lett.* **2006**, *96* (4), 047205.
- (67) Hatnean, M.; Robert, J.; Diaz, M. F.; Ressouche, E.; Cousson, A.; Pinsard-Gaudart, L.; Petit, S. Neutron Scattering Study of the Magnetoelectric Compound GaFeO<sub>3</sub>. *The European Physical Journal Special Topics* **2012**, *213* (1), 69–76.
- (68) Sharma, K.; Reddy, V. R.; Gupta, A.; Kaushik, S. D.; Siruguri, V. Anomalous Variation of the Lamb–Mössbauer Factor at the Magnetic Transition Temperature in Magnetoelectric GaFeO<sub>3</sub>. *Journal of Physics: Condensed Matter* **2012**, *24* (37), 376001.
- (69) Lefevre, C.; Roulland, F.; Thomasson, A.; Meny, C.; Porcher, F.; André, G.; Viart, N. Magnetic and Polar Properties’ Optimization in the Magnetoelectric Ga<sub>2-x</sub>Fe<sub>x</sub>O<sub>3</sub> Compounds. *The Journal of Physical Chemistry C* **2013**, *117* (28), 14832–14839.
- (70) Kundaliya, D. C.; Ogale, S. B.; Dhar, S.; McDonald, K. F.; Knoesel, E.; Osedach, T.; Lofland, S. E.; Shinde, S. R.; Venkatesan, T. Large Second-Harmonic Kerr Rotation in GaFeO<sub>3</sub> Thin Films on YSZ Buffered Silicon. *Journal of Magnetism and Magnetic Materials* **2006**, *299* (2), 307–311. <https://doi.org/10.1016/j.jmmm.2005.04.017>.
- (71) Sun, Z. H.; Dai, S.; Zhou, Y. L.; Cao, L. Z.; Chen, Z. H. Elaboration and Optical Properties of GaFeO<sub>3</sub> Thin Films. *Thin Solid Films* **2008**, *516* (21), 7433–7436.
- (72) Sun, Z. H.; Zhou, Y. L.; Dai, S. Y.; Cao, L. Z.; Chen, Z. H. Preparation and Properties of GaFeO<sub>3</sub> Thin Films Grown at Various Oxygen Pressures by Pulsed Laser Deposition. *Applied Physics A* **2008**, *91* (1), 97–100.
- (73) Trassin, M.; Viart, N.; Versini, G.; Barre, S.; Pourroy, G.; Lee, J.; Jo, W.; Dumesnil, K.; Dufour, C.; Robert, S. Room Temperature Ferrimagnetic Thin Films of the Magnetoelectric Ga<sub>2-x</sub>Fe<sub>x</sub>O<sub>3</sub>. *J. Mater. Chem.* **2009**, *19* (46), 8876–8880.
- (74) Song, S.; Jang, H. M.; Lee, N.-S.; Son, J. Y.; Gupta, R.; Garg, A.; Ratanapreechachai, J.; Scott, J. F. Ferroelectric Polarization Switching with a Remarkably High Activation Energy in Orthorhombic GaFeO<sub>3</sub> Thin Films. *NPG Asia Materials* **2016**, *8* (2), e242–e242.
- (75) Katayama, T.; Yasui, S.; Hamasaki, Y.; Itoh, M. Control of Crystal-Domain Orientation in Multiferroic Ga<sub>0.6</sub>Fe<sub>1.4</sub>O<sub>3</sub> Epitaxial Thin Films. *Applied Physics Letters* **2017**, *110* (21), 212905.
- (76) Trassin, M. Couches Minces de Ga<sub>2-x</sub>Fe<sub>x</sub>O<sub>3</sub> Par Ablation Laser Pulsée: Vers Un Matériau Magnétoélectrique à Température Ambiante, Thesis, University of Strasbourg, 2009.

- (77) Homkar, S.; Preziosi, D.; Devaux, X.; Bouillet, C.; Nordlander, J.; Trassin, M.; Roulland, F.; Lefèvre, C.; Versini, G.; Barre, S. Ultrathin Regime Growth of Atomically Flat Multiferroic Gallium Ferrite Films with Perpendicular Magnetic Anisotropy. *Physical Review Materials* **2019**, *3* (12), 124416.
- (78) Bertaut, E. F.; Bassi, G.; Buisson, G.; Chappert, J.; Delapalme, A.; Pauthenet, R.; Rebouillat, H. P.; Aleonard, R. Étude Par Effet Mössbauer, Rayons X, Diffraction Neutronique et Mesures Magnétiques de  $\text{Fe}_{1.15}\text{Ga}_{0.85}\text{O}_3$ . *Journal de Physique* **1966**, *27* (7–8), 433–448.
- (79) Levine, B. F.; Nowlin, C. H.; Jones, R. V. Magnetic Properties of  $\text{Ga}_{2-x}\text{Fe}_x\text{O}_3$ . *Physical Review* **1968**, *174* (2), 571.
- (80) Schelleng, J. H.; Rado, G. T. Direct Measurements of Anisotropy Energy and Anisotropic Magnetization in Gallium Iron Oxide. *Physical Review* **1969**, *179* (2), 541.
- (81) Pinto, A. Magnetization and Anisotropy in Gallium Iron Oxide. *Journal of Applied Physics* **1966**, *37* (12), 4372–4376.
- (82) Katayama, T.; Yasui, S.; Hamasaki, Y.; Shiraishi, T.; Akama, A.; Kiguchi, T.; Itoh, M. Ferroelectric and Magnetic Properties in Room-Temperature Multiferroic  $\text{Ga}_x\text{Fe}_{2-x}\text{O}_3$  Epitaxial Thin Films. *Advanced Functional Materials* **2018**, *28* (2), 1704789.
- (83) Stoeffler, D. First Principles Study of the Electric Polarization and of Its Switching in the Multiferroic  $\text{GaFeO}_3$  System. *Journal of Physics: Condensed Matter* **2012**, *24* (18), 185502.
- (84) Stoeffler, D. First Principles Study of the Spontaneous Electric Polarization in  $\text{Ga}_{2-x}\text{Fe}_x\text{O}_3$ . *Thin Solid Films* **2013**, *533*, 93–96.
- (85) Nakamura, S.; Morimoto, S.; Saito, T.; Tsunoda, Y. Mössbauer Study on the Polar Ferrimagnet  $\text{GaFeO}_3$ . In *Journal of Physics: Conference Series*; 2010; Vol. 200, p 012140.
- (86) Xu, K.; Feng, J. S.; Liu, Z. P.; Xiang, H. J. Origin of Ferrimagnetism and Ferroelectricity in Room-Temperature Multiferroic  $\epsilon\text{-Fe}_2\text{O}_3$ . *Phys. Rev. Applied* **2018**, *9* (4), 044011.
- (87) Sharma, K.; Reddy, V. R.; Kothari, D.; Gupta, A.; Banerjee, A.; Sathe, V. G. Low Temperature Raman and High Field  $^{57}\text{Fe}$  Mossbauer Study of Polycrystalline  $\text{GaFeO}_3$ . *Journal of Physics: Condensed Matter* **2010**, *22* (14), 146005.
- (88) Sharma, K.; Reddy, V. R.; Gupta, A.; Banerjee, A.; Awasthi, A. M. Magnetic and  $^{57}\text{Fe}$  Mössbauer Study of Magneto-Electric  $\text{GaFeO}_3$  Prepared by the Sol–Gel Route. *Journal of Physics: Condensed Matter* **2013**, *25* (7), 076002.
- (89) Singh, V.; Mukherjee, S.; Mitra, C.; Garg, A.; Gupta, R. Aging and Memory Effect in Magnetoelectric Gallium Ferrite Single Crystals. *Journal of Magnetism and Magnetic Materials* **2015**, *375*, 49–53.
- (90) Gruener, G.; Vitucci, F.; Calvani, P.; Soret, J.-C. Evidence of Large Nonlinear Magnetic Effects in the Paramagnetic Phase of  $\text{GaFeO}_3$ . *Physical Review B* **2011**, *84* (22), 224427.
- (91) Naik, V. B.; Mahendiran, R. Electrical, Magnetic, Magnetodielectric, and Magnetoabsorption Studies in Multiferroic  $\text{GaFeO}_3$ . *Journal of Applied Physics* **2009**, *106* (12), 123910.
- (92) Dugu, S.; Bhattarai, M. K.; Kumari, S.; Instan, A. A.; Pradhan, D. K.; Holcomb, M.; Scott, J. F.; Katiyar, R. S. Observation of Relaxor-Ferroelectric Behavior in Gallium Ferrite Thin Films. *Applied Surface Science* **2020**, 146459.
- (93) Roy, A.; Prasad, R.; Auluck, S.; Garg, A. Effect of Site-Disorder on Magnetism and Magneto-Structural Coupling in Gallium Ferrite: A First-Principles Study. *Journal of Applied Physics* **2012**, *111* (4), 043915.
- (94) Kalashnikova, A. M.; Pisarev, R. V.; Bezmaternykh, L. N.; Temerov, V. L.; Kirilyuk, A.; Rasing, Th. Optical and Magneto-Optical Studies of a Multiferroic  $\text{GaFeO}_3$  with a High Curie Temperature. *Jetp Lett.* **2005**, *81* (9), 452–457.
- (95) Saha, R.; Shireen, A.; Shirodkar, S. N.; Waghmare, U. V.; Sundaresan, A.; Rao, C. N. R. Multiferroic and Magnetoelectric Nature of  $\text{GaFeO}_3$ ,  $\text{AlFeO}_3$  and Related Oxides. *Solid State Communications* **2012**, *152* (21), 1964–1968.

- (96) Kundys, B.; Roulland, F.; Lefèvre, C.; Mény, C.; Thomasson, A.; Viart, N. Room Temperature Polarization in the Ferrimagnetic  $\text{Ga}_{2-x}\text{Fe}_x\text{O}_3$  Ceramics. *Journal of the European Ceramic Society* **2015**, *35* (8), 2277–2281.
- (97) Scott, J. F. Ferroelectrics Go Bananas. *Journal of Physics: Condensed Matter* **2007**, *20* (2), 021001.
- (98) Thomasson, A.; Cherifi, S.; Lefevre, C.; Roulland, F.; Gautier, B.; Albertini, D.; Meny, C.; Viart, N. Room Temperature Multiferroicity in  $\text{Ga}_{0.6}\text{Fe}_{1.4}\text{O}_3$ : Mg Thin Films. *Journal of Applied Physics* **2013**, *113* (21), 214101.
- (99) Brown Jr, W. F.; Hornreich, R. M.; Shtrikman, S. Upper Bound on the Magnetoelectric Susceptibility. *Physical Review* **1968**, *168* (2), 574.
- (100) Igarashi, J.; Nagao, T. Second Harmonic Generation in a Polar Ferrimagnet  $\text{GaFeO}_3$ . *Phys. Rev. B* **2010**, *82* (2), 024424.
- (101) Jung, J. H.; Matsubara, M.; Arima, T.; He, J. P.; Kaneko, Y.; Tokura, Y. Optical Magnetoelectric Effect in the Polar  $\text{GaFeO}_3$  Ferrimagnet. *Physical review letters* **2004**, *93* (3), 037403.
- (102) Dixit, A.; Stoeffler, D.; Alouani, M. Effect of Site Disorder on the Electronic, Magnetic, and Ferroelectric Properties of Gallium Ferrite. *Physical Review Materials* **2020**, *4* (7), 074406.
- (103) Béa, H.; Gajek, M.; Bibes, M.; Barthélémy, A. Spintronics with Multiferroics. *Journal of Physics: Condensed Matter* **2008**, *20* (43), 434221.



---

## Chapter 2

# Ga<sub>0.6</sub>Fe<sub>1.4</sub>O<sub>3</sub> thin films : growth issues

---

Our first aim within this thesis work was to demonstrate the growth of Ga<sub>0.6</sub>Fe<sub>1.4</sub>O<sub>3</sub> (GFO) thin films on SrTiO<sub>3</sub> (STO) substrates with an atomically smooth surface. As mentioned in the introduction, the growth of an atomically flat surface is required to further build high-quality, smooth interfaces with an adjacent layer. The idea is to favor the transfer of spin angular momentum in GFO from an adjacent Pt layer.

In this chapter, we will first see the methods used to grow, characterize, and optimize the GFO thin films. We will describe the reasons for the choice of STO as a substrate to grow GFO thin films and the effect of various growth conditions on the quality of the GFO thin films. We have performed an in-depth investigation of the GFO/STO interface quality using microscopic techniques and unveiled some issues which can have a wide relevance for all depositions on STO substrates. We will also present a study of the growth of GFO onto a SrRuO<sub>3</sub> (SRO) buffer layer when an SRO electrode is introduced between STO and GFO.

## 2.1 Methods

### 2.1.1 Pulsed Laser Deposition (PLD)

We used the pulsed laser deposition (PLD) technique to grow GFO thin films because it is a well-proven tool for the high-quality growth of multifunctional oxides, in which many parameters can be finely tuned to obtain the desired quality of thin films and interfaces <sup>[1]</sup>. The PLD technique allows the growth of complex crystalline structures on suitable substrates by ablating a polycrystalline target with a high energy laser under a set of controlled parameters. One of the PLD's key advantages is that it is known to allow a stoichiometric transfer of matter from the target to the film. It is thus the ideal deposition method for complex oxides. On the other hand, a drawback of this technique is the limited surface on which the sample is homogeneous (about 1 mm<sup>2</sup>), but successful efforts have been made to address this issue by demonstrating industrial scale 300 mm<sup>2</sup> wafer capabilities in some systems <sup>[2,3]</sup>.

The PLD chamber we used in our experiments was commercially obtained from the TSST company and has a base pressure of  $2 \times 10^{-8}$  mbar. The schematic of the laboratory PLD set-up is shown in Fig. 2.1 (a, c). Before the deposition, the STO (111) substrates were cleaned with acetone and isopropanol and stucked on the heater using silver paste for efficient heat conduction. The GFO polycrystalline target used for growth is prepared using the ceramic method described in <sup>[4]</sup>. The distance between the target and the substrate is fixed at 55 mm. A 248 nm KrF excimer laser beam is focused onto the GFO target with a laser fluence of 3.5 J/cm<sup>2</sup>. The laser beam ablates the target to create a plume (See Fig. 2.1 (b)) composed of energetic ionic species ejected from the GFO target. These ejected species deposit on the STO substrate to form the GFO thin film.

To optimize our GFO thin films growth, we varied parameters such as the oxygen pressure (which has an effect on the trajectory of the ejected ions in the plasma, and on the oxygen stoichiometry in the film); the temperature of the substrate (which has an effect on the crystallization and kinetics of the growth); the fluence (which administers the size of the plume and the energy of the ejected species); the laser repetition rate (which controls the growth rate), and the pulse count (which controls the thickness of the thin film).

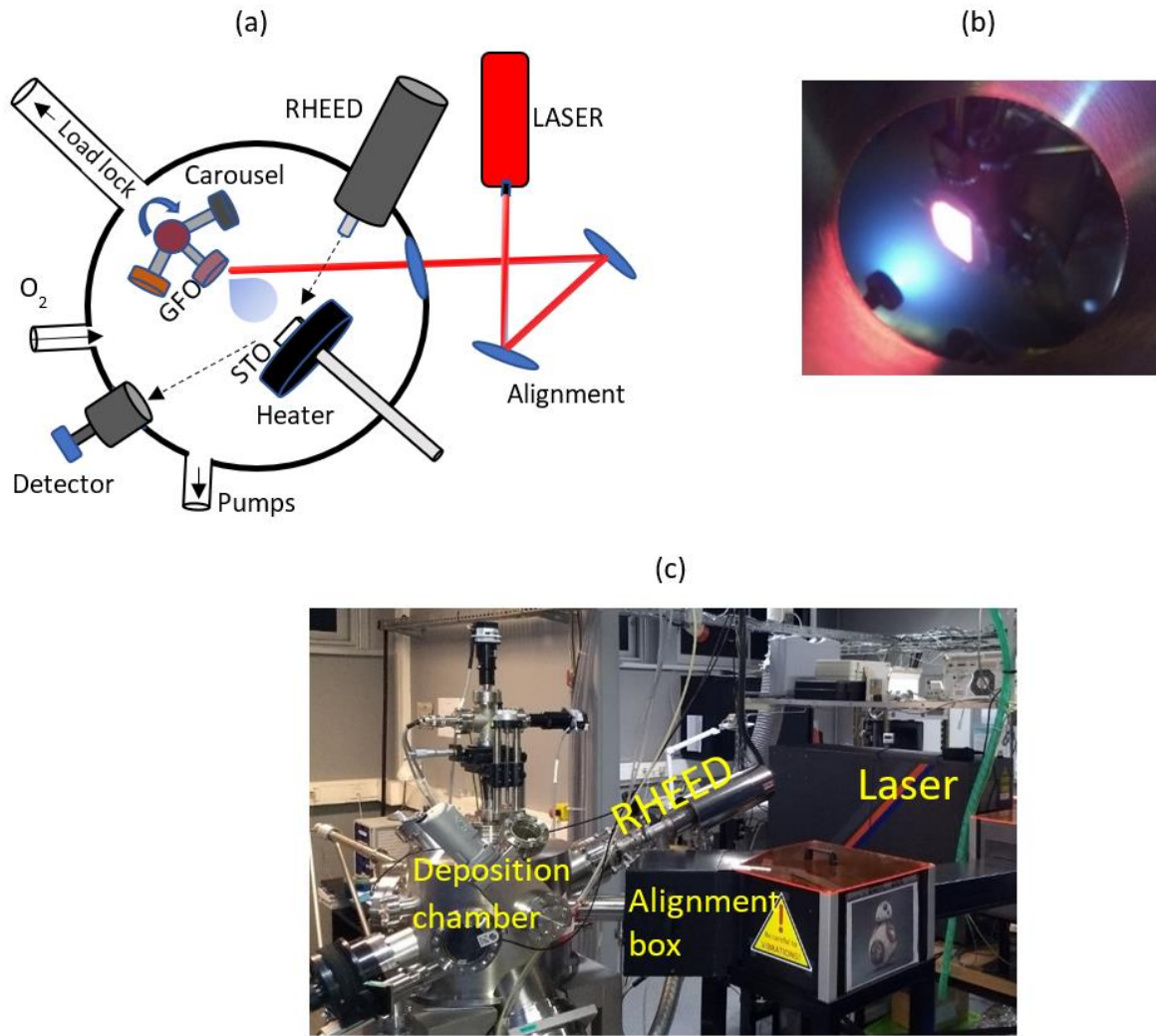


**Fig. 2.1 | The PLD technique.** (a) Schematic of our PLD set-up. (b) Real-time image during the deposition that shows the plume issued from the GFO target. (c) Picture of the PLD set-up in our lab.

Growth parameters	Values
Fluence (J/cm <sup>2</sup> )	3.5
Temperature (°C)	900
O <sub>2</sub> pressure (mBar)	0.1
Repetition rate (Hz)	2
Pulse counts	500-24000

**Table 2.1 | The set of optimized parameters used for the growth of GFO films.** The pulse count parameter is varied to study the evolution of thickness.

To achieve our aim of obtaining an atomically smooth thin film of GFO on STO (111), we used the parameters (presented in Table 2.1) which were optimized by systematically varying all the parameters one by one and checking for the films which present high crystallinity and low roughness. In this chapter, we will only present our study of GFO films with varying thicknesses, controlled by the number of pulses, keeping the other deposition parameters fixed.

For the structural and microscopic characterization of the thin films, we used various techniques such as *in situ* reflection high energy electron diffraction (RHEED), X-ray diffraction (XRD), atomic force microscopy (AFM), scanning electron microscopy (SEM), and transmission electron microscopy (TEM). We will briefly visit them in the following sections.

### 2.1.2 *In situ* RHEED

The *in situ* RHEED technique has become an indispensable tool to characterize the growth of the thin film surface prepared using physical vapor deposition methods like PLD [5]. We used *in situ* RHEED to characterize the substrate surface before growth, then follow the surface quality's real-time evolution during the growth and observe the surface quality after the growth. The information obtained from RHEED can have vast implications for engineering thin and ultra-thin GFO films.

Our RHEED set-up is implemented in the PLD set-up, as shown in Fig. 2.1 (a, c). An electron beam is produced in an electron gun through the application of a 1.4 to 1.5 mA current in a tungsten filament and acceleration of these electrons as a beam with a 35 kV voltage. The beam falls onto the STO substrate with a grazing incidence angle of 1-4 degrees, and the reflected beam is then collected using a fluorescent screen and captured by a charged coupled device (CCD) camera. The screen collects both the primary beam and the electrons diffracted after their interaction with the ordered lattice surface, thus characterizing the sample surface's reciprocal lattice. The diffraction condition in the reciprocal space is graphically demonstrated by the Ewald sphere

shown in Fig. 2.2 (a). The diffraction condition is satisfied when the reciprocal lattice nodes intercept the Ewald sphere of radius  $k = 2\pi / \lambda$ . Flat 2D surfaces of thin films show elongated rods (Fig. 2.2 (b, c)), whereas 3D surfaces show dotted patterns (Fig. 2.2 (d)). The streaky rod-like pattern observed for a 2D surface depends on the incident electrons' energy and their monochromaticity, the position of the incident beam, and the perfection of the crystalline quality of the surface.

Following the intensity of Laue spots obtained from the electron diffraction, Neave *et al.* [6] in 1983 observed oscillations for a layer-by-layer growth and demonstrated the possibility to follow the growth rate and precisely administer the thickness of the film. This is understood since each oscillation corresponds to completing an entire layer that now forms a new surface. The detailed processes of RHEED oscillations for thin-film growth and the effect of different kinematic conditions like layer-by-layer or step-flow growth can be found in a review by Hasegawa *et al.* [5]. Due to phenomenological reasons, the 3D island growth mode does not present oscillations, and only the 2D growth mode can give rise to an oscillatory pattern in RHEED [7].

The RHEED study for GFO thin film growth on the STO substrate has been performed using a high-pressure RHEED system from STAIB instruments.

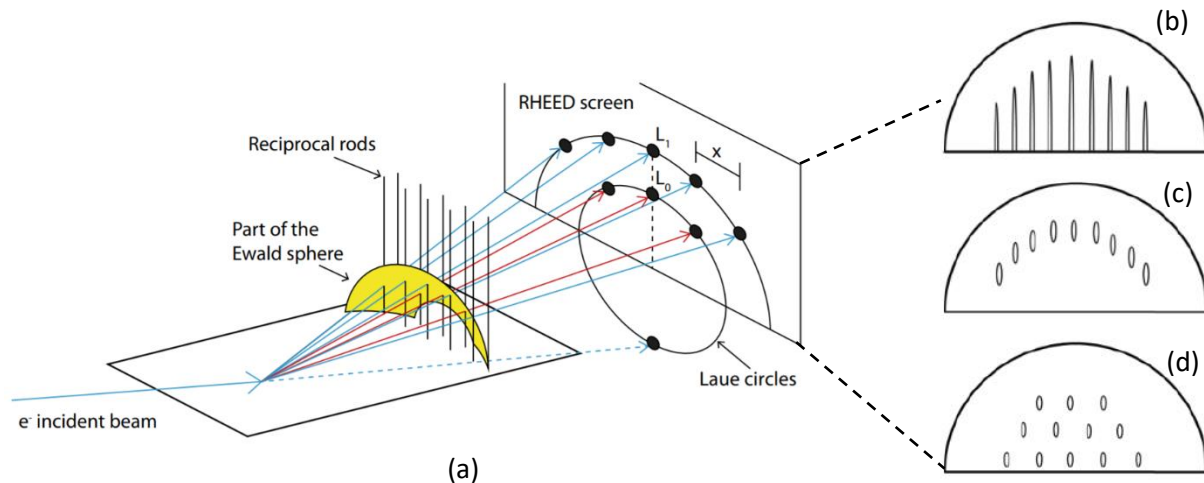


**Fig. 2.2 | A schematic representation of RHEED technique.** (a) The construction of the Ewald sphere. (b) The RHEED pattern under ideal diffraction conditions on a smooth surface. (c) The RHEED pattern under experimental conditions on a smooth surface. (d) The RHEED pattern on a rough surface. Adapted from ref. [8].

### 2.1.3 X-Ray characterization techniques

The X-rays-based characterization techniques have been one of the driving tools used by researchers to characterize crystalline materials in bulk, nanoparticles, or thin-film forms [9]. They are able to give information on the thickness of the films with X-ray reflectivity (XRR) and on their structure with the X-ray diffraction (XRD) technique [10,11]. The structural information includes the orientation, crystallinity, epitaxial relationships with the substrate, and phase purity control up to 1% sample volume.

The apparatus used for the thickness and structural characterization of our GFO thin films is a Rigaku Smartlab diffractometer. The X-rays are generated with a 9 kW Cu rotating anode source, monochromated to the  $K\alpha$  wavelength of  $\lambda = 1.54056 \text{ \AA}$ . The beam divergence is made as low as possible ( $0.4^\circ$ ), to allow the characterization of thin films in a parallel configuration.

#### X-ray reflectivity (XRR)

For XRR,  $\theta/2\theta$  scans are performed for very low angles (a few degrees), and the resulting profile is used to obtain the thickness of thin films limited up to the sub 100 nm range. In this technique, the incident X-rays are reflected from the air-film interface (if the incident angle is above the critical angle) and the film-substrate interface after penetrating the complete film layer Fig. 2.3 (a). Due to the difference in the refractive index between the film and the substrate, an interference pattern is created, which gives information on the thickness, density, and roughness through different profile features, as shown in Fig. 2.3 (b).

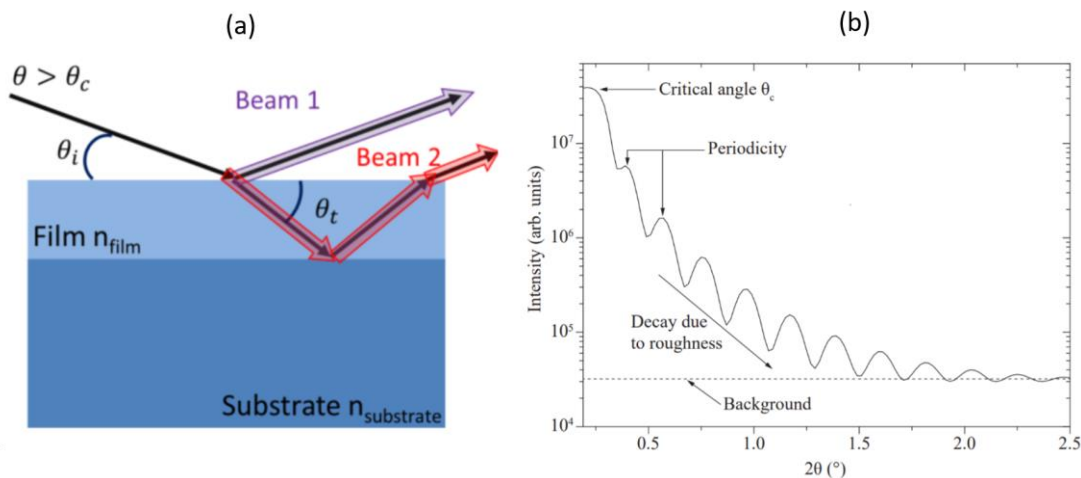


**Fig. 2.3 | The XRR technique.** (a) Schematic of XRR measurements. Adapted from ref. [12]. (b) An experimental low angle interference profile with, schematically, the main features from which are extracted the information about the thickness (from periodicity) and surface roughness (from slope). Adapted from ref. [13].

The phase difference ( $\phi$ ) between the two beams (Fig. 2.3 (a)) can be written according to Eq. 2.1 from geometric considerations. A minimum in intensity will be obtained each time  $\phi$  is an integer number of the used wavelength  $\lambda$ . The thickness of the film ( $t_{Film}$ ) can then be calculated from Eq. 2.1, issued from Eq. 2.2, considering the distance between two successive minima of oscillations as  $\delta\theta$  and the approximation that at a low angles  $\sin(\theta) \sim \theta$ .

$$\phi = \frac{1}{\lambda} \cdot \frac{2t_{Film}}{\sin(\theta_t)} = \frac{4\pi}{\lambda} \cdot t_{Film} \cdot \frac{n_{Film}}{\sin(\theta_i)} \quad (2.1)$$

$$t_{Film} = \frac{\lambda}{2 \delta\theta} \quad (2.2)$$

where,  $n_{Film}$  is the refractive index of the film,  $\theta_t$  is the refracted angle within the film and  $\theta_i$  is incidence angle <sup>[12]</sup>.

Alternatively, the thickness of the film can be calculated by taking a Fourier transform of the extracted oscillation curve. It is estimated from the Fourier peak position after modifying the horizontal axis in the scale of  $\lambda\sqrt{\sin^2 \theta_i - 2n_{Film}}$  <sup>[14]</sup>.

The model shown in Fig. 2.3 (b) and the above methods for estimating the film thickness are only valid for a single layer film growth over a substrate. For heterostructures with two or more films, the reflectivity profile must be entirely fitted to calculate each layer's thickness, density, and interface roughness separately. Before the fitting procedure, the experimental data is corrected from sample illumination variations with the incident angle, taking into account the size of the sample. Then we use the GlobalFit software to fit the profile and extract the thin film's physical parameters.

### X-ray diffraction in the $\theta$ - $2\theta$ mode

Diffraction results from coherent and elastic scattering phenomena between an incident radiation beam and matter. Crystallized matter presents periodically arranged atomic plane families, denoted by their Miller indices  $\{hkl\}$ , which will allow such phenomena for radiation wavelengths of the order of the interplanar distances  $d_{hkl}$ . The relationship between these  $d_{hkl}$  distances, the radiation wavelength  $\lambda$  and the  $2\theta$  angle between the incident and diffracted beams wavevectors,  $k_i$  and  $k_f$ , respectively, is given by the Bragg's law of diffraction given in Eq. 2.3.

$$2d_{hkl} \sin(\theta) = n\lambda \quad (2.3)$$

where  $n$  is an integer.

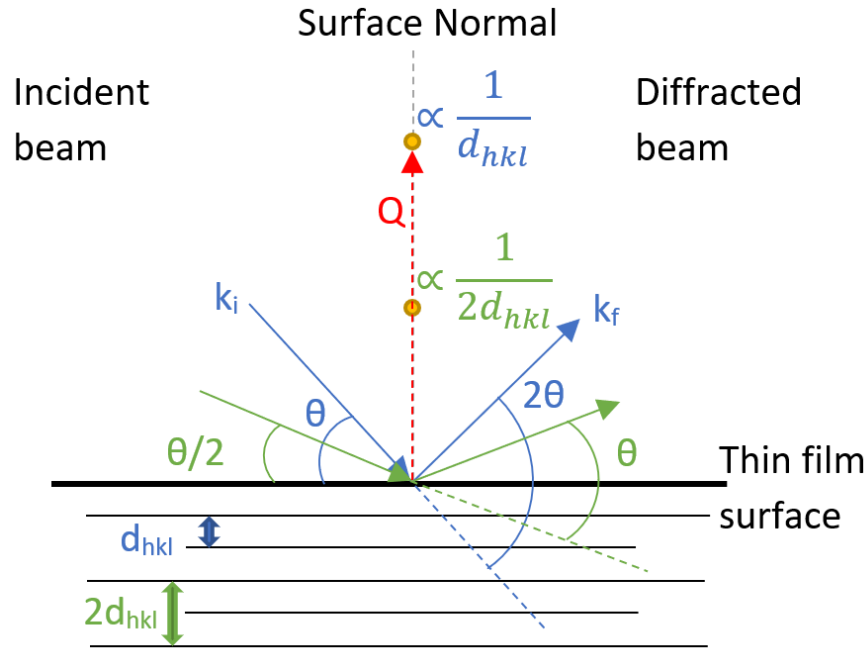


**Fig. 2.4 | Schematic of a  $\theta$ - $2\theta$  mode X-ray diffraction experiment.**

The specific angles at which the diffraction condition is satisfied present intense peaks in the  $\theta$ - $2\theta$  measurement profile. Fig. 2.4 depicts such conditions, fulfilled when the scattering vector  $\vec{Q} = \vec{k}_f - \vec{k}_i$  is one of the reciprocal lattice vectors.

Although the peaks should ideally be delta peaks, due to instrumental imperfections, as well as to some degree of matter deviation from the perfect crystal, the experimental peaks have a finite width which is given by their full width at half maximum (FWHM).

Using the set-up described in Fig. 2.4, one can also perform rocking-curve measurements to evaluate the disorientation levels in thin films. In such measurements,  $2\theta$  is kept constant, and  $\omega$ , which is the angle between the incident beam and the film surface, is scanned over a few degree angles. The oriented character of the films is characterized by the FWHM of the peak obtained in such a configuration. The lower the FWHM, the higher the orientation in the film.

$\theta$ - $2\theta$  scans only give information on the out-of-plane periodicity of the films. Other configurations have to be employed to get further information on their crystalline nature.

## Phi ( $\phi$ ) scans

Polycrystalline thin films grown on a single crystalline substrate can have different in-plane orientations called structural domains. To characterize these in-plane domains, one can position the diffractometer in diffraction conditions for a chosen asymmetric reciprocal lattice node (not along the normal to the surface of the sample), with a proper set of  $\omega$ - $2\theta$  angles (as depicted in Fig. 2.5), and perform a  $\phi$  scan by rotating the sample around its normal. The number of peaks expected in the  $\phi$  scan for a single crystalline sample depends upon the symmetry of the chosen node. Additional variants will lead to additional peaks.

## Two-dimensional reciprocal space mapping (RSM)

RSM measurements correspond to the mapping of a particular node of the reciprocal space lattice in one diffraction plane, performed by doing asymmetric  $\omega$ - $2\theta$  scans with various tilts, that is for various  $\psi$  angles (Fig. 2.5). When the mapping is performed on an asymmetric node (not along the normal to the sample), it allows estimating the in-plane lattice parameter with a high degree of accuracy. Such mappings are therefore currently used to determine if the films are strained by the substrate. The ideal case is when RSM can be performed on a zone of the reciprocal space containing nodes from both the film and the substrate.

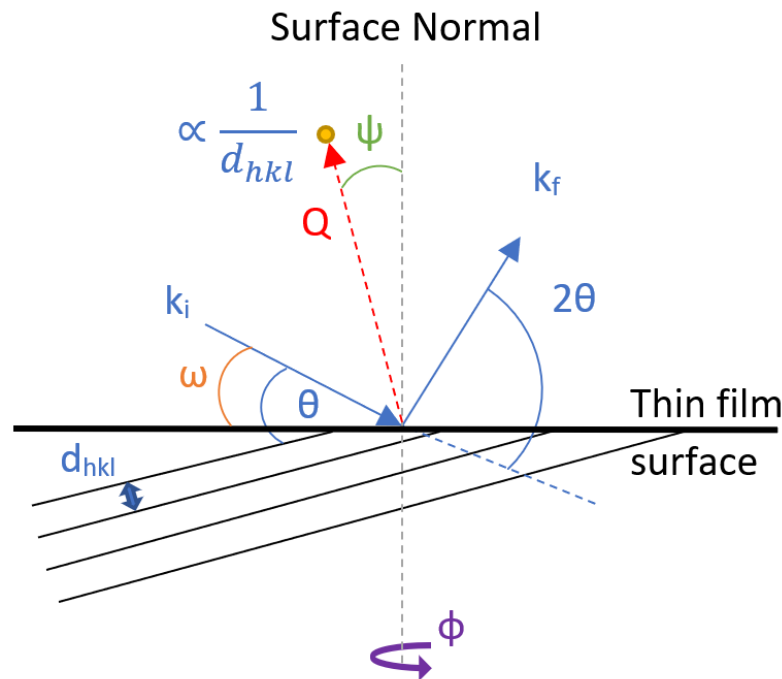


**Fig. 2.5 | Schematic of an asymmetric  $\omega$ - $2\theta$  measurement performed to scan an offset reciprocal lattice node.**

These angular positions defined by  $(\omega, 2\theta)$  can be transformed into reciprocal unit vectors ( $q_{||}$ ,  $q_{\perp}$ ) using Eq. 2.4, and 2.5.

$$q_{||} = \frac{4\pi}{\lambda} \cdot \sin \theta \cdot \sin \psi \quad (2.4)$$

$$q_{\perp} = \frac{4\pi}{\lambda} \cdot \sin \theta \cdot \cos \psi \quad (2.5)$$

Well-chosen reciprocal lattice nodes, such as  $(h0l)$  and  $(0kl)$ , can thus yield all in- and out-of-plane lattice parameters using Eq. 2.6, and 2.7:

$$a = \frac{h}{q_{||}(h0l)}, \quad c = \frac{l}{q_{\perp}(h0l)} \quad (2.6)$$

$$b = \frac{k}{q_{||}(0kl)}, \quad c = \frac{l}{q_{\perp}(0kl)} \quad (2.7)$$

### 2.1.4 Atomic Force Microscopy (AFM)

AFM is widely used to characterize the surface topography of thin films. It consists in scanning the surface of the sample with a very small tip, ideally composed of one atom only at its end, and imaging the interaction between this point and the surface to be analyzed.

It can be performed in either tapping or contact modes. Variations of AFM such as the piezo-force microscopy (PFM) and the conducting tip AFM (c-AFM) are used to study the electrical properties of the films while the magnetic-force microscopy (MFM) is used to study their magnetic behavior at the surface.

A schematic representation of the AFM set-up is presented in Fig. 2.6. The probe is supported by a cantilever attached to a piezoelectric material which allows a precise positioning of the cantilever. The tip is ideally converging to an apex made out of only a single atom. A laser is reflected on the top of the tips' lever arm and is detected by a photodiode composed of four dials. The intensity and position of the signal on the photodiode make it possible to reconstruct the topographic image.

In the contact mode, the AFM tip is hovered over the sample at a very low height (a few angstroms). A feedback loop maintains the tip at a constant height and the topography changes are registered from the moves applied to the tip to maintain its height constant.

In the AFM tapping mode, the tip oscillates at its resonant frequency and approaches the film within a few nanometers. The oscillation amplitude of the tip is modified when the tip-sample distance is modified. A feed-back loop is set-up to maintain a constant amplitude through modifications of the cantilever height. The topographic image is obtained by following the modifications in the piezo z-axis position.

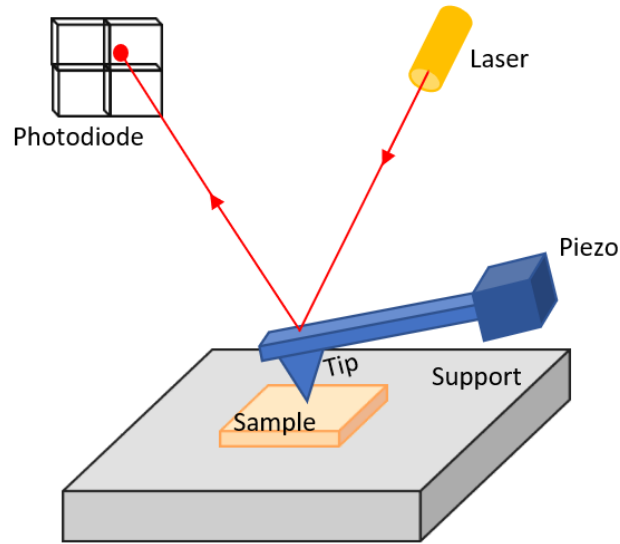


**Fig. 2.6 | Schematic representation of an AFM set-up.**

For our study, we have used a standard Dimension Icon AFM probe, from the Bruker company. We performed AFM observations in the tapping mode with a view to extract information concerning the root mean square (rms) roughness of the thin films. The rms for a 2D scan is defined as given by Eq. 2.8. :

$$R (rms) = \sqrt{\frac{1}{L_x L_y} \int_0^{L_x} \int_0^{L_y} |z^2(x, y)| dx dy} \quad (2.8)$$

where  $L_x$ ,  $L_y$  are the lengths at which we evaluate the roughness and  $z(x,y)$  is the height variation at the  $(x, y)$  position.

### 2.1.5 Scanning electron microscopy (SEM)

The surface morphology and overall composition of the films have been studied by SEM using a JEOL 6700F operated at 5 keV and coupled with energy dispersive spectroscopy (EDS). The analyses were performed by Cédric Leuvre (IPCMS, Strasbourg). These SEM observations were used for preliminary studies and are not extensively described in this thesis.

### 2.1.6 Transmission electron microscopy (TEM)

TEM allows to obtain images of matter with high resolution, down to the atomic resolution in some cases. It can be coupled to spectroscopic techniques such as energy dispersive

spectroscopy (EDS) or electron energy loss spectroscopy (EELS) which then add high resolution compositional information to the imaging. TEM is therefore widely used in material sciences to study the atomic plane distances, the structural defects, the quality of interfaces, and the chemical composition in thin layers.

In this technique an electron beam passes through a thinned sample of about 50 nm in transmission geometry. High resolution images can be obtained in two modes, the HR TEM or the HR scanning TEM (HR STEM). While for HR TEM the electron beam is parallel (perpendicular to the sample), for STEM, the beam is focused onto a focal point, scanned over the sample, and the signal is collected as a function of the beam location. The STEM configuration allows obtaining images with an atomic resolution.

Images can be formed using the un-scattered or scattered electrons to yield bright or dark field images, respectively. In bright field images, the contrast is mainly due to the diffusion of the electrons and atoms with higher atomic numbers will appear darker while zones which simply transmit electrons will appear lighter. In dark field images, only the scattered electrons are selected and build up the image. The areas where no scattering happens will appear black while zones where material is present will appear brighter. The contrast is somehow opposite to the one observed in bright mode. This mode can be used to study some crystalline features. A particularly interesting mode used in STEM is the high-angle annular dark-field (HAADF) mode for which the detector selects very large angles, above 50 mrad. STEM HAADF imaging allows for enhanced contrast, especially at low atomic numbers, compared to TEM.

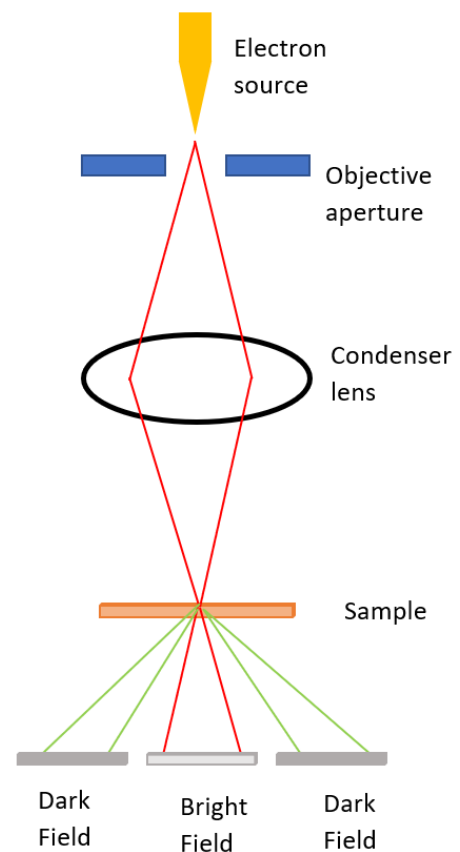


**Fig. 2.7 | Schematic of a TEM microscope, with the two different imaging modes, bright and dark field.**

TEM techniques require the sample to be very thin (ca. 20-50 nm) to allow the electron beam to be transmitted. There are various ways to prepare such thin samples. For the observations performed in this thesis, the samples were prepared by Dr. David Troadec at IEMN, Lille, France, using the focused ion beam (FIB) technique and re-thinned using precision Argon ion milling.

The TEM images of the films cross sections presented in this work were collected at 80 keV (to avoid sample damages) by Dr. Corinne Bouillet (IPCMS, Strasbourg) using a probe corrected Jeol 2100F equipped with EDS and the Gatan GIF TRIDIEM for EELS and Dr. Xavier Devaux (IJL, Nancy) using a probe corrected JEOL ARM200F equipped with the Gatan GIF Quantum SE system for EELS. To improve STEM-EELS mapping data, multivariate statistical analysis was used. The image processing was carried out using Digital Micrograph software.

## 2.2 Elaboration of Ga<sub>0.6</sub>Fe<sub>1.4</sub>O<sub>3</sub> (GFO) thin films on SrTiO<sub>3</sub> (STO) substrates

### 2.2.1 Why STO substrates?

Strontium titanate, SrTiO<sub>3</sub> (STO), is an ABO<sub>3</sub> cubic perovskite crystallizing in the space group  $Pm\bar{3}m$ . This cubic oxide has a lattice parameter of  $a = 3.9045 \text{ \AA}$  and is characterized by a density of  $5.12 \text{ g/cm}^3$ , a melting point of  $2353 \text{ K}$ , and a thermal expansion coefficient of  $9 \times 10^{-6} \text{ K}^{-1}$ .

Numerous studies related to the epitaxial growth of complex oxide thin films have employed single-crystalline STO substrates [15–17]. Such extensive research on STO has been conducted thanks to its favorable lattice matching with many functional materials [18,19], great availability in high-quality single crystals format, well-known oxygen defect chemistry [15], high melting point, similar thermal expansion coefficient as most functional oxides [8], well-established etching techniques to obtain atomically flat surfaces and a relative absence of any ferroic property [20]. It has recently garnered much attention due to its possible integration on top of Si substrates, which paves the way for the scalability of oxide functionalities into commercial devices [21,22].

For GFO thin films' growth, two substrates have been primarily used in the literature, STO and YSZ. It was demonstrated that GFO thin films grown over YSZ (100) have six in-plane structural domains separated by  $30^\circ$ , whereas GFO thin films grown over STO (111) only have three in-plane structural domains [23]. A lower number of in-plane structural domains is desired for higher symmetry, homogeneity, and simplicity purposes. It is also of some help to better understand the different ferroic properties in GFO.

In this work, we used STO (111) substrates from Furuuchi chemical corporation (Tokyo, Japan) for optimizing the growth of atomically flat GFO (001) films. The growth of these high-quality films was also exactly reproduced on STO (111) substrates obtained from Codex international (France), and the rest of the magnetic, electric, optical, and device characterizations presented in this thesis were made on these samples.

### 2.2.2 Growth and structural characterization of GFO films

The optimized parameters for the GFO films' growth are given in Table 2.1 of the PLD dedicated part of this methods chapter. In this part, we will see the effect of the GFO films thickness variation when grown on STO (111) substrates. The STO (111) substrates were cleaned with acetone and isopropanol to clean them from inorganic impurities on the surface, but they were not subjected to any HF treatment for the results presented in this section.

Performing an *in situ* RHEED monitoring of the GFO thin-film growth onto STO (111) single crystals, we evidenced a transition from a 3D island type to a 2D layer-by-layer growth. This

phenomenon is illustrated in Fig. 2.8 (a), where we show the RHEED patterns imaged at the end of the deposition for various thicknesses. A 3D growth mode is observed at 4 nm, as indicated by the dotted RHEED pattern. The RHEED pattern exhibits a transition to a state with a modulated streaky feature at 7 nm, which then becomes fully streaky at 32 nm, indicating a 2D sample surface. The 3D to 2D growth-mode transition, as observed via RHEED, thus appears for a thickness of *ca.* 7 nm. The AFM images [Fig. 2.8 (b)] also show an evolution of the surface morphology from randomized islands for 4 nm, through islands aligned in rows, and towards atomically flat films, when islands finally coalesce. This process is very similar to the one reported for the growth of SrRuO<sub>3</sub> onto STO [24]. The root-mean-square (rms) roughness value is around 1 nm at the start of the growth and progressively decreases, with the increasing film's thickness, to values comparable to the rms roughness of the substrate prior to deposition (*ca.* 0.1 nm). The growth was also monitored by RHEED from the intensity variation of the spots in the zero-order Laue zone. Figure 2.9 covers the complete deposition of the 7 nm GFO 1.4 film. The overall deposition lasted for 537 s, yielding a deposition rate of 0.0130 nm/s. The 2D growth sets in *ca.* 108 s after the growth starts and lasts for 464 s, until the growth is stopped. It shows 24 oscillations. One RHEED oscillation is 19.3 s long. It corresponds to the deposition of 0.25 nm, *i.e.*, about 1/4<sup>th</sup> of a unit cell. Such sub-unit cell growth is rare. Until now, it had been observed for the growth of some other complex cells, such as those of the spinel [25] or garnet [26] phases of iron oxides. The oscillation periodicity of 1/4<sup>th</sup> unit cell layer calculated from thickness analysis means that four oscillations correspond to one unit cell, and hence a super-periodicity of 4 could be expected in the oscillations. Surprisingly, there exists a super-periodicity in the RHEED pattern which can be observed in the magnified oscillations in Fig. 2.9, but it comprises 3 oscillations, one smaller intensity oscillation, denoted as 1, and two larger ones, denoted as 2 and 3. The existence of a three-fold periodicity in the oscillations is puzzling and will be explored further in the Ch. 5 of the thesis.

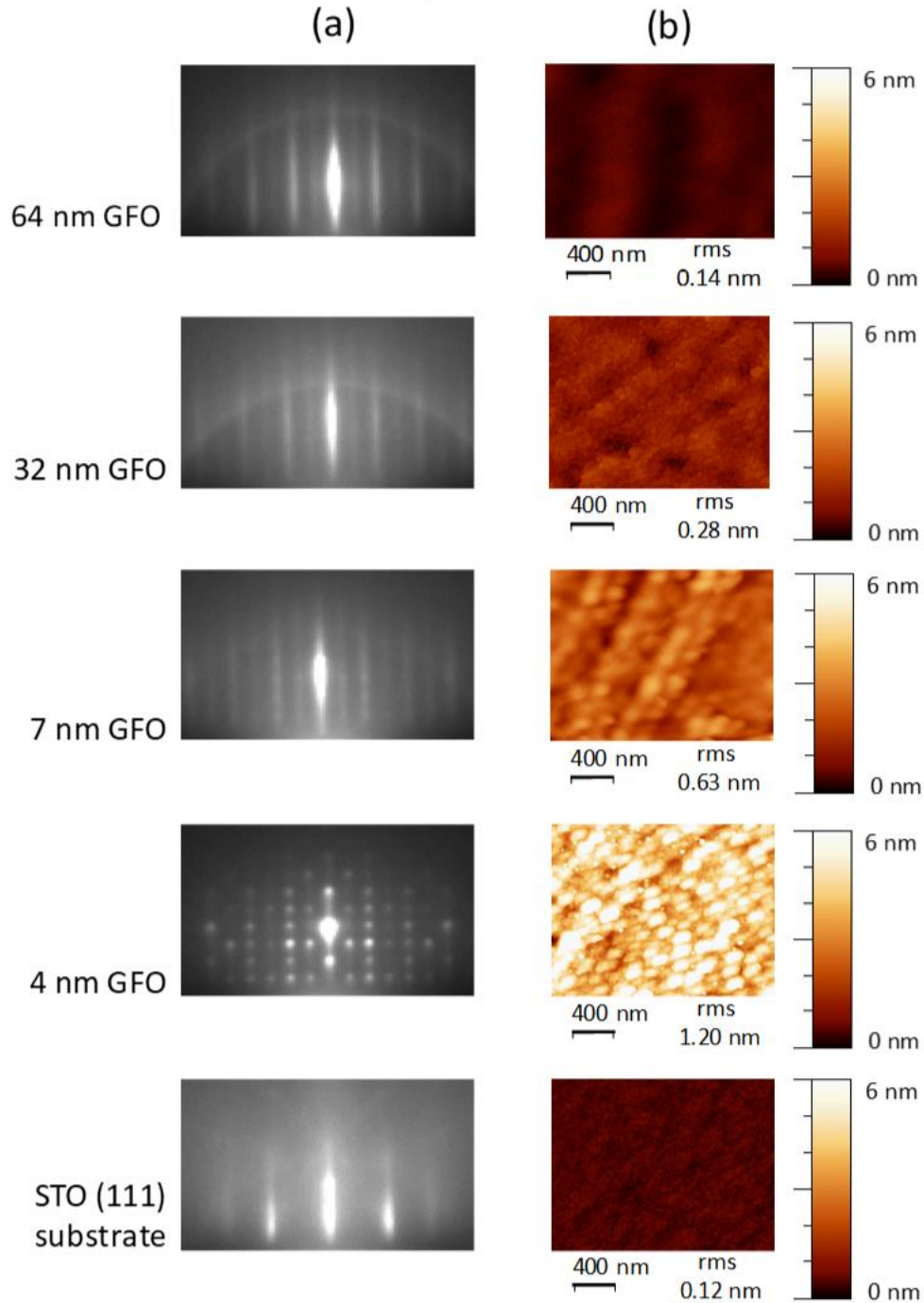


**Fig. 2.8 | Surface characterization of GFO film at various thicknesses.** (a) *In situ* RHEED patterns observed during the growth of GFO1.4 on STO (111). The patterns are taken along the  $[\bar{1}2\bar{1}]$  the direction of the substrate. The visible lines for the bare substrate correspond to STO  $10\bar{1}$  reflections, and harmonics. When the growth of GFO starts, some new features appear corresponding to GFO 020 reflections and harmonics, the azimuth being along the GFO  $[100]$  direction (in the  $Pna2_1$  space group). (b) AFM images of the surface of the samples.

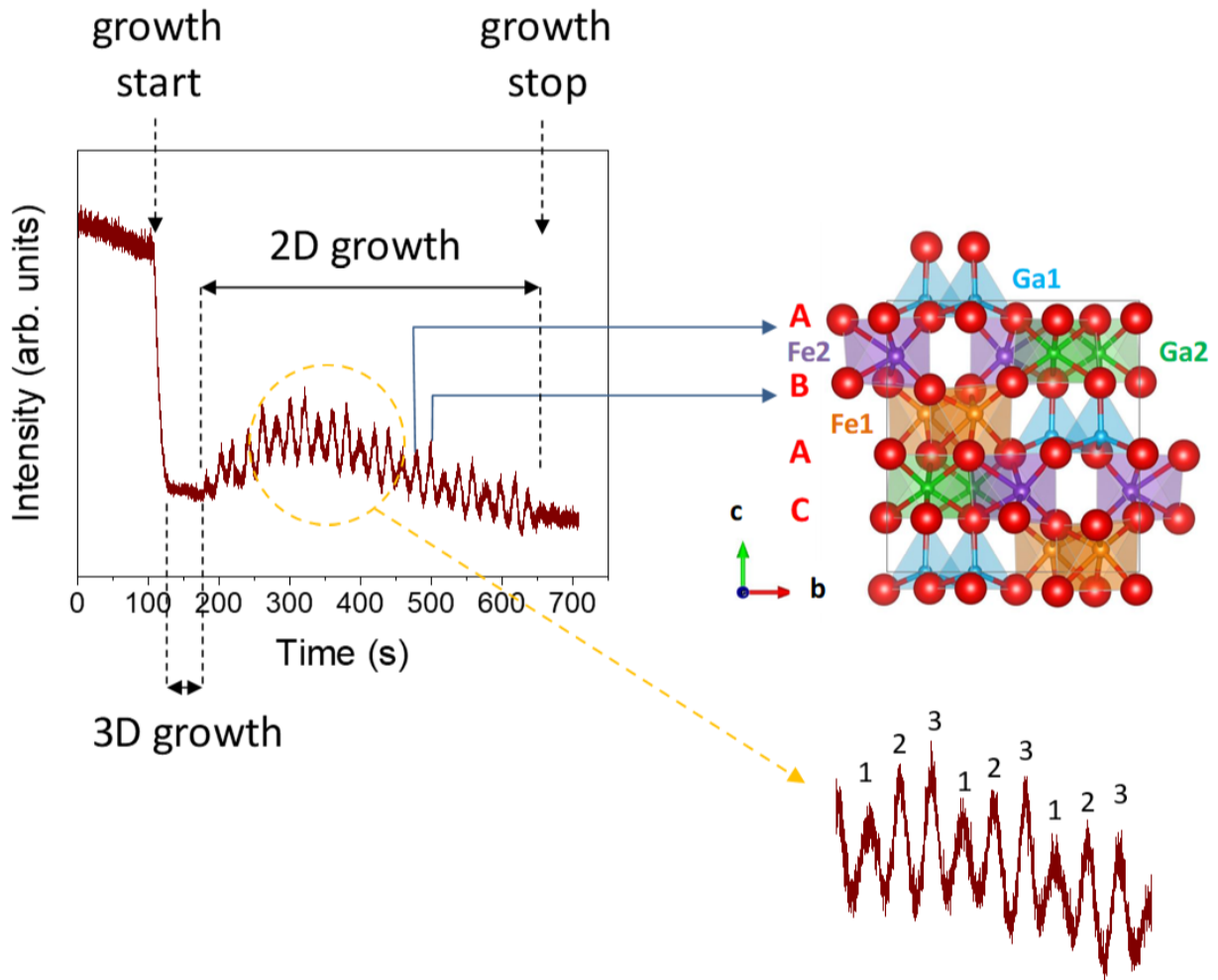


**Fig. 2.9 | The fluctuation of a spot's intensity in the zero-order Laue zone during RHEED monitoring of the 7 nm GFO film growth.** Each oscillation corresponds to the deposition of one-fourth of a GFO cell, that is, to a layer of transition-metal / oxygen polyhedra. The oscillations have an unusual 3 oscillation periodicity.

X-ray diffraction patterns of the deposited films, performed in the  $\theta$ - $2\theta$  mode, are shown in the inset of Fig. 2.10. They indicate that, for all thicknesses, the GFO thin films are well crystallized, oriented along the  $Pna2_1$  [001] axis, without any trace of a spurious phase. The observation of Laue oscillations on the zoomed GFO (004)  $\theta$ - $2\theta$  scans confirms high crystallinity and low roughness of the films (Fig. 2.10). The 00l peaks are shifted towards lower  $2\theta$  values for the lowest thicknesses, indicating a larger out-of-plane  $c$  parameter.

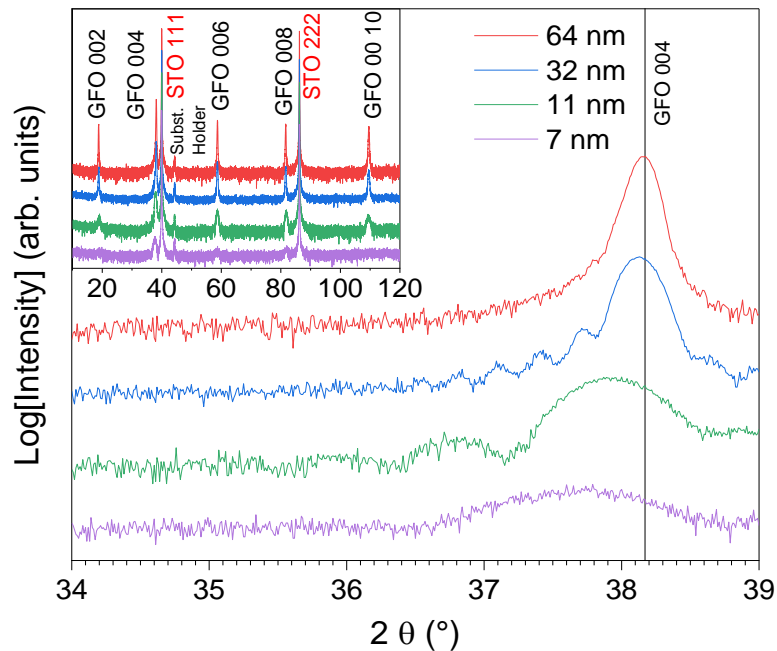


**Fig. 2.10 | X-ray diffractograms of the deposited GFO thin films in the  $\theta$ - $2\theta$  mode.** The focus is on the GFO 004 peak; the vertical black line at  $2\theta = 38.17^\circ$  that indicates the angle observed for bulk GFO  $x = 1.4$  ( $c = 0.9422 \text{ nm}$  [27]).

The in-plane relationships between the STO (111) surface and the GFO ( $ab$ ) face are determined from  $\phi$  scans performed on both STO and GFO reflections [Fig. 2.11]. GFO may adopt three directions complying with the following epitaxial relationships with STO:  $[060] \text{ GFO } (001) // [hkl] \text{ STO } (111)$  with  $[hkl]$  equal to  $[2\bar{2}0]$ ,  $[\bar{2}20]$  or  $[\bar{2}02]$ . This is in perfect agreement with the symmetry of the system, and with what has already been observed for GFO deposition on STO (111) [23,27,28].

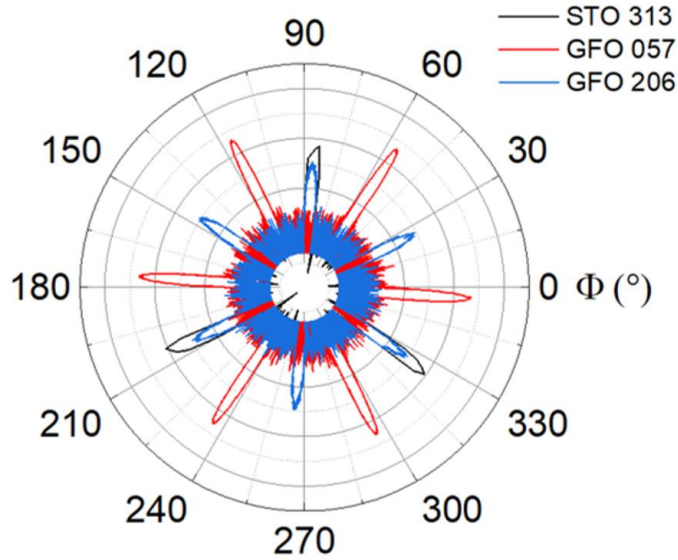


**Fig. 2.11 |** The  $\phi$  scans of the GFO 057 and 206, together with the STO 313 reflections. As observed for the 64 nm GFO thin films and is a representative of all deposited films.

The GFO cell parameters  $a$ ,  $b$  and  $c$  could be determined from the combination of  $\theta$ - $2\theta$  scans and reciprocal space mapping of the 206 and 057 reflections [Fig. 2.12 (a)]. While  $c$  decreases with increasing thicknesses (as already observed from the GFO 004 peak in the  $\theta$ - $2\theta$  scans),  $a$  and  $b$  remain essentially constant [Fig. 2.12 (b)]. The out-of-plane  $c$  parameter reaches the bulk value for thicknesses higher than 64 nm, after a decrease of  $ca.$  0.2 %. The out-of-plane expansion of the  $c$  parameter for lower thicknesses is thus not related to any substrate-induced in-plane strain since it relaxes independently from the  $a$  and  $b$  parameters. The mismatch in this GFO (001) growth on STO (111) system is large. The distances which have to be considered are (i) along the  $a_{\text{GFO}}$  direction:  $a_{\text{GFO}} = 0.5088 \text{ nm} \approx 3 d_{\text{STO } 121} = 0.4780 \text{ nm}$  (6.4 % compressive strain), and (ii) along the  $b_{\text{GFO}}$  direction:  $d_{\text{GFO } 060} = 0.1465 \text{ nm} \approx d_{\text{STO } 220} = 0.1380 \text{ nm}$  (6.1 % compressive strain) [Figs. 2.11 (a, b)]. The relatively high elastic energy introduced by this large strain value accounts for the absence of an in-plane strain state in the GFO crystal structure even for the lowest thicknesses. This might also explain the initial 3D mode growth, where totally relaxed GFO islands coalesce while the deposition proceeds to obtain a flat surface. Such a 3D-to-2D metamorphic epitaxial growth<sup>[30]</sup> mechanism has already been reported for  $\text{SrRuO}_3$ <sup>[24]</sup> on STO and for  $\epsilon\text{-Fe}_2\text{O}_3$ <sup>[31,32]</sup> which is isomorphic to GFO. In both cases, the initial 3D growth mode was accounted for by the important lattice mismatch between substrate and thin film.

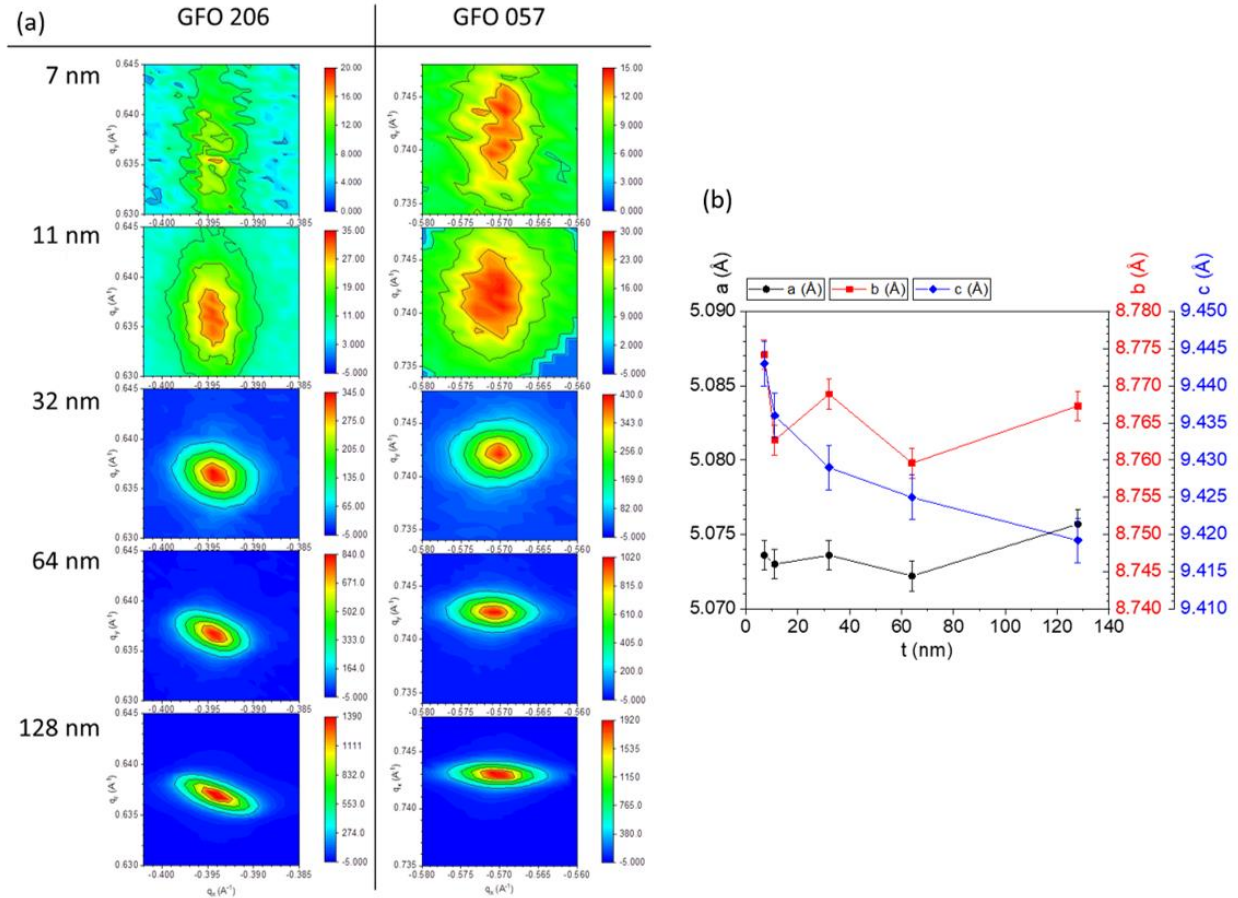
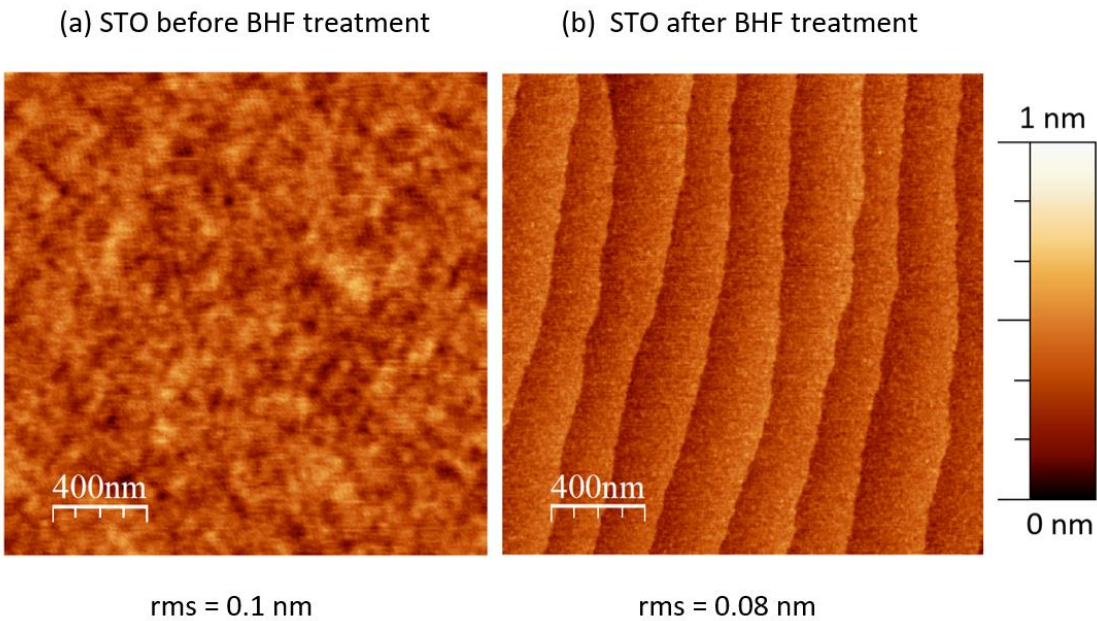


**Fig. 2.12 | The 2D RSM map and lattice parameters of GFO thin films.** (a) RSM of GFO 206 and 057 reflections ( $Pna2_1$ ) for the various deposited thicknesses. (b) Variation of both the in-plane and out-of-plane cell parameters with the thickness of the film.

### 2.2.3 Effect of a buffered hydrofluoric acid pre-treatment of the STO (111) substrates.

The growth of thin films, especially at ultra-thin regimes, is highly dependent on the surface chemistry and morphology of the substrate. To give the substrate a homogeneously single terminated layer and to decrease the surface energy, we used an etching technique wherein STO (111) substrates were sonicated in distilled water at 60°C for 20 minutes to form a  $\text{Sr}(\text{OH})_2$  layer, which is then etched by immersing the substrate in a buffered hydrofluoric acid (BHF)  $\text{NH}_4\text{F}:\text{HF}$  solution of 7:1 ratio for 23 s. The substrate is then annealed at 1000°C for 4 hours and this creates a step-terrace surface<sup>[20]</sup>. Since the observed 3D to 2D transition in our GFO thin films could most probably stem from the surface-related energies, we attempted to investigate the effect of a BHF etching of the STO (111) substrates on the 3D to 2D transition during the GFO thin films growth. Fig. 2.13 (a, b) shows an AFM image of the STO (111) substrate surface before and after etching.



After GFO growth of 32 nm

(c) On STO without any BHF treatment      (d) On STO with an BHF treatment

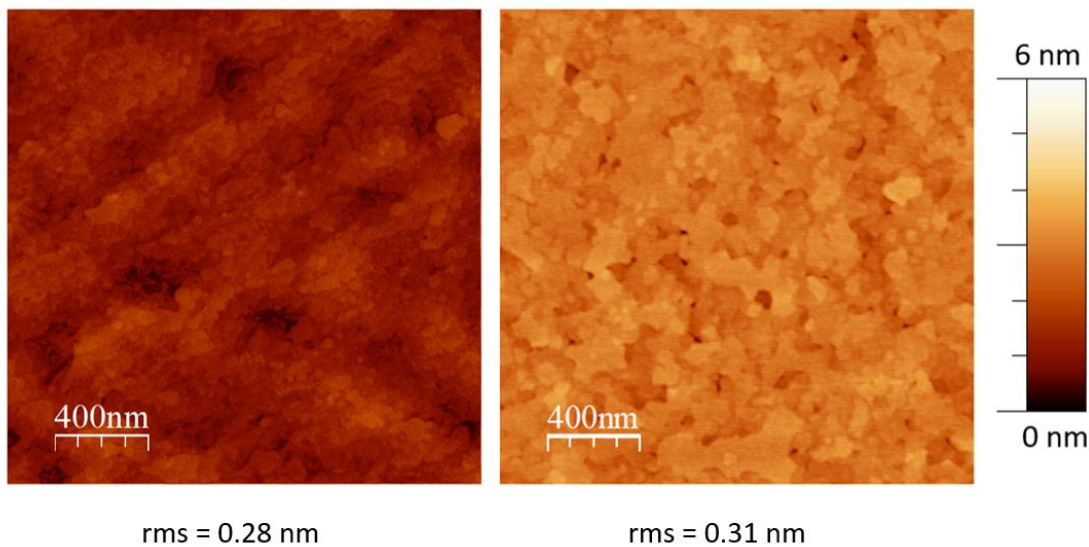


**Fig. 2.13 | AFM images of the STO (111) substrate.** (a) For as received STO substrate. (b) For STO substrate after BHF-treatment, showing an homogeneous step-terrace surface.

**AFM images of a GFO (001) film of 32 nm thickness.** (c) On as received STO substrate. (d) On BHF treated STO substrate.

Following with *in situ* RHEED the GFO thin film growth on the BHF treated step terraced STO (111) substrates also showed a 3D to 2D transition after a similar number of pulses, as for its non-HF treated counterpart. AFM images for 32 nm GFO thin films grown on STO (111) substrate before and after etching shows similar r.m.s. roughness values (Fig. 2.13 (c, d)).

The comparison of growth and structural characterizations between 32 nm GFO (001) films grown on both etched and non-etched substrates does not show any significant change in the rms roughness or X-ray diffraction peaks positions (Fig. 2.14). This leads us to surmise the possibility of a different mechanism for 3D-2D growth than the substrate surface energies, morphology, or termination layer.

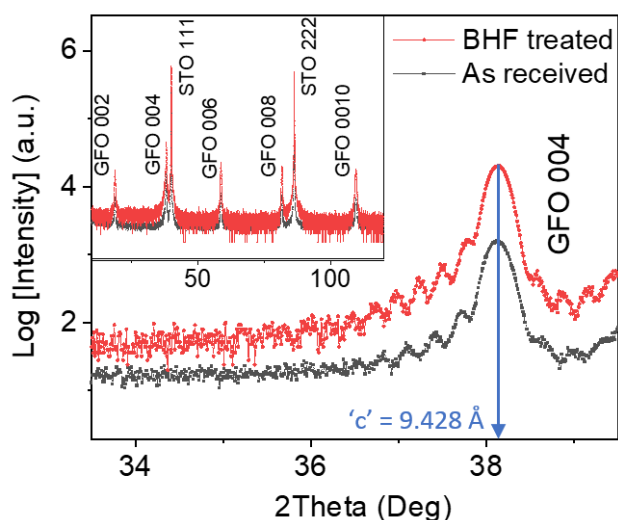


**Fig. 2.14 | Comparison of the 32 nm GFO film grown on as received and BHF treated STO (111) substrates.**

#### 2.2.4 Transmission electron microscopy study

To have some insight into the GFO films' structure and their interface with STO (111), we performed a HR STEM study. STEM HAADF images of a cross-section of the 32 nm GFO film are presented in Fig. 2.15. The interface between the STO substrate and the GFO film is well defined and the film shows the cationic pattern expected for GFO in its  $Pna2_1$  space-group structure from the beginning of the growth. A zone of darker contrast, indicating a strong evolution of the local chemical composition (lower average atomic number), is clearly visible and delimitates the first five nanometers from the rest of the film. One should note that observations of other areas of the sample reveal a slight dispersion in this delimitation position at distances between 2 and 5 nm from the substrate. Mapping the convex or concave shape formed by the four Fe<sup>2+</sup> and Ga<sup>2+</sup>

sites in-a-row (*cf.* GFO unit cell in Fig. 2.9 for the positions of Fe<sup>2+</sup> and Ga<sup>2+</sup>) allows the determination of the polarization orientation within a unit cell <sup>[29]</sup>. Surprisingly, we observe a polarization reversal as we move away from the film/substrate interface. This is the first experimental observation of ferroelectric domains in ultrathin GFO films. The domain wall imaged in Fig. 2.15 corresponds to a nominally charged tail-to-tail configuration. While the formation of neutral ferroelectric 180° domain walls normal to the surface is expected for classical systems in the ultrathin regime in the absence of charge screening <sup>[33–36]</sup>, the tail-to-tail domain wall type observed here might be due to the highly energetic switching path of GFO. The polarization switching is expected to occur along the *Pna2<sub>1</sub>*-to-*Pnna* phase-transition path, with an activation energy of 0.5-1 eV per formula unit <sup>[23,37,38]</sup>. This high switching activation energy results in a high coercive field, which would stabilize electrostatically unfavourable domain architectures. Similar charge domain walls have only been observed up to now in improper ferroelectrics such as YMnO<sub>3</sub>, in which the domain pattern is set by non-ferroelectric primary order parameter <sup>[39]</sup>. The tail-to-tail polarization configuration, with a domain boundary at ca. 5 nm from the substrate, may be at the origin of the increased out-of-plane cell parameter observed for low thicknesses. The tail-to-tail polarization domains are expected to repel each other, leading to an increase in the overall cell parameters. The phenomenon will be less and less appreciable with increasing film thicknesses.

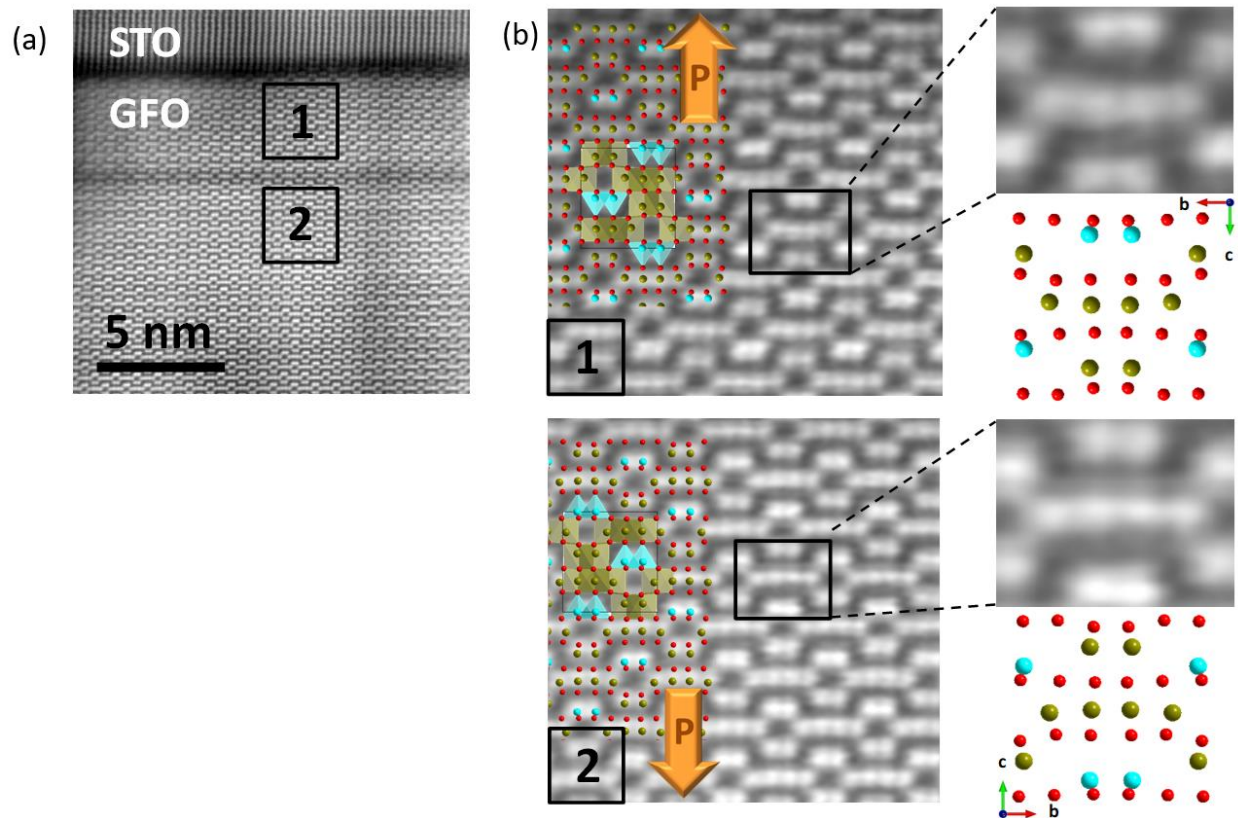


**Fig. 2.15 | A microscopic study of GFO and STO interface using HAADF HR STEM.** (a) A cross-section of the 32 nm GFO (001) film deposited on STO (111) showing that GFO grows in its expected  $Pna2_1$  structure from the growth start. A dark line delimitates a first 5 nm thick GFO layer from the rest of the layer. (b) Magnifications of zone 1, showing a polarization pointing towards the substrate, and zone 2, showing a polarization pointing outwards from the substrate. The GFO unit cell with expected atomic pattern for an observation along the [100] zone axis is superimposed on the magnifications; the orientation of the cell is recognizable from the convex or concave feature formed by the four Fe2 and Ga2 octahedral sites in a row (zoomed on the right of the figure).

To further investigate the origin of the changes in the polarization orientations during the early GFO growth stage, we performed a chemical analysis of the GFO/STO interfacial zone. Atomically resolved quantitative elemental mappings of the film at the interface with the substrate were obtained by processing the STEM-EELS spectra [Fig. 2.16]. Both the Ga and Fe maps are in perfect agreement with the expected positions of Ga majorly in the Ga1 (tetrahedral) sites, and Fe majorly in the three other (octahedral) sites [see Fig. 2.16 (a)]<sup>[29]</sup>. The zone of darker contrast, observed at the polarization reversal in Fig. 2.15 (a), is due to the presence of Fe atoms only on three consecutive cationic layers in this zone in Fig. 2.16 (a). This results in a Ga depleted zone and, Ga being a heavier atom than Fe, to a relative darker contrast. Ti migrates from the STO

substrate into the GFO film by up to *ca.* 6 %, over the first 5 nm. The profile of O is very similar to that of Ti. It shows a depletion at the interface and in the very first nanometers of the deposited film (59 at. %, to be compared to the 60% expected for GFO), and then an increasing concentration up to the unit cell orientation reversal (65 at. %). After the polarization reversal region, the O content restores to the expected value, and that of Ti becomes negligible.

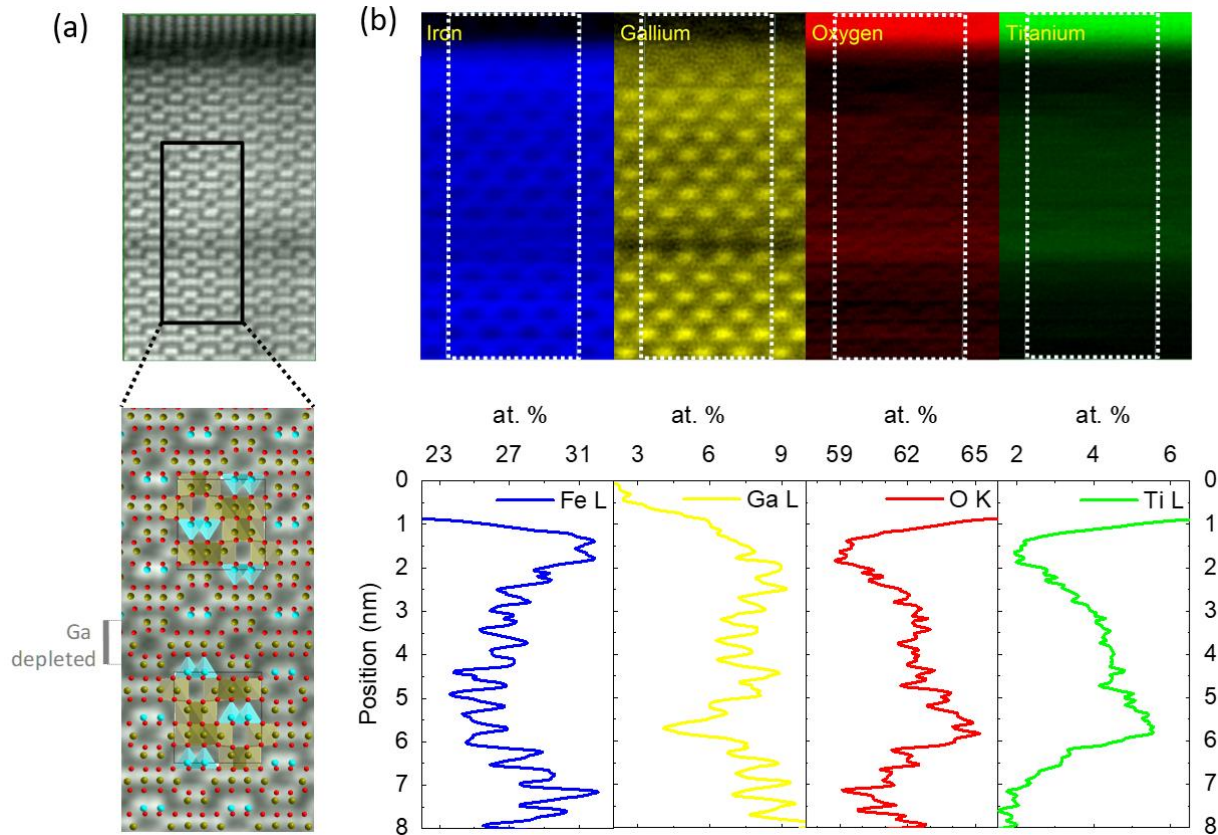


**Fig. 2.16 | STEM-EELS analysis of the interface between the STO(111) substrate and the GFO (32 nm) thin film.** (a) HAADF survey image and zoom recalling the cells' atomic positions and orientation on each side of the polarization boundary. (b) Atomically resolved quantitative elemental maps for Fe, Ga, O, and Ti with elemental profiles integrated over the zone of interest (indicated by white dotted rectangles on the maps).

When analysing the profile of the Fe  $L_{2,3}$ -edge spectra [Fig. 2.17 a-c], one can observe a significant variation between the very first deposited GFO and the rest of the film, in both the position of the lines and the intensities ratio  $I(L_3)/I(L_2)$ . The position of the Fe  $L_3$ -edge line is shifted by almost 1 eV towards lower energies in the first two deposited nanometers when compared to the rest of the film. The  $I(L_3)/I(L_2)$  ratio calculated from the method shown in Fig. 2.17 (c) increases from

3.73 in this area [zone 1 in Fig. 2.17 (a)] to 4.38 for a more inner part of the film [zone 4 in Fig. 2.17 (a)]. Both the Fe excitation edge energy and the  $I(L_3)/I(L_2)$  ratio are correlated to the Fe oxidation state<sup>[40,41]</sup>. Here, they indicate the presence of  $Fe^{2+}$  in the first deposited layers of GFO. This is a second possible explanation for the increase of the  $c$  parameter observed for the very thin films. Indeed,  $Fe^{2+}$  has a bigger radius than  $Fe^{3+}$ , both in tetrahedral and octahedral sites ( $r_{Fe_{Oh}^{2+}} = 0.78 \text{ nm} > 0.645 \text{ nm} = r_{Fe_{Oh}^{3+}} = 0.78 \text{ nm}$ , and  $r_{Fe_{Td}^{2+}} = 0.63 \text{ nm} > 0.49 \text{ nm} = r_{Fe_{Td}^{3+}}$ )<sup>42</sup>.

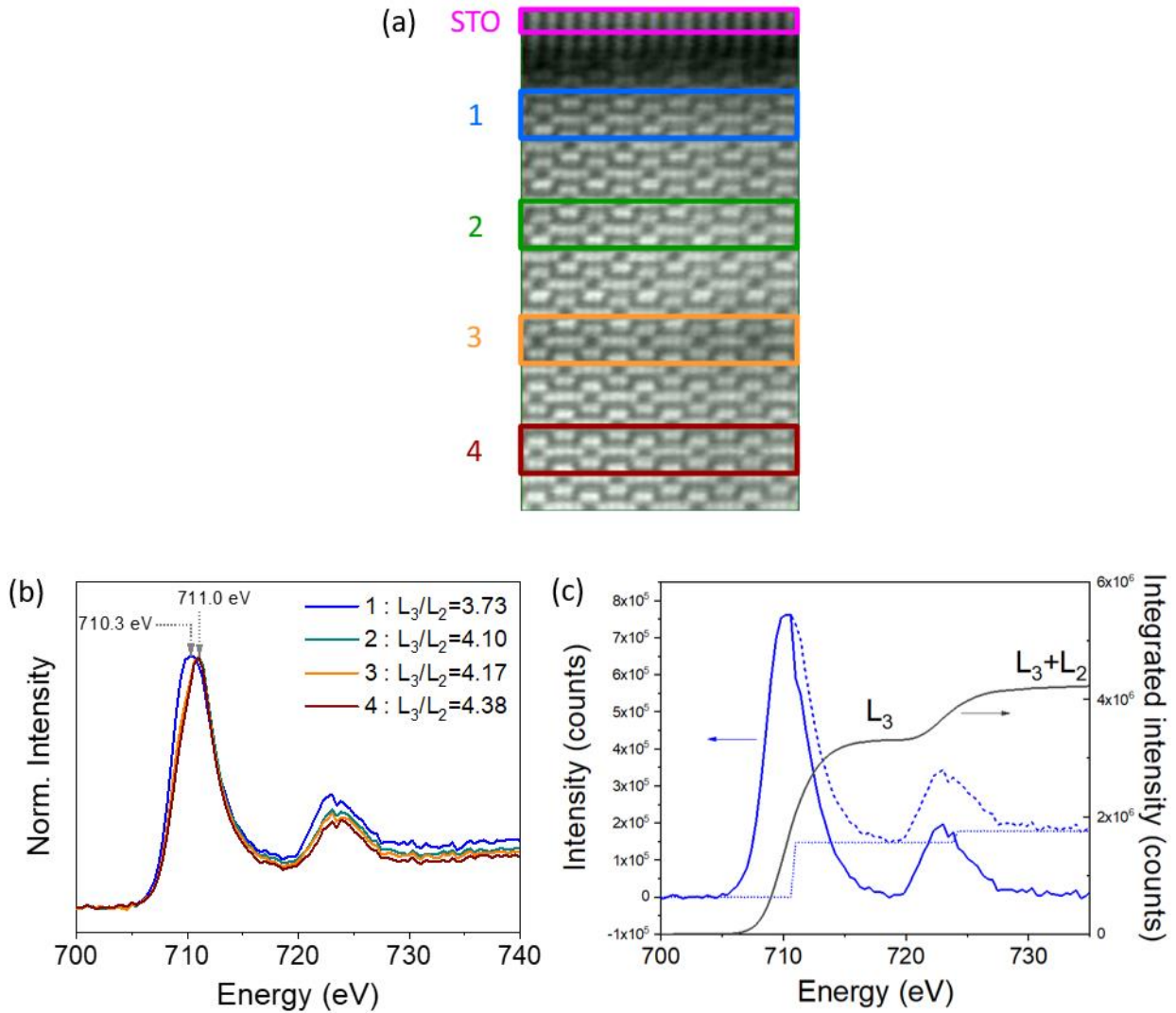


**Fig. 2.17 | EELS study of first few GFO layers.** (a) HAADF HR STEM image of the 32 nm GFO film highlighting four zones at various depths in the films for EELS. (b) The Fe  $L_{2,3}$  EELS profiles integrated on these zones. (c) The method for correcting the spectra with a step-function and integrating it to calculate  $I(L_3)/I(L_2)$ .

Both HR-TEM and EELS information can be combined to trace back the whole deposition process, from the first steps of the growth. The following hypotheses may be formulated to describe the mechanism according to which GFO films grow onto STO substrates. At the early stages of the deposition, the Ti atoms of the STO substrate are attracted to the oxidizing atmosphere at the surface of the sample and diffuse into the forming GFO film, always remaining as close as possible to the oxygen-rich atmosphere. Oxygen-driven cationic mobility has already been observed in other systems <sup>[43]</sup>. This results in an oxygen-deficient environment for the early grown GFO unit cells and, therefore, an orientation of their electric polarization towards the substrate. There is indeed a strong relationship between the oxygen concentration and the polarization orientation of polar films <sup>[44,45]</sup>. The control of the orientation of a film's polarization through the oxygen partial pressure to which it is submitted has been shown by Wang *et al.* in ultrathin PbTiO<sub>3</sub> films <sup>[46]</sup>. Fe in the first GFO deposited layers is reduced to its +II valence state, as observed by EELS. Ga, which is less prone to reduction, tends to move away from this zone, which is therefore relatively enriched in Fe [see the Fe concentration in the first deposited nanometers in Fig. 2.16. (a)]. The Ti migration from the substrate towards the surface's oxidizing atmosphere continues if the material's electric conductance allows it. It stops when the GFO film is 5 nm thick and becomes insulating enough to prevent any ionic mobility. The oxygen is then no more cornered by Ti, and the oxygen-rich atmosphere and its correlated negative charges allow a reversal of the polarization <sup>[47]</sup>, which will now point towards the surface until the end of the growth.

Thickness dependent electric polarization orientation had already been observed <sup>[48]</sup>. The phenomenon was, however, ascribed to already well-documented strain driven effects <sup>[47,49,50]</sup>. Here we show that the polarization reversal observed within the first 5 nm of the film's growth is related to important substrate-film interfacial effects in the form of ionic migration processes driven by electrostatic effects. This is the first reported demonstration of this original chemistry-based mechanism. This study has been published in Homkar *et al.* <sup>[51]</sup>.

## 2.3 Transposition of the growth conditions to another PLD chamber

We also reproduce the high-quality growth of GFO on STO in the PLD chamber used at ETH, Zürich, using the growth parameters already optimized in the PLD chamber at IPCMS, Strasbourg. The PLD chambers were produced by the same parent company (TSST, Netherlands), but PLD set-ups always have their individuality. Here they differ in aspects like the distance between target and substrate, the RHEED spot size, and some modifications made to the ETH chamber windows to accommodate the laser necessary to the second harmonic generation experiments. The optimized GFO growth parameters for thin films prepared at IPCMS, Strasbourg, and ETH, Zürich are given in Table 2.2. The deposition is also monitored with RHEED and the films are subsequently characterized with XRD and AFM, performed at ETH, Zürich (Fig 2.18 (a), (b), and (c)).

The  $\theta$ - $2\theta$  scans of films grown at ETH, Zürich (13, 40, 70 nm) show the same shift in the  $c$  lattice parameter with the thickness ( $c$  decreases with increasing thickness) as observed for films grown at IPCMS, Strasbourg (11, 32, 64 nm). All the films are epitaxially grown and exempt from any spurious phase. The RHEED patterns show a streaky specular spot indicating a 2D growth mode for 13 nm and 50 nm. RHEED does not show any clear evidence of a 3D to 2D transition for the ETH samples, as it is the case for the IPCMS ones, but this could simply originate from a different resolution of the RHEED. The AFM topography reveals distinct line patterns for the 13 nm film which has an rms roughness of 0.56 nm and a homogeneous surface for the 50 nm film with rms roughness of 0.27 nm. These results are in perfect agreement with the observations done on the GFO films prepared at IPCMS, Strasbourg. Hence, we conclude that the films prepared in ETH, Zürich are the similar high-quality films we obtained at IPCMS, Strasbourg, and probably follow a very similar dynamic of growth.

Growth parameters	IPCMS, Strasbourg	ETH, Zürich
O <sub>2</sub> pressure (mBar)	0.1	0.1
Repetition rate (Hz)	2	2
Fluence (J/cm <sup>2</sup> )	3.5	2.5 (max)
Distance between Target-Substrate (cm)	55	60
Temperature (°C)	900	800

**Table 2.2 | Comparison of the growth parameters used for PLD depositions in IPCMS, Strasbourg and ETH, Zurich.**

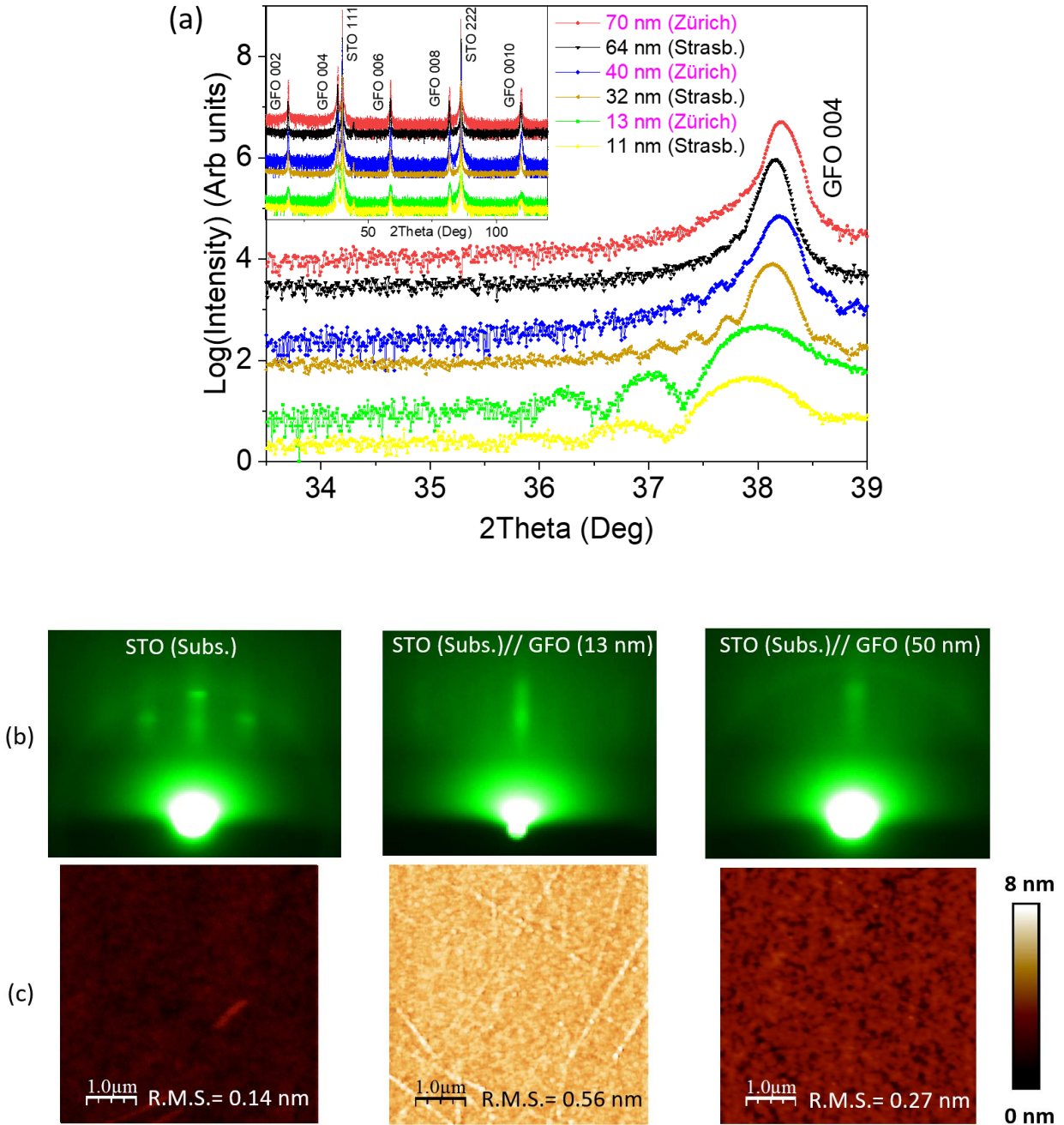


**Fig. 2.18 | Structural and surface characterization of GFO thin films in another PLD chamber.** (a) XRD  $\theta$ - $2\theta$  scans for different thickness samples prepared in both IPCMS, Strasbourg, and ETH, Zürich. (c) RHEED images. (d) AFM images of the STO substrate and GFO samples of 13 and 50 nm thickness prepared at ETH, Zürich.

## 2.4 Elaboration of $\text{Ga}_{0.6}\text{Fe}_{1.4}\text{O}_3$ thin films on $\text{SrRuO}_3$ (SRO) buffered STO substrates.

### 2.4.1 Why an SRO buffer layer?

In this section, we will present the PLD growth of GFO thin films on SRO buffered STO(111) substrates, which has been carried out in ETH Zurich, in the *in situ* second harmonic generation equipped set-up. We have three main reasons to use a SRO buffer layer. Firstly, SRO presents a very good lattice matching with the STO substrate, and due to homoepitaxy, it is also relatively easy to grow using PLD, as many studies have shown it. Secondly, we would like to use SRO as a buffer to stop the Ti insertion in the GFO matrix and change the growth kinetics towards a 2D layer-by-layer mode from the very first unit cells. Devices of such sub-10 nm films are highly desired for contemporary high-density technologies. Lastly, SRO shows a metallic conducting behavior in thin film and hence acts as a bottom electrode, which is useful for future electrical measurements, and it can also later act as a bottom electrode for polarization charge screening.

### 2.4.2 Growth of GFO/SRO//STO heterostructures

The growth duration of GFO on SRO buffered STO was kept the same as that of GFO on STO to allow effective comparison. During the growth of STO//SRO/GFO, we observe a smooth 2D growth of SRO as indicated by the RHEED pattern and a 2D growth mode for GFO at an ultra-thin regime which, eventually, changes to 3D growth mode at high thicknesses (see Fig. 2.19 (a)). This 2D growth observed from the early stages of the deposition shows low roughness (rms = 0.34 nm) as seen from AFM image in Fig. 2.19 (b) for 4 nm GFO on SRO//STO. This is different from what is observed on non-buffered STO (rms = 1.2 nm) and can be explained by the reduction/elimination of the Ti migration into GFO, allowed by inserting a 2.5 nm thick SRO layer between GFO and STO. This might have led to a change in the growth kinetics due to a change in the surface chemistry. The  $\theta$ - $2\theta$  scans show the comparison between GFO film of similar thickness (~32-34 nm) grown on STO and SRO-buffered-STO (Fig. 2.19 (c)), where they exhibit similar out-of-plane 'c' lattice parameters. The GFO film on SRO-buffered-STO is seen to have been epitaxially grown and exempt from any spurious phases. The plots in Fig. 2.20 (a, b) show the RSM corresponding to the SRO/STO 313 and GFO 2010 reflections, for both STO//GFO (32 nm) and STO//SRO (2.5 nm)/GFO (34 nm) films. These maps indicate that the GFO films are completely relaxed in both cases and have very similar parameters.

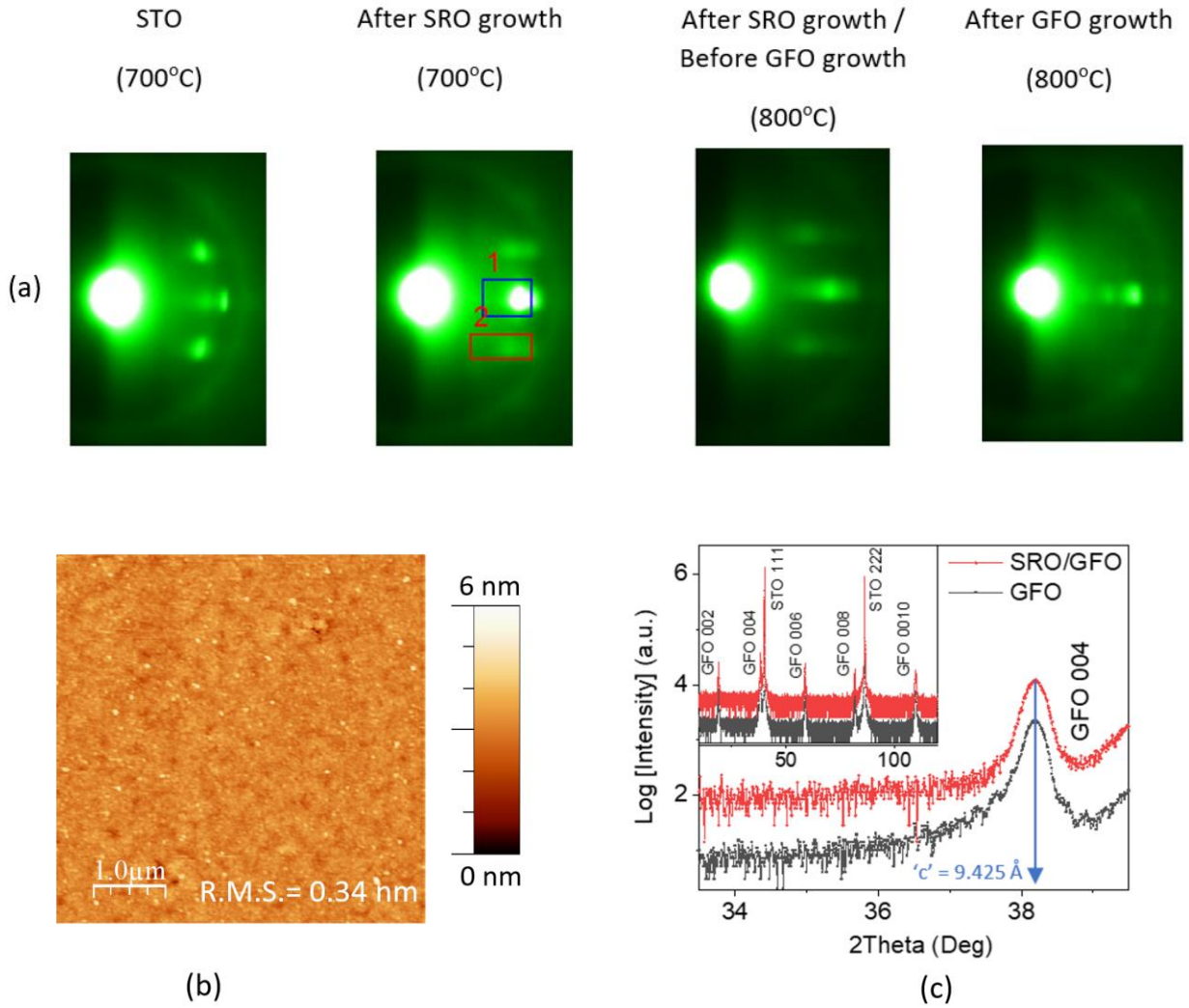


**Fig 2.19 | Surface and structural characterization of GFO thin film on SRO-buffered-STO substrate.** (a) RHEED images of STO only (Subs.), STO//SRO (electrode) and STO//SRO/GFO (Polar film). (b) AFM image of STO(Subs.)//SRO (2.5 nm)/GFO (4 nm) sample after growth. (c)  $\theta$ -2 $\theta$  scan for STO(Subs.)//GFO (39 nm) and STO(Subs.)//SRO (2.5 nm)/GFO (34.4 nm), to allow comparison.

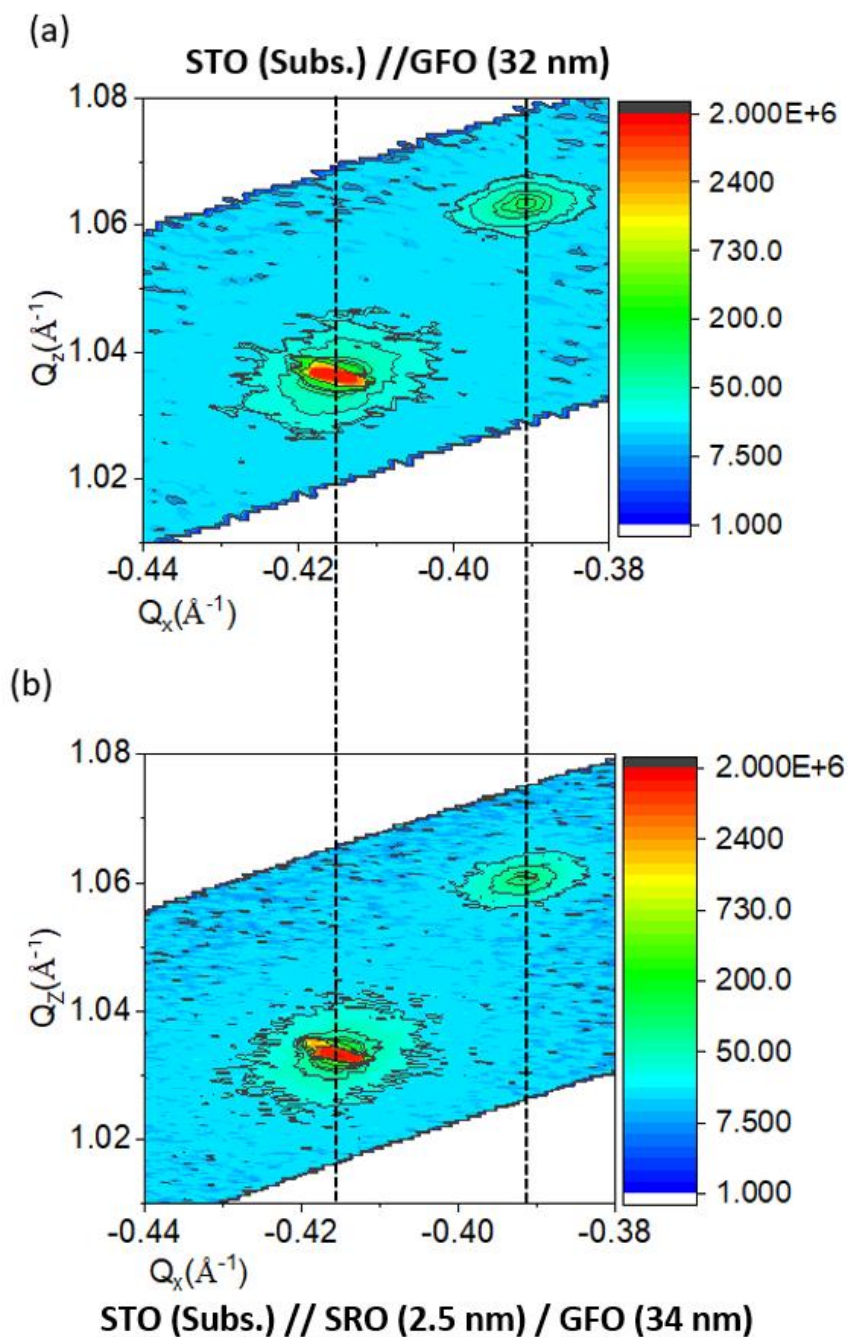


**Fig. 5.2.20 | RSM plots of GFO thin films that includes STO 313 (consequently the SRO 313) and GFO 2010.** (a) As grown on STO(111). (b) As grown on SRO-buffered-STO (111). Each graph has been obtained to include the STO, SRO and the GFO reflections in a single graph to gain insight into the strain between the substrate and the film.

### 2.4.3 Conclusions

The pulsed laser deposition of thin films of the magnetoelectric multiferroic compound  $\text{Ga}_{0.6}\text{Fe}_{1.4}\text{O}_3$  (GFO) 001 onto  $\text{SrTiO}_3$  (STO) 111 substrates has been studied from the very early steps of the growth for the first time. The growth is at first 3D, because of the mismatch between the substrate and the film, but rapidly becomes 2D. A rms roughness as low as 0.16 nm is observed for samples of approximately 10 nm thickness and up to more than 60 nm. The growth process can be monitored by RHEED and resolved to one metal-oxygen-polyhedra layer deposition corresponding to  $1/4^{\text{th}}$  of a unit cell. Important substrate-film interfacial effects are unveiled by an atomically resolved EELS study. Ionic migration processes driven by electrostatic effects result in the reversal of GFO unit-cell after 5 nm thickness. The high epitaxial quality and atomically flat growth of GFO thin films is highly reproducible, as demonstrated by growth in another PLD chamber that follows similar growth dynamics. The growth of GFO on a conducting electrode such as  $\text{SrRuO}_3$  (SRO)-buffered-STO changes the growth dynamics possibly due to the reduction or complete absence of Ti insertion in the GFO films and atomically smooth film growth is possible even at few unit-cell thickness.

The demonstration of highly epitaxial layer-by-layer growth of GFO with atomically smooth surface at sub-10nm thickness regime opens perspectives for practical applications in spintronics devices.

## 2.5 References

- (1) Eason, R. *Pulsed Laser Deposition of Thin Films: Applications-Led Growth of Functional Materials*; John Wiley & Sons, **2007**.
- (2) Lorenz, M.; Hochmuth, H.; Natusch, D.; Börner, H.; Lippold, G.; Kreher, K.; Schmitz, W. Large-area Double-side Pulsed Laser Deposition of  $\text{YBa}_2\text{Cu}_3\text{O}_{7-x}$  Thin Films on 3-in. Sapphire Wafers. *Applied physics letters* **1996**, *68* (23), 3332–3334.
- (3) Nguyen, M. D.; Tiggelaar, R.; Aukes, T.; Rijnders, G.; Roelof, G. Wafer-Scale Growth of Highly Textured Piezoelectric Thin Films by Pulsed Laser Deposition for Micro-Scale Sensors and Actuators. In *J. Phys. Conf. Ser.*; 2017; Vol. 922, p 012022.
- (4) Roulland, F.; Lefevre, C.; Thomasson, A.; Viart, N. Study of  $\text{Ga}_{(2-x)}\text{Fe}_x\text{O}_3$  Solid Solution: Optimisation of the Ceramic Processing. *Journal of the European Ceramic Society* **2013**, *33* (5), 1029–1035.
- (5) Hasegawa, S. Reflection High-energy Electron Diffraction. *Characterization of Materials* **2002**, 1–14.
- (6) Neave, J. H.; Joyce, B. A.; Dobson, P. J.; Norton, N. Dynamics of Film Growth of GaAs by MBE from RHEED Observations. *Applied Physics A* **1983**, *31* (1), 1–8.
- (7) Rijnders, A. J. H. M. The Initial Growth of Complex Oxides: Study and Manipulation. **2003**.
- (8) Gellé, F. Hétérostructures Épitaxiées Avec Des Propriétés Dépendantes de Spin et de Charges Pour Des Applications En Spintronique, Thesis, University of Strasbourg, **2019**.
- (9) Lifshin, E. *X-Ray Characterization of Materials*; John Wiley & Sons, **2008**.
- (10) Kojima, I.; Li, B. Structural Characterization of Thin Films by X-Ray Reflectivity. *Rigaku J* **1999**, *16* (2), 31–42.
- (11) Holy, V.; Baumbach, T.; Pietsch, U. *High-Resolution X-Ray Scattering from Thin Films and Multilayers*; Springer, **1999**.
- (12) Soumah, L. Pulsed Laser Deposition of Substituted Thin Garnet Films for Magnonic Applications, Thesis, Université Paris-Saclay (ComUE), **2019**.
- (13) Landgraf, B. Structural, Magnetic and Electrical Investigation of Iron-Based III/V-Semiconductor Hybrid Structures, Thesis, University of Hamburg, **2014**.
- (14) Yasaka, M. X-Ray Thin-Film Measurement Techniques. *The Rigaku Journal* **2010**, *26* (2), 1–9.
- (15) Hensling, F. V.; Xu, C.; Gunkel, F.; Dittmann, R. Unraveling the Enhanced Oxygen Vacancy Formation in Complex Oxides during Annealing and Growth. *Scientific reports* **2017**, *7* (1), 1–8.
- (16) Padilla, J. A.; Xuriguera, E.; Rodríguez, L.; Vannozzi, A.; Segarra, M.; Celentano, G.; Varela, M. Epitaxial Growth of  $\text{SrTiO}_3$  Films on Cube-Textured Cu-Clad Substrates by PLD at Low Temperature Under Reducing Atmosphere. *Nanoscale research letters* **2017**, *12* (1), 226.
- (17) Sánchez, F.; Ocal, C.; Fontcuberta, J. Tailored Surfaces of Perovskite Oxide Substrates for Conducted Growth of Thin Films. *Chemical Society Reviews* **2014**, *43* (7), 2272–2285.
- (18) Scullin, M. L.; Ravichandran, J.; Yu, C.; Huijben, M.; Seidel, J.; Majumdar, A.; Ramesh, R. Pulsed Laser Deposition-Induced Reduction of  $\text{SrTiO}_3$  Crystals. *Acta materialia* **2010**, *58* (2), 457–463.

- (19) Watanabe, S.; Hikita, T.; Kawai, M. Cleaning the Surface of SrTiO<sub>3</sub> (100) and LaAlO<sub>3</sub> (100) under Moderate Temperature Condition by Bi Adsorption/Desorption Treatment. *Journal of Vacuum Science & Technology A: Vacuum, Surfaces, and Films* **1991**, *9* (4), 2394–2396.
- (20) Biswas, A.; Yang, C.-H.; Ramesh, R.; Jeong, Y. H. Atomically Flat Single Terminated Oxide Substrate Surfaces. *Progress in Surface Science* **2017**, *92* (2), 117–141.
- (21) Li, H.; Hu, X.; Wei, Y.; Yu, Z.; Zhang, X.; Droopad, R.; Demkov, A. A.; Edwards Jr, J.; Moore, K.; Ooms, W. Two-Dimensional Growth of High-Quality Strontium Titanate Thin Films on Si. *Journal of applied physics* **2003**, *93* (8), 4521–4525.
- (22) Gu, X.; Lubyshev, D.; Batzel, J.; Fastenau, J. M.; Liu, W. K.; Pelzel, R.; Magana, J. F.; Ma, Q.; Wang, L. P.; Zhang, P. Commercial Molecular Beam Epitaxy Production of High Quality SrTiO<sub>3</sub> on Large Diameter Si Substrates. *Journal of Vacuum Science & Technology B: Microelectronics and Nanometer Structures Processing, Measurement, and Phenomena* **2009**, *27* (3), 1195–1199.
- (23) Song, S.; Jang, H. M.; Lee, N.-S.; Son, J. Y.; Gupta, R.; Garg, A.; Ratanapreechachai, J.; Scott, J. F. Ferroelectric Polarization Switching with a Remarkably High Activation Energy in Orthorhombic GaFeO<sub>3</sub> Thin Films. *NPG Asia Mater* **2016**, *8*, e242.
- (24) Sánchez, F.; García-Cuenca, M. V.; Ferrater, C.; Varela, M.; Herranz, G.; Martínez, B.; Fontcuberta, J. Transition from Three- to Two-Dimensional Growth in Strained SrRuO<sub>3</sub> Films on SrTiO<sub>3</sub> (001). *Applied Physics Letters* **2003**, *83* (5), 902.
- (25) Lefevre, C.; Demchenko, A.; Bouillet, C.; Luysberg, M.; Devaux, X.; Roulland, F.; Versini, G.; Barre, S.; Wakabayashi, Y.; Boudet, N.; Leuvre, C.; Acosta, M.; Meny, C.; Martin, E.; Grenier, S.; Favre-Nicolin, V.; Viart, N. Nondestructive Method for the Determination of the Electric Polarization Orientation in Thin Films: Illustration on Gallium Ferrite Thin Films. *Small Methods* **2017**, *1* (12)
- (26) Krockenberger, Y.; Yun, K.-S.; Hatano, T.; Arisawa, S.; Kawasaki, M.; Tokura, Y. Layer-by-Layer Growth and Magnetic Properties of Y<sub>3</sub>Fe<sub>5</sub>O<sub>12</sub> Thin Films on Gd<sub>3</sub>Ga<sub>5</sub>O<sub>12</sub>. *Journal of Applied Physics* **2009**, *106* (12), 123911.
- (27) Lefevre, C.; Roulland, F.; Thomasson, A.; Meny, C.; Porcher, F.; Andre, G.; Viart, N. Magnetic and Polar Properties' Optimization in the Magnetoelectric Ga<sub>2-x</sub>Fe<sub>x</sub>O<sub>3</sub> Compounds. *Journal of Physical Chemistry C* **2013**, *117* (28), 14832–14839.
- (28) Demchenko, A. Investigation of the Potential Offered by Gallium Iron Oxide Thin Films in Terms of Multiferroicity, Thesis, University of, Strasbourg, **2015**.
- (29) Lefevre, C.; Demchenko, A.; Bouillet, C.; Luysberg, M.; Devaux, X.; Roulland, F.; Versini, G.; Barre, S.; Wakabayashi, Y.; Boudet, N.; Leuvre, C.; Acosta, M.; Meny, C.; Martin, E.; Grenier, S.; Favre-Nicolin, V.; Viart, N. Nondestructive Method for the Determination of the Electric Polarization Orientation in Thin Films: Illustration on Gallium Ferrite Thin Films. *Small Methods* **2017**, *1*, 1700234.
- (30) Richardson, C. J. K.; Lee, M. L. Metamorphic Epitaxial Materials. *MRS Bulletin* **2016**, *41* (3), 193–198.
- (31) Ukleev, V.; Sutin, S.; Nakajima, T.; Arima, T.; Saerbeck, T.; Hanashima, T.; Sitnikova, A.; Kirilenko, D.; Yakovlev, N.; Sokolov, N. Unveiling Structural, Chemical and Magnetic Interfacial Peculiarities in ε-Fe<sub>2</sub>O<sub>3</sub>/GaN (0001) Epitaxial Films. *Scientific Reports* **2018**, *8* (1), 8741.

- (32) Gich, M.; Fina, I.; Morelli, A.; Sanchez, F.; Alexe, M.; Gazquez, J.; Fontcuberta, J.; Roig, A. Multiferroic Iron Oxide Thin Films at Room Temperature. *Advanced Materials* **2014**, *26* (27), 4645.
- (33) Fong, D. D.; Stephenson, G. B.; Streiffer, S. K.; Eastman, J. A.; Auciello, O.; Fuoss, P. H.; Thompson, C. Ferroelectricity in Ultrathin Perovskite Films. *Science* **2004**, *304* (5677), 1650–1653.
- (34) Lichtensteiger, C.; Dawber, M.; Stucki, N.; Triscone, J.-M.; Hoffman, J.; Yau, J.-B.; Ahn, C. H.; Despont, L.; Aebi, P. Monodomain to Polydomain Transition in Ferroelectric PbTiO<sub>3</sub> Thin Films with La<sub>0.67</sub>Sr<sub>0.33</sub>MnO<sub>3</sub> Electrodes. *Applied Physics Letters* **2007**, *90* (5), 052907.
- (35) Dawber, M.; Chandra, P.; Littlewood, P. B.; Scott, J. F. Depolarization Corrections to the Coercive Field in Thin-Film Ferroelectrics. *Journal of Physics: Condensed Matter* **2003**, *15* (24), L393.
- (36) Streiffer, S. t; Eastman, J. A.; Fong, D. D.; Thompson, C.; Munkholm, A.; Murty, M. R.; Auciello, O.; Bai, G. R.; Stephenson, G. B. Observation of Nanoscale 180° Stripe Domains in Ferroelectric PbTiO<sub>3</sub> Thin Films. *Physical review letters* **2002**, *89* (6), 067601.
- (37) Stoeffler, D. First Principles Study of the Electric Polarization and of Its Switching in the Multiferroic GaFeO<sub>3</sub> System. *Journal of Physics-Condensed Matter* **2012**, *24* (18), 185502.
- (38) Stoeffler, D. First Principles Study of the Spontaneous Electric Polarization in Ga<sub>2-x</sub>Fe<sub>x</sub>O<sub>3</sub>. *Thin Solid Films* **2013**, *533*, 93–96.
- (39) Meier, D.; Seidel, J.; Cano, A.; Delaney, K.; Kumagai, Y.; Mostovoy, M.; Spaldin, N. A.; Ramesh, R.; Fiebig, M. Anisotropic Conductance at Improper Ferroelectric Domain Walls. *Nature Materials* **2012**, *11* (4), 284–288.
- (40) Colliex, C.; Tahar, M.; Ortiz, C. Electron-Energy-Loss-Spectroscopy near-Edge Fine Structures in the Iron-Oxygen System. *Physical review. B, Condensed matter* **1991**, *44*, 11402–11411.
- (41) Tan, H.; Verbeeck, J.; Abakumov, A.; Van Tendeloo, G. Oxidation State and Chemical Shift Investigation in Transition Metal Oxides by EELS. *Ultramicroscopy* **2012**, *116*, 24–33.
- (42) Shannon, R. Revised Effective Ionic-Radii and Systematic Studies of Interatomic Distances in Halides and Chalcogenides. *Acta Crystallogr. Sect. A* **1976**, *32* (SEP1), 751–767.
- (43) Viart, N.; Hassan, R. S.; Ulhaq-Bouillet, C.; Meny, C.; Panissod, P.; Loison, J. L.; Versini, G.; Huber, F.; Pourroy, G.; Verbeeck, J.; van Tendeloo, G. Oxidation Processes at the Metal/Oxide Interface in CoFe<sub>2</sub>/CoFe<sub>2</sub>O<sub>4</sub> Bilayers Deposited by Pulsed Laser Deposition. *Acta Mater.* **2006**, *54* (1), 191–196.
- (44) Park, C. H.; Chadi, D. J. Microscopic Study of Oxygen-Vacancy Defects in Ferroelectric Perovskites. *Phys. Rev. B* **1998**, *57* (22), R13961–R13964.
- (45) Highland, M. J.; Fister, T. T.; Fong, D. D.; Fuoss, P. H.; Thompson, C.; Eastman, J. A.; Streiffer, S. K.; Stephenson, G. B. Equilibrium Polarization of Ultrathin PbTiO<sub>3</sub> with Surface Compensation Controlled by Oxygen Partial Pressure. *Phys. Rev. Lett.* **2011**, *107* (18), 187602.
- (46) Wang, R. V.; Fong, D. D.; Jiang, F.; Highland, M. J.; Fuoss, P. H.; Thompson, C.; Kolpak, A. M.; Eastman, J. A.; Streiffer, S. K.; Rappe, A. M.; Stephenson, G. B. Reversible Chemical Switching of a Ferroelectric Film. *Phys. Rev. Lett.* **2009**, *102* (4), 047601.
- (47) Tyunina, M.; Pacherova, O.; Peräntie, J.; Savinov, M.; Jelinek, M.; Jantunen, H.; Dejneka, A. Perovskite Ferroelectric Tuned by Thermal Strain. *Sci Rep* **2019**, *9* (1), 1–7.

- (48) Yu, X.; Wu, L.; Zhang, B.; Zhou, H.; Dong, Y.; Wu, X.; Kou, R.; Yang, P.; Chen, J.; Sun, C.-J.; Zhu, Y.; Chow, G. M. Thickness-Dependent Polarization-Induced Intrinsic Magnetoelectric Effects in  $\text{La}_{0.67}\text{Sr}_{0.33}\text{MnO}_3/\text{PbZr}_{0.52}\text{Ti}_{0.48}\text{O}_3$  Heterostructures. *Phys. Rev. B* **2019**, *100* (10), 104405.
- (49) Jang, H. W.; Baek, S. H.; Ortiz, D.; Folkman, C. M.; Das, R. R.; Chu, Y. H.; Shafer, P.; Zhang, J. X.; Choudhury, S.; Vaithyanathan, V.; Chen, Y. B.; Felker, D. A.; Biegalski, M. D.; Rzchowski, M. S.; Pan, X. Q.; Schlom, D. G.; Chen, L. Q.; Ramesh, R.; Eom, C. B. Strain-Induced Polarization Rotation in Epitaxial (001)  $\text{BiFeO}_3$  Thin Films. *Phys. Rev. Lett.* **2008**, *101* (10), 107602.
- (50) Nguyen, T. D.; Mao, S.; Yeh, Y.-W.; Purohit, P. K.; McAlpine, M. C. Nanoscale Flexoelectricity. *Adv. Mater.* **2013**, *25* (7), 946–974.
- (51) Homkar, S.; Preziosi, D.; Devaux, X.; Bouillet, C.; Nordlander, J.; Trassin, M.; Roulland, F.; Lefèvre, C.; Versini, G.; Barre, S. Ultrathin Regime Growth of Atomically Flat Multiferroic Gallium Ferrite Films with Perpendicular Magnetic Anisotropy. *Physical Review Materials* **2019**, *3* (12), 124416.



---

# Chapter 3

## $\text{Ga}_{0.6}\text{Fe}_{1.4}\text{O}_3$ thin films :

### Magnetic properties

---

Even though the magnetic properties of GFO have already been vastly explored in the literature, they are not yet completely understood. As demonstrated in the introduction part, this is due to the complex exchange interactions involved between the Fe ions in their different environments at the four cationic sites. Furthermore, owing to the technological appeal of this multifunctional GFO material, it is necessary to get a better insight into the different mechanisms at work to govern its magnetic properties at the thin/ultra-thin scales.

Therefore, in this chapter, we will present our investigation of the magnetic properties of GFO thin/ultra-thin films, both macroscopically, using superconducting quantum interference device-vibrating sample magnetometer (SQUID-VSM), and microscopically, using X-ray magnetic circular dichroism (XMCD) techniques. We will in particular lay a stress on anisotropy issues, for the overall magnetic behavior of the films, as much as for the atomic spin and orbital magnetic moments.

### 3.1 Macroscopic magnetic characterizations of $\text{Ga}_{0.6}\text{Fe}_{1.4}\text{O}_3$ (GFO) thin films.

#### 3.1.1 Methods

##### 3.1.1.1 Superconducting Quantum Interference Device – Vibrating Sample Magnetometer (SQUID-VSM)

The magnetic characteristics of the thin films were measured using a MPMS SQUID magnetometer VSM from Quantum Design <sup>[1]</sup>. A SQUID-VSM is one of the most sensitive devices used for measuring the magnetic properties of thin films <sup>[2]</sup>. The SQUID detector detects variations in the magnetic flux and can measure magnetizations as low as  $10^{-8}$  emu with a very high signal-to-noise ratio. It is based on the DC Josephson effect. A Josephson junction consists in a superconducting ring segmented by two isolation regions (for DC measurement) of very small thickness (Fig. 3.1). In the absence of any external magnetic field, the input current  $I_B$  splits into the two branches equally. If a small external magnetic field is applied to the superconducting loop, a screening current starts to circulate in the loop to cancel the applied external flux, and this creates an additional Josephson phase which is proportional to this external magnetic flux.

It is possible to work over a wide temperature range (from 2 to 400 K) and with magnetic fields of up to 7 T.

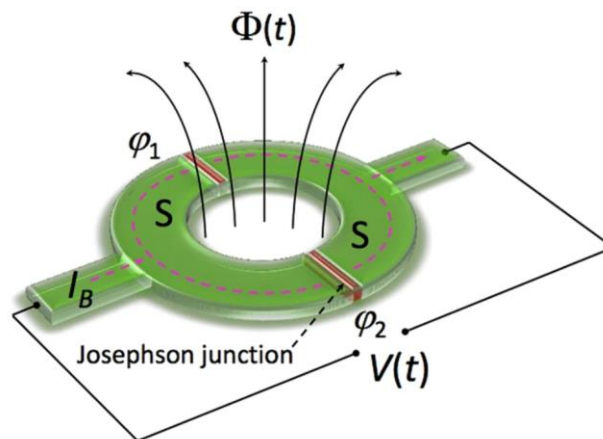


**Fig. 3.1 | Schematic of two Josephson junctions** . These junctions at the interface of 2 superconducting (S) magnets form a ring with a superconducting current ( $I_B$ ).  $\phi(t)$  is the magnetic flux which will induce phases  $\phi_1$  and  $\phi_2$  in the supercurrents at the two Josephson junctions, as measured using a voltmeter ( $V(t)$ ). Adapted from ref. <sup>[3]</sup>.

In the configuration of VSM, the sample will oscillate rapidly in a homogeneous magnetic field. As the sample moves, it will induce a variation in the magnetic flux and thus an electric current in the SQUID detector with a phase difference at Josephson junctions. The reading of this phase difference will allow to retrieve the magnetic moment of the sample.

Two types of measurements are usually carried out : firstly, magnetization ( $M$ ) as a function of temperature ( $T$ ) under a fixed magnetic field ( $H$ ) to obtain the Curie temperature ( $T_c$ ) of magnetic materials, and secondly, hysteresis cycles where we measure the magnetization as a function of the external magnetic field for a given temperature. The measurement in thin films is carried out on  $3 \times 5 \text{ mm}^2$  cut-out pieces introduced in a diamagnetic plastic straw, in either parallel configuration where the external magnetic field is applied parallel to the plane of the thin films or in perpendicular configuration where it is applied perpendicularly to the plane of the sample (Fig. 3.2). These two types of configurations make it possible to determine the easy magnetization axis and thus the magnetic anisotropy of our systems. The  $M(T)$  are always realized with increasing temperatures in a small magnetic field but can be done following two different procedures, either after cooling down in a zero field (Zero Field Cooled measurements – ZFC) or after cooling down in a non-zero magnetic field (Field Cooled measurements – FC).

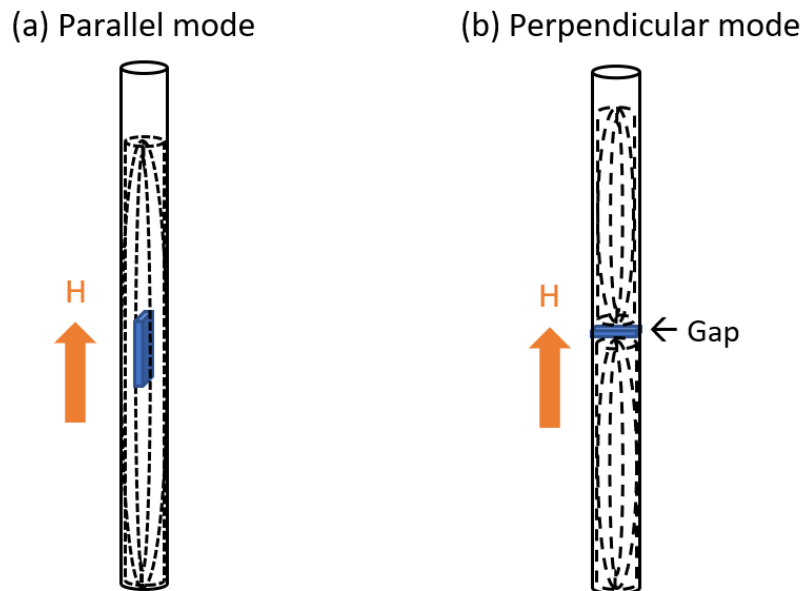


**Fig. 3.2 | Schematics of sample arrangements inside straw.** (a) For parallel measurement . (b) For perpendicular measurement. In blue the substrate and thin film sample.

### 3.1.1.2 Experimental corrections

Before measuring the magnetic properties of thin films, we remove the silver paste on the unpolished surface of substrate by mechanical polishing. The silver paste comes on the unpolished side of the substrate since it was used to fix the substrate on PLD heater to allow for a better thermal contact. Garcia *et al.* showed that the silver paste had a non-negligible magnetic moment at 300 K [4].

Additionally, the magnetic sample measurement comprises various contributions apart from the thin film itself, notably contributions from the straw and the substrate. This must be considered before analyzing the thin film magnetization. Fig. 3.3 (a, b) shows the magnetic hysteresis loop measurement for a straw and STO substrate only, in parallel and perpendicular modes. Both measurements show a diamagnetic response with negligible temperature variations, which is the signature for the diamagnetic substrate contribution.

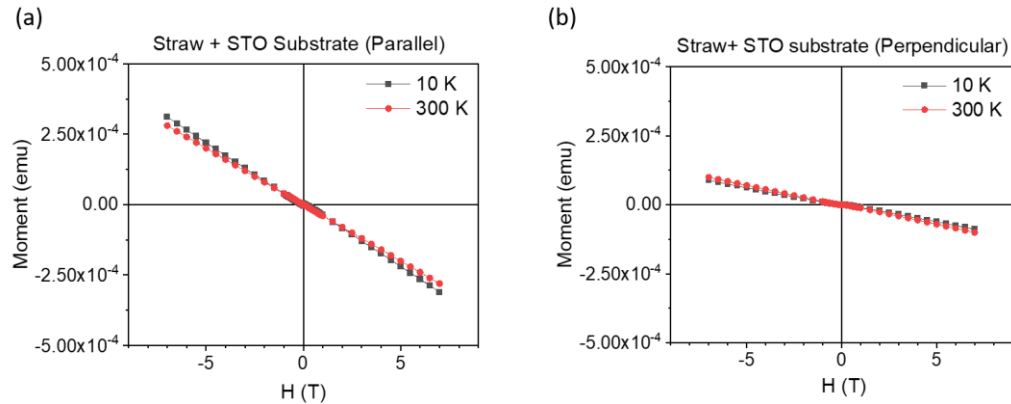


**Fig. 3.3 | Measurements for straw + STO substrate at 10 and 300 K. (a) For parallel mode. (b) For perpendicular mode.**

### 3.1.2 Magnetic characterization of the GFO thin films

Figure 3.4 illustrates the temperature dependent hysteresis loops measurements performed on all the samples with those of the 64 nm thick GFO film, in both parallel and perpendicular modes. The graphs show the raw curves (Fig. 3.4 (a)), the curves after correction from the diamagnetic contributions from the substrate and straw (Fig. 3.4 (b)), and the temperature variation of the values of the hysteresis fields measured on the loops,  $H_c$  vs T curves (Fig. 3.4 (c)). The correction from diamagnetism consists in subtracting the slope observed at high field and high temperature from all the data. At low temperatures (10 and 30 K), the slope value may be strongly stained with some apparent paramagnetism due to the existence of some void around the sample, which can arise during the preparation method. Other possible mechanisms are also explored later in the text.

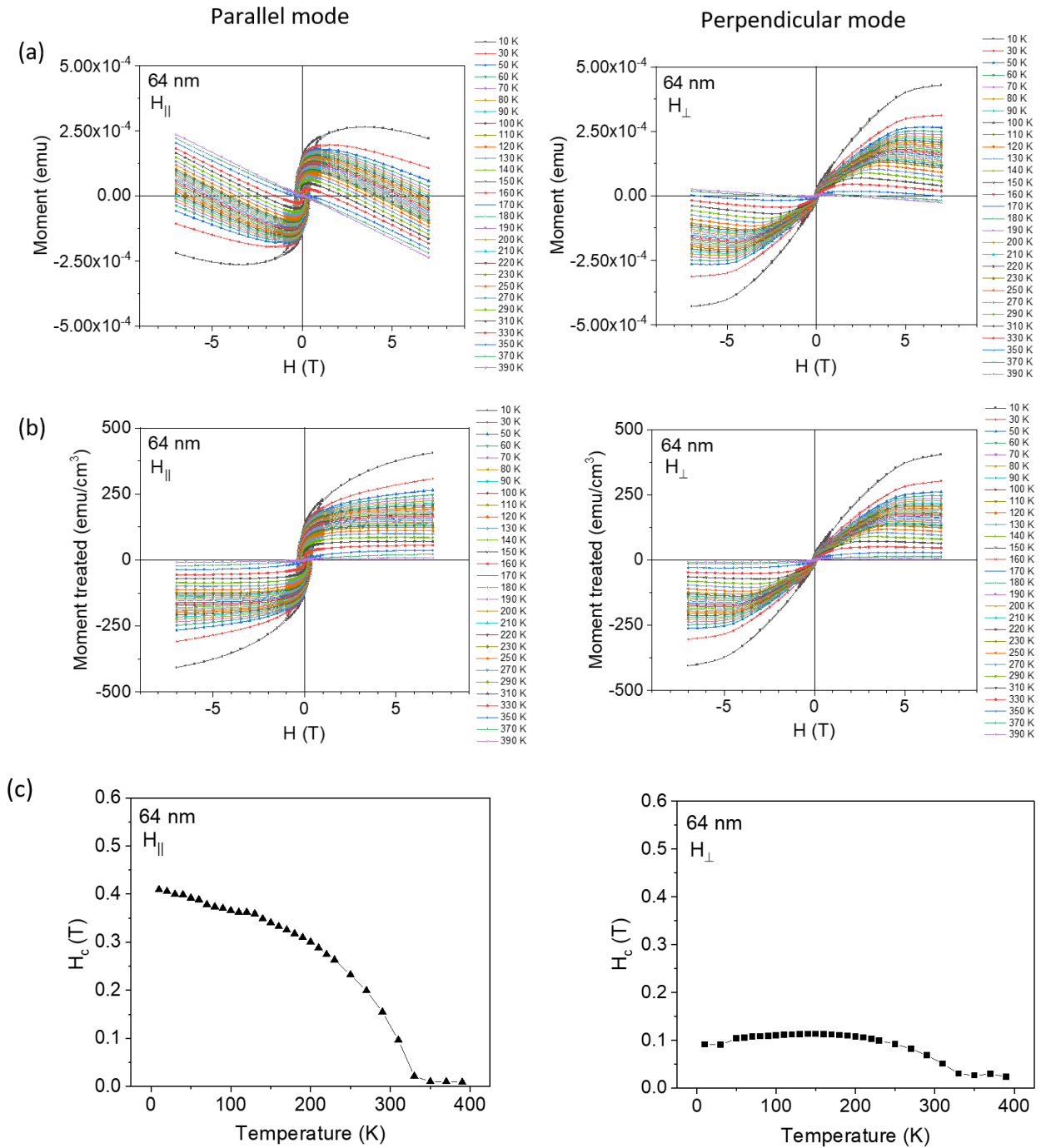


**Fig. 3.4 | Analysis of hysteresis measurements for a 64 nm thick GFO film.** Measurements are made in parallel ( $H_{||}$ ) and perpendicular ( $H_{\perp}$ ) modes over a temperature range of 10-390 K. The sample centering is done at 1000 Oe. (a) as measured raw hysteresis curves, (b) slope-corrected and volume normalized hysteresis curves, (c) temperature dependence of the coercive field ( $H_c$ ), as calculated from the all the above hysteresis loops.

The  $H_c$  vs  $T$  profile increases with decreasing temperature in the parallel mode measurement, whereas in the perpendicular mode, the  $H_c$  vs  $T$  profile increases with the decreasing temperature until 150 K, after which it starts decreasing. The  $H_c$  is negligible above 350 K, indicating that the  $T_c$  is close to this temperature, as expected from previous measurements.

The FC-ZFC measurements performed on the 64 nm GFO thin films in both parallel and perpendicular modes are shown in Figure 3.5. For the FC measurement, the sample was cooled under a 7 T field and the measurements were performed during heating at 5K/min under a magnetic field of 1000 Oe. The magnetic moment decreases with increasing temperatures for both FC-ZFC modes and the  $T_c$  is measured to be close to 350 K from both parallel and perpendicular measurements.

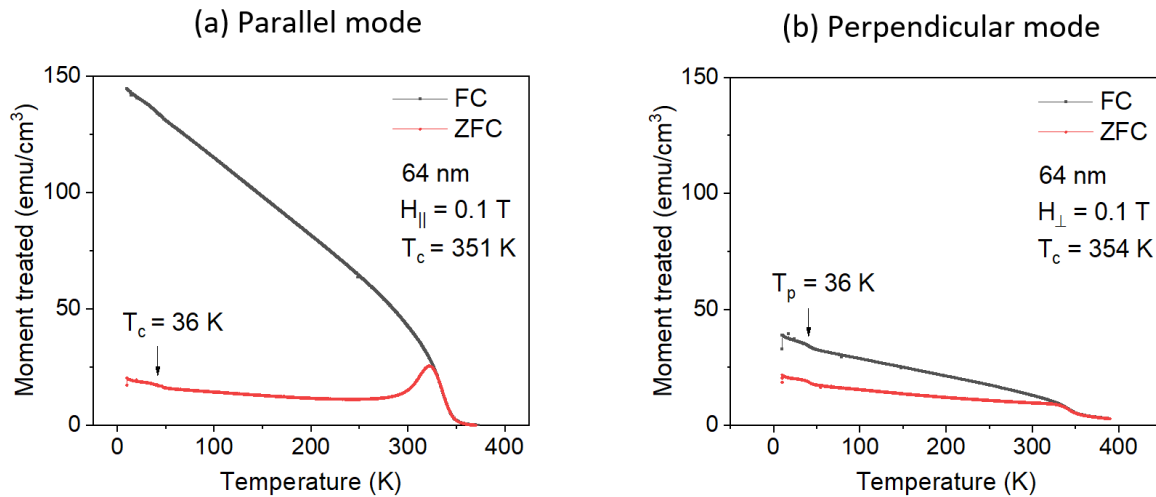


**Fig. 3.5 | Temperature dependence of magnetization measured in FC and ZFC configurations for a 64 nm GFO film.** (a) For parallel ( $H_{||}$ ) mode. (b) For perpendicular ( $H_{\perp}$ ) mode.

The presence of a pinch in both the FC and ZFC curves at ca. 36 K may be due to some spin-flip transition in the structure, originating to some overcoming of the antiferromagnetic interactions between the cationic sites. This can in particular be considered for the tetrahedral site which is known to be less strongly coupled to the other ones (Fig. 1.20). Something similar has been observed in  $\epsilon$ - $\text{Fe}_2\text{O}_3$  at 50 K which has been ascribed to a meta magnetic transition [5].

Now we move towards exploring the magnetic properties for other thicknesses. We have also performed magnetic hysteresis loop measurements on the GFO thin films of 32 nm, 11 nm, and 7 nm thicknesses. The room-temperature saturation magnetization is ca. 100  $\text{emu}/\text{cm}^3$  for samples thicker than 11 nm, as already observed for GFO 1.4 thin films of high thickness (ca. 100

nm) [6]. It decreases to ca. 80 emu/cm<sup>3</sup> for the 7 nm film. The hysteresis loops for all these thicknesses are corrected from substrate and straw contributions, as explained for the case of 64 nm films, and the normalized magnetization versus magnetic field curves are shown in Fig. 3.6. The magnetization easy axis of the films is strongly dependent upon the films thickness. Strikingly, while magnetization is in-plane for films with a thickness of 11 nm or above, it is out-of-plane for the 7 nm-thick sample. This behaviour, observed at room temperature (Fig. 3.6 (a)), is clearly confirmed by low temperature measurements (Fig. 3.6 (b)). It had never been observed before for GFO thin films. Films presenting out-of-plane magnetization are of high interest for spintronic based applications. They indeed address the current challenge to develop high quality sub-10 nm thick ferrimagnetic insulating films with perpendicular magnetic anisotropy which are desired for efficient spin current transmission in ferromagnetic/Pt spin Hall effect driven systems [7].

To further explore the potential offered by the magnetic anisotropy modulation, it is imperative to have a full understanding of the magnetic anisotropy in this system first. This we will explore in the next section.

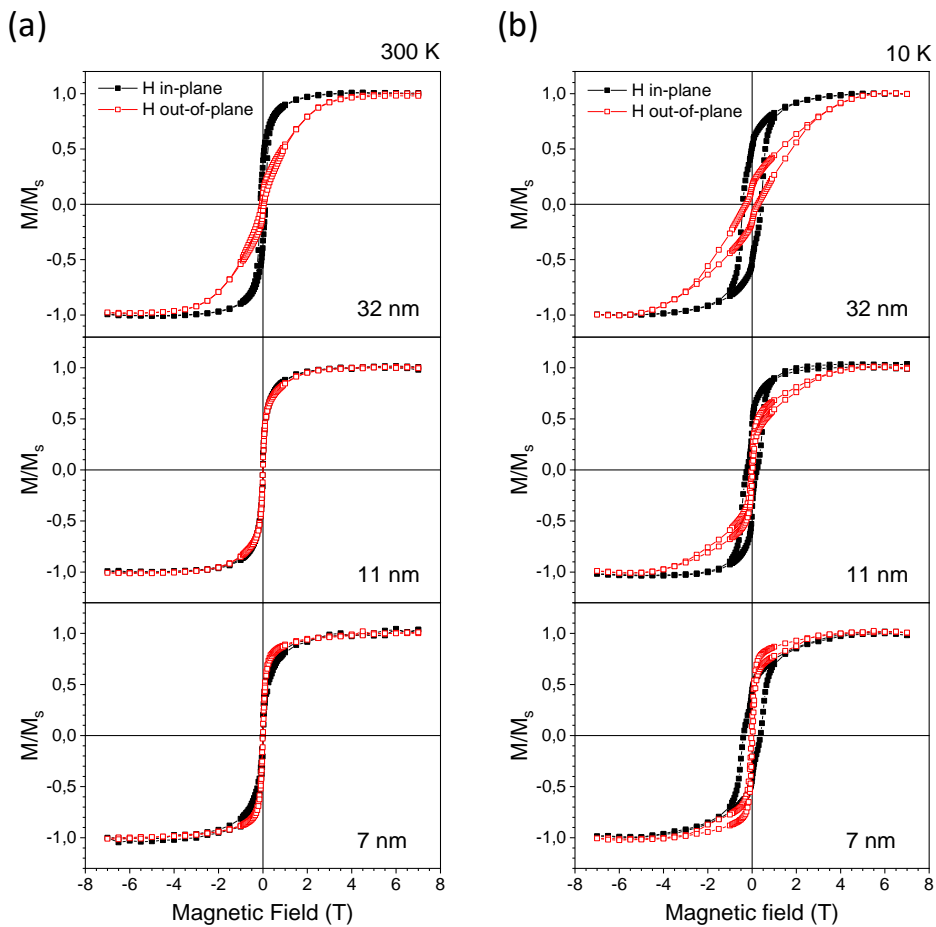


**Fig. 3.6 | Magnetic hysteresis loops measurements in the parallel and perpendicular modes for GFO films of various thicknesses. (a) Measured at 300 K. (b) Measured at 10 K.**

### 3.2 Magnetic Anisotropy

Magnetic anisotropy (MA) reflects the variation in space of the magnetic properties of a system, in relation with the directional dependence of its magnetic energy. Depending on the magnetic history of the material, there are usually two directions along which the orientation of the magnetization requires less energy, 180° from each other. The axis corresponding to these directions is called the ‘easy’ axis of magnetization, and it is an energetically favorable axis for spontaneous magnetization [8]. On the contrary, the axis along which the magnetic energy is the highest and along which reorientation of all magnetic domains usually requires high field, is conventionally called the ‘hard’ axis. Several factors can affect the MA, which prominently include crystallographic structure, shape, morphology, and stoichiometry, for materials in their bulk form. In the case of thin films, in addition to the factors mentioned above, contributions due to strain, surfaces and interfaces, which are usually insignificant in bulk, can become critical.

We will see in this section that the MA of GFO thin films in an ultra-thin regime are heavily affected by contributions due to surface, interface and morphology of the films.

Typically, the total anisotropy energy of magnetization in relation to the angular orientation of magnetization in polycrystalline thin films is expressed as given by the following equations [8,9].

$$E = -K_{eff} \cos^2\theta \quad (3.1)$$

$$K_{eff} = K_V + \frac{K_S}{t} \quad (3.2)$$

In Eq. 3.1,  $K_{eff}$  is the effective anisotropy constant in the magnetic material and  $\theta$  is the angle between magnetization and the easy axis. Eq. 3.2 is relevant for thin films, with  $K_V$  and  $K_S$  being the bulk and surface contributions, respectively, to the anisotropy constant of the film. The volume term  $K_V$  consists of magneto-crystalline, shape, and strain. For ultra-thin films, the surface term becomes dominant in  $K_{eff}$ .

Materials with all kinds of magnitudes of MA find applications, from the low MA materials, used as transformers or inductors, to the high MA ones which can be used as hard magnets in recording media devices.

An effective and deterministic control over the MA axis of the material is extremely interesting from both the application and fundamental aspects. For example, currently a large amount of effort is being put into tailoring exotic multifunctional thin films to exhibit perpendicular anisotropy due to the promises of perpendicular magnetization in high density recording applications [10,11] which combined with their multifunctional aspect such as magnetoelectricity (see Ch. 1) creates new avenues in low power spintronics [12,13].

### 3.2.1 Types of Anisotropies

#### 3.2.1.1 Magneto-crystalline Anisotropy

The magneto-crystalline anisotropy is an intrinsic anisotropy of magnetization which is affected by the symmetry of the crystal structure of the material. It originates from the attraction or repulsion exerted on the electrons of an ion by the electric field created by the neighboring ions, which is called the crystal field. In the case where neither the orbitals nor the crystal field have a spherical symmetry, this results in a preferential orientation of the electronic distribution and of its associated orbital moment. Since the spin moment will tend to get aligned with the orbital moment through the spin-orbit coupling, it is the global magnetic moment of the atom which will have a preferential crystallographic orientation <sup>[8,14]</sup>. For transition metal oxides, the 3d electrons are the external electrons and are strongly coupled to the neighboring crystal field. This coupling is in competition with the intra-atomic electrostatic repulsion and the electronic distribution adopts a configuration which minimizes its interaction with the crystal field. This modifies the values of the spin and orbital moments. When the crystal field is isotropic, the orbital moment is very small, and the spin moments can almost freely orient in any direction without any energetic difference for the system. The magnetic anisotropy is low. However, when the crystal field is uniaxial, the orbital moment is not zero anymore and it is maximum for a peculiar crystallographic orientation, which, thanks to the spin orbit coupling becomes the magnetization easy axis. For the body centered cubic Fe unit cell shown in Fig 3.7 (a), for example, the close-packing <111> direction is a hard axis while the <100> direction is an easy axis.

In the case of GFO, the easy axis is the 'a' ('c') axis, in the orthorhombic  $Pna2_1(Pc2_1n)$  space group setting <sup>[15]</sup>. The free energy term F of the magneto-crystalline anisotropy for orthorhombic symmetry can be written according to Eq. 3.3, which, as described in <sup>[16]</sup>, transforms into Eq. 3.4 for independent variables T (Temperature),  $H_M$  (induced magnetization) and  $\theta$  (angle between magnetization and easy axis).

$$F = K_0 + K_{1b}\alpha_b^2 + K_{1c}\alpha_c^2 + K_{2b}\alpha_b^4 + K_{2c}\alpha_c^4 + K_{2ab}\alpha_b^2\alpha_c^2 \quad (3.3)$$

$$\tilde{F}(T, H_M, \theta) = K_{00}(T) - M_{00}(T)H_M - \frac{1}{2}\chi(T)H_M^2 + [K_{1b}(T) - M_{1b}(T)H_M] \sin^2 \theta + [K_{1c}(T) - M_{1c}(T)H_M] \sin^4 \theta, \quad (3.4)$$

where  $K_0$  and  $K_{00}(T)$  are isotropic terms,  $K_{1b}$  and  $K_{2b}$  are the first and second order anisotropic terms along the 'b' axis,  $K_{1c}$  and  $K_{2c}$  are the first and second order anisotropic terms along the 'c' axis,  $K_{2ab}$  is second order anisotropic term in the a-b plane,  $\alpha_b$  and  $\alpha_c$  are directional cosine terms,  $M_{00}, M_{1b}, M_{1c}$  are the spontaneous magnetization components and  $\chi(T)$  is the susceptibility term. The magneto-crystalline anisotropy constant  $K_{MC}$  will depend on  $K_{00}$ ,  $K_{1b}$  and  $K_{1c}$ .

### 3.2.1.2 Shape Anisotropy

The shape of a magnetic material, regardless of the nature of this material, can affect the magnetic anisotropy direction (Fig. 3.7 (b)). This anisotropy is entirely based on magneto-static dipolar interactions, which are long range interactions<sup>[11]</sup> and hence can be affected by sample boundaries that are defined by shape of the material. As can be expected, the shape anisotropy is null in the case of spherical samples, since magnetic charges are homogeneously spread. In the case of thin films, the effective magneto-static energy per unit volume is expressed by Eq. 3.5<sup>[17]</sup>. It can be noted from the equation that the energy of the system is lower if the magnetic orientation is within the plane of the thin film. The shape anisotropy constant  $K_{Sh}$  given by Eq. 3.6<sup>[17]</sup> is quite considerable in thin films and contributes heavily in the  $K_V$  volume anisotropy term.

$$E_d = \frac{1}{2} \mu_0 M_S^2 \cos^2 \theta \quad (3.5),$$

$$K_{Sh} = \frac{1}{2} \mu_0 M_S^2 \quad (3.6),$$

Here,  $E_d$  is dipolar energy term and  $\theta$  is the angle between the magnetization axis and surface normal to thin film,  $\mu_0$  is vacuum permeability constant and  $M_S$  is uniform saturation magnetization.

### 3.2.1.3 Surface Anisotropy

The origin of the surface anisotropy is mainly the symmetry breaking at interfaces and surfaces, where the orbital degrees of freedom are affected by the asymmetry and are different from the bulk ones<sup>[11]</sup>. The effect exists in all films at the boundaries, but in thicker films, the exchange interaction between spins along with the magneto-crystalline and shape anisotropies are the major effects. Let us consider a material in the form of thin film, for which the magneto-crystalline anisotropy favours an in-plane magnetization. As the film gets thinner, surface anisotropy due symmetry breaking perpendicular to film, may try to orient the spins out-of-plane and if it is strong, then due to exchange interaction the total magnetization easy axis can be directed out-of-plane (Fig. 3.7 (c)). Eq. 3.7 gives the thickness  $t$  dependence of the effective anisotropy constant  $K_{eff}$ . It is dominated by the surface term  $K_S$  at low thickness regime.  $K_S$  can be calculated from  $K_{eff}$  by linearly fitting the  $K_{eff} \cdot t$  vs.  $t$  plot. In our example case,  $K_{eff}$  is negative in-plane for high thicknesses ; extrapolating it to the thickness where it becomes positive allows determining a threshold thickness for re-orientation of magnetization to out-of-plane direction. This becomes especially interesting from an application point of view as both sub-nanometer films and out-of-plane anisotropy are desired for high density storage media<sup>[10,11,18]</sup>. A famous example of tailoring the anisotropy by controlling the thickness is that of Co/Pt or Co/Pd layers, where below a Co thickness of 1.8 nm, the films show an out-of-plane magnetization<sup>[9]</sup>.

$$K_{eff}.t = K_V.t + K_S \quad (3.7)$$

A linear fit of  $K_{eff}.t$  vs.  $t$ , according to Eq. 3.7, can also give both the bulk part of the anisotropy constant  $K_V$ , which is the slope, and its surface contribution  $K_S$ , which is the intercept.

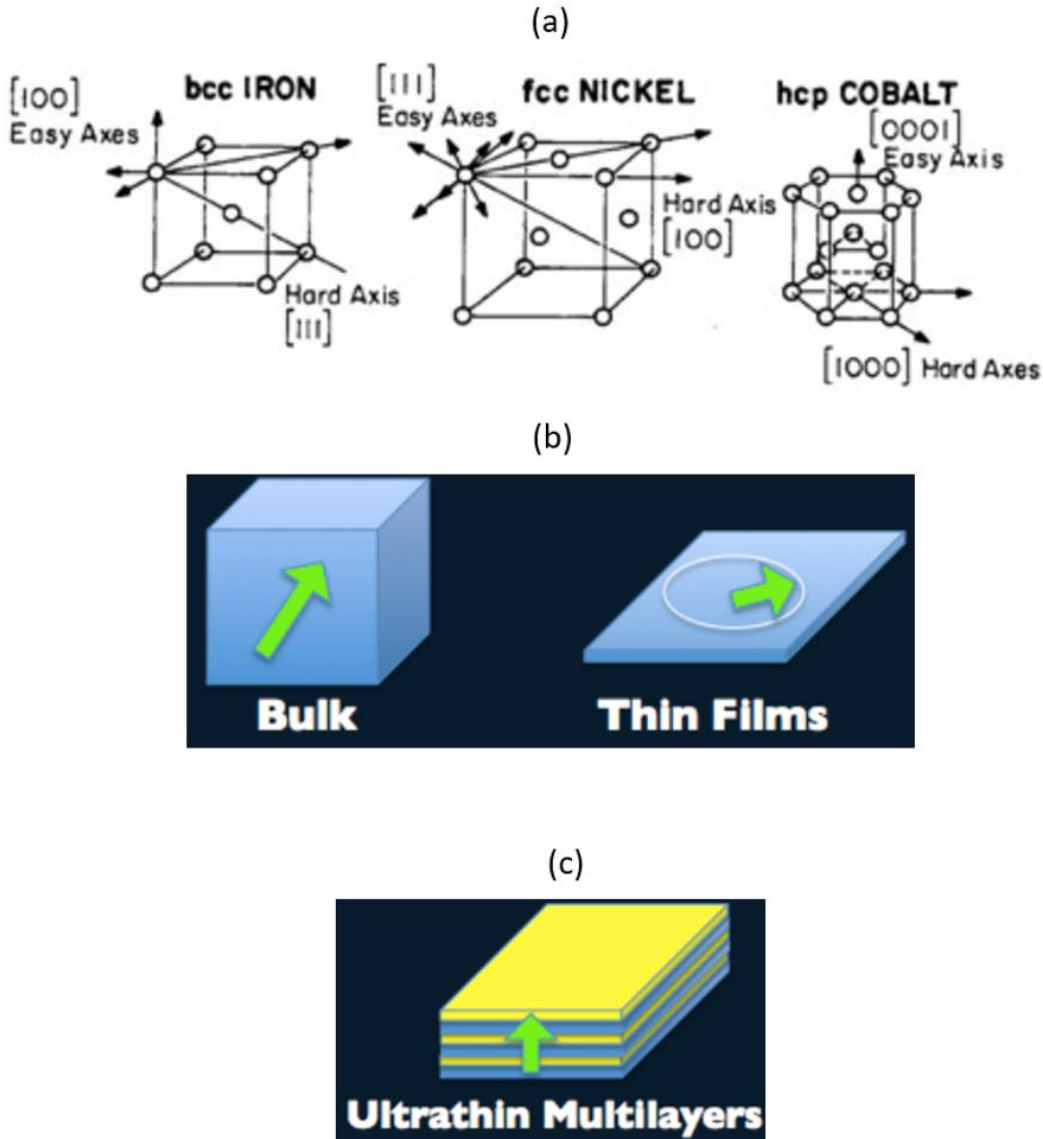


**Fig. 3.7 | Few relevant types of magnetic anisotropies in thin films.** (a) Magneto-crystalline anisotropy in the body centered cubic Fe, face centered Ni and hexagonal close packed Co unit cells in various directions. Adapted from ref. [8]. (b) Shape anisotropy due to magneto-static consideration in bulk and thin films. Adapted from ref. [19]. (c) Surface anisotropy in ultra-thin multilayers. Adapted from ref. [19,20].

### 3.2.1.4 Strain Anisotropy

The magneto-elastic strain anisotropy in thin films is caused by the lattice mismatch between the film and the substrate and can be coherent or incoherent in nature. Coherent anisotropy is caused by films under tensile or compressive strain and is given by Eq. 3.8. Incoherent anisotropy can be observed on relaxed films with misfit dislocations, grown on a substrate with high lattice mismatch, and is given by Eq. 3.9. The coherent part of the strain contributes to the volume anisotropy and the incoherent part of the strain to the interface anisotropy <sup>[9]</sup>. In GFO thin films, there is no strain in the plane of the films (the GFO in-plane cell parameters are not bound to those of the substrate and follow those expected for bulk). For low thicknesses, the out-of-plane cell parameter is however different from the one expected for bulk, and this will result in a contribution to a coherent anisotropy  $K_{St}$ . The large lattice mismatch between GFO and the STO substrates will also yield an incoherent anisotropy term  $K_\lambda$  to the overall  $K_S$ .

$$K_{St} = -\frac{3}{2}\lambda\sigma\cos^2\theta \quad (3.8),$$

$$K_\lambda = -\frac{3}{4}\lambda Gb \quad (3.9),$$

where  $\lambda$  is the magneto-striction constant,  $\sigma = \epsilon G$  is stress,  $\epsilon$  is strain,  $G$  is the shear modulus and  $b$  is the Burgers vector.  $\theta$  is the angle between magnetization and stress.

The contribution from  $K_\lambda$  can be positive or negative depending on the sign of the magneto-striction constant  $\lambda$  of the film ; this value was not found for GFO in the literature. The magneto-elastic coupling constant, which has been calculated for GFO <sup>[21]</sup>, might be used to calculate  $\lambda$ , but it is as of now out of the scope of this project.

### 3.2.1.5 Growth induced Anisotropy

This effect concerns the effects of nuances in growth morphologies which affect the magnetic energy state in the film at a given orientation with respect to growth. This has been shown to be of relevance in ferrite or garnet films and amorphous films <sup>[9]</sup>. In a complex mixed oxide system (like GFO), atoms can occupy various sites, which may vary from one deposition to another, and this will have an influence on the magnetic symmetry of the system. This effect comes under volume anisotropy and is given by Eq. 3.10,

$$E_G = K_G \sin^2\theta \quad (3.10),$$

Where  $E_G$  is the growth anisotropy energy,  $K_G$  is the growth anisotropy constant,  $\theta$  is the angle between magnetization and the direction of the film growth.

### 3.2.1.6 Exchange anisotropy

Exchange related magnetic anisotropy is widely used in giant magneto-resistive (GMR) devices and has become essential in today's magnetic recording systems. Exchange interaction allows to pin the magnetization direction of a ferromagnet, when put in close proximity to an antiferromagnet. For this chapter, we will not go into details of exchange anisotropy because this phenomenon will not be of importance in our study.

### 3.2.2 Determination of the magnetic anisotropy in GFO thin films.

The method to determine the magnetic anisotropy in a ferromagnetic or ferrimagnetic material can be broadly classified into two types: dynamic and static. In the dynamical methodologies, the magnetization dynamics is studied with different techniques like ferromagnetic resonance (FMR) or Brillouin light scattering (BLS), where the magnetization is perturbed from its equilibrium position and the relaxation processes are studied to calculate the magnetic anisotropy<sup>[11]</sup>. In the static techniques, several studies can be conducted using angle resolved torsion magnetometry, magneto optical Kerr effect (MOKE) or vibrating sample magnetometry (VSM) with a superconducting quantum interference device (SQUID) to measure magnetization loops<sup>[11]</sup>. In this latter case, the mostly used technique for the determination of anisotropy with a good approximation is what is called the area method. Since the FMR conditions were not experimentally accessible to us for our GFO films, we have focused our study of the magnetic anisotropy in this system with the use of SQUID performed magnetization loops measurements. We will therefore only detail hereafter the area method which we have used for the estimation of the magnetic anisotropy in GFO thin films from these measurements.

#### Area Method

The area method is a classical textbook method<sup>[8]</sup> which can be used to evaluate the magnetic anisotropy in thin films using  $M$  vs.  $H$  magnetization loops. It is based on the fact that the anisotropy energy stored in a crystal magnetized in a particular direction is given by the area between the  $M$  vs.  $H$  curve and the  $M$ -axis when the field  $H$  is applied in that particular direction. However, even in the easy direction, this area is usually not zero, because the field must overcome hindrances to domain wall motion. These hindrances are assumed to be the same for any direction of the applied field. Therefore, the real anisotropy energy, free of the effects of domain wall motion, will be considered to be equal to the area between the curve measured in the considered non-easy direction and the one measured in the easy one. All hysteretic magnetization curves are made anhysteretic by averaging the two branches<sup>[22–24]</sup>.

In this section we will employ this technique to estimate the magnetic anisotropy of various GFO thin films, and the effect of thickness and temperature on these anisotropies. We will also compare them with other values reported in the literature to evaluate possible errors of this technique.

GFO thin films of various thicknesses were grown onto STO substrates under the conditions mentioned in chapter 2. The  $M$  vs.  $H$  magnetization loops were measured for roughly  $3 \times 4 \text{ mm}^2$  samples, stuck in a straw, with the use of a SQUID detection VSM. The field  $H$  was aligned parallel (Para) or perpendicular (Perp) to the films. Fig 3.8 shows the saturation normalized data (from 0 to  $+H$ ) for magnetization measurements carried out at 10 K in films with the following thicknesses : 125 nm (2a), 64 nm (2b), 32 nm (2c), 11 nm (2d), 7 nm (2e) and 4 nm (2f), in both Para and Perp set-ups. The magnetic easy axis for the thicker films lies in-plane, as expected for films of a material presenting an easy ' $a$ ' axis according to magneto-crystalline anisotropy (the films growth is oriented along the ' $c$ ' axis), enforced as well by the shape anisotropy which further lowers the magnetic energy for an in-plane orientation. As the thickness approaches the ultra-thin regime of  $t \leq 11 \text{ nm}$ , it can be observed that the magnetic energy required for achieving saturation along the hard axis is lower than its bulk counterpart, and, at 7 nm, the films shows a perpendicular easy axis orientation. The 4 nm thin film is an exception and shows a very low anisotropy, which can be explained by its grainy morphology that increases magnetic energy due to grain boundaries <sup>[25]</sup> as well as high roughness which should lead to magnetic pinning due to defects <sup>[26]</sup>. Another reason that could explain change at 4 nm is the negative interface anisotropy constant  $K_\lambda$  due to incoherent stress from lattice mismatch <sup>[9]</sup> at GFO/STO interface. The two main components of the magnetic anisotropy that will be considered here are the bulk and surface terms,  $K_V$  and  $K_S$ . The effective anisotropy  $K_{eff}$  is obtained by multiplying the area between the easy and hard axes  $M/M_s$  loops shown in Fig. 3.8 with the saturation magnetization  $M_s$ . It is expected to follow  $K_{eff} \cdot t = K_V \cdot t + K_S$ . The plot of  $K_{eff} \cdot t$  vs.  $t$  at 10 K and 310 K is shown in Fig. 3.9 (a-b).  $K_{eff}$  is negative as the magnetic anisotropy is in-plane. The negative slope observed here is mainly due to the shape anisotropy <sup>[11]</sup> in the film. Fitting the curves gives  $K_V = -2.637 (63) \cdot 10^5 \text{ J/m}^3$  at 10 K and  $-0.721 (42) \cdot 10^5 \text{ J/m}^3$  at 310 K, as the slope, and  $K_S = 1.21 (37) \text{ mJ/m}^2$  at 10 K and  $0.37 (25) \text{ mJ/m}^2$  at 300 K, as the intercept. The x axis intercept gives the perpendicular magnetic reorientation thickness  $t_{PMR} = 4.6 \pm 1.5 \text{ nm}$  (10 K) and  $5.13 \pm 3.9 \text{ nm}$  (310 K).

These anisotropy values can be compared to values found in the literature, and measured by Bertaut <sup>[15]</sup> in bulk  $\text{Ga}_{2-x}\text{Fe}_x\text{O}_3$  ( $x = 1.15$ ) at 20 K ( $K = 4.54 \cdot 10^5 \text{ J/m}^3$ ) and by Katayama <sup>[27]</sup> in thin film GFO ( $x = 1.4$ ) only at 300 K ( $K = 1.1 \cdot 10^5 \text{ J/m}^3$ ). We note that some previous work have also been carried out on calculation of anisotropy values using other techniques such as torque magnetometry by Schelleng and Rado on bulk  $\text{Ga}_{2-x}\text{Fe}_x\text{O}_3$  ( $x \approx 1.11$ ) <sup>[16]</sup>, and using ferromagnetic resonance (FMR) on bulk samples of similar stoichiometry by Dweck <sup>[28]</sup>. The anisotropy values presented by these studies is not comparable with our thin films due to their different stoichiometry, size and measurement technique.

The magnetic anisotropies of other materials of interest, at 300 K, are given for comparison's sake in Table 3.1. GFO's high anisotropy makes it a material of choice for applications in magnetic recording media devices or as high frequency microwave absorber.

Metals (in $10^5 \text{ J/m}^3$ )			Alloys (in $10^5 \text{ J/m}^3$ )			Oxides (in $10^5 \text{ J/m}^3$ )		
Fe (bcc) [8]	Co (hcp) [8]	Ni (fcc) [8]	$\text{Ni}_{81}\text{Fe}_{19}$ [8]	$\text{YCo}_5$ [8]	$\text{SmCo}_5$ [8]	$\text{BiFeO}_3$ [29]	$\epsilon\text{-Fe}_2\text{O}_3$ [30]	$\text{Y}_3\text{Fe}_5\text{O}_{12}$ [31]
0.48	4.5	-0.05	$\sim 0$	55	77	1.01	0.03	0.006

**Table 3.1. | Anisotropy values of some metals, alloys, and some oxides at 300 K (150 K for  $\text{BiFeO}_3$ ).**

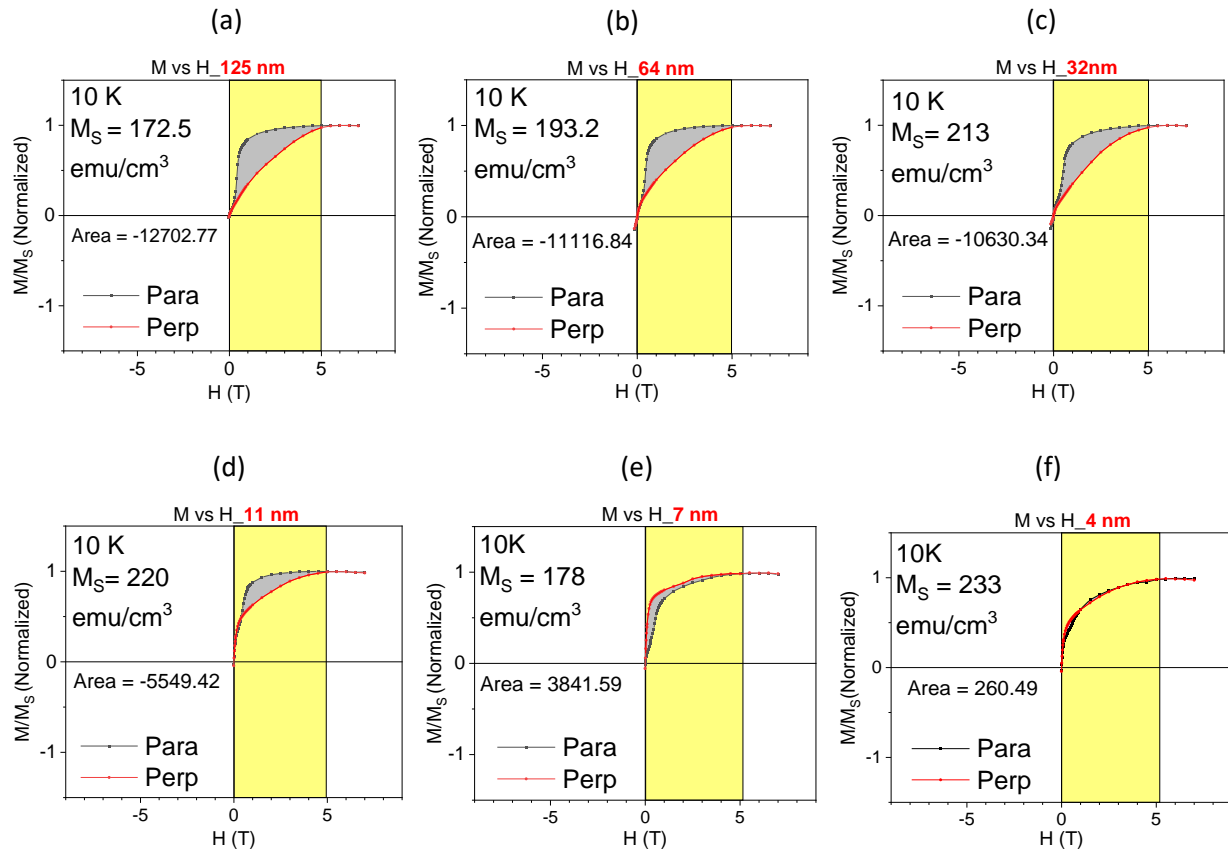


**Fig. 3.8 | M vs. H anhysteretic curves at 10 K for parallel and perpendicular set-ups, with H between 0 and +7 T. For (a) 125 nm. (b) 64 nm. (c) 32 nm. (d) 11 nm. (e) 7 nm. (f) 4 nm. The area enclosed between the easy- and hard-magnetization curves is shown in shaded grey and corresponds to  $K_{\text{eff}}$  when multiplied by the saturation magnetization value  $M_s$ . The H range taken into consideration is highlighted in yellow, taking into consideration the H required to reach  $M_s$ .**

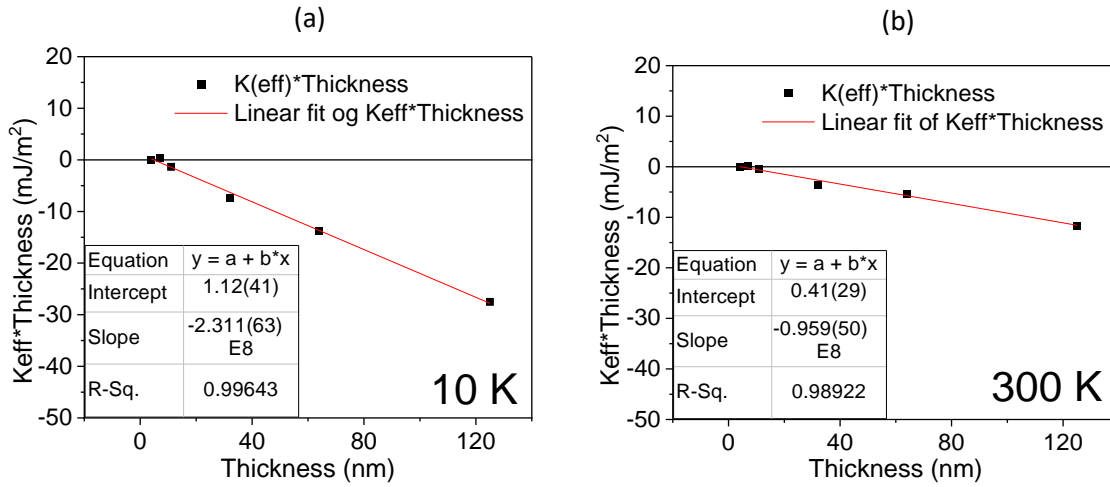


**Fig. 3.9 | Thickness dependence of  $K_{eff} * Thickness$ .**  $K_{eff}$  = (area between easy and hard axes magnetization loops)\*( $M_S$ ) values obtained from Fig. 3.8. For (a) 10 K. (b) 300 K.

The temperature dependence of  $K_{eff}$  for the various grown thicknesses is given in Fig 3.10. (a).  $K_{eff}$  increases with decreasing temperatures and the increase rate in  $K_{eff}$  with decreasing temperatures is increasing with increasing thickness. This is implied by the fact that the contribution from the surface anisotropy  $K_S$  is dominating for thinner films and counters the volume anisotropy  $K_V$ , as they have opposite signs. The evolution of  $K_S$  and  $K_V$  with temperature is also calculated following the procedure described above for temperatures ranging from 10 K to 390 K (i.e., above the Curie temperature). As can be observed,  $K_S$  increases and  $K_V$  decreases with decreasing temperatures. For thin films of 7 and 11 nm, the  $K_S$  contribution is significant and  $K_V$  is no longer dominating. This competition explains the rate of change in  $K_{eff}$  is lower for 7 and 11 nm in Fig. 3.10 (a).

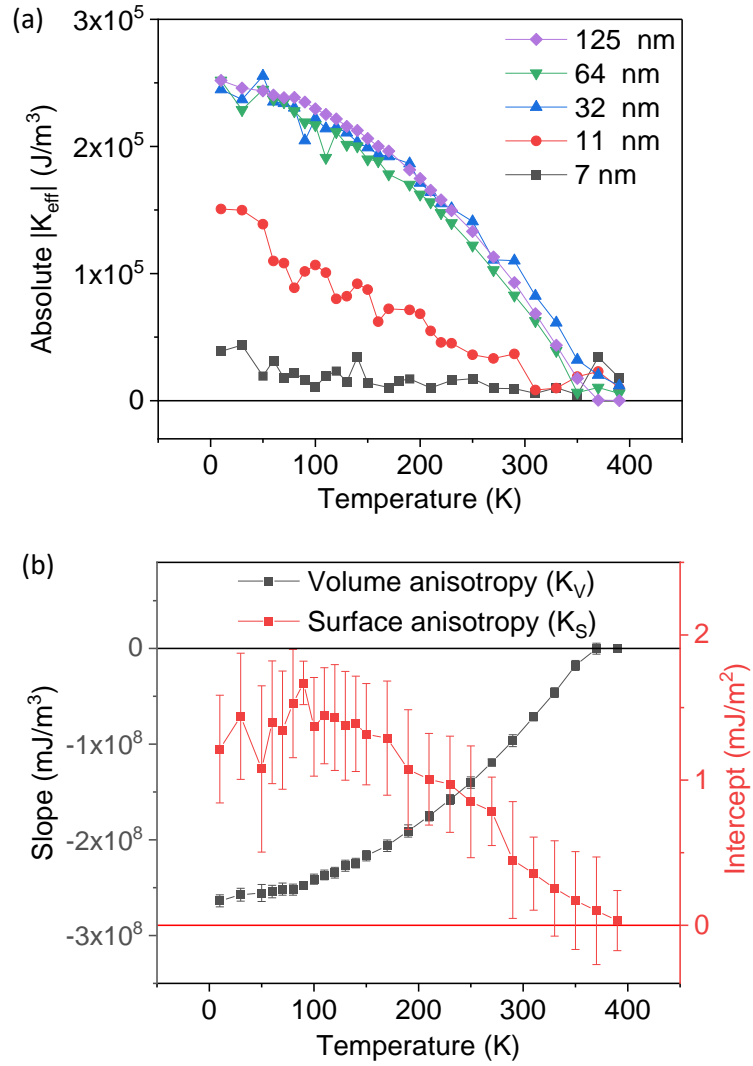


**Fig. 3.10 | Temperature dependence of anisotropy values for GFO films.** (a) Temperature dependence of the absolute value of  $K_{eff}$  for the various deposited thicknesses. (b) Temperature dependence of the volume and surface anisotropies calculated from fitting  $K_{eff}$  \* thickness vs. thickness curves at all temperatures.

The contribution of the shape anisotropy  $K_{Sh}$  to the volume anisotropy  $K_V$  can be calculated using Eq. 3.6. Table 3.2 gathers the values of  $K_{eff}$ ,  $K_V$  and  $K_{Sh}$  for all thicknesses at 10 and 310 K. The contribution from the shape anisotropy to the bulk value is about 8%. The shape anisotropy is thus not the dominating factor in  $K_V$ , in contrast to what is observed in Fe thin films [20]. Here, the magnetocrystalline part of the anisotropy,  $K_{Mc}$ , is probably the most significant

contribution, since other anisotropies, originating from strain,  $K_{St}$  (mostly out-of-plane), or growth,  $K_G$  (mostly in-plane), are expected to contribute to a much lesser extent.

Temperature (K)	$K_{eff}$ (J/m <sup>3</sup> )	$K_V$ (J/m <sup>3</sup> )	$K_{Sh}$ (J/m <sup>3</sup> )	$K_{Sh}/K_V$
10	$-2.52 * 10^5$	$-2.63(6) * 10^5$	$-0.19 * 10^5$	7.3 %
310	$-0.62 * 10^5$	$-0.71(4) * 10^5$	$-0.06 * 10^5$	8.4 %

**Table 3.2 | Effective, bulk and shape anisotropies, respectively,  $K_{eff}$ ,  $K_V$ , and  $K_{Sh}$ .** ( $K_{Sh}$  is calculated using the saturation magnetization measured for the 64 nm thick sample.)

### 3.2.3 Conclusions for magnetic properties measured using SQUID-VSM

We have presented magnetic properties of GFO thin films with an in-depth study of hysteresis measurements carried out at various temperatures and thicknesses. These measurements depict the GFO films are magnetic at room temperature with a saturation of about 100 emu/cm<sup>3</sup> and a Curie temperature ( $T_c$ ) of 360 K. We demonstrate that the magnetization which is in-plane for thick films changes to out-of-plane for thinner films.

We have reviewed different types of magnetic anisotropies relevant to the context of GFO thin films. We have determined effective magnetic anisotropy by measuring the area difference between parallel and perpendicular anhysteretic curves in GFO thin films. The effective magnetic anisotropy is higher in GFO as compared to some other functional oxides. The value of effective magnetic anisotropy is resolved into contributions from shape and surface anisotropies and temperature dependence of these anisotropies is demonstrated in GFO for the first time.

This study forms a base understanding of magnetic anisotropy in our thin films and is essential for future prospect of modulation of magnetic anisotropy using gate voltage.

### 3.3. Microscopic magnetic characterizations of Ga<sub>0.6</sub>Fe<sub>1.4</sub>O<sub>3</sub> (GFO) thin films.

#### 3.3.1 An introduction to X-ray magnetic circular dichroism (XMCD) - a powerful characterization tool for magnetism

Dichroism is a property of a material that shows different absorption coefficients for light traveling with different polarization states.<sup>[32]</sup> Circular dichroism involves the differential absorption of light-wave depending on its polarization's circular helicity, left or right, when incident on a material <sup>[33,34]</sup>. This type of dichroism results in a powerful characterization tool in the X-ray frequency range, the X-ray magnetic circular dichroism (XMCD).<sup>[35–37]</sup> XMCD spectra result from the difference between the X-ray absorption spectroscopy (XAS) spectra measured using circular polarization of X-rays of opposed helicities and/or for sample magnetizations of opposite orientations.

The XAS spectra result from core-level absorptions in the highly energetic X-rays frequency range (Fig. 3.11 (a-c)). The dipole allowed excitations result in high absorption cross-sections when probed with high energy synchrotron radiation X-ray sources, which produces an enhanced signal. Synchrotron sources also allow high-speed scanning of various energies in a reproducible way and allow the observation of different excitations from the low energy 1s-2p transitions (300-700 eV), 2p-3d transitions (350-950 eV) to the high energy 2p-4d transitions (2000-3500 eV). XAS allows element specificity since the energy required for excitation of electrons from a core level varies with the shielding provided by other electrons in the outer levels. It also allows identifying the different valence states of an element, its environment (octahedral, tetrahedral, etc...) and gives insight into the state of the material in which this element is involved (crystalline, amorphous, thin-film, structural distortions, etc...) <sup>[37]</sup>.

XAS spectroscopy can be performed with various kinds of light polarizations, linear or circular. This yields a variety of XAS-based techniques such as X-ray natural linear dichroism (XNLD),<sup>[38]</sup> X-ray magnetic linear dichroism (XMLD),<sup>[39]</sup> X-ray natural circular dichroism (XNCD),<sup>[40]</sup> and X-ray magnetic circular dichroism (XMCD) (Fig. 3.11 (b, c)).

In this thesis, we will focus on the XAS spectra resulting from the 1s-2p transitions for O and 2p-3d transitions for Fe in the Ga<sub>0.6</sub>Fe<sub>1.4</sub>O<sub>3</sub> (GFO) ferrimagnetic thin films, for both linear and circular polarizations, respectively. The aim is to understand the microscopic nature of the 3d magnetism of Fe and its dependence on the film's thickness and temperature in GFO films, especially in the ultra-thin regime. To understand Fe's 2p-3d transitions, we first delve into the electronic phenomenon that gives rise to this transition. The 2p shell, for which the orbital angular momentum  $l = 1$  and the spin quantum number  $s = \frac{1}{2}$ , presents, because of the spin-orbit interaction, two different energy levels of total angular momentum  $j = \frac{1}{2}$  and  $\frac{3}{2}$ . The 2p-3d transition is labeled as the L-edge absorption spectroscopy with the L<sub>2</sub> edge corresponding to the

absorption of X-rays by 2p electrons with  $j = \frac{1}{2}$  and the  $L_3$  edge to the absorption of X-rays by 2p electrons with  $j = \frac{3}{2}$ . The schematic of the absorption of linearly polarized light is shown in Fig. 3.11 within a one-electron model in which electron correlations are not considered. Within this one-electron model, the ratio of white line intensities between the  $L_3$  and  $L_2$  edges is 2:1 (because the  $j = \frac{3}{2}$  states have twice as many degenerate states as the  $j = \frac{1}{2}$  ones), with a separation of  $\frac{3}{2}$  times the spin-orbit coupling of the 2p shell (due to Lande's interval rule) <sup>[41]</sup>. Although the one-electron model is used in many instances to illustrate the phenomenon conceptually, it does not represent the real systems in many cases. For instance, it was experimentally found that the  $L_3/L_2$  ratio (also called the branching ratio) differs from 2:1 as predicted by the one-electron model <sup>[41,42]</sup>. Van Der Laan and Thole <sup>[43,44]</sup> explained this phenomenon by the multiplet effects caused by a strong overlap of the core 2p wave function with the valence 3d wave function, which results in a spread of the final energies. The multiplets are determined by Slater integrals, which depend on the size of the electron-electron repulsion between orbitals and are different for different elements. The crystal field and the spin and orbital polarization of the d-electrons determine the shape of the  $L_3$  and  $L_2$  peaks and are different for different materials <sup>[45]</sup>. The relevance of the crystal field multiplet model and its use to approximately simulate both  $L_3$  and  $L_2$  edges has been shown for the 3d transition metal compounds <sup>[46,47]</sup>. This way, although the one-electron model does not present an accurate description, it is widely used to visualize the transitions phenomenologically.

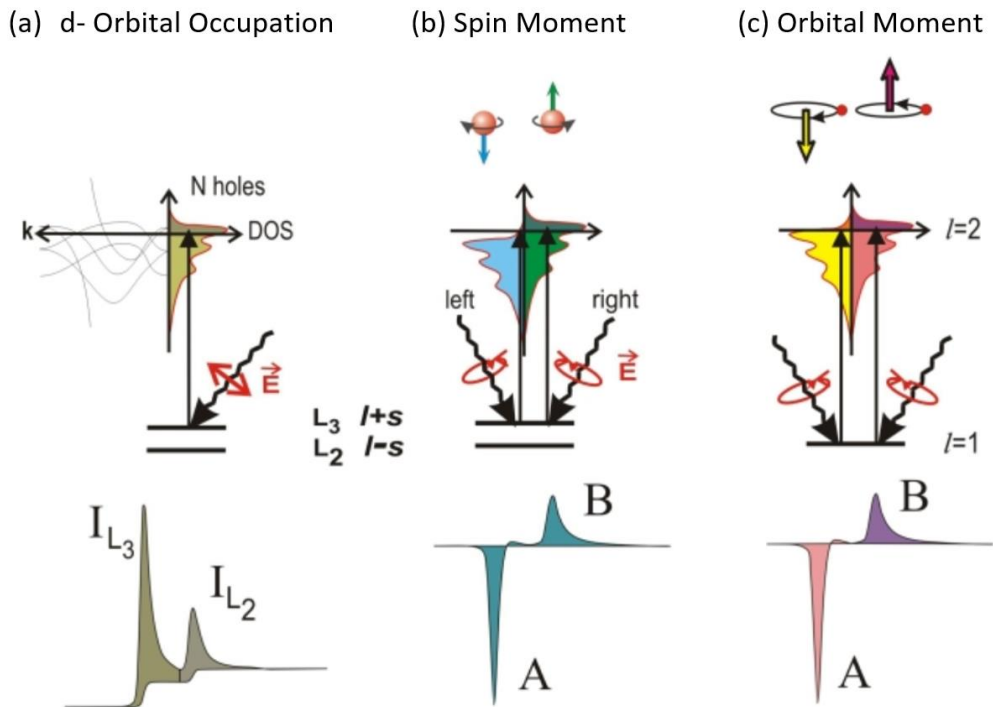


**Fig 3.11 | Schematic of the electronic transitions due to X-ray absorption in the one-electron model.** For (a) conventional L-edge absorption and (b-c) X-ray magnetic circular dichroism. Adapted from ref. [36].

Now, we look at the fundamental processes behind the XMCD spectra, which can be understood from the schematic of the one-electron model illustrated in Fig. 3.11 (b, c) and explained as follows. Let's consider a right circularly polarized photon with an angular momentum  $\hbar$  absorbed at the  $L_3$  edge; it will transfer its angular momentum to an electron spin *via* spin-orbit coupling and excite it from the  $2p_{3/2}$  shell to the unoccupied 3d shell above the Fermi level [36]. Similarly, a left circularly polarized photon with angular momentum  $-\hbar$  absorbed will transfer its angular momentum to an electron spin and excite it to an unoccupied 3d shell. However, since an opposite angular momentum is transferred in each case, the excited electrons will have opposite spins. In a magnetic material, due to exchange interactions, the 3d shell has a higher density of states (DOS) available above the Fermi level for one spin state (say  $s = \frac{1}{2}$ ) than the other (say  $s = -\frac{1}{2}$ ). This is indicated by the splitting of the band in Fig. 3.11 (b). The excitation probabilities thus vary between the two spin states. Since the excited electron's spin state is also guided by the circular helicity of the photon polarization, the XAS intensity will depend upon the helicity of the circular polarization. The difference between the XAS signals measured for each helicity is referred to as the XMCD signal and gives a direct probe of the band spin splitting in the transition element's 3d shell. In the schematic of Fig 3.11 (b), the XMCD signals originating from the  $L_3$  and

$L_2$  edges, respectively named 'A' and 'B' peaks, are of opposite signs. This is because the  $2p_{3/2}$  ( $l+s$ ) and  $2p_{1/2}$  ( $l-s$ ) have opposite spin-orbit coupling. Similarly, if the valence shell possesses an orbital momentum, it will contribute to the 'A' and 'B' peaks shown in Fig. 3.11 (c). The spin moment can be calculated from the A and B peak intensities using  $[A-2B]$ , and the orbital moment is measured after taking a sum over  $[A+B]$  to eliminate the spin contribution <sup>[36]</sup>. This leads us to the derivation of some general sum rules presented by P. Carra *et al.* and B.T. Thole *et al.*, in their respective iconic papers <sup>[48,49]</sup>. The equations given in Eq. 3.11 and 3.12 here below quantitatively allow to calculate the spin and orbital moments.

$$\frac{L_Z}{N_h} = \frac{\int_{j_+ + j_-} (\mu_+ - \mu_-) d\omega}{\int (\mu_+ + \mu_- + \mu_0) d\omega} \cdot \frac{2l(l+1)}{c(c+1) - l(l+1) - 2} \quad (3.11)$$

$$\frac{2S_Z}{N_h} = -2 \cdot \frac{\int_{j_+} \left( (\mu_+ - \mu_-) - \frac{(c+1)}{c} \frac{\mu_+ - \mu_-}{\mu_+ + \mu_-} \right) d\omega}{\int (\mu_+ + \mu_- + \mu_0) d\omega} \cdot \left( \frac{\frac{l(l+1) - 2 - c(c+1)}{3c} + \frac{l(l+1)[l(l+1) + 2c(c+1) + 4] - 3(c-1)^2(c+2)^2}{6lc(l+1)} \frac{T_Z}{S_Z} \right)^{-1} \quad (3.12)$$

where  $\frac{L_Z}{N_h}$  is the orbital moment,  $m_{orb}$ , per hole,  $\frac{2S_Z}{N_h}$  the spin moment,  $m_{spin}$ , per hole,  $c$  the angular momentum of the electronic state to be excited (for an  $L_{2,3}$  edge, it is the  $2p$  shell, i.e.  $c = 1$ ),  $l$  the angular momentum of the electronic state to be probed (for an  $L_{2,3}$  edge, it is the  $3d$  shell, i.e.  $l = 2$ ),  $\mu_+$  and  $\mu_-$  the absorption coefficients observed for the right and left circularly polarized light,  $\mu_0$  the absorption coefficient for linearly polarized light,  $N_h$  the available number of holes in the probed ( $3d$ ) shell, given by  $N_h = (4l + 2 - n)$ ,  $n$  being the number of electrons occupying the shell,  $j_{\pm} = c \pm 1/2$ ,  $\omega$  is the frequency,  $\langle T_Z \rangle$  is the expected value of the magnetic dipole operator, which affects the anisotropy of the atomic cloud on the field of spins, due to spin-orbit coupling or crystal-field <sup>[50]</sup>. This factor appears to be sufficiently quenched to have a very low value in Fe atoms and can be neglected compared to the ground-state expected value of total spin  $\langle S_Z \rangle$  <sup>[49,51]</sup>, especially for the cubic symmetry. The  $\langle T_Z \rangle$  factor correction is, however, non-negligible for other symmetries (like octahedral and tetrahedral), high atomic numbers such as in  $4f$  metals, ultra-thin films, and surfaces <sup>[51,52]</sup>. Depending on the sign of the  $\langle T_Z \rangle$  factor, the spin moment is overestimated or underestimated.

Using the notations of Chen *et al.* <sup>[53]</sup>, after replacing the isotropic signal used for normalization  $\int (\mu_+ + \mu_- + \mu_0)$  by  $\int (\mu_+ + \mu_- + \frac{1}{2}(\mu_+ + \mu_-))$  [since the value of  $\mu_0$  is not easily accessible], the sum rules for the  $L_{2,3}$  edges are given in Eq. 3.13 and 3.14 :

$$m_{orb}(m_L \text{ at } 3d) = -\frac{4 \int_{L_3+L_2} (\mu_+ - \mu_-) d\omega}{3 \int_{L_3+L_2} (\mu_+ + \mu_-) d\omega} \cdot N_h = -\frac{2q}{3r} \cdot N_h \quad (3.13)$$

$$m_{spin}(m_S \text{ at } 3d) = -\frac{6 \int_{L_3} (\mu_+ - \mu_-) d\omega - 4 \int_{L_3+L_2} (\mu_+ - \mu_-) d\omega}{\int_{L_3+L_2} (\mu_+ + \mu_-) d\omega} \cdot N_h \cdot \left(1 + \frac{7 \langle T_Z \rangle}{2 \langle S_Z \rangle}\right)^{-1}$$

$$m_{spin}(m_S \text{ at } 3d) = -\frac{3p-2q}{r} \cdot N_h \cdot \left(1 + \frac{7 \langle T_Z \rangle}{2 \langle S_Z \rangle}\right)^{-1}$$

$$\mathbf{m}_{spin} + 7 \langle T_Z \rangle (m_S \text{ at } 3d) \approx -\frac{3p-2q}{r} \cdot N_h \quad (3.14)$$

where  $L_3$  and  $L_2$  are the integrations  $p = \int_{L_3} (\mu_+ - \mu_-) d\omega$  ,  $q = \int_{L_3+L_2} (\mu_+ - \mu_-) d\omega$  ,  $r = \frac{1}{2} \int_{L_3+L_2} (\mu_+ + \mu_-) d\omega$  and can be derived from the XAS and XMCD graphs, as shown in Fig. 3.12 (a, b).

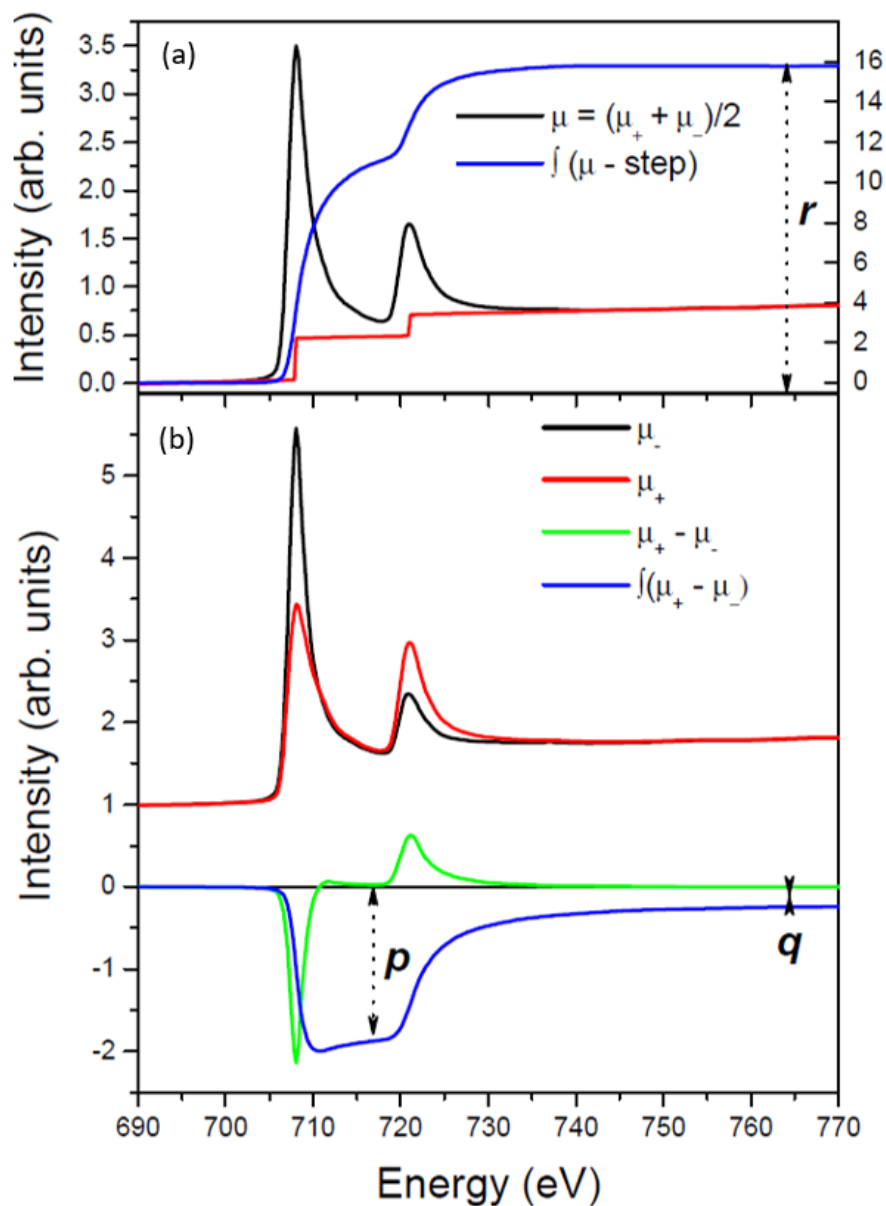


**Fig. 3.12 | A model of the XAS and XMCD spectrum.** (a) Average XAS (black) calculated from right and left circularly polarized light and the integral (blue) after using a step correction method (red). (b) Comparison between spectra obtained with the right (black) or left (red) circularly polarized lights. The difference between them results in the XMCD spectrum (green). The integral of this difference (blue) is used to calculate the parameters for the sum-rules. Adapted from ref. [50].

The sum-rules mentioned above can only be applied when the magnetic moments are all fully saturated by the magnetic field in the direction of the X-ray beams, and the X-rays have 100 % polarization in the given circular helicity direction. The factor  $r$  is proportional to the probed number of 3d holes and is calculated by integrating an average white line intensity after background correction given by a step method. Determination of this factor is sometimes non-trivial due to the non-linear background signals which distort the XMCD data. This becomes increasingly important in ultra-thin films where the absorption data is smaller, and background effects can dominate. Therefore, a small error in the exact background measurement can lead to a high error in the measured  $r$  value, which can also propagate significant error in the calculation of  $m_L$  and  $m_S$ .

The ratio  $\frac{m_L}{m_S}$  is therefore often used since it neither depends on the magnetic saturation nor on the circular polarization rate <sup>[53]</sup>. It does not require the  $r$  parameter for calculation, hence removing errors associated with the integration range, the hole count, or an improper continuum step correction. This makes the  $\frac{m_L}{m_S}$  ratio a more reliable and physical factor to consider compared to  $m_S$  or  $m_L$  separately <sup>[36,37,42,45]</sup>. To minimize other possible instrumental problems, the XMCD signal is measured using all possible combinations of alternate magnetic fields and circular polarizations: (+H, + $\phi$ ), (+H, - $\phi$ ), (-H, + $\phi$ ), and (-H, - $\phi$ ). This important statistic also improves the reproducibility of data and the reliability for the application of the sum rules <sup>[54]</sup>.

XAS, and subsequently XMCD spectra, are commonly measured by three modes: transmission yield, fluorescence yield, and total electron yield (TEY) <sup>[55]</sup>. The transmission yield mode is a direct measurement method where the X-rays pass through the sample, and the loss of intensity due to absorption is measured. A large drawback of this mode is that it only allows a maximum sample thickness of approximately 100 nm due to too large absorption at higher thicknesses. Fluorescence yield measurement is an indirect method where the fluorescence originating from the gradual decay of the electrons promoted to the 3d states is measured. A major drawback of this method, especially for the 3d transition metals L-edge, is the self-absorption problem. The TEY mode is a rather popular method to measure XAS/XMCD spectra, especially in thin films and at L<sub>2,3</sub> edges. This is a method in which all the ejected electrons (photoelectrons, Auger electrons, or secondary electrons) are counted through the measurement of a sample current. The measured number of electrons is equal to the number of holes formed after an X-ray photon's absorption. The measured number of emitted electrons is equal to the number of holes formed after an X-ray photon's absorption. The mean-free path of electrons is very small, and the TEY measurement is extremely surface sensitive, with only a ca. 2-5 nm depth probed <sup>[56,57]</sup>. A possible drawback of this method is the charging effects in semiconductors or insulating samples at low temperatures <sup>[58]</sup>, distorting the XAS/XMCD spectra.

Apart from the charging effects, some other issues might be critical when analyzing XMCD spectra, such as the presence of multiple valence states or environments, magnetic bias, normalization issues, saturation effect, background issues, and the integration range.

The presence of a small amount of mixed-valence state (e.g. the presence of Fe<sup>2+</sup> in a Fe<sup>3+</sup> system) will affect the XAS signal [54]. It is also sensitive to the local symmetry and can distinguish between octahedral and tetrahedral coordination [59].

The normalization of the dichroism spectra with an average L<sub>3</sub> peak height allows for calculating magnetic information on a per-atom basis.

A magnetic bias can affect the electrons' behavior in a complex manner due to Lorentz forces and will have a strong incidence in the TEY mode. This must be considered, especially for magnetic field sweep measurements. For magnetic field sweep (hysteresis loop) measurements, the normalized intensity is calculated from the interpolated CL (circular left) and CR (circular right) XAS data using Eq. 3.15 below.

$$\text{Norm. Intensity} = \frac{(CL - CR) * 2}{(CL + CR)} \quad (3.15)$$

If the magnetic bias effect is corrected and the beam of correct quality, the TEY mode can be used to make a field-dependent XMCD measurement separately on different elements, giving a high-quality element-specific hysteresis loop [60].

Saturation effects related to self-absorption phenomena may arise when the electron yield sampling depth is larger than or comparable to the incident X rays' absorption depth. This is easily the case with X-ray absorption lengths at the L<sub>2,3</sub> edge thresholds being rather short (ca. 20 nm) for transition metals, such as Fe. The X-rays that reach the deeper layers have undergone an absorption that differs from one energy to another and which is globally stronger at the L<sub>3</sub> edge than the L<sub>2</sub> one. This phenomenon has been thoroughly studied and described by Nakajima *et al.* [61], who propose an absorption correction factor,  $f_{corr}$ , considering that the escape probability of the electrons from the surface exponentially decays along with the thickness. (Eq. 3.16) :

$$f_{corr}(t, \theta) = \left(1 + \frac{\lambda_e}{\lambda_x \cdot \cos(\theta)}\right) * \left(\frac{1}{1 - e^{-t \cdot \left(\frac{1}{\lambda_e} + \frac{1}{\lambda_x \cdot \cos(\theta)}\right)}}\right) \quad (3.16)$$

where  $t$  is the sample thickness,  $\lambda_e$  is the electron sampling or escape depth,  $\lambda_x$  is the X-ray penetration length (attenuation length),  $\theta$  is the X-ray incidence angle relative to the normal incidence (0° for normal incidence (NI), 60° for grazing incidence (GI)),  $\lambda_x \cdot \cos(\theta)$  is then the X-ray penetration depth [61]. The experimental data is multiplied by this correction factor prior to treatment. We used a  $\lambda_e$  value of 5 nm, and  $\lambda_x$  values of 25.3 nm for L<sub>3</sub>, 65.3 nm for L<sub>2</sub>, as found in [62]. As an example, for XAS experiments in NI on the 64 nm thick sample, the correction factors were 1.20 and 1.08 at L<sub>3</sub> and L<sub>2</sub> edges, respectively.

The saturation effect is very important for ultra-thin films <sup>[63]</sup> as well as for measurements performed at angles lower than normal incidence (e.g. grazing angles) <sup>[64]</sup>. Deviations of the spin and orbital moments from their true values by 20% and 100%, respectively, can be observed if it is not taken into account.

The background issue comes from possible incorrect background subtraction or variations in the background subtraction for each XAS spectrum. The background to be applied to raw XAS spectra is a step-like function, to correct from the excitation of photoelectrons in continuum states from the absorption edges <sup>[65]</sup> (Fig. 3.12 (a), red step curve).

An incorrect integration range can also introduce errors in calculating the parameters  $p$ ,  $q$ ,  $r$  (Fig. 3.12 (a)) required for the application of sum-rules. Although the integration range should ideally be infinite, practically the range selected is from just before the  $L_3$  edge until the integration value saturates above the  $L_2$  edge, which is in many cases roughly 20 eV wide <sup>[65]</sup>.

All these factors must be carefully considered during the analysis to extract meaningful information from the XMCD data.

### 3.3.2 XMCD for GFO – pre-existing works

In this manuscript, the system under consideration, GFO 1.4, is a room-temperature ferrimagnetic material with an orthorhombic structure and four different cationic sites. For such a composition, the iron cations mainly occupy octahedral sites only, while the tetrahedral sites are occupied with Ga. The Fe ions in all the sites are in the  $Fe^{3+}$  oxidation state. This means that the 3d shell is half-filled, and following Hund's rule, no orbital moment is expected to be observed.

A XAS/XMCD study by Kim *et al.* <sup>[58]</sup> at the Fe  $L_{2,3}$  edges on untwined single crystals of GFO 1.0 at 190 K however showed that there exists an important orbital moment ( $m_L$ ) on Fe of  $0.017 \mu_B/Fe$  (Fig. 3.13 (a)). They explain this apparent anomaly by structural distortions of the Fe atoms' environment in the Fe1, Fe2, and Ga2 octahedra, produced by off-centering movements (Fig. 3.13 (b)), and that lead to some charge transfer. They support this claim from the O K-edge spectra that show Fe-O bonding anisotropy in-plane (Fig. 3.13 (b)), hinting anisotropic hybridization between Fe(3d)- O(2p) orbitals.

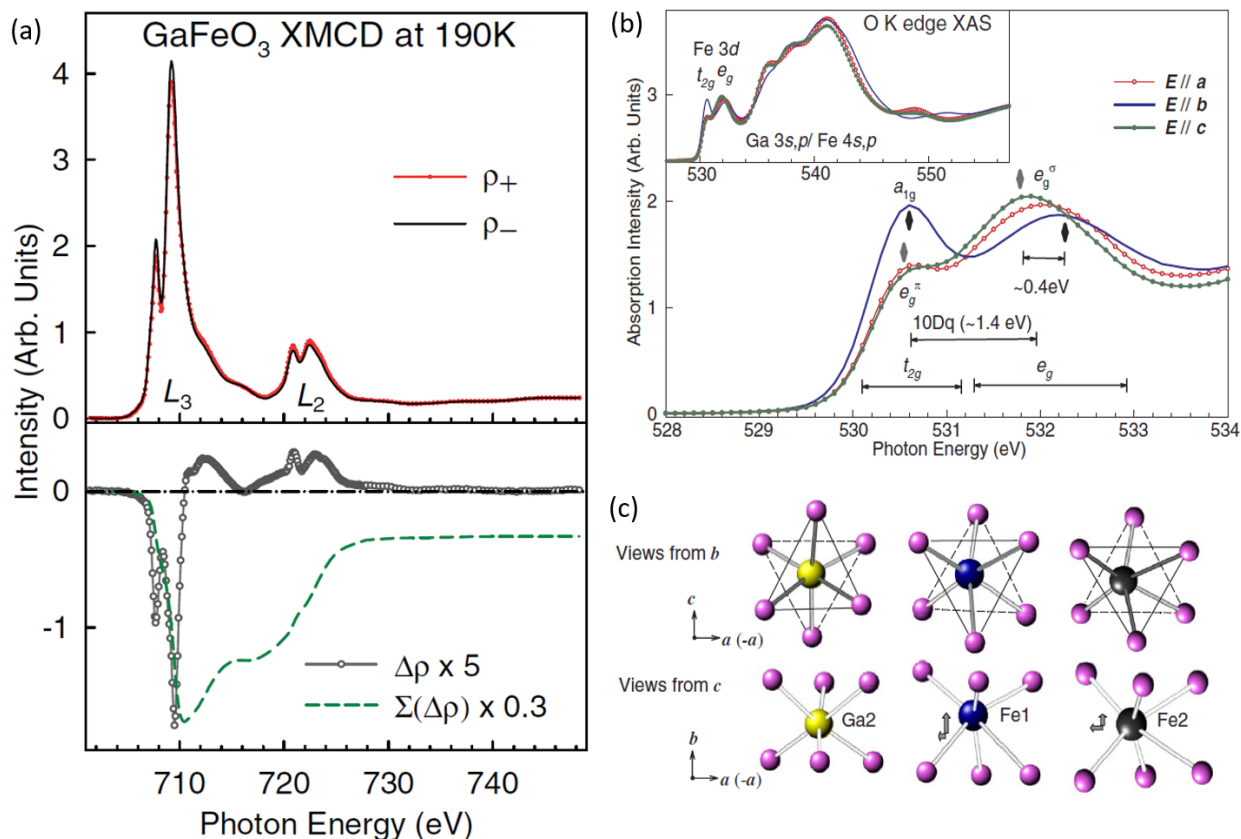


**Fig. 3.13 | Results of XAS/XMCD on bulk GFO sample.** (a) Fe L-edge XAS/ XMCD study performed on single-crystalline GaFeO<sub>3</sub> at 190 K showing a non-zero  $m_L$ . (b) the O K-edge XAS spectra obtained in the 528-534 eV range. The inset shows the full scan range. (c) A model for the distortion of the FeO<sub>6</sub> octahedra due to Fe movements. Adapted from ref. [58].

One can fully explain this through the following geometric considerations. In the GFO structure, the FeO<sub>6</sub> octahedra have two of their triangular faces positioned parallel to the a-b plane. They may be trigonally distorted in the out-of-plane direction, as shown in Fig. 3.14 (a) because of the displacement of Fe<sup>3+</sup> in the 'c' direction. The octahedral symmetry ( $O_h$ ) is then distorted into a trigonal symmetry ( $D_{3d}$ ) with a 3-fold rotational axis [66]. The three degenerated  $t_{2g}$  orbitals are separated into  $a_{1g}^g$  and  $e_g^\pi$  orbitals and the  $e_g$  orbitals become  $e_g^\sigma$  orbitals. The  $D_{3d}$  symmetry itself suffers from some off-centering of the Fe ions, and the  $e_g^\sigma$  degeneracy is further lifted between in-plane and out-of-plane directions (Fig 3.14 (a)). The schematic in Fig. 3.15 (a) shows the Fe 2p to Fe 3d transitions for such distorted FeO<sub>6</sub> octahedra.

The distortions of the FeO<sub>6</sub> octahedra can be accessed via O K-edge X-ray absorption spectroscopy, which involves the dipole symmetry allowed transitions from the O atoms 1s to 2p states (Fig. 3.15 (b)). This results from the existence of some hybridization between the O 2p and

Fe 3d to form the FeO<sub>6</sub> octahedra bonds [67]. The O K-edge XAS can therefore be used to probe the Fe 3d e<sub>g</sub>/t<sub>2g</sub> anisotropy and reflects the their unoccupied density of states [68].

The experimentally measured m<sub>L</sub> value in GFO 1.0 has been supported by first-principle calculations by Han *et al.* (m<sub>L</sub> = 0.02 μ<sub>B</sub>/Fe) [69], Roy *et al.* (m<sub>L</sub> = 0.025 μ<sub>B</sub>/Fe) [70] and Ibrahim *et al.* (m<sub>L</sub> = 0.018 μ<sub>B</sub>/Fe) [71]. A recent theoretical study by Dixit *et al.* [72] confirmed the role of the distorted GFO structure claimed by Kim *et al.* and calculated spin and orbital momentum values of m<sub>S</sub> = 0.777 μ<sub>B</sub>/Fe and m<sub>L</sub> = 0.008 μ<sub>B</sub>/Fe, respectively.

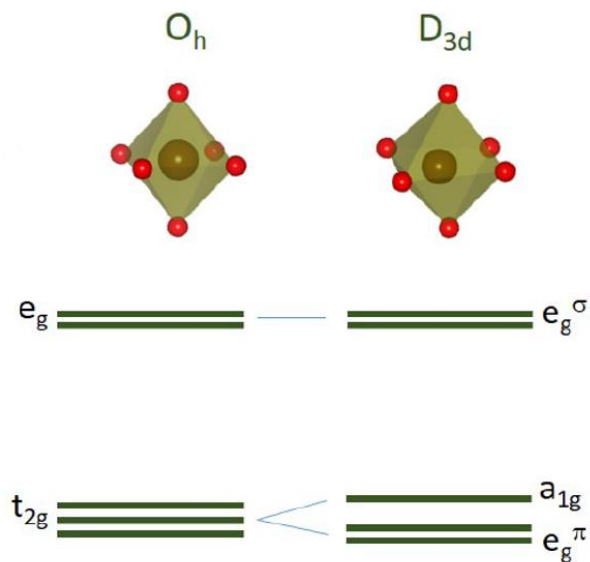


**Fig. 3.14 | The FeO<sub>6</sub> octahedral (O<sub>h</sub>) and trigonal (D<sub>3d</sub>) polyhedra.** Adapted from ref. [73].

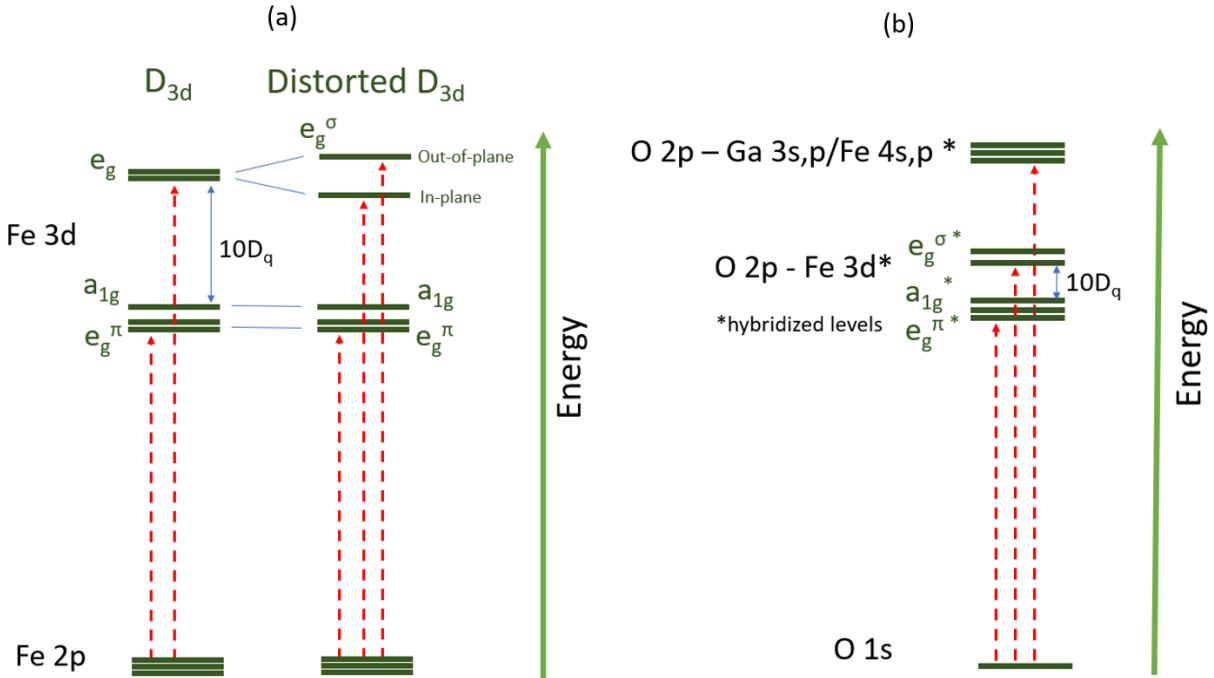


**Fig. 3.15 | Energetic diagrams.** (a) For Fe 2p to 3d possible transitions in the  $D_{3d}$  and distorted  $D_{3d}$  symmetries. (b) For the transitions from O 1s to O 2p – Fe 3d and O 2p – Ga 3s,p/Fe 4s,p hybridized states. The hybridization between the Fe 3d and O 2p orbitals in  $\text{FeO}_6$  yields bonding orbitals lower in energy than O 2p orbitals [67].

Recently, XAS/XMCD studies of GFO x have also been realized on thin films of ca. 60 nm, grown on YSZ (111), by Zhong *et al.* for  $x = 1$  and 1.4, at 300 and 80 K [74], and another one on GFO thin films of 70 nm grown on STO (111) [75], by Katayama *et al.* for  $x = 1.4$  at 35 K. However, no quantitative analysis of  $m_S$  or  $m_L$  was made in either study. Furthermore, to the best of our knowledge, XAS/XMCD studies have never been performed for GFO at ultra-thin film regime.

The isostructural compound to GFO, which contains only Fe,  $\epsilon\text{-Fe}_2\text{O}_3$ , also demonstrates a non-zero  $m_L$ , in the form of nano-particles, despite the  $\text{Fe}^{3+} d^5$  configuration. This moment has a non-monotonic temperature variation with a minimum of  $m_L$  at 120 K (Fig. 3.16 (a, c)), whereas no such anomaly is observed for  $m_S$  (Fig. 3.16 (b)) [76]. The probe of the orbital moment temperature evolution in  $\epsilon\text{-Fe}_2\text{O}_3$  was conducted to explore the possible implications of commensurate-to-incommensurate transition at 120 K, evidenced by the sudden decrease in field cool (FC)/ zero-field cool (ZFC) measurements from 120 K to low temperature and a decline in  $H_c$  (and  $M_r/M_S$ ) at 120 K that is recovered at lower temperatures (further details on the magnetic characteristics of  $\epsilon\text{-Fe}_2\text{O}_3$  can be obtained in the review by Tucek *et al.* [77]). These anomalies are attributed to a change in the Fe-O bond length, further implying the significant role of distortions in the observed anomalies.

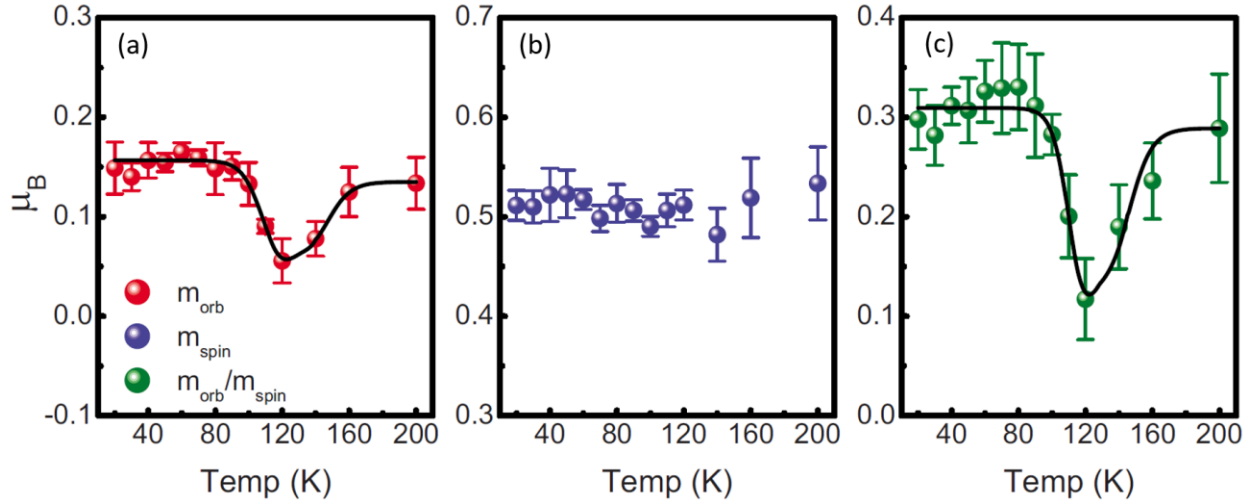


**Fig. 3.16 | The temperature evolution for the iso-structural  $\epsilon\text{-Fe}_2\text{O}_3$  compound in the form of nano-particles. (a)  $m_{orb}$  ( $m_L$ ), (b)  $m_{spin}$  ( $m_S$ ) and (c)  $m_{orb}/m_{spin}$  ( $\frac{m_L}{m_S}$ ). Adapted from ref. [76].**

This evidence of structural-distortions-driven non-zero  $m_L$  motivated us to pursue a similar study in the thin/ultra-thin GFO films, which have contemporary technological appeal. The existence of  $m_L$  in GFO thin films had not been demonstrated. The temperature dependence of  $m_L$  had never been investigated, even in bulk. The study of the orbital moment in GFO films, therefore, could have important implications such as :

- (a) answering fundamental questions concerning the effect of the orbital anisotropy on the magnetic anisotropy (see Ch.3.2) in ultra-thin films or the effect of temperature on  $m_L$ ,
- (b) for applications related to the control of the orbital degree of freedom, for example through the application of an electric field, since  $m_L$  finds its origins in crystalline distortions, which could be controlled by electrostatic means [78,79].

### 3.3.3 XMCD for GFO – Our work

#### 3.3.3.1 Experimental

We have thus performed XMCD studies of our GFO films to get insights into the orbital moment behavior, varying both the films thicknesses and the temperature. The measurements were performed on the DEIMOS beamline at the SOLEIL synchrotron source (Saint Aubin, France), with the help of the beamline contacts Fadi CHOUEIKANI and Philippe OHRESSER. We have obtained XMCD from XAS spectra measured at temperatures between 4 and 300 K, with a combination of alternating circular polarization (left/right) and magnetic fields ( $\pm 6.5$  T) at the Fe  $L_{2,3}$  edge. For the 4 K measurements, the field was applied in both normal (NI) and grazing incidence (GI) geometries (see Fig. 3.17). For the other temperatures the measurements were only performed in the NI. A combination of 16 (8) spectra was acquired for the NI (GI), with alternating magnetic fields and beam polarizations. We also obtained XAS spectra with linear polarizations at the O K-edge for NI and GI geometry, without a magnetic field, in both vertical and horizontal configurations. We have observed the evolution of element-specific XMCD spectra as a function of the magnetic field at both the Fe and Ga  $L_{2,3}$  edges.

This XMCD study has been performed on the exact samples on which the anisotropy study had already been performed by SQUID measurement, described in section 3.1.2. This will allow quantitative comparison between the magnetization measured by SQUID and the spin and orbital moments deduced from the XMCD analysis. Fig 3.18 shows a schematic and real picture of the Deimos beamline instrument at the synchrotron Soleil (Paris). The samples are positioned as shown in Fig 3.18 (a) inset, on a copper plate.

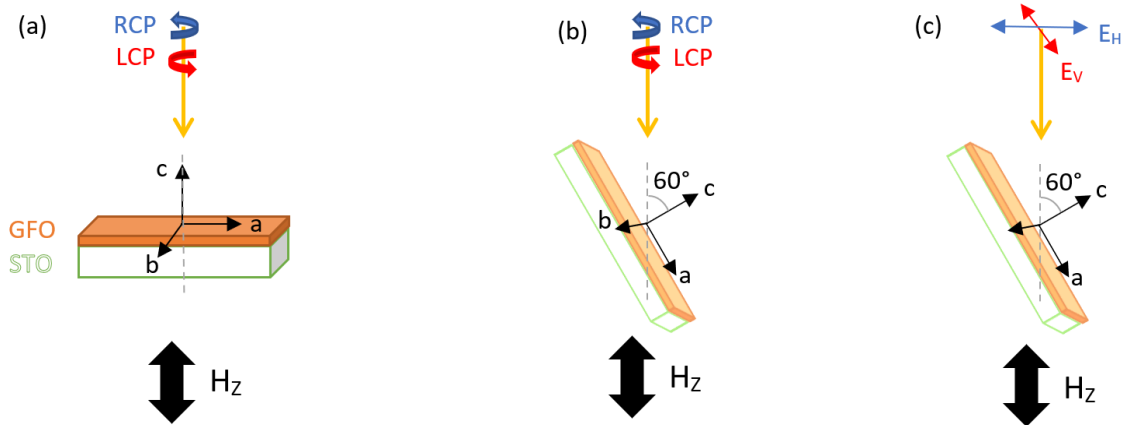


**Fig. 3.17 | Illustration of the various geometries used for the XAS.** (a) Normal Incidence (NI) for the right (RCP) and left circularly polarized (LCP) x-rays (b) Grazing Incidence (GI) for the RCP and LCP x-rays – the incident beam makes a  $60^\circ$  angle with the surface normal. (c) Grazing Incidence (GI) geometry for the horizontal ( $E_H$ ) and vertical ( $E_V$ ) linearly polarized x-rays – the incident beam makes a  $60^\circ$  angle with the surface normal.

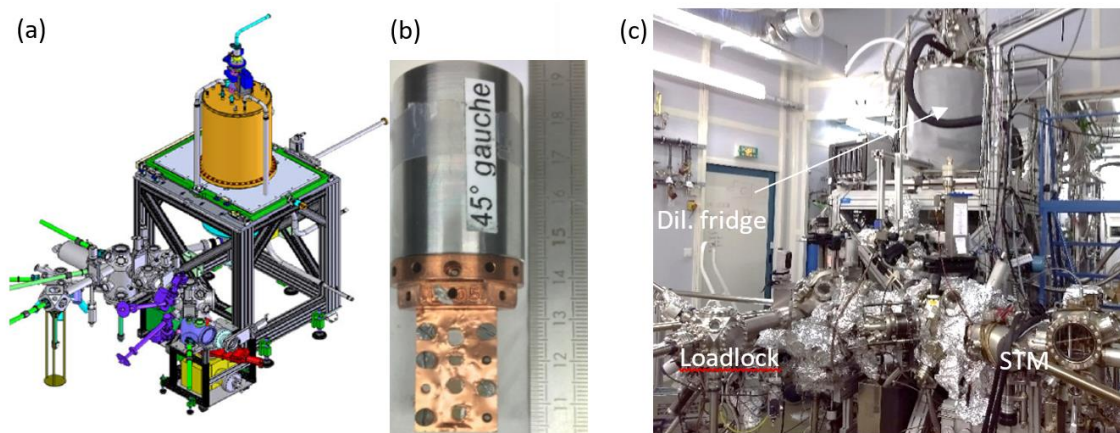


**Fig. 3.18 | Experimental XMCD technique.** (a) Schematic of the set-up on the DEIMOS beamline at the SOLEIL synchrotron source. A dilution refrigerator cryo-chamber is installed that allows XAS measurements on the sample from 350 K down till a few hundred milli-K. *Adapted from a tutorial in "International school on Synchrotron and Magnetism," Mittlewih, France* <sup>[54]</sup>. (b) a photo of the sample holder, with samples loaded. The holes in the Cu plate allow the X-ray beam to interact with a disk-shaped part of the sample. The backside also can hold four samples, thus allowing to load eight samples at a time. (c) a picture of the DEIMOS beamline instrument shows the dilution refrigerator (dil. fridge), the loading place (loadlock), as well as some other attached devices which were not used for our experiments such as a scanning tunnelling microscope (STM).

The GFO thin films, even though semiconducting, did not show any charging issues over the entire studied temperature range (4-300 K). The possible samples contamination issues have been addressed by a full range XAS (350-1150 eV) scan to identify the presence of unwanted elements. To avoid magnetic bias issues, all the scans were normalized with an average  $L_3$  peak height. The spectra were corrected from saturation effects by multiplying their  $L_3$  and  $L_2$  parts with the appropriate correction factors, calculated for each different film thickness and measurement angle. To remove background issues which may impact the measurement of the 'r' parameter required for sum-rules calculation, we subtract the average of all XAS with a step-like function. The background is corrected by subtracting a linear contribution from the data for both XAS and XMCD. To remove background issues which may impact the measurement of the 'r' parameter required for sum-rules calculation, the background setp-like function which is to be removed is designed from the average of all XAS spectra. The integration range for the Fe L edges is set from 675-775 eV. The upper limit is chosen as the energy for which the integrated signals reach saturation. It is relatively high, which can be explained by an important contribution from spin-polarized extended x-ray absorption fine spectra (SPEXAFS) in the oscillations above the  $L_2$  edge in XMCD measurements. Such SPEXAFS oscillations are usually considered as interesting to be measured because of their strength at the 5d L-edges of Gd, Eu, and Ho <sup>[80]</sup>, but rather insignificant in the case of the 3d L-edge XMCD measurements. This SPEXAFS contribution has however been observed to contribute to Fe L-edge XMCD measurement in  $Fe_3O_4$  <sup>[81]</sup>, where it has been strongly established that a wide energy range was required for the XMCD measurements, especially for a correct analysis of orbital moment. The observation of SPEXAFS oscillation at 3d edge is rather rare and an in-depth analysis into these oscillations can give perspectives on the information of local magnetic nature in GFO thin films.

### **3.3.3.2 Contamination issues – Wide range spectra**

Full energy range XAS scans of thin films of various thicknesses have been performed to explore possible contaminations that evade detection in other characterization techniques but can be detected in synchrotron X-ray absorption owing to its high brilliance of X-rays and element-specific sensitivity.

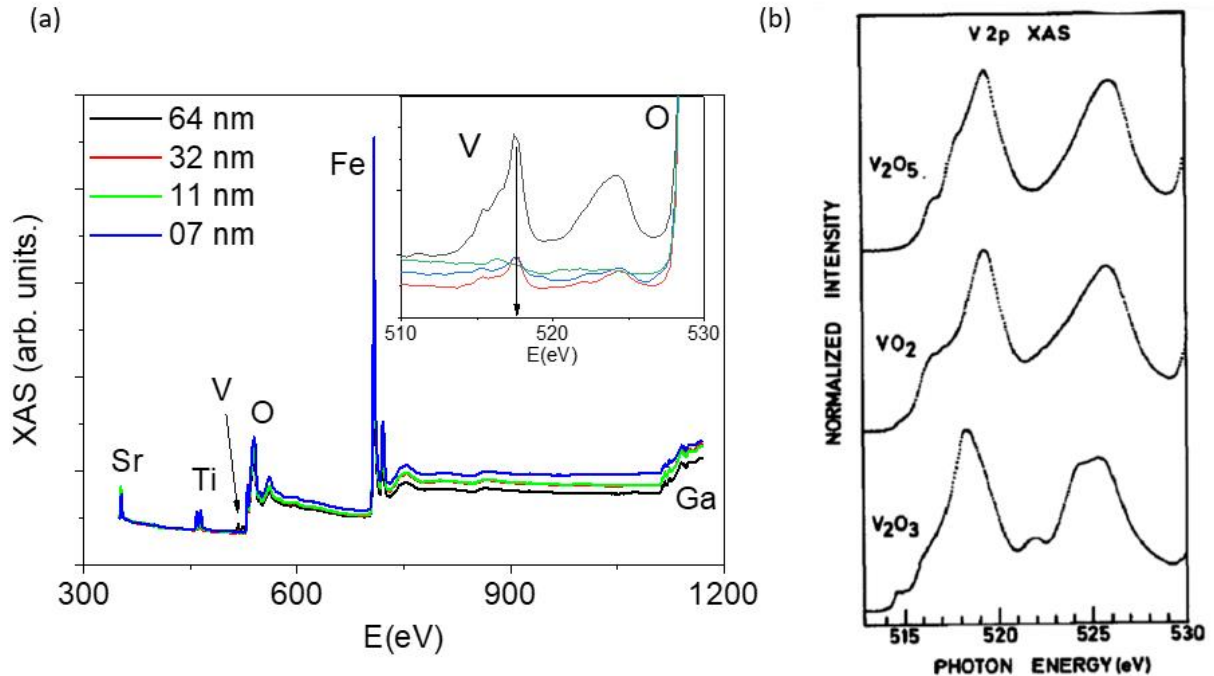


**Fig. 3.19 | Elemental contamination issues.** (a) Full energy range (350-1150 eV) X-ray absorption scans for various GFO films thicknesses, with identified elements. Inset shows a 510-530 eV zoom displaying vanadium 2p XAS peaks. (b) The vanadium 2p XAS measured for different vanadium oxidation states. Adapted from ref. [82].

Apart from the elemental absorption peaks expected for STO (*Subs.*)/GFO thin films, we also observe the presence of a small amount of vanadium (V) in the samples. This can be seen on Fig 3.19 (a). These peaks are compared with the V peaks measured for different oxidation states [82]. The peaks positions of  $V_2O_3$  closely match with the observed peaks and hints at a possible  $V^{3+}$  oxidation state. The stark contrast in peak intensity between V and other elements indicates the presence of only a very small amount of V. This small presence of V has been ascribed to a previous growth of V-containing oxides in the PLD chamber, in vacuum conditions. Due to the highly non-volatile nature of metallic V, it remains present in the chamber on the walls even after a PLD chamber annealing and only slowly diffuses in the chamber during the growth of GFO due to the high temperature (900°C) involved. Therefore, the V contamination scales proportionately with the films thickness, since the longer the time of growth, the more important the diffusion phenomenon. This contamination was not evidenced by X-ray diffraction measurements; this either indicates that V is incorporated in amorphous compounds or that the contamination is less than  $\sim 1\%$  of the sample volume.

### 3.3.3.3 Elemental Hysteresis

We performed elemental hysteresis loop measurements in ultra-thin GFO films of 7 nm at 4 K for Fe in GI geometry at the  $L_3$  edge to compare information from this microscopic hysteresis loop with the macroscopic SQUID hysteresis loop. The normalized intensity is calculated from the Eq. 3.15 mentioned in the introduction. The loop shows a large coercive field  $H_c$  of  $\sim 0.5$  T and a saturation field of  $\sim 2$  T (Fig. 3.20), and is very comparable to the hysteresis loops measured by SQUID with the applied field in-plane.

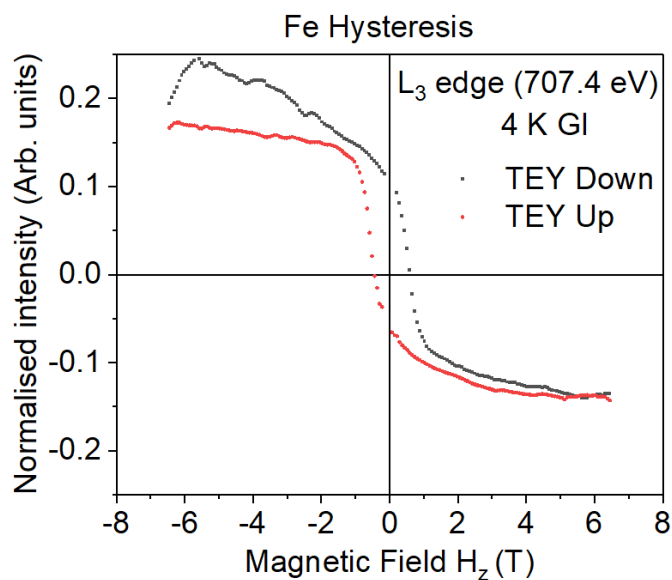


**Fig. 3.20 | Normalised hysteresis loop measured at the Fe  $L_3$  edge, on 7 nm GFO thin films in GI geometry and at 4K.**

We also performed XAS/XMCD and hysteresis measurements for Ga at its  $L_3$  and  $L_2$  edges, in GI, for the 7 nm thick film, at 4 K. The measurements are presented in Fig. 3.21 (a, b). They show a finite signal for XMCD on Ga at the  $L_3/L_2$  edge taken from 1100 to 1200 eV, thus indicating the presence of magnetism on Ga. This is an indicator of the strong hybridization between the Fe and Ga orbitals. The normalized hysteresis measurements performed at both the  $L_3$  and  $L_2$  edge are shown in Fig. 3.21 (c, d). The  $L_3$  curve, even though stained by some drift, globally shows parallel coupling with Fe at its own  $L_3$  edge. As expected, the loop for Ga at the  $L_2$  edge shows the opposite feature. Both  $L_2$  and  $L_3$  Ga hysteresis loops have similar features to those observed for Fe, in terms of coercive and saturation fields, confirming the strong coupling between the two elements, through orbital hybridization.

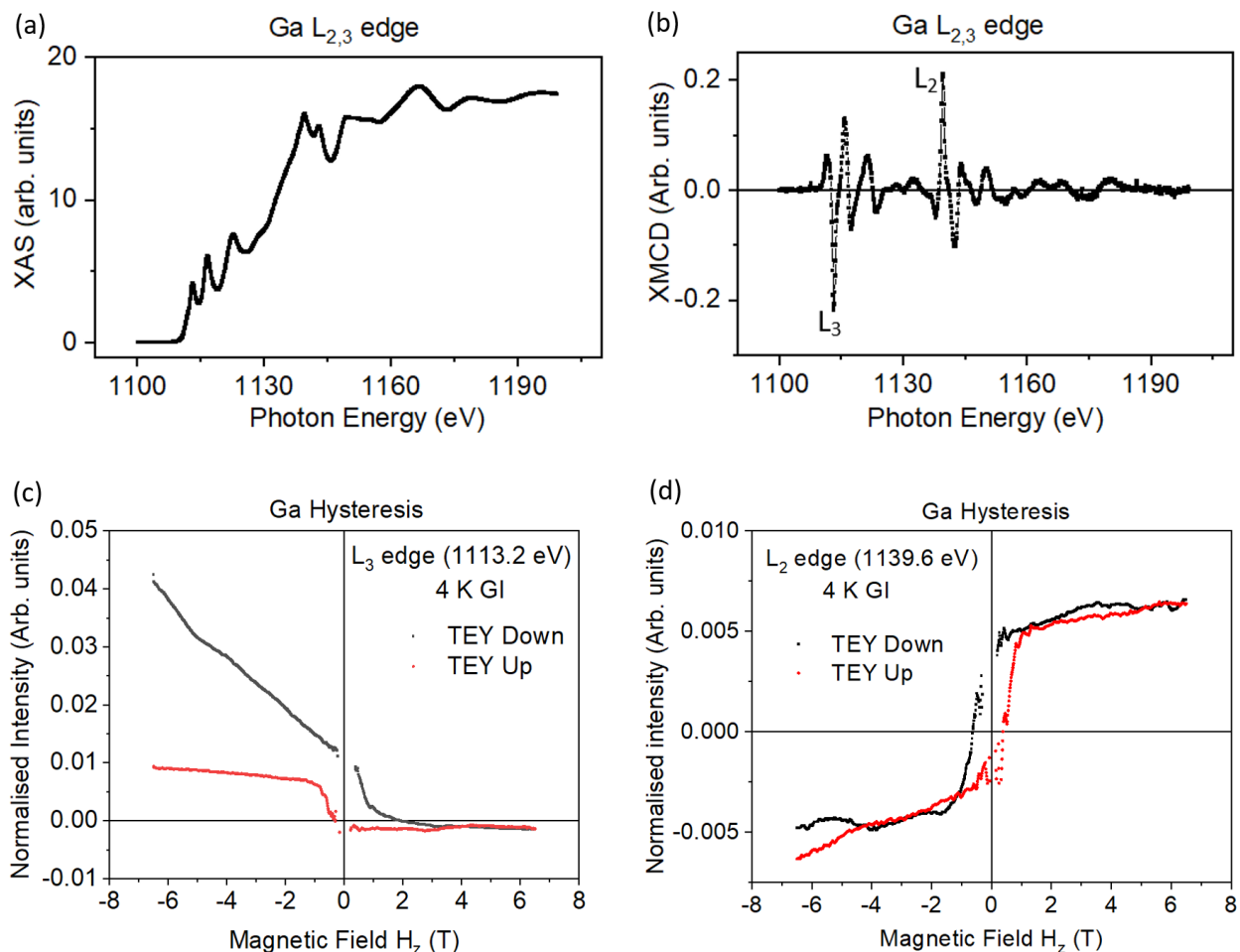


**Fig. 3.21 | X-ray spectroscopy at 4K on the Ga  $L_{2,3}$  edge in the GI mode on a 7 nm thick GFO thin film.** (a) Averaged and normalised XAS measurement. (b) Averaged and normalised XMCD measurement. (c) Normalised hysteresis measurement at the Ga  $L_3$  edge. (d) Normalised hysteresis measurement at the Ga  $L_2$  edge.

### 3.3.3.4 Evidence of a non-zero orbital moment

We will now focus on the XAS and XMCD spectra obtained at the Fe  $L_{2,3}$  edge for the relatively thick GFO film of 64 nm thickness, at 4 K, in GI geometry, that is, for a magnetic field applied mostly in-plane. The spectra are shown in Fig. 3.22. The XMCD data integration shows that there is a non-vanishing negative value of 'q'. Sum rules indicate that the orbital moment is directly proportional to the 'q' value. The sign of  $m_L$  depends on its sign. If q is negative(/positive),  $m_L$  will be parallel(/anti-parallel) to the  $m_S$  direction. Therefore, since we observe a non-vanishing

negative 'q' value, it means that Fe in our GFO film has a finite 'm<sub>L</sub>' parallel to m<sub>s</sub>. This result is similar to that already obtained by Kim *et al.*<sup>[58]</sup> (Fig. 3.13 (a)) for GFO 1.0 single crystals at 190 K. After considering sum-rules errors, the experimental low temperature value of m<sub>L</sub> = 0.011 μ<sub>B</sub>/Fe is measured, which is in agreement with the calculation derived m<sub>L</sub> = 0.008 μ<sub>B</sub>/Fe<sup>[69–72]</sup>.

As exposed in the XMCD literature review section above, they attribute the existence of this finite m<sub>L</sub> to the distortions in the FeO<sub>6</sub> octahedra of GFO, caused by the movement of Fe ions at the Fe1, Fe2, and Ga2 octahedral sites, and argue that these distortions lead to charge transfer, probably due to anisotropic bonding in FeO<sub>6</sub> octahedra, as observed by O K-edge spectroscopy leading to a non-zero orbital moment<sup>[58]</sup>.

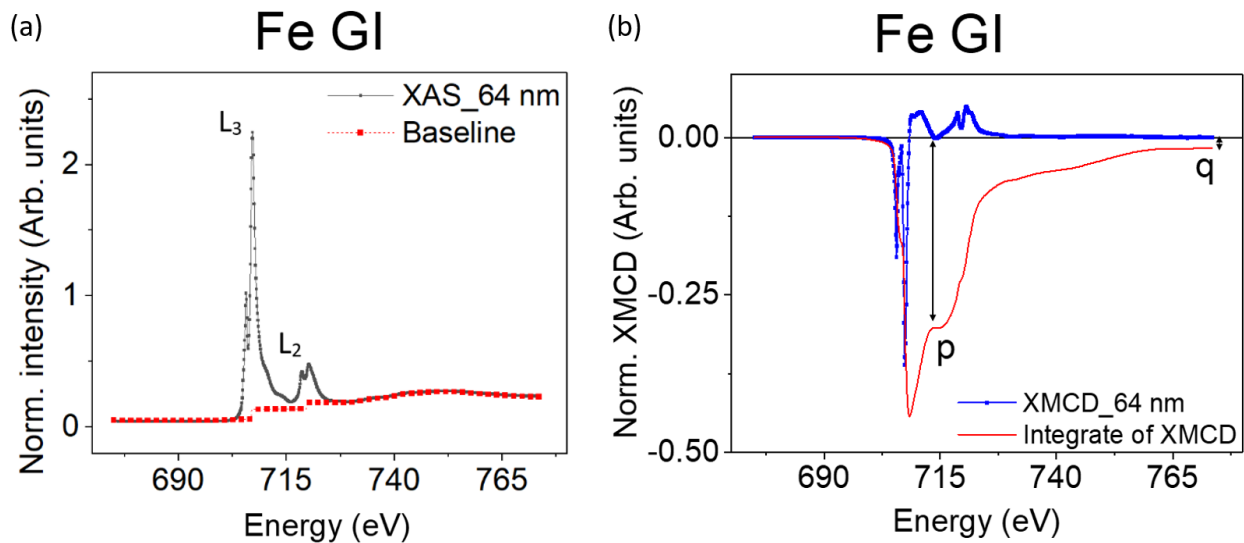


**Fig. 3.22 | X-ray spectroscopy at 4K on the Fe L<sub>2,3</sub> edge in the GI mode on a 64 nm thick GFO thin film.** (a) The averaged and normalized XAS. (b) The averaged, normalized, and saturation corrected XMCD spectra.

To investigate if similar mechanisms as those reported by Kim *et al.*<sup>[58]</sup> have led to the non-zero positive m<sub>L</sub> in our GFO thin films, we must check if there exists distortions in the FeO<sub>6</sub> octahedra. We have thus performed XAS measurements at the O K-edge with linearly polarized light, for different directions of the polarization, which correspond to different crystallographic directions. Fig. 3.23 (a) shows the O K-edge XAS taken with a linear polarization along the a, b, and c crystal axes of the 64 nm GFO film. Focusing on the energy range 527-532 eV, which gives information on the hybridization of the O 2p with the Fe 3d orbitals, we observe a change in the XAS peak intensities between the out-of-plane 'c' and in-plane 'a-b' axes (*Pna2<sub>1</sub>*). This is an indication of a strong orbital anisotropy between the in-plane and out-of-plane directions, hence of distortions.

These results, therefore, hint us towards the existence of distortion-related non-zero orbital moment in GFO thin films, as had been already observed by Kim *et al.* [58] in bulk.

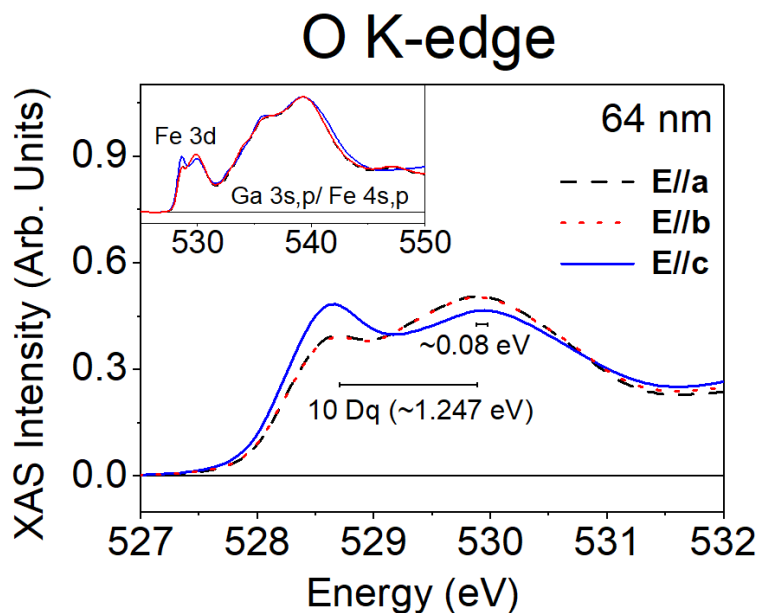


**Fig. 3.23 | O K-edge spectra in the 527-532 eV energy range to observe the Fe 3d – O 2p hybridization features for 64 nm thick GFO film. The inset shows the full scan range.**

To explore the anisotropy of the magnetic moments carried by Fe, both  $m_s$  and  $m_L$ , we need to look at the XAS and XMCD measurements in both GI and NI geometry. We have already seen GI mode measurements, and now we move towards NI geometry measurements, still for a 64 nm GFO thin film, at 4 K and for the Fe  $L_{2,3}$  edge. The XAS and XMCD spectra are shown in Fig. 3.24. The two peaks of the  $L_2$  edge show inversed relative intensity between the GI and NI modes (Inset of Fig. 3.24 (a)). This is a hint of anisotropy of spin and/or orbital density on the Fe ions. Surprisingly, the XMCD integral now shows a non-vanishing positive value of ‘q’, in contrast to the negative ‘q’ value observed for the GI geometry. The  $m_L$  orientation with respect to  $m_s$  changes sign between NI and GI geometries since the  $m_L$  is anti-parallel to  $m_s$  for the NI geometry while it is parallel to  $m_s$  for the GI geometry. The NI configuration mostly probes the out-of-plane projection of the orbital moment and the GI one, the in-plane one. We thus have an experimental hint that the orbital moment varies in space, and differs for differing crystallographic orientations.

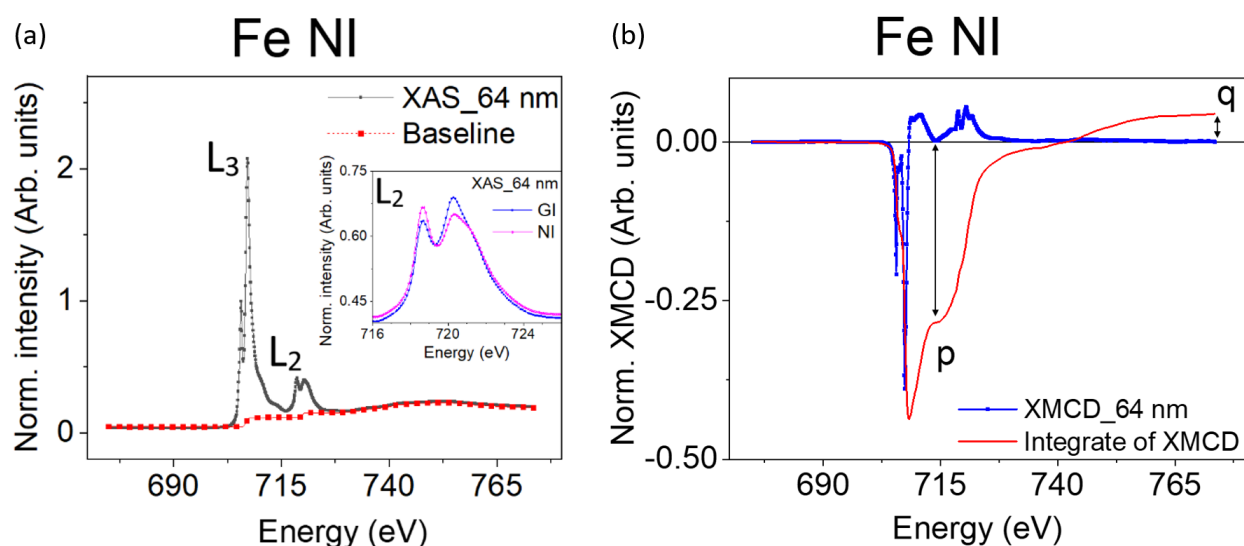


**Fig. 3.24 | X-ray spectroscopy at 4K on the Fe  $L_{2,3}$  edge in the NI mode on a 64 nm thick GFO thin film.** (a) The averaged and normalized XAS. Inset shows Fe  $L_2$  edge peak comparison between NI and GI modes. (b) The averaged, normalized, and saturation corrected XMCD spectra.

To understand why the orbital moment  $m_L$  is anisotropic, we consider the distortions of the  $\text{FeO}_6$  octahedra, which are the origin of the non-zero  $m_L$ . Arima *et al.* have shown that the  $\text{Fe}^{3+}$  ions at the distorted and antiferromagnetically coupled Fe1 and Fe2 octahedral sites are displaced along the out-of-plane 'c' axis in opposite directions [83]. The extent of the off-centering of the  $\text{Fe}^{3+}$  ions determines the hybridization strength [58] and hence the orbital moment. These unequal and opposite displacements (shown by the dotted arrow in Fig. 3.25 (a)) of  $\text{Fe}^{3+}$  create an unequal and opposite orbital moment for the Fe1 and Fe2 sites, which results in a net  $m_L$  along the 'a' axis hence making it the easy axis for magnetism in GFO [58]. If the field applied along the out-of-plane direction is strong enough, the spin moments align with the field. It is expected that the orbital moments would follow the spin moments, but the orbital moments are also strongly coupled to the lattice, i.e. to the distorted  $\text{FeO}_6$  octahedra. The positions of the cations in the film have been determined by resonant elastic X-ray scattering (REXS) experiments (with a software coded by our colleague Dr. Christophe Lefèvre) and confirm that the Fe1 and Fe2 octahedra are differently distorted, with opposite signs displacement of the Fe in each case, and a stronger one for Fe2 [73] (Fig. 3.26 (a, b)). Therefore, considering all the clues described above, a hypothesis was proposed by our colleague Dr. Daniele Preziosi to explain the negative orbital moment sign in the out of plane direction [73]. The orbital moments at the highly distorted Fe2 sites, due to stronger orbital-lattice coupling, remain locked in-plane, whereas the orbital moment of the less distorted Fe1 site can align along the spin direction, creating a net  $m_L$  opposite to  $m_S$  (Fig. 3.25 (b)). This explains how the relative signs of  $m_L$  and  $m_S$  can change between in-plane and out-of-plane directions.

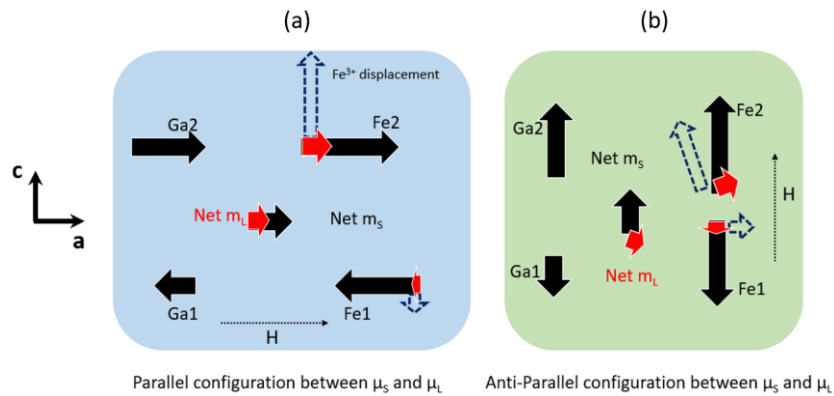


**Fig. 3.25 | A schematic model to visualize the relative spin and orbital moments of Fe at Fe1, Fe2, Ga1, and Ga2 sites.** (a) For an in-plane magnetic field (along the 'a' axis). (b) For an out-of-plane magnetic field (along the 'c' axis). The length of the arrows are related to the Fe occupation of the considered site. Adapted from ref. [73].

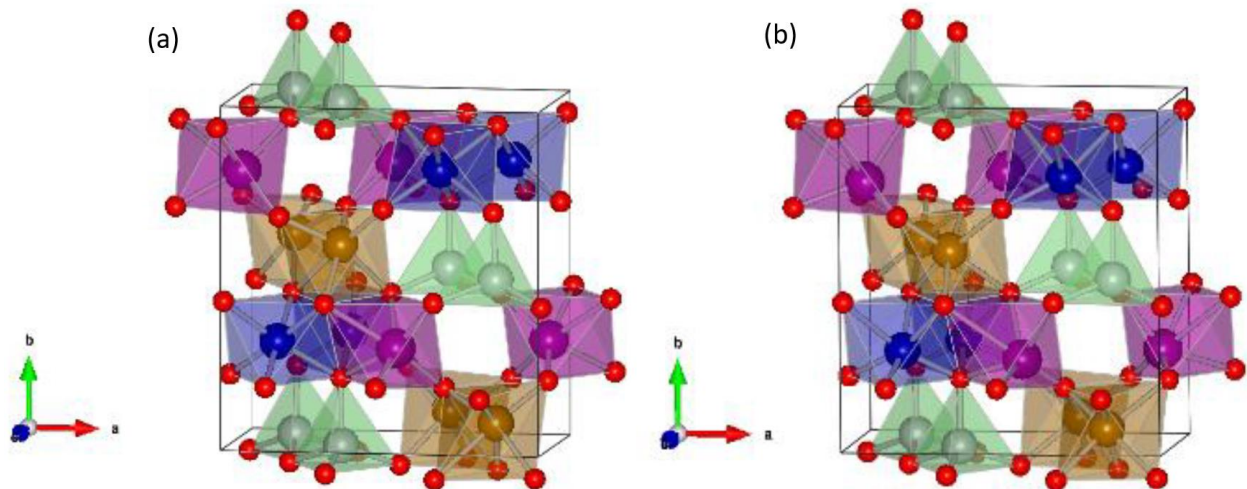


**Fig. 3.26 | GFO unit cell.** (a) For GFO bulk. (b) For GFO thin film, as determined from REXS experiments. Adapted from ref. [73].

### A remark on the validity of sum rules in the GFO case

The values of  $m_s$  and  $m_L$  can normally be quantified using the sum-rules (Eq. 3.13 and 3.14). A question arises, though, concerning the validity of the sum rules in a complex structure such as

GFO. It has indeed been reported that the sum rules are not always applicable <sup>[84]</sup>, particularly among materials which hosts different sites for a considered cation, such as GFO for the Fe ions. The composition  $x = 1.4$  is probably the most favourable one for the GFO compound, since practically all Fe ions are hosted within similar octahedral sites for this composition.

In order to have a certain perspective on the reliability and error margin of sum rules in a system like GFO, we have compared, in Table 3.3, the values of the spin moments we obtain from sum rules on our thin films with those measured on thin films or bulk by other groups, as well as with values measured using other techniques like SQUID. The values reported for SQUID measurements account for the total magnetic moment, which is an addition of the spin and orbital magnetic moments. We observe a 20% variation among the moment values measured by SQUID by different authors on GFO 1.0 single crystals. A 30% variation is observed between the SQUID values obtained for single crystals and for films (for  $x=1$ ), and similarly between thin films of various thicknesses (for  $x = 1.4$ ). We cannot make such comparisons for values measured by XMCD, for they are too scarce. But the discrepancy between the SQUID and XMCD values measured on thin films for the same compositions are not larger than these percentages, which motivates us not to discard the sum rules in our case.

<b>M<sub>S</sub> @ 4K (in μ<sub>B</sub>/Fe)</b>	Single crystal	Thick films (≥ 100 nm)	Thin film (64 nm*)
x = 1.0 (SQUID <sup>#</sup> )	0.79 <sup>[21]</sup> , 0.76 <sup>[83]</sup> , 0.87 <sup>[58]</sup> , 0.69 <sup>[85]</sup> .	0.585 (on YSZ) <sup>[86]</sup> , 0.55 (on STO) <sup>[75]</sup>	-
x = 1.4 (SQUID <sup>#</sup> )	-	1.034 (on YSZ) <sup>[86]</sup> , 1.2 (on STO) <sup>[75]</sup>	0.78
x = 1.0 (XMCD)	0.86 <sup>[58]</sup>	-	-
x = 1.4 (XMCD)	-	-	0.65

\*This work, # The m<sub>S</sub> values reported for SQUID are actually m<sub>S</sub> + m<sub>L</sub>

**Table 3.3 | Comparison of magnetic moment values reported in the literature by SQUID or XMCD with the measured values in this work.**

### 3.3.3.5 Thickness dependence of the spin and orbital moments in GFO thin films

To investigate the effect of the films thickness on the microscopic magnetic measurements, we perform XAS and XMCD studies on 32 nm, 11 nm, and ultra-thin 7 nm thick GFO films, in a similar way as what was done on the 64 nm one. The thickness-dependent profiles of m<sub>S</sub>, m<sub>L</sub>, and m<sub>S</sub>/m<sub>L</sub> (calculated without r) are shown in Fig. 3.27.

We first focus our attention on the  $m_s$  values (Fig. 3.27 (a)). Both GI and NI  $m_s$  values follow the same thickness evolution as the saturation magnetic moments measured by SQUID, that is they show a relatively weaker value for the thinner sample of 7 nm.

Differences between the XMCD and SQUID values first come from the fact that the moment measured with SQUID is a total moment, including an orbital part, and secondly from quite large error bars in both measurement techniques. In SQUID, the error can come from corrections in the substrate's diamagnetic slope, film volume, and atomic lattice lengths that propagate error for calculating value in  $\mu_B/\text{Fe}$  from emu. In XMCD, the error comes from the 'r' and 'N<sub>h</sub>' values of the sum-rules, the correction of  $-7 \langle T_z \rangle$  since the value given is for  $m_s + 7 \langle T_z \rangle$  and  $\langle T_z \rangle$  (can be positive or negative) may not be negligible in GFO as explained before, correction from the 30° offset to in-plane for GI geometry, high surface contribution (from the surface 2-5 nm) which can show differences when compared to the SQUID bulk values. One should also note that the SQUID measurements were performed at 10 K while the XMCD ones were performed at 4 K. In our GFO thin films, the discrepancy between SQUID and XMCD moment values is about 15% for 64 nm, 22 % for 32 nm, 25 % for 11 nm, and 21 % for 7 nm. This relatively high discrepancy is in the expected error range, when considering that values extracted from SQUID and XMCD experiments very commonly have a 10-20 % discrepancy, resulting from  $m_s$  estimation errors from sum rules [36,37,42,45].

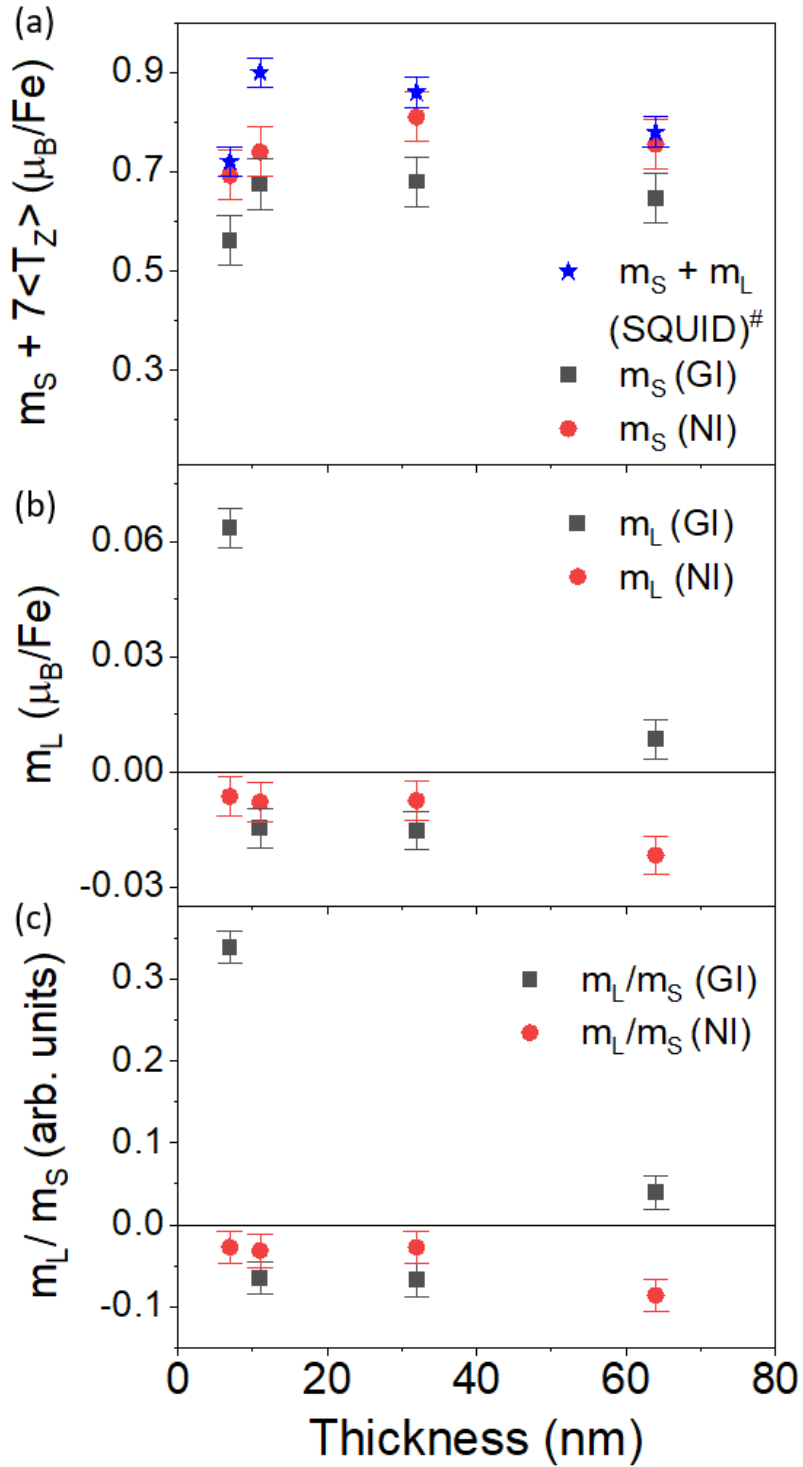


**Fig. 3.27 | Experimental values extracted from XMCD using sum-rules for GI and NI geometries for all films thicknesses. (a)  $m_S$ . (b)  $m_L$ . (c)  $m_L/m_S$ . # The values reported for SQUID are  $m_S + m_L$ .**

We now focus on the evolution of the orbital moment (Fig. 3.27 (b, c)). The sign of  $m_L$  remains negative (i.e.  $m_L$  anti-parallel to  $m_S$ ) for all thicknesses in the NI geometry. In GI, however, it changes sign from positive ( $m_L$  parallel to  $m_S$ ) for 64 nm to negative ( $m_L$  anti-parallel to  $m_S$ ) for 32 and 11 nm back to positive again for 7 nm. This anomalous change in the sign of the orbital moment with thickness is puzzling. It is probably related to the change of the unit cell orientation observed at about 5 nm away from the STO // GFO interface on the HR-STEM image (see Ch.2, Fig. 2.15). The 11 and 32 nm thick films are therefore the witnesses of opposing polarizations, quasi annihilating each other since of quasi equal values. This will have a strong impact on the  $\text{FeO}_6$  octahedra's distortions, on the cations displacement possibilities and in particular on their response to the solicitation of a magnetic field. A simple inversion in their response between Fe1 and Fe2 (Fig. 3.25 (a)) will for example explain this  $m_L$  sign reversal. The cell's distortions are recovered for the 64 nm film, since phenomena located at 5 nm away from the substrate will have much less importance at such high thickness. If this mechanism was confirmed, it would be an interesting manifestation of the electrical polarization as a lever on the magnetic anisotropy.

### 3.3.3.6 Temperature evolution of the orbital moment in GFO films

In a previous study Tseng *et al.* [76] demonstrated that  $\epsilon\text{-Fe}_2\text{O}_3$ , an isostructural compound to GFO only containing Fe cations, also showed a non-zero orbital moment, which had a non monotonous temperature dependence, with a minimum in  $m_L$  for 120 K. This particular feature was accompanied by a strong decrease of the coercive field of the magnetization hysteresis loops of the compound. Based on the measurements performed on GFO by Kim *et al.* [58] and Arima *et al.* [83], but without any actual temperature dependence study of the orbital moment, and without any temperature dependence of the coercive field, these authors conclude that there is no orbital instability in the temperature range of 120 K for GFO. In their review [77], Tucek *et al.* compare the magnetic field cooled curves of  $\epsilon\text{-Fe}_2\text{O}_3$  and  $\epsilon\text{-Ga}_{0.47}\text{Fe}_{1.53}\text{O}_3$ , and note that, while there is a decrease in the magnetic moment below 120 K for the former, there is no such variation for the latter, further strengthening the idea of an absence of instability in GFO at 120 K.

This assertion however strongly depends on the way the magnetic measurements are handled and a modification of the orbital moment in GFO in a smaller extent than what is observed for  $\epsilon\text{-Fe}_2\text{O}_3$ , could be completely masked by the behavior of the predominating  $m_S$ . We have therefore first performed a study of the temperature dependence of the coercive field in our GFO films, in both parallel and perpendicular configurations, by SQUID. Magnetization hysteresis loops are measured every 10 or 20 K in temperature range of 4 to 300 K and the measured coercive field  $H_c$  is plotted as a function of the temperature for the 64 nm sample (Fig. 3.28). If the plot shows no particular anomaly for the parallel measurement, for which the expected increase of  $H_c$  is observed when lowering the temperature, the perpendicular measurements show an anomalous maximum in the curve at approximately 150 K. The anomaly in temperature dependence of  $H_c$  is not as glaring as in the case of  $\epsilon\text{-Fe}_2\text{O}_3$ , but it is there and could signify a drastic change in the

microscopic magnetic properties <sup>[87]</sup> of GFO films below 150 K, which fully justifies their deeper temperature study through an XMCD study.

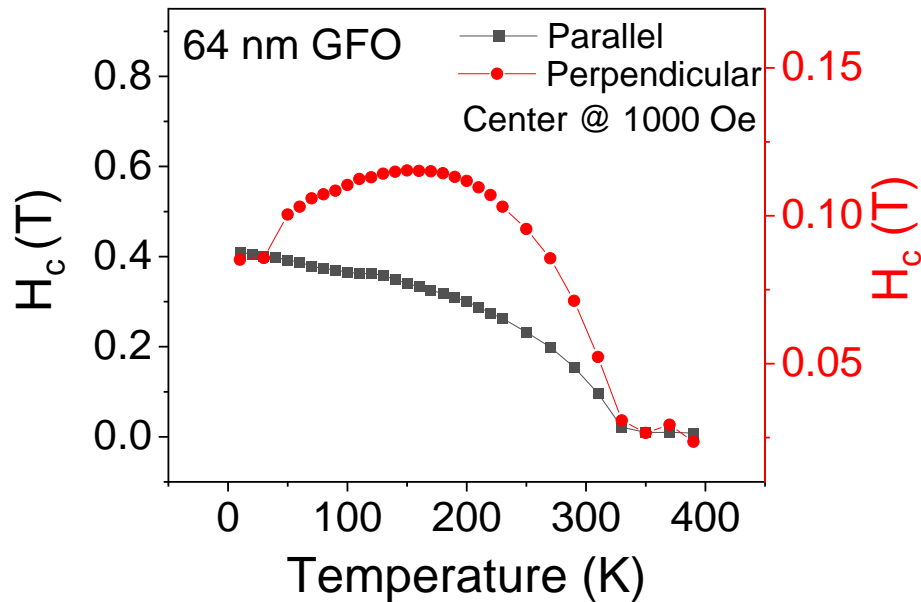


**Fig. 3.28 | Temperature dependence of  $H_c$  for the 64 nm GFO thin film in both parallel and perpendicular measurement modes.**

To explore the microscopic mechanism behind the anomalous change in  $H_c$ , we focus our microscopic measurements in NI geometry since the anomaly was observed for perpendicular mode measurements.

Fig. 3.29 shows the XMCD signal and its integration for the 64 nm sample at different temperatures. Interestingly, the XMCD data quality stayed stable over the whole temperature range, which is unexpected since the role of the charging effect in insulating films like GFO is expected to be higher at lower temperatures. The XMCD data scales along with temperature and is the smallest for 300 K since it is near the magnetic ordering temperature  $T_c = 360$  K for our GFO films. Preliminary inspection of the XMCD data (in blue) shows that some data features are non-uniform over the temperature range. Particularly, the relative intensity between the 2 (negative) peaks observed at the  $L_3$  edge is seen to change drastically at 120 K to the point that both peaks' intensity is similar. Surprisingly, these relative peak intensities are recovered as the temperature is lowered to 20 K (and even 4 K, Fig. 3.24 (b)). Such a change in intensity between the 2 negative peaks at Fe  $L_3$  edge was claimed by Zhong *et al.* <sup>[74]</sup> for GFO 1.0 thin films at 80 K but was not observed for higher Fe concentrations. Due to a very limited number of data points (only two temperatures : 80 K, 300 K) and no quantitative analysis, no further conclusion could be made.

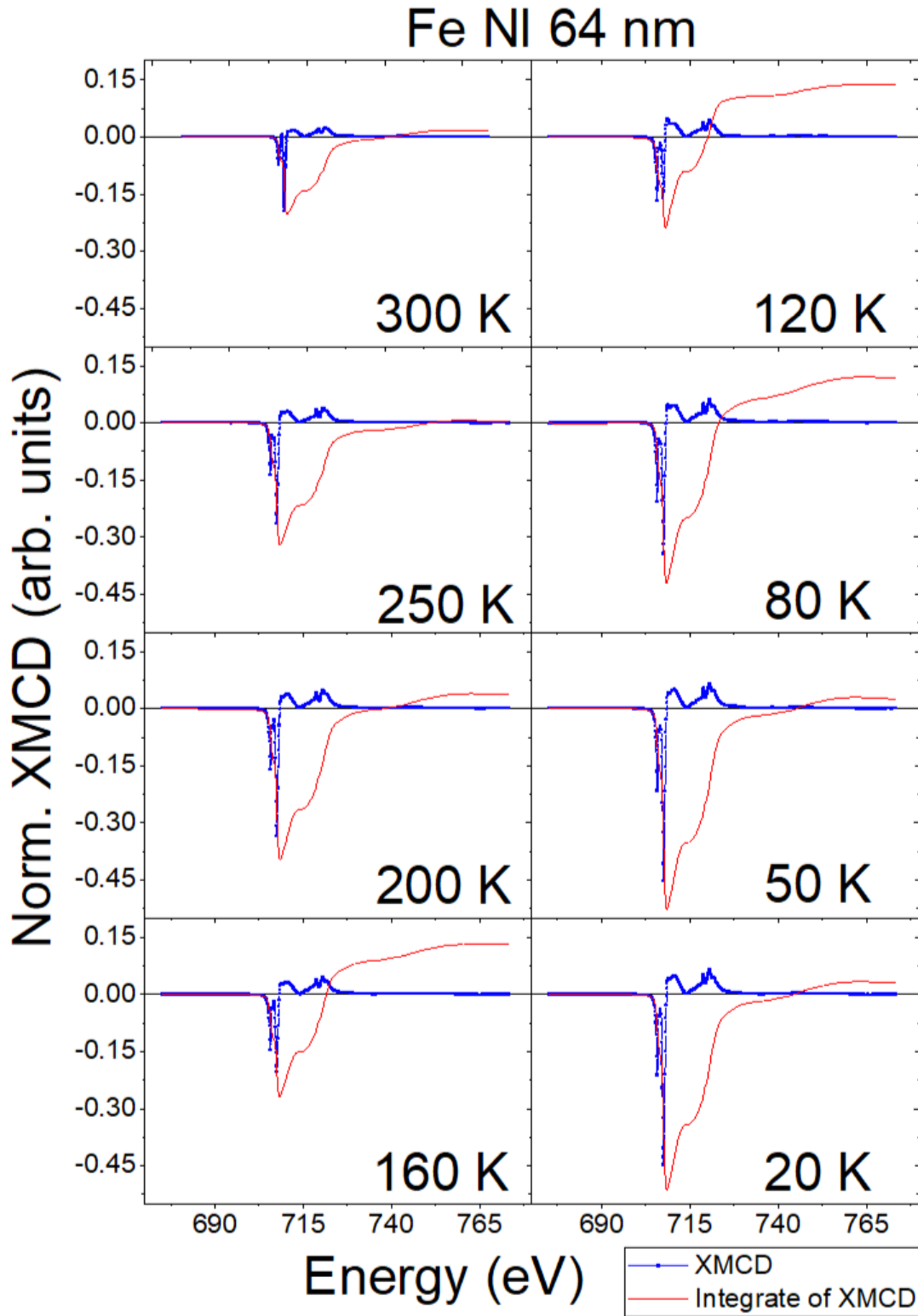


**Fig. 3.29** | Averaged, normalized and saturation corrected XMCD signal, together with its integration, for measurements performed at the Fe  $L_{2,3}$  edge on the 64 nm GFO thin films in NI geometry, at eight different temperatures.

We observed a finite positive ‘q’ value (red XMCD integral) at all the measured temperatures, suggesting anti-parallel alignment of  $m_S$  and  $m_L$ . This follows the 4 K measurement, as seen in Fig. 3.24 (b). Applying the sum-rules to the p, q, and r values obtained from these XAS/XMCD measurements, we obtain the temperature evolution of  $m_S$ ,  $m_L$  and  $\frac{m_L}{m_S}$  (Fig. 3.30 (a-c) black points for the 64 nm sample). The  $m_S$  values obtained from XMCD decrease monotonically with temperature and the temperature profile is comparable to the profile obtained with SQUID for the same sample. We note that a non-monotonous behaviour with temperature is observed for both  $m_L$  and  $\frac{m_L}{m_S}$  and is characterized by a minimum at ca. 120 K. This had never been observed. This anomaly observed for GFO at 120 K has some similarity to the one observed in  $\epsilon$ -Fe<sub>2</sub>O<sub>3</sub> (3.16), but one must highlight the fact that, here  $m_L$  is negative, while it was positive for  $\epsilon$ -Fe<sub>2</sub>O<sub>3</sub>, and perhaps the underlying physical processes could differ. Moreover, GFO is in the form of thin films, and the measurements are made along a defined axis direction (the ‘c’ axis), whereas  $\epsilon$ -Fe<sub>2</sub>O<sub>3</sub> was in nano-particles morphology, and no clear measurement axis was defined. Hence the systems may not be exactly comparable either. Additionally, the dip in  $\epsilon$ -Fe<sub>2</sub>O<sub>3</sub> was characterized by a change in bond length, but the evolution of the bonds length studied by EXAFS for a GFO 1.0 powder did not show any anomaly in this temperature range [88]. Since the morphology, stoichiometry, and growth method play a crucial role in the bond lengths, we cannot however rule out yet the possibility of bond length change near 120 K in our GFO thin films.

A Raman spectroscopy study performed by Mukherjee *et al.* [89,90] suggests an abrupt change in the spin-phonon coupling strength below 180 K and a spin-glass like behaviour below 210 K, both suggesting an alteration in the spin-dynamics below 180 K. As can be observed from Fig. 3.30 (b, c) for 64 nm,  $m_L$  and  $\frac{m_L}{m_S}$  start to change significantly only below 200 K. It is possible that the change in spin dynamics below 200 K, evidenced by Mukherjee *et al.* [89,90], could influence the orbital moment  $m_L$  *via* the spin-orbit coupling. To explore this idea, we calculate the branching ratio ( $\frac{I_{L_3}}{I_{L_2}}$ ) from XAS spectra and then analyse its temperature profile. The branching ratio indeed shows the strength of the spin-orbit coupling and is calculated using Eq. 3.17 [43].

$$\frac{\langle L.S \rangle}{N_h} = \frac{I_{L_3} - (2 * I_{L_2})}{I_{L_3} + I_{L_2}} \quad (3.17)$$

where L is the orbital angular momentum, S the spin angular momentum,  $\langle L.S \rangle$  the spin-orbit coupling,  $N_h$  the number of holes ( $\approx 5$ ),  $I_{L_3}$  and  $I_{L_2}$  the areas under the Fe L<sub>3</sub> and L<sub>2</sub> edges, respectively.

The graph in 3.30 (d) plots the temperature dependence of the branching ratio, which shows a minimum at 120 K. It is improbable that this minimum at 120 K originates from a change in  $N_h$  because, the  $N_h$  values which would have to be considered for such a change need to be varied

by about 1 whole electron which is too high for  $N_h \approx 5$ . Therefore, this anomalous behaviour at 120 K must be the result of a change in spin-orbit coupling in the GFO thin film. This would indeed imply a change in the spin dynamics.

Following the measurements in 64 nm, similar temperature evolution measurements are also made for the 32, 11, and ultra-thin 7 nm GFO films, and the results of final  $\frac{m_L}{m_S}$  (since the calculation is without errors from the 'r' parameter) are presented in Fig. 3.30 (c).

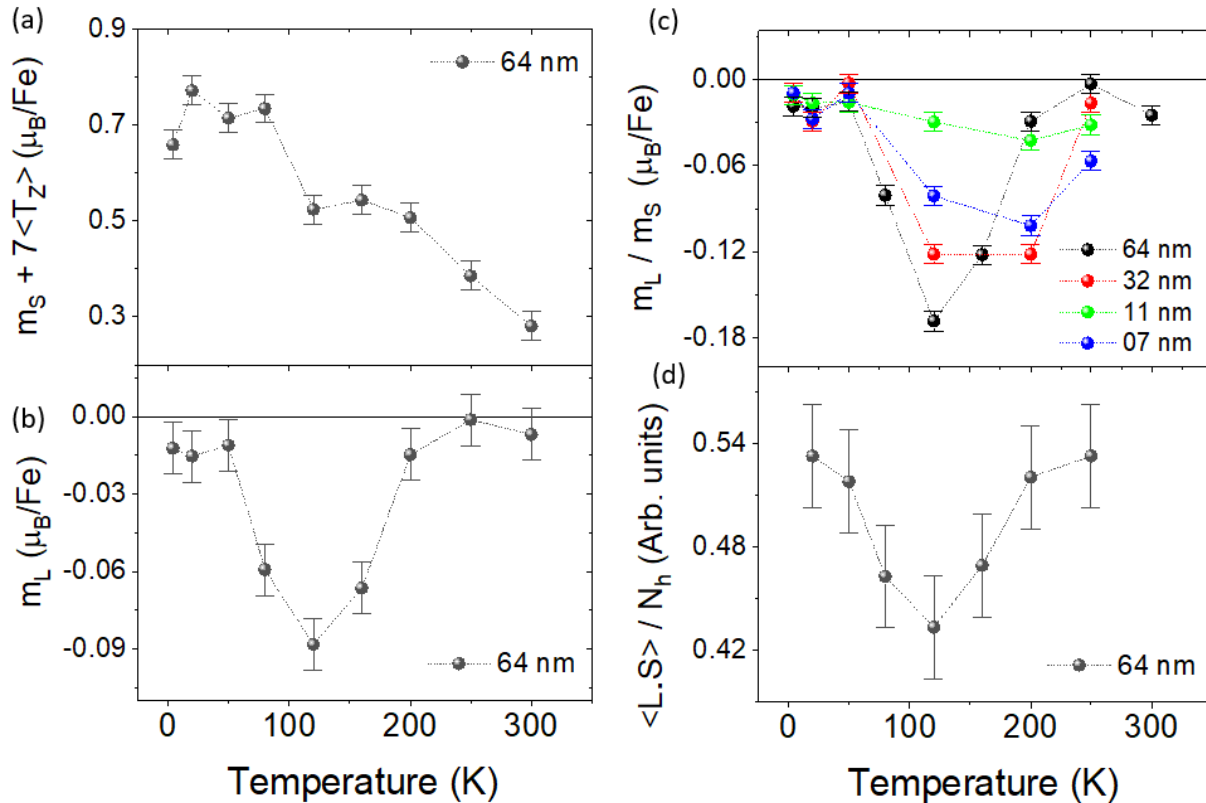


**Fig. 3.30 | Temperature evolution of experimental values extracted from XMCD using sum-rules.** (a)  $m_S$  for 64 nm. (b)  $m_L$  for 64 nm. (c)  $\frac{m_L}{m_S}$  for 64, 32, 11, and 07 nm. (d) From the area under  $L_3$  and  $L_2$  edges in the XAS curves, we calculate  $\frac{\langle L.S \rangle}{N_h}$  and plot its temperature evolution.

The temperature evolution of  $\frac{m_L}{m_S}$  is different for the different sample thicknesses. A possible shift in the temperature minimum is observed from 120 K for 64 nm to 200 K for 07 nm, but more data points are required to verify this claim. Although a clear non monotonous behaviour is observed for the 07, 32, and 64 nm thicknesses, interestingly, the 11 nm sample does not show a significant change in this temperature range. Since at 11 nm, the polarization from the first 5 nm and that from the next 5 nm face opposite each other, it can be postulated that the intrinsic

electric field for the 11 nm is less than in the samples of other thicknesses. This could signify that the intrinsic electric field can play a crucial role in the observed anomaly at 120 K.

The possible mechanism could be as follows: the presence (absence) of the electric field imposed by the electric polarization of GFO can affect the octahedral distortions by altering the O ligand field in  $\text{FeO}_6$  octahedra and changing the hybridization and charge transfer between  $\text{Fe}3d$ - $\text{O}2p$ . This modification of the hybridization alters  $m_L$  through the magneto-structural coupling yielding a way for an electric-field control of  $m_L$ . If we assume that our postulate is correct, then this means that we can control the change in spin-orbit coupling strength by the intrinsic electric field (by the movement of ions), which then hints us towards an indirect magnetoelectric effect (or magnetostrictive magnetoelectric coupling) in GFO. The calculations made by Dixit *et al.* [72] also show that a direct mechanism fails to explain the magnetoelectric effect, and therefore, it is highly probable that an indirect mechanism is the main cause of the magnetoelectric effect in GFO. Albeit, more systematic experiments are required to conclusively prove the relation between the electric field and the anomaly at 120 K, which can then bring fresh new perspectives toward possibly building future single-phase MESO devices [91].

### 3.3.4 Conclusions for magnetic properties measured using XAS / XMCD.

The XAS/XMCD measurements performed using synchrotron X-ray sources have yielded interesting new insights into GFO thin films' microscopic magnetism. We confirm the presence of a non-zero orbital moment ( $m_L$ ), as observed in bulk. We confirm the bond anisotropy which stems from distortions in  $\text{FeO}_6$  octahedra by O K-edge spectroscopy. This distortion in  $\text{FeO}_6$  octahedra leads to a charge-transfer between Fe and O, giving an apparent finite orbital moment. We observe an unusual dependence of this orbital moment on the crystallographic direction, from being parallel to the spin moment for in-plane directions (from the thin-film frame of reference) to being anti-parallel to the spin moment for out-of-plane direction. This change in  $m_L$  is attributed to the strong orbital-lattice coupling in GFO. The observation of a change in  $m_L$  with thickness further supports the hypothesis of a strong orbital-lattice and hence magneto-structural coupling, linked with the distortions in  $\text{FeO}_6$  octahedra.

The elemental hysteresis curve shows that the Ga element also possesses a magnetic moment. There is a strong resemblance between the Ga and Fe loops, due to important hybridization phenomena between the two elements within the GFO cell.

The magnetic measurements showed an abnormal change in the coercive field at 150 K for out-of-plane measurements. Microscopic XAS/XMCD measurements, which showed a non-monotonous behavior of  $m_L$  with temperature, give an explanation to this change in  $H_c$  with temperature. A minimum in  $m_L$  and the spin-orbit coupling was observed near 120 K, which signifies an extremum as well in the magneto-crystalline effect. The temperature profile of  $m_L$  for other thicknesses shows a quasi absence of anomaly for the 11 nm thickness, which could imply

that the anomaly is strongly related to the presence of an electric field within the GFO cell, and is therefore an evidence of an indirect magnetoelectric effect in GFO.

GFO is therefore an excellent playground for sophisticated fundamental physics with high implications for futuristic devices.

### 3.4 References

- (1) Design, Q. Magnetic Property Measurement System: SQUID VSM User's Manual. *San Diego: Quantum Design* **2009**.
- (2) Clarke, J. Squid Fundamentals. In *SQUID Sensors: Fundamentals, Fabrication and Applications*; Weinstock, H., Ed.; Springer Netherlands: Dordrecht, 1996; pp 1–62.
- (3) Solinas, P.; Gasparinetti, S.; Golubev, D.; Giazotto, F. A Josephson Radiation Comb Generator. *Sci Rep* **2015**, *5* (1), 12260.
- (4) Garcia, M. A.; Fernandez Pinel, E.; de la Venta, J.; Quesada, A.; Bouzas, V.; Fernández, J. F.; Romero, J. J.; Martín González, M. S.; Costa-Krämer, J. L. Sources of Experimental Errors in the Observation of Nanoscale Magnetism. *Journal of Applied Physics* **2009**, *105* (1), 013925.
- (5) Kurmoo, M.; Rehspringer, J.-L.; Hutlova, A.; D'Orléans, C.; Vilminot, S.; Estournès, C.; Niznansky, D. Formation of Nanoparticles of  $\epsilon$ -Fe<sub>2</sub>O<sub>3</sub> from Yttrium Iron Garnet in a Silica Matrix: An Unusually Hard Magnet with a Morin-Like Transition below 150 K. *Chem. Mater.* **2005**, *17* (5), 1106–1114.
- (6) Thomasson, A.; Cherifi, S.; Lefevre, C.; Roulland, F.; Gautier, B.; Albertini, D.; Meny, C.; Viart, N. Room Temperature Multiferroicity in Ga<sub>0.6</sub>Fe<sub>1.4</sub>O<sub>3</sub>:Mg Thin Films. *J Appl Phys* **2013**, *113* (21), 214101.
- (7) Quindeau, A.; Avci, C. O.; Liu, W.; Sun, C.; Mann, M.; Tang, A. S.; Onbasli, M. C.; Bono, D.; Voyles, P. M.; Xu, Y.; Robinson, J.; Beach, G. S. D.; Ross, C. A. Tm<sub>3</sub>Fe<sub>5</sub>O<sub>12</sub>/Pt Heterostructures with Perpendicular Magnetic Anisotropy for Spintronic Applications. *Advanced Electronic Materials* **2017**, *3* (1), 1600376.
- (8) Cullity, B. D.; Graham, C. D. *Introduction to Magnetic Materials*; John Wiley & Sons, **2011**.
- (9) Den Broeder, F. J. A.; Hoving, W.; Bloemen, P. J. H. Magnetic Anisotropy of Multilayers. *Journal of magnetism and magnetic materials* **1991**, *93*, 562–570.
- (10) Iwasaki, S. Perpendicular Magnetic Recording. *IEEE Transactions on Magnetics* **1980**, *16* (1), 71–76.
- (11) Johnson, M. T.; Bloemen, P. J. H.; Den Broeder, F. J. A.; De Vries, J. J. Magnetic Anisotropy in Metallic Multilayers. *Reports on Progress in Physics* **1996**, *59* (11), 1409.
- (12) Trassin, M. Low Energy Consumption Spintronics Using Multiferroic Heterostructures. *Journal of Physics: Condensed Matter* **2016**, *28* (3), 033001.
- (13) Tudu, B.; Tiwari, A. Recent Developments in Perpendicular Magnetic Anisotropy Thin Films for Data Storage Applications. *Vacuum* **2017**, *146*, 329–341.
- (14) de Lacheisserie, É. du T. *Magnétisme*; EDP sciences, 2012; Vol. 2.
- (15) Bertaut, E. F.; Bassi, G.; Buisson, G.; Chappert, J.; Delapalme, A.; Pauthenet, R.; Rebouillat, H. P.; Aleonard, R. Étude Par Effet Mössbauer, Rayons X, Diffraction Neutronique et Mesures Magnétiques de Fe<sub>1.15</sub>Ga<sub>0.85</sub>O<sub>3</sub>. *Journal de Physique* **1966**, *27* (7–8), 433–448.
- (16) Schelleng, J. H.; Rado, G. T. Direct Measurements of Anisotropy Energy and Anisotropic Magnetization in Gallium Iron Oxide. *Physical Review* **1969**, *179* (2), 541.
- (17) Dubowik, J. Shape Anisotropy of Magnetic Heterostructures. *Phys. Rev. B* **1996**, *54* (2), 1088–1091.

- (18) Victora, R. H.; Xue, J.; Patwari, M. Areal Density Limits for Perpendicular Magnetic Recording. *IEEE transactions on magnetics* **2002**, *38* (5), 1886–1891.
- (19) Krishnan, K. M.; Pakhomov, A. B.; Bao, Y.; Blomqvist, P.; Chun, Y.; Gonzales, M.; Griffin, K.; Ji, X.; Roberts, B. K. Nanomagnetism and Spin Electronics: Materials, Microstructure and Novel Properties. *J Mater Sci* **2006**, *41* (3), 793–815.
- (20) Bruno, P.; Renard, J.-P. Magnetic Surface Anisotropy of Transition Metal Ultrathin Films. *Applied Physics A* **1989**, *49* (5), 499–506.
- (21) Levine, B. F.; Nowlin, C. H.; Jones, R. V. Magnetic Properties of  $\text{Ga}_{2-x}\text{Fe}_x\text{O}_3$ . *Physical Review* **1968**, *174* (2), 571.
- (22) Castro, G. M. B.; Geshev, J.; Schmidt, J. E.; Saitovich, E. B.; Nagamine, L. C. C. M. Cone Magnetization State and Exchange Bias in  $\text{IrMn}/\text{Cu}/[\text{Co}/\text{Pt}]_3$  Multilayers. *Journal of Applied Physics* **2009**, *106* (11), 113922.
- (23) Bland, J. A. C.; Heinrich, B. *Ultrathin Magnetic Structures I: An Introduction to the Electronic, Magnetic and Structural Properties*; (Eds.); Springer Science & Business Media., **2006**; Vol. 1.
- (24) Bloemen, P. J. H.; de Jonge, W. J. M. Magnetic Anisotropy of  $\text{Co}/\text{Ni}/\text{Co}/\text{Pt}$  Multilayers. *Journal of Magnetism and Magnetic Materials* **1992**, *116* (1–2), L1–L6.
- (25) Zhao, Y.-P.; Gamache, R. M.; Wang, G.-C.; Lu, T.-M.; Palasantzas, G.; De Hosson, J. T. M. Effect of Surface Roughness on Magnetic Domain Wall Thickness, Domain Size, and Coercivity. *Journal of Applied Physics* **2001**, *89* (2), 1325–1330.
- (26) Chen, T.-Y.; Erickson, M. J.; Crowell, P. A.; Leighton, C. Surface Roughness Dominated Pinning Mechanism of Magnetic Vortices in Soft Ferromagnetic Films. *Physical Review Letters* **2012**, *109* (9), 097202.
- (27) Katayama, T.; Yasui, S.; Hamasaki, Y.; Itoh, M. Control of Crystal-Domain Orientation in Multiferroic  $\text{Ga}_{0.6}\text{Fe}_{1.4}\text{O}_3$  Epitaxial Thin Films. *Applied Physics Letters* **2017**, *110* (21), 212905.
- (28) Dweck, J. Ferromagnetic Resonance in the Highly Anisotropic Ferrimagnet Gallium Iron Oxide. *Physical Review* **1968**, *168* (2), 602.
- (29) Rusakov, V. S.; Pokatilov, V. S.; Sigov, A. S.; Matsnev, M. E.; Pyatakov, A. P. Analysis of the Magnetic Structure of the  $\text{BiFeO}_3$  Multiferroic by Mössbauer Spectroscopy. In *Doklady Physics*; Springer, **2018**; Vol. 63, pp 223–226.
- (30) Ahamed, I.; Pathak, R.; Skomski, R.; Kashyap, A. Magnetocrystalline Anisotropy of  $\epsilon\text{-Fe}_2\text{O}_3$ . *AIP Advances* **2018**, *8* (5), 055815.
- (31) Hansen, P. Anisotropy and Magnetostriction of Gallium-substituted Yttrium Iron Garnet. *Journal of Applied Physics* **1974**, *45* (8), 3638–3642.
- (32) Sears, F. W.; Zemansky, M. W.; Young, H. D. *University Physics*; Addison-Wesley, **1987**.
- (33) Atkins, P.; De Paula, J. *Elements of Physical Chemistry*; Oxford University Press, USA, **2013**.
- (34) Solomon, E. I.; Lever, A. B. P. *Inorganic Electronic Structure and Spectroscopy, Applications and Case Studies*; Wiley-Interscience, **1999**; Vol. 2.
- (35) Schütz, G.; Wagner, W.; Wilhelm, W.; Kienle, P.; Zeller, R.; Frahm, R.; Materlik, G. Absorption of Circularly Polarized x Rays in Iron. *Physical review letters* **1987**, *58* (7), 737.
- (36) Stöhr, J. Exploring the Microscopic Origin of Magnetic Anisotropies with X-Ray Magnetic Circular Dichroism (XMCD) Spectroscopy. *Journal of Magnetism and Magnetic Materials* **1999**, *200* (1–3), 470–497.

- (37) Beaurepaire, E.; Bulou, H.; Joly, L.; Scheurer, F. Magnetism and Synchrotron Radiation: Towards the Fourth Generation Light Sources. *Springer* **2013**, *26*, 44.
- (38) Stöhr, J.; Baberschke, K.; Jaeger, R.; Treichler, R.; Brennan, S. Orientation of Chemisorbed Molecules from Surface-Absorption Fine-Structure Measurements: CO and NO on Ni (100). *Physical Review Letters* **1981**, *47* (5), 381.
- (39) van der Laan, G.; Thole, B. T.; Sawatzky, G. A.; Goedkoop, J. B.; Fuggle, J. C.; Esteva, J.-M.; Karnatak, R.; Remeika, J. P.; Dabkowska, H. A. Experimental Proof of Magnetic X-Ray Dichroism. *Physical Review B* **1986**, *34* (9), 6529.
- (40) Goulon, J.; Goulon-Ginet, C.; Rogalev, A.; Gotte, V.; Malgrange, C.; Brouder, C.; Natoli, C. R. X-Ray Natural Circular Dichroism in a Uniaxial Gyrotropic Single Crystal of LiIO<sub>3</sub>. *The Journal of chemical physics* **1998**, *108* (15), 6394–6403.
- (41) de Groot, F. M.; Hu, Z. W.; López, M. F.; Kaindl, G.; Guillot, F.; Tronc, M. Differences between L<sub>3</sub> and L<sub>2</sub> X-ray Absorption Spectra of Transition Metal Compounds. *The Journal of chemical physics* **1994**, *101* (8), 6570–6576.
- (42) De Groot, F. M. F. X-Ray Absorption and Dichroism of Transition Metals and Their Compounds. *Journal of Electron Spectroscopy and Related Phenomena* **1994**, *67* (4), 529–622.
- (43) Thole, B. T.; Van der Laan, G. Branching Ratio in X-Ray Absorption Spectroscopy. *Physical Review B* **1988**, *38* (5), 3158.
- (44) Van der Laan, G.; Thole, B. T. Local Probe for Spin-Orbit Interaction. *Physical review letters* **1988**, *60* (19), 1977.
- (45) Haverkort, M. W. Spin and Orbital Degrees of Freedom in Transition Metal Oxides and Oxide Thin Films Studied by Soft X-Ray Absorption Spectroscopy. *arXiv preprint cond-mat/0505214* **2005**.
- (46) Thole, B. T.; Van Der Laan, G.; Butler, P. H. Spin-Mixed Ground State of Fe Phthalocyanine and the Temperature-Dependent Branching Ratio in X-Ray Absorption Spectroscopy. *Chemical physics letters* **1988**, *149* (3), 295–299.
- (47) de Groot, F. M.; Fuggle, J. C.; Thole, B. T.; Sawatzky, G. A. 2p X-Ray Absorption of 3d Transition-Metal Compounds: An Atomic Multiplet Description Including the Crystal Field. *Physical Review B* **1990**, *42* (9), 5459.
- (48) Thole, B. T.; Carra, P.; Sette, F.; van der Laan, G. X-Ray Circular Dichroism as a Probe of Orbital Magnetization. *Physical review letters* **1992**, *68* (12), 1943.
- (49) Carra, P.; Thole, B. T.; Altarelli, M.; Wang, X. X-Ray Circular Dichroism and Local Magnetic Fields. *Physical Review Letters* **1993**, *70* (5), 694.
- (50) Kanamori, J. Anisotropy and Magnetostriction of Ferromagnetic and Antiferromagnetic Materials. In *Magnetism*; Elsevier, 1963; pp 127–203.
- (51) Stöhr, J.; König, H. Determination of Spin-and Orbital-Moment Anisotropies in Transition Metals by Angle-Dependent X-Ray Magnetic Circular Dichroism. *Physical review letters* **1995**, *75* (20), 3748.
- (52) van der Laan, G. Microscopic Origin of Magnetocrystalline Anisotropy in Transition Metal Thin Films. *Journal of Physics: Condensed Matter* **1998**, *10* (14), 3239.
- (53) Chen, C. T.; Idzerda, Y. U.; Lin, H.-J.; Smith, N. V.; Meigs, G.; Chaban, E.; Ho, G. H.; Pellegrin, E.; Sette, F. Experimental Confirmation of the X-Ray Magnetic Circular Dichroism Sum Rules for Iron and Cobalt. *Physical review letters* **1995**, *75* (1), 152.

- (54) Tutorial. Tutorial and lecture series in “International school on Synchrotron and Magnetism” Mittlewahr, Alsace, France. <http://mw2018.u-strasbg.fr/>.
- (55) Chen, Y.-C. XMCD Investigations on New Hard Magnetic Systems. **2018**.
- (56) Abbate, M.; Goedkoop, J. B.; De Groot, F. M. F.; Grioni, M.; Fuggle, J. C.; Hofmann, S.; Petersen, H.; Sacchi, M. Probing Depth of Soft X-ray Absorption Spectroscopy Measured in Total-electron-yield Mode. *Surface and Interface Analysis* **1992**, *18* (1), 65–69.
- (57) Lin, F.; Nordlund, D.; Markus, I. M.; Weng, T.-C.; Xin, H. L.; Doeff, M. M. Profiling the Nanoscale Gradient in Stoichiometric Layered Cathode Particles for Lithium-Ion Batteries. *Energy & Environmental Science* **2014**, *7* (9), 3077–3085.
- (58) Kim, J.-Y.; Koo, T. Y.; Park, J.-H. Orbital and Bonding Anisotropy in a Half-Filled GaFeO<sub>3</sub> Magnetoelectric Ferrimagnet. *Phys. Rev. Lett.* **2006**, *96* (4), 047205.
- (59) Crocombette, J. P.; Pollak, M.; Jollet, F.; Thromat, N.; Gautier-Soyer, M. X-Ray-Absorption Spectroscopy at the Fe L 2, 3 Threshold in Iron Oxides. *Physical Review B* **1995**, *52* (5), 3143.
- (60) Goering, E.; Fuss, A.; Weber, W.; Will, J.; Schütz, G. Element Specific X-Ray Magnetic Circular Dichroism Magnetization Curves Using Total Electron Yield. *Journal of Applied Physics* **2000**, *88* (10), 5920–5923.
- (61) Nakajima, R.; Stöhr, J.; Idzerda, Y. U. Electron-Yield Saturation Effects in L-Edge X-ray Magnetic Circular Dichroism Spectra of Fe, Co, and Ni. *Phys. Rev. B* **1999**, *59* (9), 6421–6429.
- (62) Huang, D. J.; Chang, C. F.; Chen, J.; Lin, H.-J.; Chung, S. C.; Jeng, H.-T.; Guo, G. Y.; Wu, W. B.; Shyu, S. G.; Chen, C. T. Orbital Moments of CrO<sub>2</sub> and Fe<sub>3</sub>O<sub>4</sub> Studied by MCD in Soft X-Ray Absorption. *Journal of electron spectroscopy and related phenomena* **2004**, *137*, 633–639.
- (63) Thole, B. T.; Van der Laan, G.; Fuggle, J. C.; Sawatzky, G. A.; Karnatak, R. C.; Esteva, J.-M. 3d X-Ray-Absorption Lines and the 3d<sub>9</sub> 4f<sub>N+1</sub> Multiplets of the Lanthanides. *Physical Review B* **1985**, *32* (8), 5107.
- (64) Gota, S.; Gautier-Soyer, M.; Sacchi, M. Fe 2p Absorption in Magnetic Oxides: Quantifying Angular-Dependent Saturation Effects. *Phys. Rev. B* **2000**, *62* (7), 4187–4190.
- (65) Xu, Y.; Awschalom, D.; Nitta, J. *Handbook of Spintronics*; Springer Netherlands, **2016**.
- (66) Khomskii, D. *Transition Metal Compounds*; Cambridge University Press, **2014**.
- (67) You, L.; Zheng, F.; Fang, L.; Zhou, Y.; Tan, L. Z.; Zhang, Z.; Ma, G.; Schmidt, D.; Rusydi, A.; Wang, L. Enhancing Ferroelectric Photovoltaic Effect by Polar Order Engineering. *Science advances* **2018**, *4* (7), eaat3438.
- (68) De Groot, F. M. F.; Grioni, M.; Fuggle, J. C.; Ghijsen, J.; Sawatzky, G. A.; Petersen, H. Oxygen 1s X-Ray-Absorption Edges of Transition-Metal Oxides. *Physical Review B* **1989**, *40* (8), 5715.
- (69) Han, M. J.; Ozaki, T.; Yu, J. Magnetic Ordering and Exchange Interactions in Multiferroic Ga FeO<sub>3</sub>. *Physical Review B* **2007**, *75* (6), 060404.
- (70) Roy, A.; Prasad, R.; Auluck, S.; Garg, A. Effect of Site-Disorder on Magnetism and Magneto-Structural Coupling in Gallium Ferrite: A First-Principles Study. *Journal of Applied Physics* **2012**, *111* (4), 043915.
- (71) Ibrahim, F.; Alouani, M. Impact of Excess Iron on the Calculated Electronic and Magnetic Properties of Gallium Ferrite. *Physical Review B* **2012**, *85* (17), 174411.
- (72) Dixit, A.; Stoeffler, D.; Alouani, M. Effect of Site Disorder on the Electronic, Magnetic, and Ferroelectric Properties of Gallium Ferrite. *Physical Review Materials* **2020**, *4* (7), 074406.

- (73) Preziosi, D.; Homkar, S.; Lefevre, C.; Salluzzo, M.; Viart, N. Unusual directional dependent magnetic orbital moment obtained from X-ray magnetic circular dichroism in an oxide multiferroic system. Submitted to *Physical Review B* (2020).
- (74) Zhong, G.; Bitla, Y.; Wang, J.; Zhong, X.; An, F.; Chin, Y.-Y.; Zhang, Y.; Gao, W.; Zhang, Y.; Eshghinejad, A.; Esfahani, E. N.; Zhu, Q.; Tan, C.; Meng, X.; Lin, H.-J.; Pan, X.; Xie, S.; Chu, Y.-H.; Li, J. Tuning Fe Concentration in Epitaxial Gallium Ferrite Thin Films for Room Temperature Multiferroic Properties. *Acta Materialia* **2018**, *145*, 488–495.
- (75) Katayama, T.; Yasui, S.; Hamasaki, Y.; Shiraishi, T.; Akama, A.; Kiguchi, T.; Itoh, M. Ferroelectric and Magnetic Properties in Room-Temperature Multiferroic  $\text{Ga}_x\text{Fe}_{2-x}\text{O}_3$  Epitaxial Thin Films. *Advanced Functional Materials* **2018**, *28* (2), 1704789.
- (76) Tseng, Y.-C.; Souza-Neto, N. M.; Haskel, D.; Gich, M.; Frontera, C.; Roig, A.; van Veenendaal, M.; Nogués, J. Nonzero Orbital Moment in High Coercivity  $\epsilon$ - $\text{Fe}_2\text{O}_3$  and Low-Temperature Collapse of the Magnetocrystalline Anisotropy. *Phys. Rev. B* **2009**, *79* (9), 094404.
- (77) Tuček, J.; Zbořil, R.; Namai, A.; Ohkoshi, S.  $\epsilon$ - $\text{Fe}_2\text{O}_3$ : An Advanced Nanomaterial Exhibiting Giant Coercive Field, Millimeter-Wave Ferromagnetic Resonance, and Magnetoelectric Coupling. *Chem. Mater.* **2010**, *22* (24), 6483–6505.
- (78) Chen, L.; Xu, C.; Tian, H.; Xiang, H.; Íñiguez, J.; Yang, Y.; Bellaiche, L. Electric-Field Control of Magnetization, Jahn-Teller Distortion, and Orbital Ordering in Ferroelectric Ferromagnets. *Physical Review Letters* **2019**, *122* (24), 247701.
- (79) Tazaki, R.; Fu, D.; Itoh, M.; Daimon, M.; Koshihara, S. Lattice Distortion under an Electric Field in  $\text{BaTiO}_3$  Piezoelectric Single Crystal. *Journal of Physics: Condensed Matter* **2009**, *21* (21), 215903.
- (80) Schütz, G.; Fischer, P.; Attenkofer, K.; Knülle, M.; Ahlers, D.; Stähler, S.; Detlefs, C.; Ebert, H.; de Groot, F. M. F. X-ray Magnetic Circular Dichroism in the near and Extended Absorption Edge Structure. *Journal of Applied Physics* **1994**, *76* (10), 6453–6458.
- (81) Goering, E.; Gold, S.; Lafkioti, M.; Schütz, G. Vanishing Fe 3d Orbital Moments in Single-Crystalline Magnetite. *EPL* **2005**, *73* (1), 97.
- (82) Abbate, M.; Pen, H.; Czyżyk, M. T.; De Groot, F. M. F.; Fuggle, J. C.; Ma, Y. J.; Chen, C. T.; Sette, F.; Fujimori, A.; Ueda, Y. Soft X-Ray Absorption Spectroscopy of Vanadium Oxides. *Journal of electron spectroscopy and related phenomena* **1993**, *62* (1–2), 185–195.
- (83) Arima, T.; Higashiyama, D.; Kaneko, Y.; He, J. P.; Goto, T.; Miyasaka, S.; Kimura, T.; Oikawa, K.; Kamiyama, T.; Kumai, R. Structural and Magnetoelectric Properties of  $\text{Ga}_{2-x}\text{Fe}_x\text{O}_3$  Single Crystals Grown by a Floating-Zone Method. *Physical Review B* **2004**, *70* (6), 064426.
- (84) Wu, R.; Wang, D.; Freeman, A. J. First Principles Investigation of the Validity and Range of Applicability of the X-Ray Magnetic Circular Dichroism Sum Rule. *Physical review letters* **1993**, *71* (21), 3581.
- (85) Tachiyama, K.; Yasui, S.; Rao, B. N. A.; Dazai, T.; Usami, T.; Taniyama, T.; Katayama, T.; Hamasaki, Y.; Yu, J.; He, H. Magnetic Properties of Single Crystal  $\text{GaFeO}_3$ . *MRS Advances* **2019**, *4* (1), 61–66.
- (86) Trassin, M.; Viart, N.; Versini, G.; Barre, S.; Pourroy, G.; Lee, J.; Jo, W.; Dumesnil, K.; Dufour, C.; Robert, S. Room Temperature Ferrimagnetic Thin Films of the Magnetoelectric  $\text{Ga}_{2-x}\text{Fe}_x\text{O}_3$ . *J. Mater. Chem.* **2009**, *19* (46), 8876–8880.

- (87) Tucek, J.; Zboril, R.; Namai, A.; Ohkoshi, S.  $\epsilon$ -Fe<sub>2</sub>O<sub>3</sub>: An Advanced Nanomaterial Exhibiting Giant Coercive Field, Millimeter-Wave Ferromagnetic Resonance, and Magnetoelectric Coupling. *Chemistry of Materials* **2010**, *22* (24), 6483–6505.
- (88) Basu, S.; Singh, R.; Das, A.; Roy, T.; Chakrabarti, A.; Nigam, A. K.; Jha, S. N.; Bhattacharyya, D. Temperature Dependent EXAFS Study of Chromium-Doped GaFeO<sub>3</sub> at Gallium and Iron Edges. *The Journal of Physical Chemistry C* **2015**, *119* (4), 2029–2037.
- (89) Mukherjee, S.; Garg, A.; Gupta, R. Spin Glass-like Phase below ~210 K in Magnetoelectric Gallium Ferrite. *Applied Physics Letters* **2012**, *100* (11), 112904.
- (90) Mukherjee, S.; Garg, A.; Gupta, R. Probing Magnetoelastic Coupling and Structural Changes in Magnetoelectric Gallium Ferrite. *Journal of Physics: Condensed Matter* **2011**, *23* (44), 445403.
- (91) Manipatruni, S.; Nikonov, D. E.; Lin, C.-C.; Gosavi, T. A.; Liu, H.; Prasad, B.; Huang, Y.-L.; Bonturim, E.; Ramesh, R.; Young, I. A. Scalable Energy-Efficient Magnetoelectric Spin–Orbit Logic. *Nature* **2018**.



---

# Chapter 4

## Ga<sub>0.6</sub>Fe<sub>1.4</sub>O<sub>3</sub> thin films :

### Investigation of the electrical polarization

---

The behavior of the electrical polarization of GFO thin films is difficult to tackle because of important leakage currents, especially at ultra-thin scales. The non-centrosymmetric character of the material, origin of the polarization, can be characterized using an optical probe such as second harmonic generation. Therefore, in this chapter, we will present our investigation of the electric polarization of GFO in thin/ultra-thin films, using *ex situ* and state-of-the-art *in situ* optical characterization techniques that probe the ferroic state due to symmetry breaking. We will also unveil some never-addressed symmetry issues in the GFO crystalline cell, thanks to a monitoring from the very first deposited unit cells at ultra-thin regimes.

## 4.1 Introduction to the second harmonic generation (SHG) technique

The electrical characterization techniques used to probe the polarization of ferroelectric (FE) oxides in thin films have to face critical points such as leakage currents or electrode-ferroelectric interface issues (Schottky barrier, screening length, etc...). The non-linear optical probing technique based on laser-induced optical second harmonic generation (SHG) is an interesting alternative tool to address the characterization of the electrical polarization, even in leaky FE oxide thin films <sup>[1]</sup>.

Reviews on the physics of SHG and on its potential as a technique to probe the spontaneous electric polarization and access to polar domain states can be found in the literature <sup>[1-4]</sup>. I will only briefly recall the main aspects of the technique here below.

Non-centrosymmetric materials can generate non-linear effects such as second or higher harmonic generation, apart from the conventional linear optical effects. Ferroelectric materials are such non-centrosymmetric materials. Their polarization  $P$  will interact with a light of frequency  $\omega$  through the alternating electric field  $E(\omega)$  to give a frequency dependent polarization  $P(\omega)$ . The expression of  $P(\omega)$  with  $E(\omega)$  and other higher powers of  $E(\omega)$  of the light wave is given in Eq. 4.1 <sup>[1]</sup> :

$$P(\omega) = P_0 + \varepsilon_0 \chi E(\omega) + \chi^{(2)} E(\omega)^2 + \chi^{(3)} E(\omega)^3 + \dots \quad (4.1)$$

where  $P(\omega)$  and  $E(\omega)$  are the polarization and electric-field, respectively, for a light frequency  $\omega$ ,  $P_0$  is a constant polarization independent of time,  $\varepsilon_0$  is the vacuum permittivity, and  $\chi^{(n)}$  are  $n^{\text{th}}$  order tensors. The material structure determines the number and nature of the allowed tensor components <sup>[5]</sup>.

SHG will result in the generation of a light having a frequency  $2\omega$ , double of the incident light frequency, as depicted in Fig 4.1 (a). This  $2\omega$  light frequency interacts with the polarization  $P$  to give the SHG only contribution  $P(2\omega)$  which is described by Eq. 4.2:

$$P_i(2\omega) = \varepsilon_0 \sum_{j,k} \chi^{(2)}_{ijk} E_j(\omega) E_k(\omega) \quad (4.2)$$

where the  $ijk$  notations specify the  $xyz$  crystallographic axes, and  $\chi^{(2)}_{ijk}$  is a tensor component of the second-order tensor  $\chi^{(2)}$  which characterizes the ferroelectric state.

The intensity of the double-frequency light emitted from the induced polarization  $P(2\omega)$  is given by Eq. 4.3:

$$I_{SHG} \propto |P(2\omega)|^2 \propto |\chi^{(2)} t_{Film}|^2 \propto |P_s \cdot t_{Film}|^2 \quad (4.3)$$

Where  $P_s$  is the spontaneous polarization and  $t_{film}$  the thickness of the film.

The SHG intensity is thus proportional to  $\chi^{(2)}$  which is determined by the material symmetry [2]. This makes SHG a direct probe to access the point group symmetry of the material. Owing to its non-invasive, non-destructive, and symmetry sensitive nature, it is regarded as an optimal tool to access information about polar states in materials in their various forms. SHG can be operated in a laboratory environment; it does not necessitate any time-consuming and destructive sample preparation; it is contact-free and does not suffer from any electrical leakage or mechanical vibration issues; it faces no diffraction resolution challenges. It thus has important advantages over the other conventional polarization probes such as I-V loops, scanning piezoelectric probe, high-resolution microscopy, or any other synchrotron X-ray probes. In particular, the use of SHG is relevant in the field of thin/ultra-thin materials where the large leakage currents render the electrical characterization of polar state impractical. Currently, oxide thin/ultrathin films are the subjects of intense SHG investigation. Some oxide films, which have coupled multiferroic properties, are technologically promising for increased data density storage [6] and their integration into a combination of polarization-based spintronics devices with enhanced power efficiency has recently been realized [7,8]. The determination of the polarization dynamics using SHG in these multiferroic thin/ultra-thin oxide films is therefore of great fundamental and technological importance [1-4,9-12]. Fundamentally, accessing these states at reduced dimensionality may lead to interesting new physics of novel states in multiferroics.

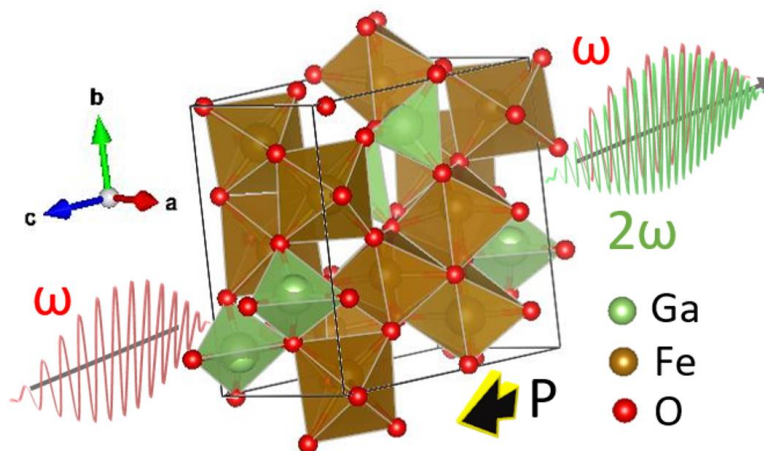


**Fig 4.1 | Schematic of SHG frequency doubling from a  $\text{Ga}_{0.6}\text{Fe}_{1.4}\text{O}_3$  unit cell with polarization  $P$  along the  $c$  axis ( $Pna2_1$ ) and the light passing through the unit cell along the  $c$  axis.**

SHG studies in the thin/ultra-thin regimes allow getting insight into the polar state evolution of the material with thickness, permit access to buried interfacial states in heterostructures, to the mapping of ferroic domains, and to the effect of epitaxial strain between the film and the substrate. This is possible since surfaces and interfaces also break the inversion symmetry and

contribute to the SHG signal. The symmetry sensitive nature of SHG therefore allows mapping surface, interface, and bulk symmetries in films and heterostructures. Some particularly interesting points include the diagnostics of symmetries at sub-unit cell growth, or of the modifications in the depolarizing field in ultra-thin films, and the effect of charge screening environment on domain formation in thin films<sup>[2-4,9-12]</sup>. Once the surface-related phenomena excluded, the remaining SHG signal is a positive indicator of the existence of a net polarization in the film.

The polarization in the films induces bound surface charges on both opposite sides of the films (Fig 4.2, for GFO on STO substrate) giving rise to the depolarizing field effect. This effect creates an intrinsic effective field ( $E_d$ ) opposite to the polarization ( $P$ ). Since this field varies with the thickness of the film, the emergence of  $P$  is thickness dependent, with the existence of a critical thickness below which the polar state is quenched<sup>[2,13,14]</sup>. The role of the bound charges and depolarizing effects has been evidenced by SHG studies in many thin-film systems, notably in BiFeO<sub>3</sub> (BFO)<sup>[9,15]</sup>, BaTiO<sub>3</sub> (BTO)<sup>[15,16]</sup>, PbTiO<sub>3</sub> (PTO)<sup>[17,18]</sup> and PbZr<sub>0.2</sub>Ti<sub>0.8</sub>O<sub>3</sub> (PZT)<sup>[14]</sup>. The depolarizing field is prominent in the ultra-thin regime<sup>[2]</sup>, and is also greatly influenced by the surrounding environment. The existence of gas pressure on top of the film, the presence or absence of an electrode, and the interface chemistry determines the efficiency of the charge screening and the extent of the depolarization field effect<sup>[19-22]</sup>. Usually, as a consequence of the depolarizing field, the ferroelectric polarization in thin films breaks down into domains to minimize energy, resulting in a net-zero polarization<sup>[23]</sup>. This is what has been observed for the thin films of BFO, BTO, PTO, and PZT mentioned above when they are grown in an environment devoid of charge screening (over an insulating layer, over an insulating substrate, or even over a metal if there is an insulating dead-layer in between). In such a case, there will be no SHG obtained during the growth for such samples even if the growth temperature is below the transition temperature<sup>[2,15]</sup>. It is possible to observe an SHG signal only in the case of a single domain or a net effective polarization.

While polar domains have become much sought-after in the recent decade with the domain wall nanoelectronics<sup>[24]</sup>, a robust single domain polar state is still desired to ease the control of the switching dynamics and is essential for many capacitors and ferroelectric applications like ferroelectric field-effect transistors or ferroelectric tunnel junctions<sup>[25,26]</sup>. To stabilize a single polar state, it is necessary to eliminate the domain formation by mitigating the depolarizing electric field. This can be done by sandwiching the ferroelectric material between two conducting electrodes or in a combination of an electrode and charge screening environment. An electrode provides a charge screening for the bound charges since the moving charges in the electrodes generate a counter electric field ( $-E_d$ ) that minimizes the depolarizing electric field (Fig. 4.2). This allows the stabilization of a single polar state, as it has been shown in BTO, BFO, PTO, and PZT<sup>[14,16,26,27]</sup> with the insertion of SRO as a metal electrode.

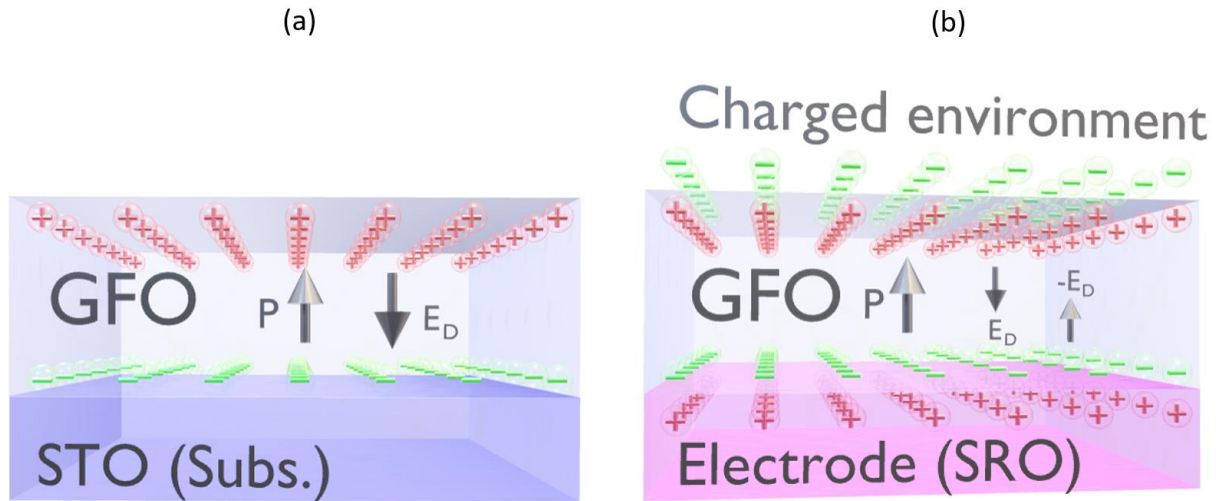


**Fig 4.2 | Schematic of polarization related effects in epitaxial thin films (such as GFO).** (a) The depolarizing field ( $E_d$ ) which counters the polarization ( $P$ ) and (b) is countered itself through charge screening, to stabilize a single domain polar state.

## 4.2 Our SHG investigation

In this section, we will report on the investigation of SHG related effects in  $\text{Ga}_{0.6}\text{Fe}_{1.4}\text{O}_3$  (GFO) thin films, which has been performed in collaboration with ETH, Zürich. Some SHG studies were already reported in the literature for GFO in its bulk form [28–33], but very little was done on thin films [34,35], and nothing at ultra-thin scales. This study presents a comprehensive SHG study of GFO films with a focus on ultra-thin scales using both *ex situ* and *in situ* methodologies, which are complementary to each other and have their own separate advantages. In the *ex situ* method, the GFO films are grown in a PLD chamber (IPCMS, Strasbourg) and taken out of the chamber to be measured in an SHG set-up (ETH, Zürich) in a transmission geometry. The *in situ* method is a state-of-the-art technique where the SHG signal is observed during the growth of the sample, in reflection geometry (ETH, Zürich). It gives knowledge of the polarization state during the growth (usually performed at high temperatures) as well as after the growth, during the cooling down, allowing us to obtain the polarization Curie temperature ( $T_c$ ) by extrapolation. Both the *ex situ* and *in situ* methods are explained in detail in the sections below.

### 4.2.1 *Ex situ* SHG measurements.

The *ex situ* SHG set-up which has been used for this work (Fig. 4.3) is the one of the laboratory for Multifunctional Ferroic Materials of ETH-Zürich. It has been extensively described in Ref. [2,3], in which all experimental details concerning the set-up can be found. I will recall some of its main features here below, as well as how it has been used for the study of our samples which are GFO thin films.

The incident radiation consists in 1200 nm light pulses emitted from an amplified Ti: Sapphire (Ti: Sa) system at a 1 kHz frequency with an optical parametric amplifier. The light pulses have a photon energy of 1.03 eV, a pulse length of 40 fs, and a pulse energy of 20  $\mu\text{J}$ . Light is sent onto the sample (the back of the STO (111) substrate onto which the GFO thin film is grown is polished to allow measurement in transmission mode) at a chosen tilt angle  $\theta$  ( $\theta = -30^\circ$  to  $+30^\circ$  with  $\theta = 0^\circ$  being when the light is parallel to the sample normal). The light polarization is selected via a polarizer. A low pass filter only allows  $E(\omega)$ , with  $\omega$  equal to 1200 nm, to reach the sample. After the sample, a bandpass filter filters away the 1200 nm primary wavelength and only lets the SHG generated wavelength of 600 nm through. The primary pulse is many times brighter than the SHG signal and the role of the bandpass filter is to cut the primary pulse to protect the sensitive detection system. An analyzer is then set to select one polarized component of  $E(2\omega)$ . To probe the symmetry of the emitted light and compare it with the expectations from point group consideration, we perform measurements with various polarizer/analyzer configurations. We have performed SHG anisotropy measurements by setting a parallel arrangement of both the

polarizer and analyzer, and simultaneously rotating them over 360°. The 0° corresponds to the vertical laboratory axis, whereas 90° corresponds to the horizontal laboratory axis. Different phase shifts between analyzer and polarizer allow accessibility to the various tensor components of  $\chi_{ijk}$ .

For an incident wave vector traveling in the  $\hat{z}$  direction, the resulting SHG generated from the sample is sensitive to any polar distortion in the plane perpendicular to  $\hat{z}$ . Since the sample surface breaks inversion symmetry in the out of plane direction  $\hat{z}$ , it yields an SHG signal. This surface SHG signal can in some cases be even stronger than the SHG signal originating from polarization. It is possible to tune the surface and polarization contributions by tilting the sample. In the case of GFO, we expect an out-of-plane polarization which will be probed only if the light has a tilt to the sample normal direction.

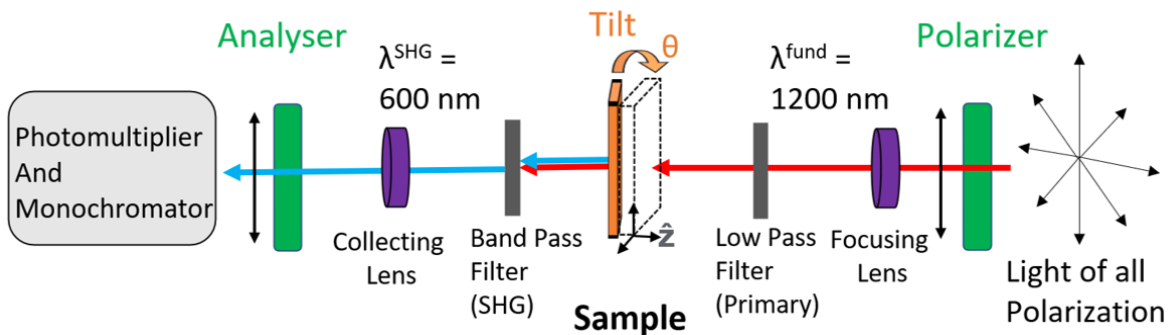


**Fig. 4.3 | Experimental set-up for *ex situ* optical second-harmonic generation in transmission geometry [Laboratory for Multifunctional Ferroic Materials, ETH-Zürich].** A fundamental wavelength of 1200 nm was used for the SHG characterization of the polarization state of the GFO thin films. The direction of the light polarization of the incident beam was set by the Polarizer (rotatable  $\lambda/2$ -wave plate) and the detected SHG light-polarization is selected by the Analyser (rotatable Glan-Taylor prism), where the vertical direction corresponds to 0° and the horizontal direction to 90°. The sample was tilted along the horizontal axis to access the out-of-plane component of the spontaneous polarization of the GFO thin films. The SHG signal at 600 nm was finally measured using a monochromator and photomultiplier system.

We studied GFO thin films of various thicknesses (between 7 and 32 nm) grown onto STO(111) substrates. To assess the polar state of the film, we tilt the sample from  $\theta = +30$  to  $-30^\circ$  relative to the surface normal. The dependence of the SHG signal on the incident and detected light polarization (same for both) for different tilts is shown in Fig. 4.4 for a STO substrate alone, and Fig. in 4.5 for a 32 nm GFO film deposited onto a STO substrate. A first observation is that there is no considerable difference between the intensity and lobe symmetry of the SHG signals

observed for the reference double side polished STO substrate (Fig 4.4) and for the GFO film sample at  $0^\circ$  tilt (Fig 4.5 (a)). This is expected for an out-of-plane (OOP) polarization of GFO, for which the SHG contribution will be zero at  $0^\circ$  tilt. The 6 lobes observed at  $0^\circ$  tilt for both samples are SHG signals related to the STO(111) substrate only and are due to its surface contribution of surface symmetry  $3m$  [36]. The surface contribution from STO (111) is lower for analyzer/polarizer positions equal to 10/10, 70/70, 130/130, 190/190, 250/250, and 310/310. We can expect this surface contribution to interfere with the polar GFO SHG signal in some configurations. This information will be useful when we will consider separating the total SHG signal due to STO//GFO from the contribution only due to the GFO polarization, by choosing these points mentioned above, where the STO contribution is low.

Now, let us consider the effect of the tilt on the SHG signal. Here we take the STO//GFO (32 nm) thin-film system and tilt it from  $\theta = -30^\circ$  to  $+30^\circ$  in increments of  $10^\circ$  to obtain the SHG signal evolution shown in Fig 4.5. It is apparent that the signal intensity increases and that its symmetry is modified as we tilt the sample. As we tilt it towards  $-30^\circ$  we see a stronger signal appearing along two symmetrical lobes and as we tilt towards  $+30^\circ$  we see a stronger signal along 4 symmetrical lobes. To investigate the reasons behind this, let us analyze the effect of the tilt on the double side polished STO(111) substrate (without any GFO film). Fig. 4.4 shows that the  $\pm 30^\circ$  tilt still retains the 6-lobe symmetry of the STO(111) substrate surface. However, if the SHG signal is practically the same for  $0^\circ$  and  $+30^\circ$  tilt, the  $-30^\circ$  tilt presents a small change in the intensity of two of the lobes. This could be explained either by some non-homogeneities in the STO crystal or by the possible presence of a small polar entity in STO, due to oxygen vacancies [36] or to localized distortions at an atomic level [37] (its existence in bulk STO is highly debated by the community). Still, even with this, the STO substrate SHG alone cannot explain the observations of Fig 4.5. This leaves us with the polar properties of the GFO film or the interface between GFO and STO. If the interface between GFO and STO was the sole reason for the SHG signal, the effect should have been the same on both the  $+30^\circ$  and  $-30^\circ$  tilt, which is not the case. Additionally, it also cannot single-handedly explain the increase in the SHG signal. The only probable hypothesis to explain the observations of Fig 4.5 is ascribed to the  $x$ - $y$  component of the GFO non-centrosymmetric unit cell polarization. Since the  $x$ - $y$  component increases at a higher tilt, it also explains why the signal increases with the tilt.

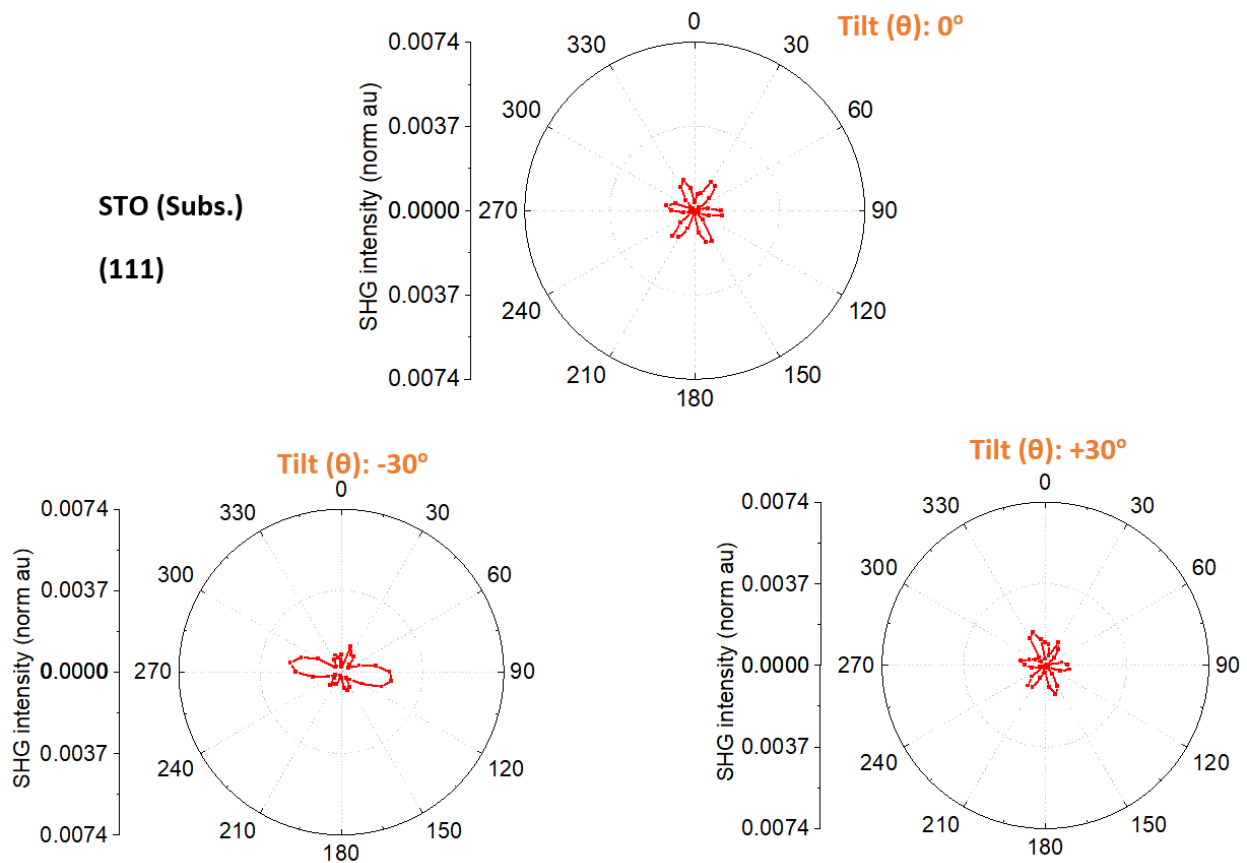


**Fig. 4.4 |** The SHG signal measured with analyzer and polarizer parallel to each other for double-side polished STO(111) substrate. The measurement is made at a tilt of 0°, -30°, and +30°.

This observation of an SHG signal indicating a non-zero polarization of GFO films grown on insulating STO substrate is surprising. The films was rather expected to show an overall zero polarization because of the action of the depolarizing field in such an insulating environment. This non-zero net polarization may be explained by the high activation energy required for the GFO polarization to switch, resulting in an unusually high coercive field of  $1400 \text{ kV.cm}^{-1}$  [38]. Such high activation energy can impede the formation of up-down polarization domains, hence allowing the possibility of a net polarization.

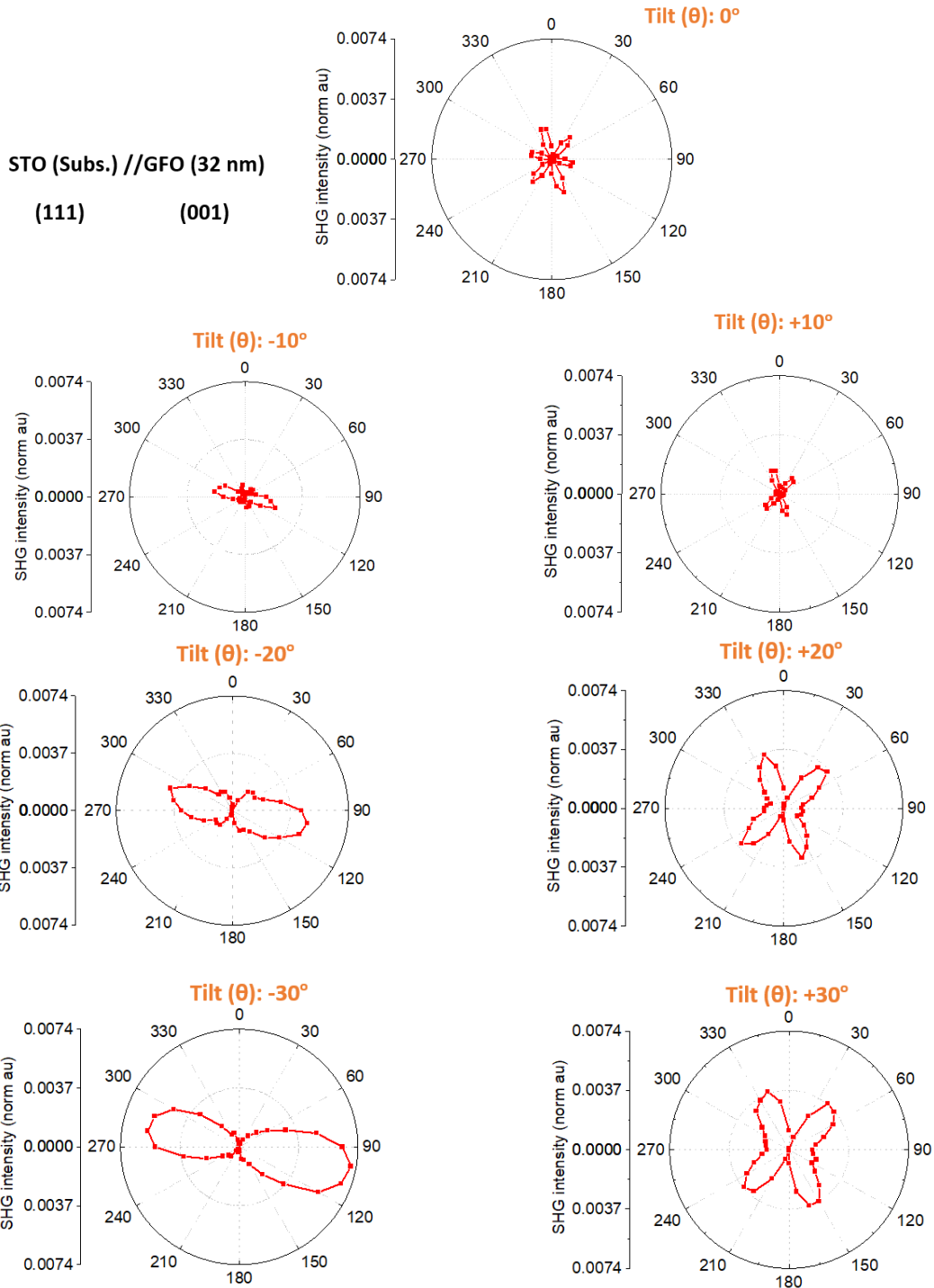


**Fig 4.5 | The SHG signal measured for STO//GFO(32 nm) between -30° and +30° tilts with the analyzer and polarizer parallel to each other. The plotted signal is the normalized SHG signal, which is the raw data normalized according to  $SHG(Norm) = \frac{[SHG(raw)+0.002]}{(ref. signal)^2}$ . The normalization allows us to minimize the effects of noise in the measured signal and fluctuation in the reference signal. The scales are kept uniform in all plots for easy comparison.**

The allowed SHG components of bulk GFO related to its polarization are set by its orthorhombic  $mm2$  point group, with five independent elements of symmetry rank 3 tensors <sup>[39]</sup>. However, in the case of our thin films, due to the averaging over the three in-plane  $120^\circ$ -rotated crystallographic variants (see Ch. 2), the effective point-group symmetry increases to  $6mm$ . This point group symmetry holds only three independent components, thus simplifying the SHG analysis. The difference in the SHG patterns obtained with different tilts, observed in Fig 4.5, is related to these 3-independent SHG components. It yields the 2-lobe symmetry for  $-30^\circ$  and an apparent 4-lobe symmetry for  $+30^\circ$ , approaching a 2-lobe symmetry with higher tilt angles. The double lobe mainly along the horizontal direction (along with the projection of the spontaneous polarization  $P_s$ ) is in good agreement with the  $mm2$  point group averaged over the three crystallographic variants, and with previous bulk <sup>[28]</sup> and thin film <sup>[35]</sup> measurements. We observe an offset in the lobes concerning this horizontal direction that is attributed to the interference of the SHG originating from the STO substrate surface with the OOP-SHG contributions from the film.

Now we move to the quantitative analysis of the SHG signal. For any tilt angle different from  $0^\circ$  there will be a non-zero in-plane component of the OOP polarization. Any combination of the analyzer/polarizer positions except 0/0 allows quantifying this OOP film polarization component. The 90/90 and 270/270 will give the maximum signal. But since at these angles the STO surface contribution is still present, a more suitable analyzer/polarizer angle for analysis is 70/70 which has a lower SHG contribution from STO, as mentioned earlier. The SHG signal intensity at 70/70 is plotted against the tilt for 32 nm in Fig. 4.6 (a) and fitted with a  $\sin^2(x)$  function, according to Eq. 4.4 :

$$y = y_0 + A * (\sin(x))^2, \quad (4.4)$$

where  $y_0$  is a constant,  $A$  is the fitting parameter and  $x$  is the tilt angle.

The OOP SHG component is the  $A$  parameter in the fit, which is proportional to the SHG contribution from the GFO film. The thickness dependence of the GFO electric polarization was studied by performing tilt dependent SHG measurements [Fig. 4.6 (a-c)] on a set of GFO films with varying thicknesses. Reference measurements were carried out on the bare STO substrate, as shown in Fig. 4.6 (d). The extracted OOP component of the SHG signal for all GFO thicknesses is plotted in Fig. 4.6 (e). The error bars denote the error in the fitting of the observed data with the  $\sin^2(x)$  function. Some SHG intensity is already present for the thinnest sample of 7 nm and it increases with thickness.

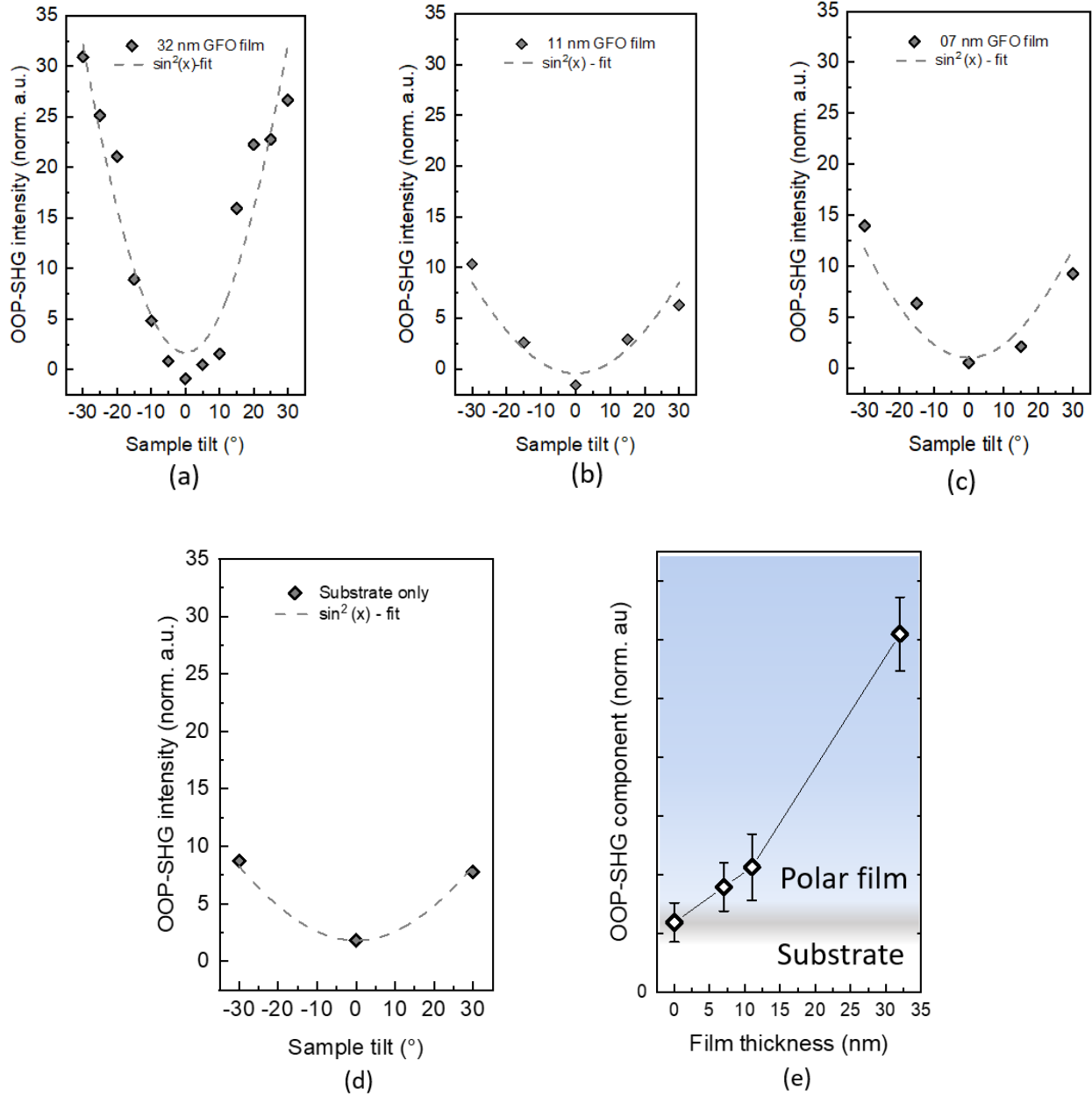


**Fig. 4.6 | The SHG signal measured in the analyzer/polarizer 70/70 configuration for a tilt ranging from 30° to -30° . For the thicknesses (a) 32 nm GFO. (b) 11 nm GFO. (c) 7 nm GFO samples. (d) STO substrate. The data plotted in (e) is the OOP-SHG (normalized) component parameter  $A$  extracted from a  $\sin^2(x)$  fitting of the data (Eq. 4.4) with respect to the film thickness. The solid line is just a guide to the eyes. The error bars in (e) represent the curve fitting error in (a-d). The increasing OOP signal with thickness confirms the observation of polarization in GFO.**

#### 4.2.1.1 Conclusion on the *ex situ* measurements

*Ex situ* SHG measurements performed on GFO films of various thicknesses allowed evidencing the onset of a polarization for thicknesses as low as 7 nm. This indicates that the depolarization field is not strong enough, even at such low thicknesses to quench the polarization completely. To probe the possibility of a critical thickness for the onset of the polarization in GFO, we use *in situ* SHG probing technique explained in our next section.

#### 4.2.2 *In situ* SHG (ISHG) measurements.

The use of *in situ* optical SHG with a sensitivity to the growth of one monolayer was first observed by Shen *et al.* in 1988 for the growth of Sn on GaAs<sup>[40]</sup>. This technique was later used to probe the time-reversal symmetry breaking induced by the ferromagnetic (FM) order in Ni<sup>[41]</sup> and Co<sup>[41]</sup> in 1999. However, it is only recently that a standalone *in situ* set-up, developed by our colleagues of the Laboratory for Multifunctional Ferroic Materials of ETH-Zürich, has been employed to study the SHG due to space-inversion symmetry breaking induced by ferroelectric (FE) order in epitaxial oxide thin films<sup>[2,9,15,16,27,42,43]</sup>.

The *in situ* second harmonic generation (ISHG) allows direct access to the spontaneous polarization (P) of a thin film in real-time during its growth and lets the user track the evolution of the polarization with thickness. Such a technique that allows studying the polarization at each step of the growth is of peculiar interest, especially in an oxide system that grows epitaxially with sub-monolayer accuracy<sup>[2,42]</sup>. An atomic precision level of control over ferroic functionalities (in this case, FE) in ultra-thin regimes is at the helm of the success boat for oxide spintronics, since a change of sub-unit cell thickness can have a critical impact on the ferroelectric functionality<sup>[14,44–47]</sup>. It grants us a license to conveniently manipulate and engineer ferroelectric functionality by controlling various electrostatic processes via strain, interface chemistry, charge screening, and deposition conditions in general<sup>[2,9,15]</sup>. ISHG is notably advantageous to probe the depolarization field effects in an ultra-thin regime where these effects are particularly strong.

##### 4.2.2.1 Investigating ISHG signal during GFO growth on STO.

In the following section, using the ISHG technique, we unveil, for the very first time, the advent of polarization and its evolution with thickness in GFO thin films grown with PLD at 800 °C. The ISHG technique is also sensitive to structural inversion symmetry breaking and it can follow layer-by-layer growth with sub-unit-cell resolution<sup>[42]</sup>. This allowed us to extract some hitherto unknown information about the sub-unit-cell growth in GFO thin films, which will be presented here. This study is expanded by depositing thin films on insulating STO and conducting SRO-buffered-STO substrates, to study the polarization in different screening environments. The ISHG technique uses a state-of-the-art set-up that has a remarkable integration of the SHG technique

with the PLD, where growth can be simultaneously followed using the *in situ* RHEED technique. The ISHG set-up is shown in Fig. 4.7.

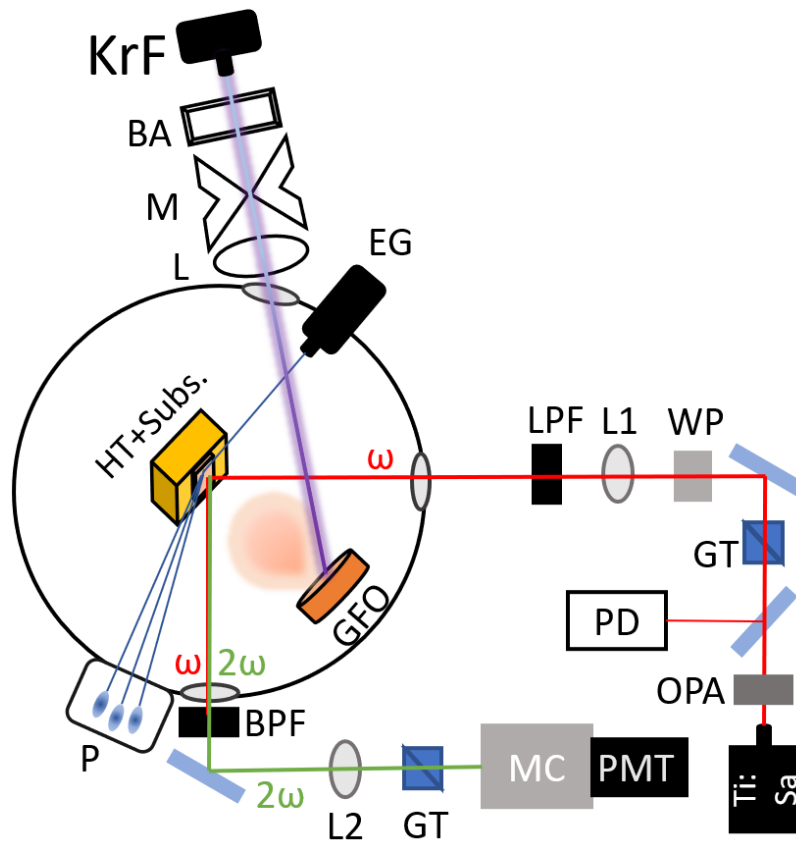


**Fig. 4.7 | Experimental set-up for *in situ* optical second harmonic generation (ISHG) in reflection geometry.** The elaboration of the film is performed thanks to the ablation of a rotating GFO target by an excimer KrF laser. The 248 nm beam goes through a beam attenuator (BA), a metal mask (M), which is used to clean the beam profile, and a lens (L) which is used to focus. A monitoring of the growth is performed by a RHEED set-up which uses an electron gun (EG) to generate an electron beam which is reflected from the sample on a heater (HT) and is finally captured by a phosphor screen (P). The SHG set-up in itself is according to the following : a fundamental wavelength of 800 nm ( $\omega$ ) produced by a titanium sapphire (Ti: Sa) amplified laser with a  $\sim 100$  femtosecond pulse and guided inside an optical parametric oscillator (OPA) is used for the SHG characterization of the polarization state of the GFO thin films. The direction of the light polarization of the incident beam is set by the Polarizer (rotatable  $\lambda/2$ -wave plate) and the detected SHG light-polarization is selected by the Analyzer (rotatable Glan-Taylor (GT) prism). The SHG signal at 400 nm ( $2\omega$ ) is finally measured using a monochromator (MC) and photomultiplier (PMT) system. The femtosecond laser is split by a beam splitter, one beam is considered as a reference beam and goes towards a photodiode (PD) and the second one travels

via a Glan-Taylor (GT) prism, motorized half-waveplate (WP), a focusing lens (L1) and a low pass filter (LPF). The incoming reflected beams are filtered for only SHG wavelength via a bandpass filter (BPF) and collected using the collecting lens (L2). An 800 nm wavelength is used in the *in situ* set-up, instead of the 1200 nm that is used in the *ex situ* set-up, to maximize the signal strength which has less attenuation at 800 nm than at 1200 nm for this particular configuration used in the *in situ* set-up (mirrors, lens, STO substrate, etc... that also generate SHG). A 1200 nm wavelength is used in *ex situ* to avoid SHG interference from STO which is rather high near 830 nm and weakens near 1200 nm.

Now, we look at the results of ISHG experiments performed on GFO (001) thin films grown on STO (111) substrates. The growth temperature of GFO is performed at 800°C but since the ferroelectric  $T_c$  of the GFO polarization has not been explicitly measured yet, a forecast of polarization at this high temperature is non-trivial. An article by Song *et al.*, which demonstrates the ferroelectric nature of GFO grown on SRO-buffered STO, has theoretically calculated (using DFT) the stability of the polar  $Pna2_1$  phase up to 1368 K (1095°C) [38]. The plot in Fig 4.8 (b) for GFO thin film at 800°C presents a 6-fold symmetry which is markedly different and higher in intensity compared to the plot in Fig 4.8 (a) for STO at 800°C. This demonstrates experimentally the existence of a non-centrosymmetric structure (which leads to polarization) in GFO at least up to 800°C. The 6-fold symmetry observed here for the GFO thin films could be due to the existence of 3 structural domains each separated by 120° (see Ch. 2). Although the polarization  $P$  is expected to be out of plane in all these variants, a small tilt from this out-of-plane polarization could result in 3 different polarizations from the 3 structural domains. Since according to Neumann's symmetry principle, there are equal chances of existence for all variants, the appearance and onset of a spontaneous polarization have identical chances for each of them [48].

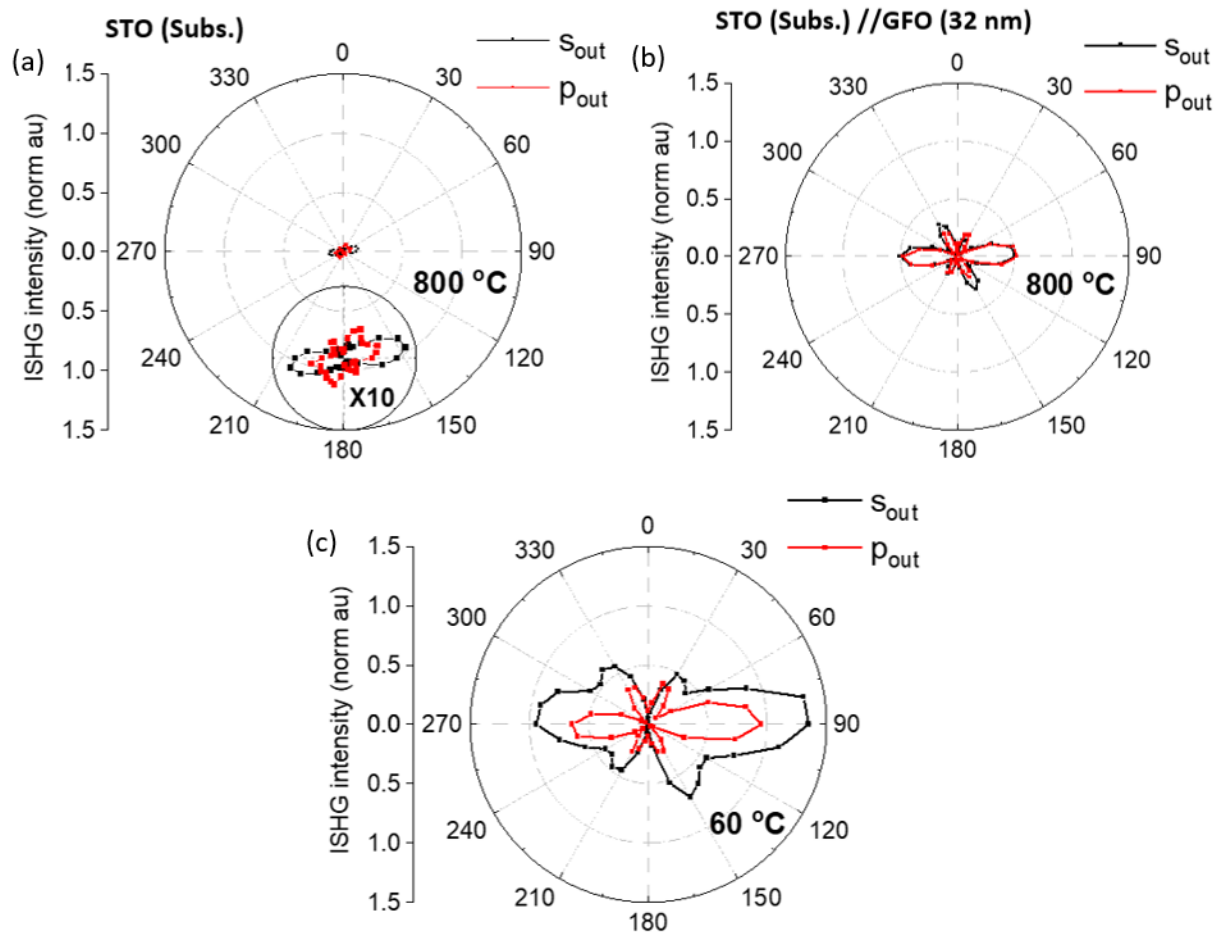


**Fig. 4.8 | The polar plots measured in reflection geometry.** For (a) the STO substrate at 800 °C, (b) the STO (Subs.)//GFO (film) at 800 °C, and (c) STO (Subs.)//GFO (film) at 60 °C. If the analyzer and polarizer are parallel, we have  $S_{out}$  and if they are perpendicular to each other, therefore with a 90° phase shift, we have  $P_{out}$ .

The evolution of the normalized ISHG signal with the thickness of the GFO film grown on STO can be seen in Fig. 4.9 (a-c). These three graphs show the evolution of ISHG signal at polarizer/analyzer angles of 30/30, 90/90, and 150/150 from the polar plot (from the 3 maxima in Fig. 4.8 (b)). The signal at 90/90 corresponds to the surface normal component of the polarization but is seen to have a large surface-related contribution, interfering with the main polarization signal. This can be seen by the sudden increase of the ISHG signal as the deposition starts, which is marked with a grey area. The decrease of this signal along with thickness is explained by the destructive interference between the increasing polarization-related ISHG signal and the decreasing surface-related signal. When the polarization signal is high enough to completely counter the surface signal, the only contribution to the ISHG signal is from the film

polarization and hence the ISHG signal rises again. The 30/30 and 150/150 points allow to observe the polarization signal without a significantly large surface contribution. The 30/30 signal has a very small surface-related component which is quickly suppressed probably by the onset of the polarization and we observe an increase in the ISHG signal starting from just a few nanometers thickness. The signal observed in the 150/150 configuration shows a similar behavior and confirms the existence of spontaneous polarization in GFO at 800°C, even in the absence of any conducting bottom electrode.

Due to the important phenomenon related to surface-interference in the first few 6-7 nm of the GFO thin film, the exact nature of the polarization and the quantification of the critical thickness are inconclusive.

The surface-related signal of Fig 4.9 (a-c) shows oscillatory behavior at the start of the growth (see the zoomed version in Fig 4.11 (a-c)), which is ascribed to the sensitivity of the SHG signal to some inversion symmetry breaking related to the 1/4<sup>th</sup> sub-unit cell growth of GFO thin film that was demonstrated by RHEED oscillations in Chapter 2.

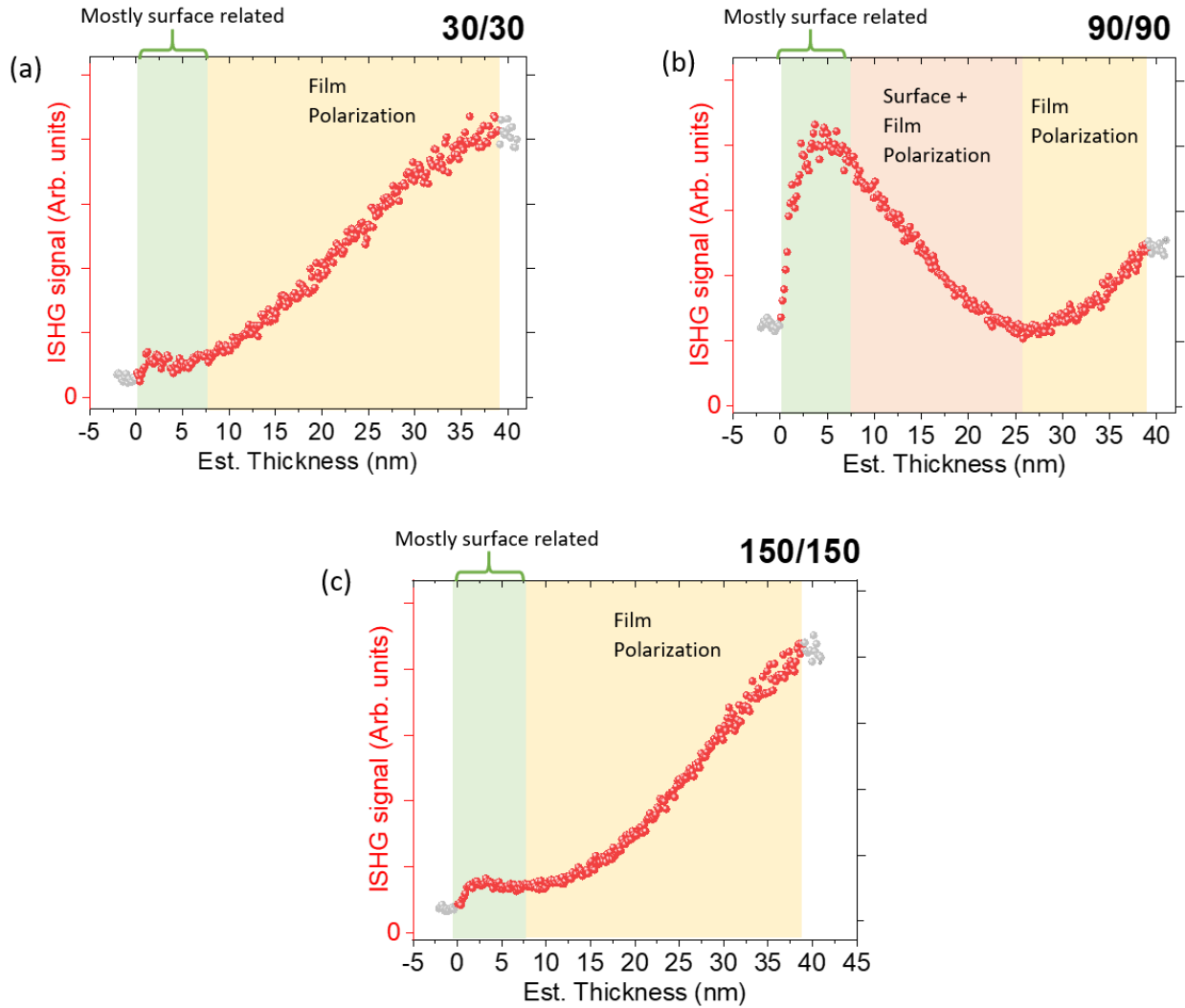


**Fig. 4.9 | ISHG signal for certain analyzer/polarizer angles.** (a) 30/30, (b) 90/90 and (c) 150/150. The start and end of the ISHG signal are greyed since no growth was made during this time. The light green box delineates a zone for which there is a strong input from the surface, the orange box delineates a zone in which there are destructive interferences between the surface and the film polarization and the yellow box delineates a zone only related to the spontaneous polarization of the films.

#### 4.2.2.2 Evidencing the electrical ordering temperature

We look at this ISHG signal in 90/90 while cooling the GFO film below 800°C to estimate the effect of temperature on the GFO polarization. The cooling can lead to the reorientation of the polar tilt in the film towards the easy direction, which is in this case the out-of-plane direction (which corresponds to the 90/90 polarizer/analyzer position), to minimize static energy <sup>[48]</sup>. The ISHG

signal at 90/90 increases linearly with decreasing temperature (Fig. 4.10), which implies that the spontaneous polarization increases as a square root function (Eq. 4.3) with decreasing temperature. This is similar to what happens for magnetization, which is a Brillouin function of temperature, if we consider that the Brillouin function can be approximated by a square root function <sup>[49]</sup>. Extrapolating the linear regression above the 800°C growth temperature until the background/zero scales provides an estimation of the Curie temperature for the polarization in GFO thin films in the range of 950-1100°C (1223-1373 K). This is in close agreement with the theoretical prediction of the polar phase stability limit of 1368 K <sup>[38]</sup>.

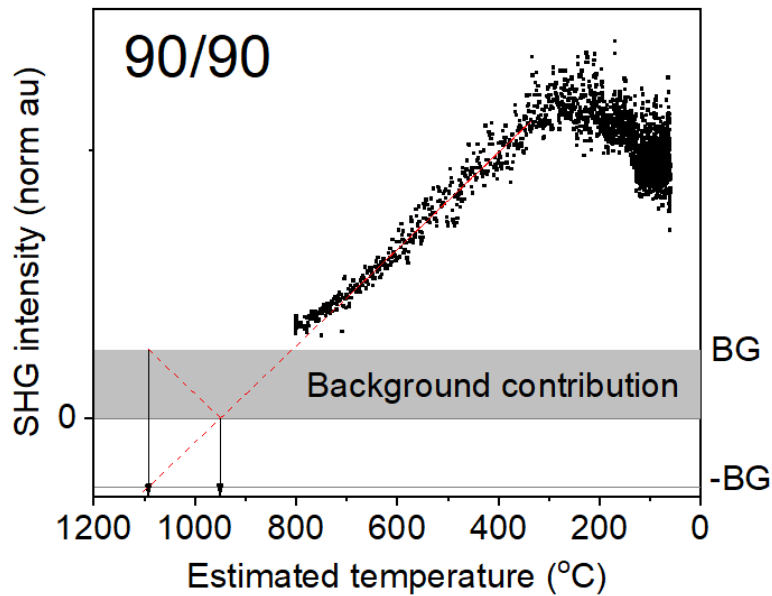


**Fig. 4.10 | Temperature evolution of ISHG signal while cooling down, after the GFO film growth.** The background contribution is due to SHG contribution from the surface, interface, lenses, and other material independent contributions. The linear extrapolation is extended until -BG and a range of temperatures from the intersection with 0 till the intersection with -BG is considered to estimate the  $T_c$  range.

#### 4.2.2.3 Evidencing sub-unit cell symmetry

Now we discuss in more detail the surface-related contribution. The zoomed-in data from the possible surface contribution part of Fig. 4.9 (a-c) is shown in Fig. 4.11 (a-c), along with a 3-point moving average to reduce noise in the data and allow better visualization. An oscillatory pattern is observed in the ISHG signal and presents 4 oscillations, followed by a contribution from the spontaneous onset of polarization both in all 3 measurements with 30/30, 90/90 and 150/150.

Such oscillations in the ISHG during the growth has been recently observed in  $\text{RMnO}_3$  (R= Y, Er, Tb) and has been attributed to the sensitivity of SHG to an inversion-symmetry breaking within the unit-cell. The sub-unit cell growth observed by RHEED for  $\text{RMnO}_3$  is a favorable element for the presence of such an unconventional symmetry breaking <sup>[42]</sup>.

It is well known that such an inversion-symmetry breaking engineering at the surface and interfaces is highly desirable since a non-centrosymmetric structure in functional materials invokes novel ground states that lead to hitherto unknown functionalities in the material <sup>[50]</sup>, such as ferroic functionality <sup>[51,52]</sup>, valley-electronics <sup>[53]</sup>, edge-states <sup>[54]</sup> and non-linear optics in 2D layers <sup>[55]</sup>. The deterministic control of such a functionality in a single material by monitoring and engineering the ultra-thin sub-unit cell growth is one of the core aspects of research in materials engineering <sup>[42]</sup>.

The observation of an oscillatory pattern in  $\text{RMnO}_3$  was explained by the arrangement of  $\text{MnO}_5$  bipyramids in half unit-cells, which creates a non-centrosymmetric structure for the first half-unit cell, leading to SHG. The adjunction of the other half-unit cell results in a centrosymmetric unit-cell structure that negates the SHG down to zero, hence generating an SHG oscillation of 1 unit-cell. The RHEED also shows a half-unit cell growth, which clarifies the origin of symmetry.

In the case of the GFO ultrathin films, however, the investigation into the origin of oscillations is not so obvious due to the complexity of the GFO crystal structure. First, we note that the single SHG oscillation is 1.5 unit-cell ( $\sim 1.4$  nm), instead of 1 unit-cell, which is quite puzzling. On the other hand, the RHEED pattern shows a peculiar 3 oscillations-periodicity (Fig 4.12 (b), brown curve [see more in Ch. 2]) (one short peak followed by a 2 taller ones). We did not expect any periodicity differentiation in the RHEED oscillations since the RHEED analysis shows that each RHEED oscillation is associated with  $1/4^{\text{th}}$  of a unit cell, conforming with the ABAC oxygen stacking-based structure.

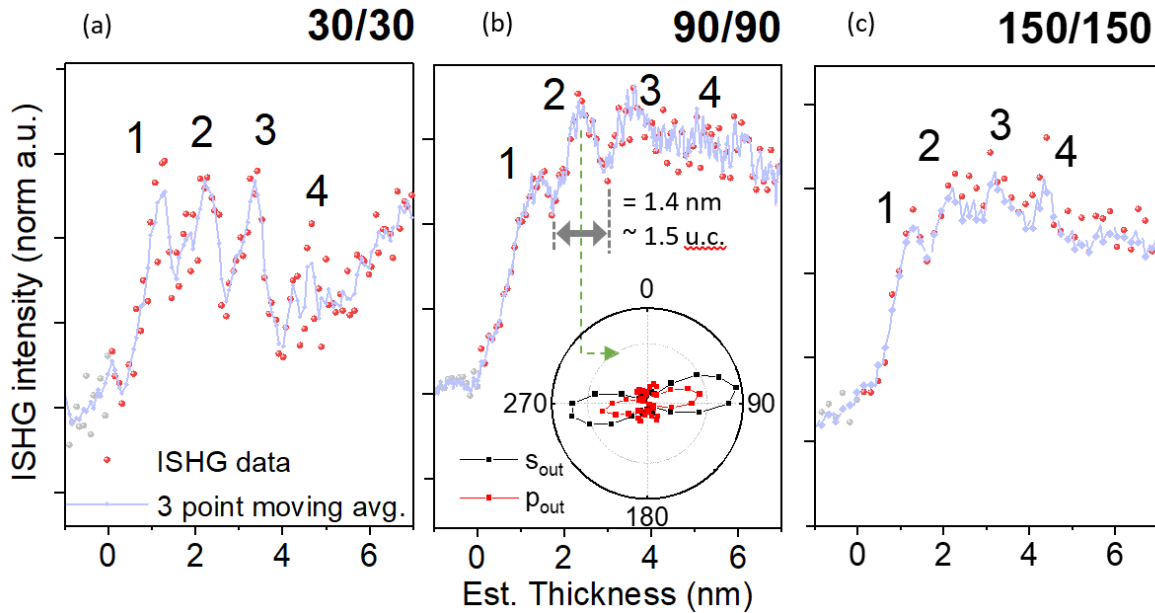


**Fig. 4.11 |** The ISHG data from Fig. 4.9 (a, b, and c) is zoomed from 0 to 7 nm to focus on surface related effects. A 3-point moving average is plotted to reduce the noise of the data and view the oscillation pattern in a statistically better way. Inset graph provides the polar plot observed after 1.5 SHG oscillation (which corresponds to 2 and  $\frac{1}{4}$  GFO unit cells, i.e. 9 GFO sub-unit cells (of  $\frac{1}{4}$  th of a cell)).

The 3 peak-pattern we observe in RHEED indicates a special symmetry-related feature of the growth process of GFO. Why does SHG detect a 1.5 unit-cell (6 sub-unit-cells) periodicity when there is a perfectly defined one-unit cell (4 sub-unit cell) structure that already exists? Is it somehow related to the 3 sub-unit-cell pattern we observe in RHEED? Can we postulate that SHG detects a 3 sub-unit-cell asymmetry, which is then probably negated by another 3 sub-unit-cell to create this 6 sub-unit cell super-cell?

To bring light onto these issues, we inspect more closely the crystal structure of GFO, looking for this centrosymmetric structure of 1.5 unit supercell. To find a periodicity that contains both 4 sub-units as well as 3 sub-units symmetry factors, it might be beneficial to look at a consolidated group made from their least common multiple (LCM) of 12 sub-unit cells. Fig 4.12 (a) shows a  $3 \times 3 \times 3$  unit-cell (i.e.,  $12 \times 12 \times 12$  sub-unit cells) projected perpendicularly to the  $[110]$  direction. We divide this super unit cell into 4 equal parts along the  $c$  direction, each containing 3 sub-unit cells and we hypothesize that the growth of each part leads to an asymmetric crystal structure along the  $c$  axis. In the first part of the red box '3', we see LMLN layers assigned to polyhedral layers of 4 sub-unit cells that make a complete unit cell. In this part, the  $\mathbf{M}$  and  $\mathbf{N}$  sub-unit layers of GFO generate asymmetry which is countered by  $\mathbf{M}'$  and  $\mathbf{N}'$  due to translational symmetry

between them along the  $c$  axis, while all the L sub-unit cell layers of GFO have a center of inversion within the octahedra (as shown in the zoomed version of Fig. 4.13 (c) by the yellow line). There is no difference in the crystalline structure between N, N' or M, M' sub-units. These are only notations to discuss which sub-unit cell generates asymmetry and which counters it in the given model. There is no L' since the L sub-unit does not create any asymmetry. It is well established that either inversion symmetry or translational symmetry must be broken at surfaces or interfaces of films for the generation of an SHG signal, due to incompleteness of the crystal [56].

Furthermore, the two red boxes highlighted in Fig 4.12 (a), numbered '3' (because it corresponds to oscillation no. 3), and '2' (because it corresponds to oscillation no. 2) are images of one another through a  $180^\circ$  rotation around the  $c$  axis. This will reinforce the SHG signal cancellation phenomenon at their interface. In summary, we propose a  $1*1*3$  extended unit-cell as a new super-unit cell with each SHG oscillation corresponding to half of it, i.e.  $1*1*1.5$  super-unit-cell. The RHEED data is perfectly compatible with this SHG analysis, as seen from Fig 4.12 (b), where each short peak is attributed to a change in the nature of the symmetry. The change in crystal symmetry along the growth direction has indeed high implications for the RHEED reflection patterns [57]. RHEED oscillations are strongly influenced by the surface terminations and this was for example used to detect the termination inversions in  $\text{SrRuO}_3$  from  $\text{RuO}_2$  to  $\text{SrO}$  [58] and in  $\text{SrTiO}_3$ , where a phase shift in oscillations is observed for different terminations [30]. Although a  $1/4^{\text{th}}$  sub-unit-cell growth has been observed by RHEED oscillations for other systems, no distinct patterns were observed in these oscillations [59], as it is the case here. It is because of the complex crystal structure of GFO that such a distinct 3-peaks-pattern is observed. GFO is thus a singular case of oxide system which boasts a highly complex crystal structure, an epitaxial layer-by-layer growth mode, where one can not only monitor the  $1/4^{\text{th}}$  sub-unit cell growth *via* RHEED but also can choose an exact termination point to engineer different types of surface asymmetries, by combining the distinct 3-peaks-pattern of RHEED oscillations and the associated ISHG oscillations of 6 sub-unit cell. Such a precise and *in situ* control over symmetries at ultrathin scales is unprecedented and of particular interest in a multiferroic magneto-electric material like GFO.

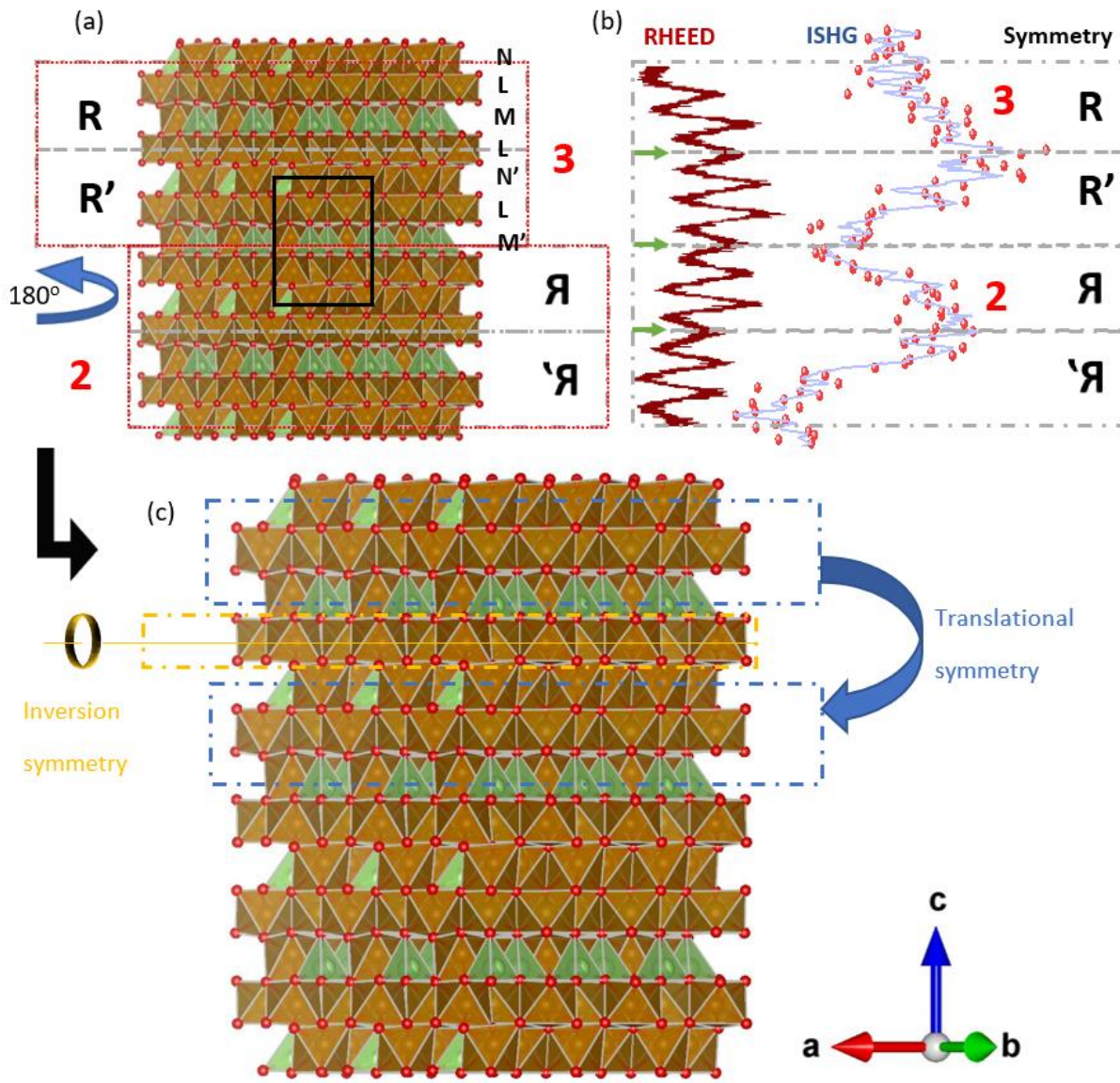


**Fig. 4.12 | Proposal for a new model based on symmetry considerations to explain oscillation in ISHG data during growth of first few unit cells.** (a) Scheme of 3\*3\*3 GFO unit cells projected perpendicularly to the [110] axis, with the growth vector  $c$  axis along the vertical ( $Pna2_1$ ). In this GFO ( $x = 1.4$ ) unit cell, only the Ga1 site contains Ga and all other sites contain Fe. A solid black line indicates a single unit cell. The 3\*3\*3 super-cell is divided equally into 2 parts, namely '2' and '3', as shown by the red dotted line border. These are further equally divided into 2 parts by a grey dashed line. The parts '2' and '3' can be obtained from each other by performing a  $180^\circ$  rotation around the  $c$  axis. (b) The RHEED data (from Ch.3) for the 7 nm sample is shown here to be compared with the ISHG signal of the oscillations '2' and '3' of Fig. 4.9(b) 90/90 data. Some parallels are drawn as guides for the eye. The grey dash-dot box is the equivalent of the super cell in (a) divided into 4 boxes. The green arrows indicate the line of symmetry inversion. One SHG period corresponds to 6 RHEED periods.

#### 4.2.2.4 Insertion of a conducting electrode – Interface-related effects and influence of the depolarizing field

The GFO thin film is also grown on an SRO buffered STO substrate in ETH, Zürich to observe the effects of a bottom electrode on the polar nature of the GFO thin film. Since the presence of such a bottom electrode will reduce the depolarizing field, we can compare STO//SRO/GFO and STO//GFO films to study the effect of the depolarizing field on the GFO polarization. A more detailed analysis related to the growth of GFO on the SRO-buffered-STO substrate can be found in Ch. 2.

The polar plot in Fig 4.13 (a) shows a low signal for the SRO-buffered-STO substrate and, due to the low thickness of SRO (or to the fact that SRO is very similar to STO), the symmetry from the STO surface at 800°C is maintained, as can be seen when compared to Fig. 4.8 (a). The growth of GFO on SRO-buffered-STO shows a prominent 2-lobe symmetry at 800° C (Fig 4.13 (d)) which is very different from the 6-lobe symmetry observed when GFO is directly grown on STO at 800° C (Fig. 4.8 (b)). The effective shielding of bound surface charges allowed by the conducting bottom electrode is anisotropic and strongly favors an out-of-plane direction for the electric polarization. The possibility for a tilt of the GFO polarization, away from the rigorously out-of-plane direction, is therefore very limited in that case. It could explain why we do not see the in-plane projections of these tilts for the three structural domains located at 120° from each other, which would have resulted in a 6-fold symmetry for the lobes. Instead, here we only have a single out-of-plane domain which leads to only a 2-lobe symmetry in SRO/GFO, as observed on the 90/90 polar plots. Such a single polar domain growth due to charge screening has already been observed in a few other compounds such as BFO <sup>[9,15]</sup>, BTO <sup>[15,16]</sup>, or PTO <sup>[17]</sup>.

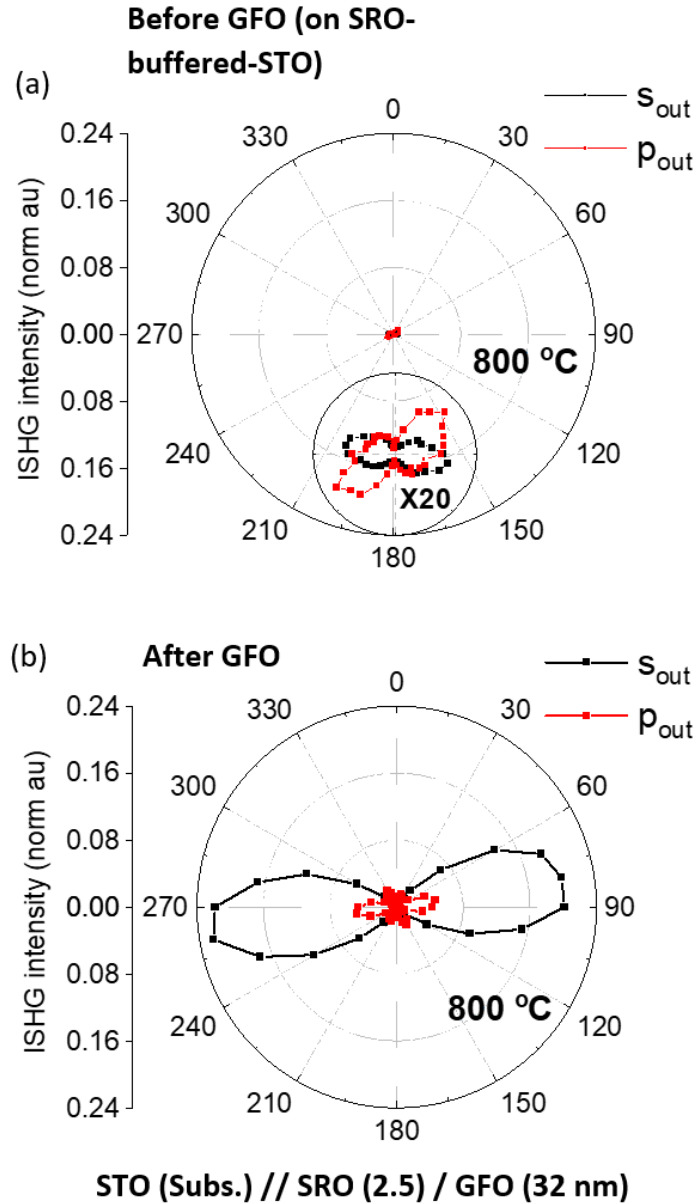


**Fig. 4.13 | ISHG polar plots are shown for the growth of STO(Subs.)//SRO(2.5 nm)/GFO (34.4 nm) at 800 °C.** (a) Before the GFO growth (SRO buffer already is grown). (b) After the GFO growth. A many-fold increase of the signal and a 2-lobe symmetry diagnoses a single polar domain growth in GFO ultra-thin films in 90/90 configuration.

The plots in Fig. 4.14 depict the evolution of the ISHG signal along with the GFO growth on SRO-buffered-STO for polarizer/analyzer angles of (a) 90/90 and (b) 150/150. The idea is to visualize the thickness evolution of these 2 polar plots for STO//SRO/GFO and compare them with that obtained for STO//GFO shown in Fig. 4.9 (b and c). We note that the ISHG signal increases with

thickness for 90/90 while it stays constant at a very low value for 150/150. The 2-lobe symmetry is thus probably kept throughout the whole growth process; there is at least no modification in the 150/150 direction. Hence, it is highly probable that no additional symmetry or phase-transition exists during the growth of GFO on the SRO-buffered-STO substrate (at least until a probed thickness of ca. 35 nm).

Looking more closely at the 90/90 signal we can identify 3 separate parts categorized by a change in the ISHG signal slope. Since the SHG signal due to the formation of a new GFO surface and the interface between GFO and SRO breaks the inversion symmetry, we see a sudden increase in the signal within the growth of the first two GFO sub-unit cells. This is similar to the case of the STO/GFO interface where we also see a sudden increase, although the different terminations of the substrate (SrO, RuO<sub>2</sub>, TiO<sub>2</sub>) could cause the first layers to grow differently. The first part of the signal (green), as the growth starts, is due to the surface related signal mixed with signals of SHG oscillations originating from the sub-unit cell growth. This overshadows the direct information on the critical thickness for the polarization onset in GFO ultra-thin film, as can be more clearly seen in the zoomed-in Fig 4.14 (c).

The second part (orange) of Fig 4.14 (a) is due to the thickness dependence of the depolarizing field where size effects lead the depolarizing field to increase sharply at ultra-low thickness. In the third part (yellow), the evolution of the ISHG signal is not hindered by the depolarization effects and it increases until it reaches the polarization value  $P_{SA}$ . Then, the polarization value does not increase further and seems to saturate. Even though the concept is still under investigation, we think the saturation at  $P_{SA}$  is due to self-absorption (SA) in the films. This is when the thickness is high enough that the SHG from the bottom layers is shielded/scattered due to the important thickness of top layers. Such an evolution in the ISHG signal has been observed before and has been explained similarly for the flagship ferroelectric thin film materials of BFO and BTO [9,15]. Since ISHG is still an evolving technique, other explanations for saturation may also exist, such as a non-polar growth due to the release of strain with thickness, for example.

The calculation of the critical thickness in the GFO thin film is not straightforward as explained before due to the many surface-related phenomena happening in the ultra-thin regime. We try to observe it by back extrapolating the linear curve due to the depolarization field effect to the background value and 0 value to estimate a range of values for the critical thickness. Carefully measuring these values, we find that the critical thickness lies within 0.47-1.90 nm (~ 0.5-2.0 GFO unit cells). This is lower than that observed for other comparable functional ferroelectric oxides like BFO (4 unit cells), BTO (4 unit cells), and PZT (3 unit cells) [14], which shows the sturdy nature of the GFO polarization that requires a very high depolarization field to quench its polarization, which is only possible at ultra-low thickness.

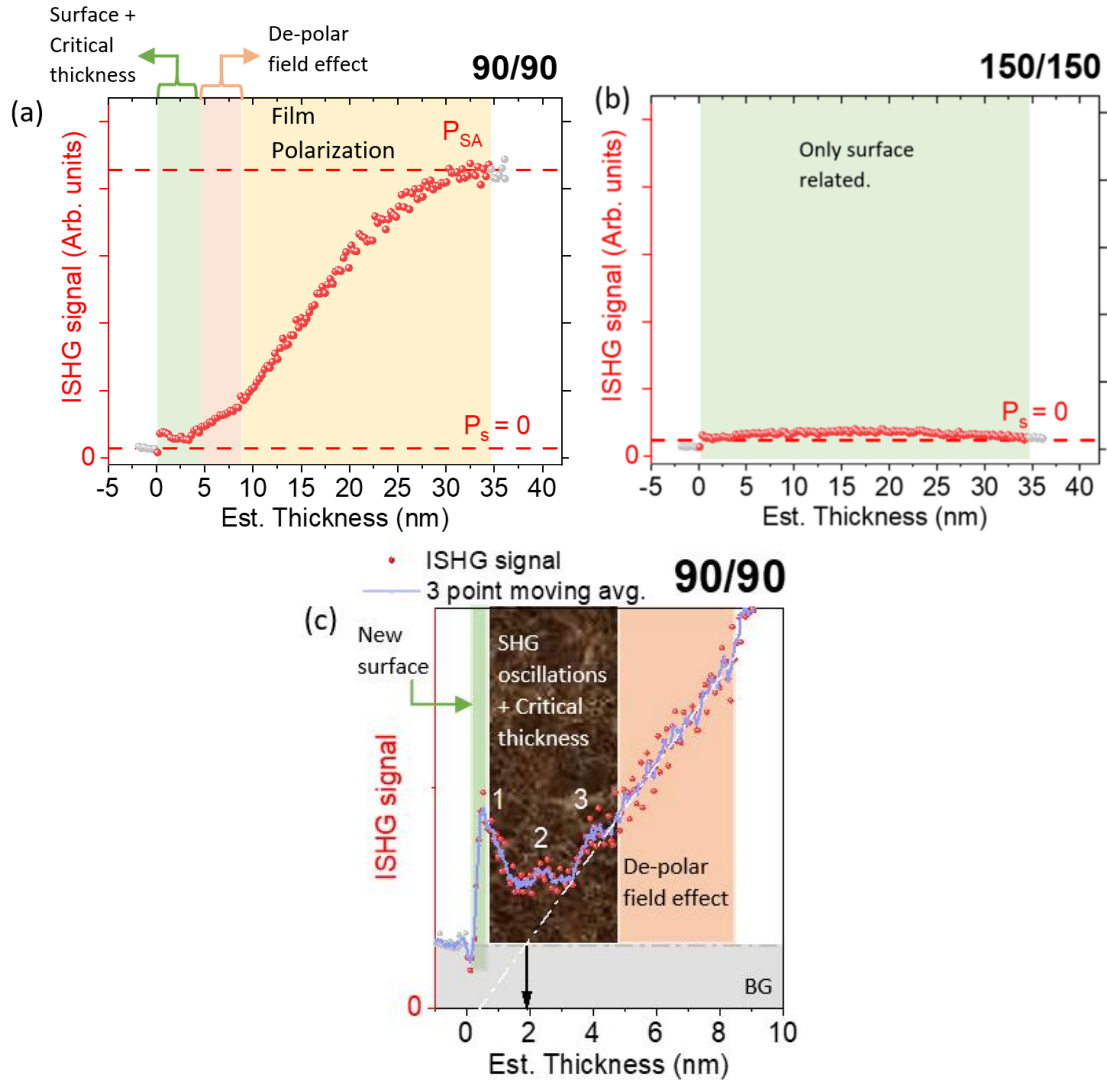


**Fig. 4.14 | ISHG signal vs. the GFO estimated thickness (nm) for the STO//SRO/GFO sample.** The evolution with thickness is presented for analyzer/polarizer angles of (a) 90/90. (b) 150/150. The 90/90 shows a deterministic single polar domain growth. The observed signal remains very low for the 150/150 configuration. Figure (c) shows a zoomed-in version of (a) to allow discussing in detail phenomena at ultra-thin scales like surface-related signal, SHG oscillations, critical thickness for the onset of the polarization, and thickness dependent depolarization field effect.

#### 4.2.2.5 Conclusion on the *in situ* measurements

We have investigated the early stages of GFO growth in STO//GFO and STO//SRO/GFO thin-film architectures by *in situ* SHG. We have obtained some completely original information on the sub-unit growth mode of GFO, and have been able to corroborate these findings with results obtained by RHEED. It has also been possible to evaluate the ferroelectric critical temperature  $T_c$  for GFO

in thin films, within the 950-1100°C (1223-1373 K) range. This is in good agreement with theoretical calculations which predicted a polar phase stability limit of 1368 K <sup>[38]</sup>.

When the GFO growth is performed directly onto STO, the high surface component of the SHG signal does not allow an easy determination of the critical thickness at which the polarization is established in the GFO films. We have inserted a conducting SRO electrode between the STO substrate and the GFO films, in STO//SRO/GFO heterostructures, in order to study the effect of the absence of a depolarization field on the GFO polarization. In this configuration, the surface impact onto the SHG signal happened to be much lower than for the direct growth onto STO and an estimation of the critical thickness was possible. It yielded a value between 0.5 and 2 unit cells, which is very low when compared to other ferroelectric materials. This confirms the stiffness of the electric polarization in GFO, and its impressive resistance towards the depolarizing field.

As a perspective, we propose to study *in situ*, *via* ISHG, a heterostructure in which the charge screening in the GFO single polar domain is suppressed by sandwiching the GFO film between two SRO films, a conducting one, at the bottom, and a non-conducting one, on top. The idea is to disrupt the charge screening due to the atmospheric adsorbates sitting on the STO//SRO/GFO film by growing a non-conducting single unit-cell SRO on top of the stack <sup>[25]</sup>. This has been shown to trigger the formation of domains in a single polar domain thin film. This would allow determining the ultimate resistance of the GFO cell towards a depolarizing field.

### 4.3 References

- (1) Denev, S. A.; Lummen, T. T. A.; Barnes, E.; Kumar, A.; Gopalan, V. Probing Ferroelectrics Using Optical Second Harmonic Generation. *Journal of the American Ceramic Society* **2011**, *94* (9), 2699–2727.
- (2) Nordlander, J.; De Luca, G.; Strkalj, N.; Fiebig, M.; Trassin, M. Probing Ferroic States in Oxide Thin Films Using Optical Second Harmonic Generation. *Applied Sciences* **2018**, *8* (4), 570.
- (3) Trassin, M.; Luca, G. D.; Manz, S.; Fiebig, M. Probing Ferroelectric Domain Engineering in BiFeO<sub>3</sub> Thin Films by Second Harmonic Generation. *Advanced Materials* **2015**, *27* (33), 4871–4876.
- (4) Matsubara, M.; Manz, S.; Mochizuki, M.; Kubacka, T.; Iyama, A.; Aliouane, N.; Kimura, T.; Johnson, S. L.; Meier, D.; Fiebig, M. Magnetoelectric Domain Control in Multiferroic TbMnO<sub>3</sub>. *Science* **2015**, *348* (6239), 1112–1115.
- (5) Birss, R. R. *Symmetry and Magnetism*; North-Holland Amsterdam, 1964; Vol. 863.
- (6) Manipatruni, S.; Nikonov, D. E.; Lin, C.-C.; Gosavi, T. A.; Liu, H.; Prasad, B.; Huang, Y.-L.; Bonturim, E.; Ramesh, R.; Young, I. A. Scalable Energy-Efficient Magnetoelectric Spin–Orbit Logic. *Nature* **2018**.
- (7) Chanthbouala, A.; Crassous, A.; Garcia, V.; Bouzehouane, K.; Fusil, S.; Moya, X.; Allibe, J.; Dlubak, B.; Grollier, J.; Xavier, S. Solid-State Memories Based on Ferroelectric Tunnel Junctions. *Nature nanotechnology* **2012**, *7* (2), 101–104.
- (8) Pan, C.; Naeemi, A. An Expanded Benchmarking of Beyond-CMOS Devices Based on Boolean and Neuromorphic Representative Circuits. *IEEE Journal on Exploratory Solid-State Computational Devices and Circuits* **2017**, *3*, 101–110.
- (9) De Luca, G.; Strkalj, N.; Manz, S.; Bouillet, C.; Fiebig, M.; Trassin, M. Nanoscale Design of Polarization in Ultrathin Ferroelectric Heterostructures. *Nature Communications* **2017**, *8* (1), 1419.
- (10) Lofland, S. E.; McDonald, K. F.; Metting, C. J.; Knoesel, E.; Murakami, M.; Aronova, M. A.; Fujino, S.; Wuttig, M.; Takeuchi, I. Epitaxy, Texturing, and Second-Harmonic Generation in BiFeO<sub>3</sub> Thin Films. *Physical Review B* **2006**, *73* (9), 092408.
- (11) Fiebig, M.; Fröhlich, D.; Sluyterman v. L, G.; Pisarev, R. V. Domain Topography of Antiferromagnetic Cr<sub>2</sub>O<sub>3</sub> by Second-harmonic Generation. *Applied physics letters* **1995**, *66* (21), 2906–2908.
- (12) Mishina, E. D.; Buryakov, A. M.; Sherstyuk, N. E.; Sigov, A. S.; Rasing, T. Nonlinear-Optical Study of Magnetoelectric Interactions in Multilayer Structures. *Ferroelectrics* **2016**, *500* (1), 37–46.
- (13) Junquera, J.; Ghosez, P. Critical Thickness for Ferroelectricity in Perovskite Ultrathin Films. *Nature* **2003**, *422* (6931), 506–509.
- (14) Gao, P.; Zhang, Z.; Li, M.; Ishikawa, R.; Feng, B.; Liu, H.-J.; Huang, Y.-L.; Shibata, N.; Ma, X.; Chen, S. Possible Absence of Critical Thickness and Size Effect in Ultrathin Perovskite Ferroelectric Films. *Nature communications* **2017**, *8* (1), 1–8.

- (15) De Luca, G. Controlling Ferroic Domain Architecture in Oxide Heterostructures, Thesis, ETH Zurich, **2017**.
- (16) Strkalj, N.; De Luca, G.; Campanini, M.; Pal, S.; Schaab, J.; Gattinoni, C.; Spaldin, N. A.; Rossell, M. D.; Fiebig, M.; Trassin, M. Depolarizing-Field Effects in Epitaxial Capacitor Heterostructures. *Phys. Rev. Lett.* **2019**, *123* (14), 147601.
- (17) Lichtensteiger, C.; Fernandez-Pena, S.; Weymann, C.; Zubko, P.; Triscone, J.-M. Tuning of the Depolarization Field and Nanodomain Structure in Ferroelectric Thin Films. *Nano letters* **2014**, *14* (8), 4205–4211.
- (18) Streiffer, S. t; Eastman, J. A.; Fong, D. D.; Thompson, C.; Munkholm, A.; Murty, M. R.; Auciello, O.; Bai, G. R.; Stephenson, G. B. Observation of Nanoscale 180° Stripe Domains in Ferroelectric PbTiO<sub>3</sub> Thin Films. *Physical review letters* **2002**, *89* (6), 067601.
- (19) Zubko, P.; Gariglio, S.; Gabay, M.; Ghosez, P.; Triscone, J.-M. Interface Physics in Complex Oxide Heterostructures. **2011**.
- (20) Stephenson, G. B.; Highland, M. J. Equilibrium and Stability of Polarization in Ultrathin Ferroelectric Films with Ionic Surface Compensation. *Physical Review B* **2011**, *84* (6), 064107.
- (21) Lichtensteiger, C.; Dawber, M.; Stucki, N.; Triscone, J.-M.; Hoffman, J.; Yau, J.-B.; Ahn, C. H.; Despont, L.; Aebi, P. Monodomain to Polydomain Transition in Ferroelectric PbTiO<sub>3</sub> Thin Films with La<sub>0.67</sub>Sr<sub>0.33</sub>MnO<sub>3</sub> Electrodes. *Applied Physics Letters* **2007**, *90* (5), 052907.
- (22) Wang, R. V.; Fong, D. D.; Jiang, F.; Highland, M. J.; Fuoss, P. H.; Thompson, C.; Kolpak, A. M.; Eastman, J. A.; Streiffer, S. K.; Rappe, A. M. Reversible Chemical Switching of a Ferroelectric Film. *Physical review letters* **2009**, *102* (4), 047601.
- (23) Tagantsev, A. K.; Cross, L. E.; Fousek, J. *Domains in Ferroic Crystals and Thin Films*; Springer, **2010**; Vol. 13.
- (24) Catalan, G.; Seidel, J.; Ramesh, R.; Scott, J. F. Domain Wall Nanoelectronics. *Reviews of Modern Physics* **2012**, *84* (1), 119.
- (25) Spaldin, N. A.; Ramesh, R. Advances in Magnetoelectric Multiferroics. *Nature materials* **2019**, *18* (3), 203.
- (26) Fong, D. D.; Kolpak, A. M.; Eastman, J. A.; Streiffer, S. K.; Fuoss, P. H.; Stephenson, G. B.; Thompson, C.; Kim, D. M.; Choi, K. J.; Eom, C. B. Stabilization of Monodomain Polarization in Ultrathin PbTiO<sub>3</sub> Films. *Physical review letters* **2006**, *96* (12), 127601.
- (27) Nordlander, J.; Maillard, A.; Fiebig, M.; Trassin, M. Emergence of Ferroelectricity at the Morphotropic Phase Boundary of Ultrathin BiFeO<sub>3</sub>. *arXiv:2005.09685 [cond-mat]* **2020**.
- (28) Ogawa, Y.; Kaneko, Y.; He, J. P.; Yu, X. Z.; Arima, T.; Tokura, Y. Magnetization-Induced Second Harmonic Generation in a Polar Ferromagnet. *Phys. Rev. Lett.* **2004**, *92* (4), 047401.
- (29) Kalashnikova, A. M.; Pisarev, R. V.; Bezmaternykh, L. N.; Temerov, V. L.; Kirilyuk, A.; Rasing, Th. Optical and Magneto-Optical Studies of a Multiferroic GaFeO<sub>3</sub> with a High Curie Temperature. *Jetp Lett.* **2005**, *81* (9), 452–457.
- (30) Yamamoto, S.; Omi, T.; Akai, H.; Kubota, Y.; Takahashi, Y.; Suzuki, Y.; Hirata, Y.; Yamamoto, K.; Yukawa, R.; Horiba, K. Element Selectivity in Second-Harmonic Generation of GaFeO<sub>3</sub> by a Soft-X-Ray Free-Electron Laser. *Physical Review Letters* **2018**, *120* (22), 223902.
- (31) Matsubara, M.; Kaneko, Y.; He, J.-P.; Okamoto, H.; Tokura, Y. Ultrafast Polarization and Magnetization Response of Multiferroic GaFeO<sub>3</sub> Using Time-Resolved Nonlinear Optical Techniques. *Phys. Rev. B* **2009**, *79* (14), 140411.

- (32) Eguchi, K.; Tanabe, Y.; Ogawa, T.; Tanaka, M.; Kawabe, Y.; Hanamura, E. Second-Harmonic Generation from Pyroelectric and Ferrimagnetic GaFeO<sub>3</sub>. *J. Opt. Soc. Am. B, JOSAB* **2005**, *22* (1), 128–137.
- (33) Igarashi, J.; Nagao, T. Second Harmonic Generation in a Polar Ferrimagnet GaFeO<sub>3</sub>. *Phys. Rev. B* **2010**, *82* (2), 024424.
- (34) Zhong, G.; Bitla, Y.; Wang, J.; Zhong, X.; An, F.; Chin, Y.-Y.; Zhang, Y.; Gao, W.; Zhang, Y.; Eshghinejad, A.; Esfahani, E. N.; Zhu, Q.; Tan, C.; Meng, X.; Lin, H.-J.; Pan, X.; Xie, S.; Chu, Y.-H.; Li, J. Tuning Fe Concentration in Epitaxial Gallium Ferrite Thin Films for Room Temperature Multiferroic Properties. *Acta Materialia* **2018**, *145*, 488–495.
- (35) Kundaliya, D. C.; Ogale, S. B.; Dhar, S.; McDonald, K. F.; Knoesel, E.; Osedach, T.; Lofland, S. E.; Shinde, S. R.; Venkatesan, T. Large Second-Harmonic Kerr Rotation in GaFeO<sub>3</sub> Thin Films on YSZ Buffered Silicon. *Journal of Magnetism and Magnetic Materials* **2006**, *299* (2), 307–311.
- (36) Zhao, R.; Jin, K.; Guo, H.; Lu, H.; Yang, G. A Study on Surface Symmetry and Interfacial Enhancement of SrTiO<sub>3</sub> by Second Harmonic Generation. *Science China Physics, Mechanics and Astronomy* **2013**, *56* (12), 2370–2376.
- (37) Stone, G.; Ophus, C.; Birol, T.; Ciston, J.; Lee, C.-H.; Wang, K.; Fennie, C. J.; Schlom, D. G.; Alem, N.; Gopalan, V. Atomic Scale Imaging of Competing Polar States in a Ruddlesden–Popper Layered Oxide. *Nature communications* **2016**, *7* (1), 1–9.
- (38) Song, S.; Jang, H. M.; Lee, N.-S.; Son, J. Y.; Gupta, R.; Garg, A.; Ratanapreechachai, J.; Scott, J. F. Ferroelectric Polarization Switching with a Remarkably High Activation Energy in Orthorhombic GaFeO<sub>3</sub> Thin Films. *NPG Asia Materials* **2016**, *8* (2), e242–e242.
- (39) <http://lampx.tugraz.at/~hadley/ss2/crystalphysics/crystalclasses/crystalclasses.html> (accessed Aug 27, **2020**).
- (40) Stehlin, T.; Feller, M.; Guyot-Sionnest, P.; Shen, Y.-R. Optical Second-Harmonic Generation as a Surface Probe for Noncentrosymmetric Media. *Optics letters* **1988**, *13* (5), 389–391.
- (41) Jähnke, V.; Conrad, U.; Güdde, J.; Matthias, E. SHG Investigations of the Magnetization of Thin Ni and Co Films on Cu (001). *Applied Physics B: Lasers & Optics* **1999**, *68* (3).
- (42) Nordlander, J.; Rossell, M. D.; Campanini, M.; Fiebig, M.; Trassin, M. Inversion-Symmetry Engineering in Sub-Unit-Cell-Layered Oxide Thin Films. *arXiv:2005.09083 [cond-mat, physics:physics]* **2020**.
- (43) Nordlander, J.; Campanini, M.; Rossell, M. D.; Erni, R.; Meier, Q. N.; Cano, A.; Spaldin, N. A.; Fiebig, M.; Trassin, M. The Ultrathin Limit of Improper Ferroelectricity. *Nature Communications* **2019**, *10* (1), 5591.
- (44) Liao, Z.; Huijben, M.; Zhong, Z.; Gauquelin, N.; Macke, S.; Green, R. J.; Van Aert, S.; Verbeeck, J.; Van Tendeloo, G.; Held, K. Controlled Lateral Anisotropy in Correlated Manganite Heterostructures by Interface-Engineered Oxygen Octahedral Coupling. *Nature materials* **2016**, *15* (4), 425–431.
- (45) Lu, H.; Liu, X.; Burton, J. D.; Bark, C.; Wang, Y.; Zhang, Y.; Kim, D. J.; Stamm, A.; Lukashev, P.; Felker, D. A. Enhancement of Ferroelectric Polarization Stability by Interface Engineering. **2012**.
- (46) Fong, D. D.; Stephenson, G. B.; Streiffer, S. K.; Eastman, J. A.; Auciello, O.; Fuoss, P. H.; Thompson, C. Ferroelectricity in Ultrathin Perovskite Films. *Science* **2004**, *304* (5677), 1650–1653.

- (47) Gradauskaite, E.; Campanini, M.; Biswas, B.; Schneider, C. W.; Fiebig, M.; Rossell, M. D.; Trassin, M. Robust In-Plane Ferroelectricity in Ultrathin Epitaxial Aurivillius Films. *Advanced Materials Interfaces* **2020**, 2000202.
- (48) Zheludev, I. S. Ferroelectricity and Symmetry. In *Solid State Physics*; Elsevier, 1971; Vol. 26, pp 429–464.
- (49) Arrott, A. S. Approximations to Brillouin Functions for Analytic Descriptions of Ferromagnetism. *Journal of Applied Physics* **2008**, 103 (7), 07C715.
- (50) Hwang, H. Y.; Iwasa, Y.; Kawasaki, M.; Keimer, B.; Nagaosa, N.; Tokura, Y. Emergent Phenomena at Oxide Interfaces. *Nature materials* **2012**, 11 (2), 103–113.
- (51) Sai, N.; Meyer, B.; Vanderbilt, D. Compositional Inversion Symmetry Breaking in Ferroelectric Perovskites. *Physical review letters* **2000**, 84 (24), 5636.
- (52) Becher, C.; Trassin, M.; Lilienblum, M.; Nelson, C. T.; Suresha, S. J.; Yi, D.; Yu, P.; Ramesh, R.; Fiebig, M.; Meier, D. Functional Ferroic Heterostructures with Tunable Integral Symmetry. *Nature communications* **2014**, 5 (1), 1–6.
- (53) Yao, W.; Xiao, D.; Niu, Q. Valley-Dependent Optoelectronics from Inversion Symmetry Breaking. *Physical Review B* **2008**, 77 (23), 235406.
- (54) Yin, X.; Ye, Z.; Chenet, D. A.; Ye, Y.; O'Brien, K.; Hone, J. C.; Zhang, X. Edge Nonlinear Optics on a MoS<sub>2</sub> Atomic Monolayer. *Science* **2014**, 344 (6183), 488–490.
- (55) Kumar, N.; Najmaei, S.; Cui, Q.; Ceballos, F.; Ajayan, P. M.; Lou, J.; Zhao, H. Second Harmonic Microscopy of Monolayer MoS<sub>2</sub>. *Physical Review B* **2013**, 87 (16), 161403.
- (56) Bennemann, K. H. *Non-Linear Optics in Metals*; Oxford University Press, 1998.
- (57) Hasegawa, S. Reflection High-energy Electron Diffraction. *Characterization of Materials* **2002**, 1–14.
- (58) Choi, J.; Eom, C.-B.; Rijnders, G.; Rogalla, H.; Blank, D. H. Growth Mode Transition from Layer by Layer to Step Flow during the Growth of Heteroepitaxial SrRuO<sub>3</sub> on (001) SrTiO<sub>3</sub>. *Applied physics letters* **2001**, 79 (10), 1447–1449.
- (59) Reisinger, D.; Blass, B.; Klein, J.; Philipp, J. B.; Schonecke, M.; Erb, A.; Alff, L.; Gross, R. Sub-Unit Cell Layer-by-Layer Growth of Fe<sub>3</sub>O<sub>4</sub>, MgO, and Sr<sub>2</sub>RuO<sub>4</sub> Thin Films. *Applied Physics A* **2003**, 77 (5), 619–621.

---

# Chapter 5

## Functionality of $\text{Ga}_{0.6}\text{Fe}_{1.4}\text{O}_3$ thin films in spintronics

---

This chapter aims at exploring functionalities that GFO could endorse in spintronics systems. In particular, we have considered its potential in ferrimagnetic (FM) / heavy metal (HM) heterostructures for a magnetic-field-free-manipulation of the magnetization of the FM, where GFO would be the FM layer, and Pt the HM. In such FM/HM heterostructures, some pure spin currents are created in the heavy metal (HM) layer by spin Hall effect (SHE), and the injection of this spin current in the adjacent ferrimagnetic (FM) layer with manipulation of its magnetization orientation is studied. We could evidence an important spin Hall induced anisotropic magnetoresistance in the Pt, indicating the relevance of the system for spintronics applications.

While the elaboration-related aspects of this study were realized as part of this thesis at the IPCMS, Strasbourg, the spintronics-related characterizations (ferromagnetic resonance study, magneto-transport characterizations) were realized by our colleagues Dr. Carlos Rojas-Sanchez, Dr. Sébastien Petit-Watelot, and Dr. Elodie Martin at the Institut Jean Lamour (IJL) in Nancy. The analysis of the data they acquired was conducted as part of this thesis in close collaboration with them.

## 5.1 FM/HM: Magnetic axis manipulation in GFO/Pt heterostructures *via* SHE in Pt

### 5.1.1 Growth of GFO/Pt heterostructures on STO (111)

As discussed in the introduction, since spin-orbit interaction is the basis for the SHE, a material with high spin-orbit coupling is required to generate pure spin current through SHE. Materials with a high atomic number ( $Z$ ) are well-suited because spin-orbit interaction is directly proportional to  $Z^4$ <sup>[1]</sup>. Platinum (Pt) with  $Z=78$  was one of the earliest employed heavy metals for that purpose<sup>[2,3]</sup>. It has proven to be an excellent candidate for generating pure spin currents through spin Hall effect, which were then used to be injected into and switch some metallic magnets<sup>[4–10]</sup> as well as some oxides<sup>[11–14]</sup>. Other heavy metals like Tantalum (Ta)<sup>[4]</sup> and Tungsten (W)<sup>[15]</sup>, as well as some topological insulators like  $\text{Bi}_2\text{Se}_3$ <sup>[16]</sup> and  $\alpha\text{-Sn}$ <sup>[17]</sup> (through Rashba spin-orbit effect<sup>[18]</sup>) have shown a higher spin Hall angle than Pt, but Pt remains the first choice of researchers for observing spin Hall dynamics or switching<sup>[19]</sup> because of its low resistivity. It is also generally regarded as a better option in place of the alternatives mentioned above due to availability and relative ease in growth.

We have demonstrated the growth of atomically smooth GFO (001) on STO (111) in earlier chapters; now, we look at the growth of Pt on top of a GFO layer. We considered a Pt thickness of 5 nm for generating spin currents, since some detailed studies have suggested this thickness to be optimum for SHE induced spin currents after examining factors such as spin diffusion length ( $\lambda_{sd}$ ), spin memory loss (SML) at the interface<sup>[20]</sup> and spin Hall torque efficiency per applied electric field unit<sup>[9]</sup>.

We calibrated the Pt deposition rate from a thickness vs. pulse numbers graph (Fig 5.1 (a)), and determined the appropriate number of pulses required for 5 nm Pt from this graph. These films were grown at room temperature (27°C) under vacuum, *i.e.*, a base pressure of  $5 \cdot 10^{-8}$ , on  $\text{SiO}_2$  substrates for calibration, with a laser fluence of 4 J and a repetition rate of 10 Hz. The inset of Fig 5.1 (a) depicts an AFM image for such a 22 nm Pt film, which exhibits a low rms roughness of 0.29 nm. Such a low roughness is kept for deposition onto GFO thin films, provided that the roughness of the GFO film itself is not too high. On Fig 5.1 (b) one can see an AFM image for a 5 nm Pt film deposited on a 7 nm GFO (001) oriented sample for which the roughness reaches 1.2 nm, while for a deposition on a 32 nm thick GFO, the roughness stays at the low value of 0.3 nm (Fig 5.1 (c)). The difference can be attributed to the higher roughness of the GFO surface for 7 nm compared to 32 nm (as shown in chapter 2). The AFM morphology of Pt on  $\text{SiO}_2$  is continuous and even. The morphology of Pt on GFO (001) looks less homogeneous and follows the morphology of GFO (001). We have carried out a structural analysis of an as-grown Pt/GFO//STO heterostructure by X-ray diffraction and transmission electron microscopy.

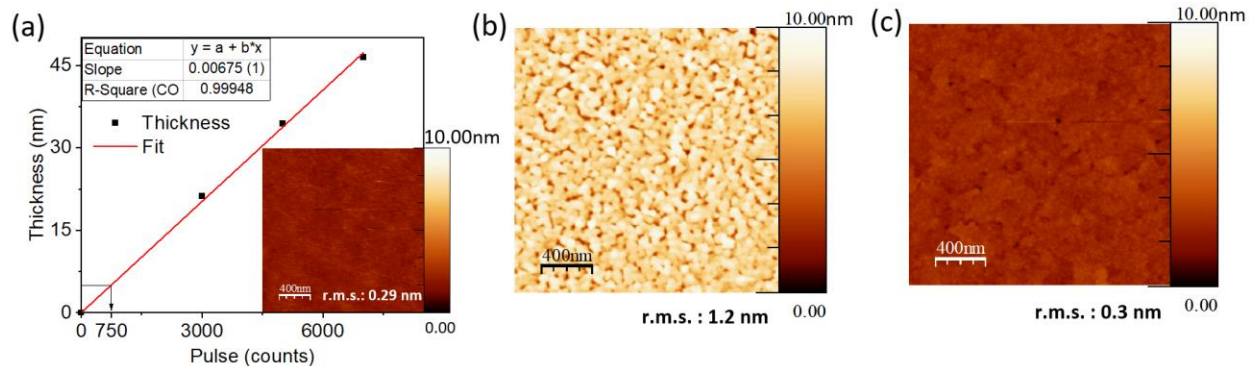


**Fig. 5.1 | Thickness optimization and surface characterization of Pt.** (a) Thickness vs. pulse counts for Pt thin films grown on amorphous SiO<sub>2</sub> substrates by PLD. The thickness was determined from reflectometry measurements. Inset shows the AFM observation for 22 nm Pt grown on SiO<sub>2</sub>, and AFM image for 5 nm thick Pt grown on (b) 7 nm and (c) 32 nm thick GFO (001)// (STO 111).

The  $\theta$ - $2\theta$  scans of the Pt(5nm) / GFO(32 nm) // STO(111) [denoted as **G32**] and Pt(5nm) / GFO(7nm) // STO(111) [denoted as **G7**] films are shown in Fig 5.2 (a). For both films, Pt grows along its [111] direction and GFO along its [001] direction on STO (111). The inset shows the full scan range demonstrating a clean and oriented sample with no spurious phases. We interpret the observation of Laue oscillations for both GFO 004 and Pt 111 reflections as an evidence of the high crystallinity and smooth interface between GFO and Pt. Fitting the arrow marked oscillations, we obtain a thickness of 31 nm for GFO and 5 nm for Pt, which agrees with reflectometry measurements. The high-quality interface evidence is corroborated with the TEM images (Fig. 5.3 (a) and (b)) which show a sharp interface. The elemental mapping of the interface (Fig. 5.3 (c)) shows no interdiffusion between Pt and GFO.

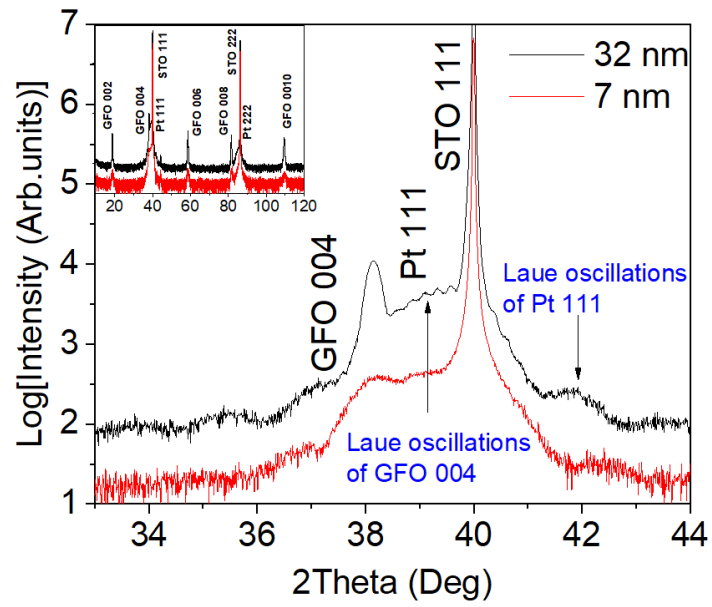


**Fig. 5.2 |  $\theta$ - $2\theta$  measurement for Pt(5 nm) /GFO //STO heterostructures grown by PLD, with a focus on the GFO 004 and STO 111 reflections. The Inset shows a full scan.**

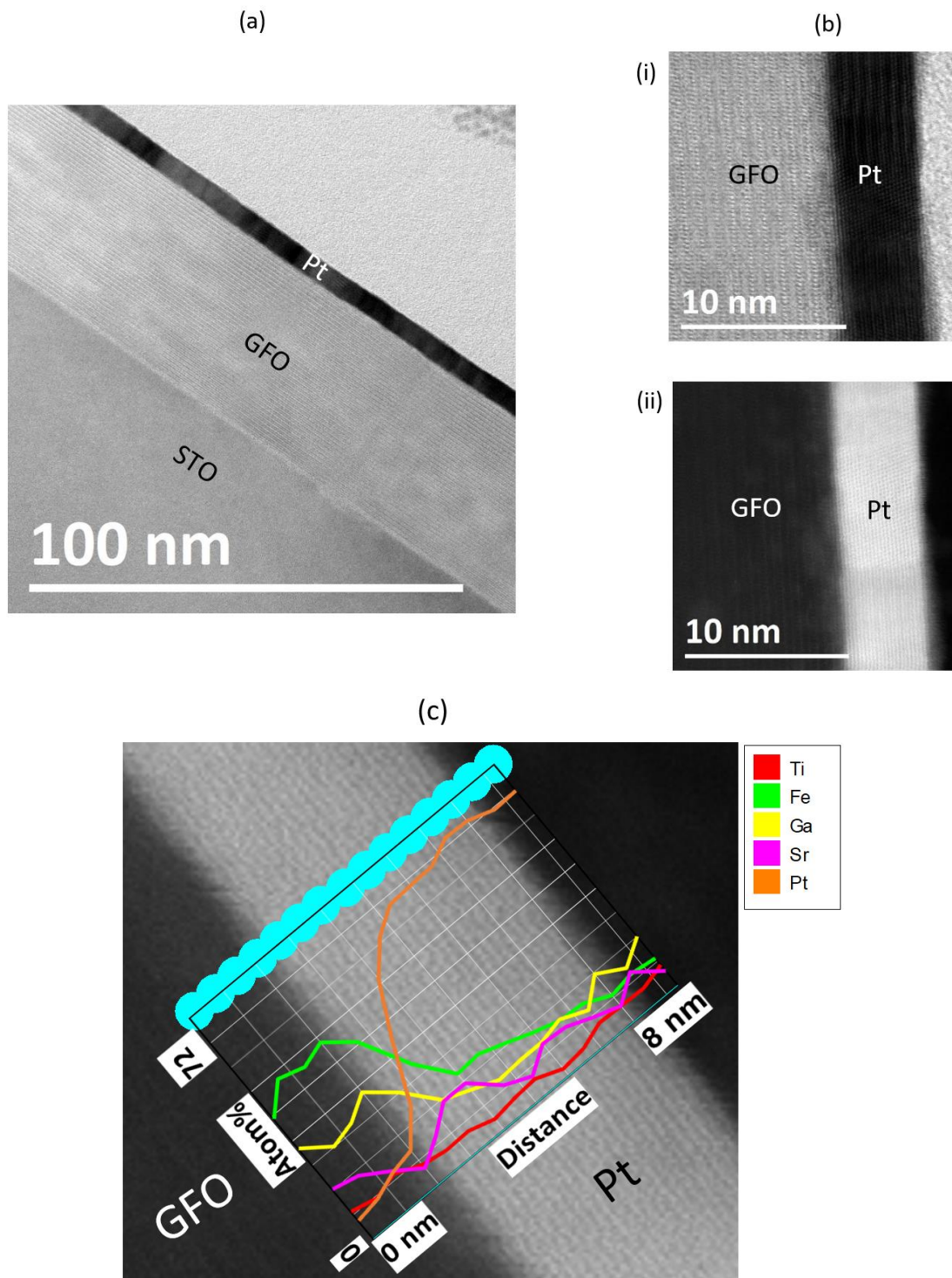


**Fig. 5.3 | Microscopic characterization of Pt/GFO//STO heterostructure.** (a) HR-STEM cross section image of heterostructure showing low roughness films and smooth interfaces. (b) zoomed-in view of the GFO/Pt interface in (i) bright and (ii) dark field modes. (c) elemental EDX analysis of the interface to map potential interdiffusion between Pt and GFO.

To investigate the effect of the Pt deposition on the magnetic properties of GFO, we have measured some hysteresis loops (Fig. 5.4 (a, b)) and FC/ZFC measurements (Fig. 5.5 (a, b)) by SQUID on G32 and G7 films. These curves show that the easy magnetic axis is in the plane of the GFO thin film for both G32 and G7 films. This result is in contradiction with the out-of-plane magnetization which was observed for the 7 nm standalone GFO film (without Pt on top). It appears as if the Pt deposition has changed the magnetic easy axis orientation for this film. A possible explanation could be that the surface anisotropy, which plays a dominant role in determining the easy magnetization axis at ultra-thin regimes, is altered due to a newly created interface between GFO and Pt. The saturation magnetization at 10 K is similar for both G32 and G7 samples, but at 300 K, it changes from 100 emu/cm<sup>3</sup> for G32 to 50 emu/cm<sup>3</sup> for G7.

The FC/ZFC curves in Fig. 5.5 (a, b) allow determining the ferrimagnetic ordering temperatures  $T_c$  for both films.  $T_c$  is of 364 K for G32 and 344 K for G7, that is a 20 K difference. This change is significant, and since  $T_c$  is within the 300 K range, this can explain why the magnetic moment is reduced from G32 to G7 at 300 K. Apart from  $T_c$ , the FC/ZFC curves do not show any anomalous transitions at different temperatures.

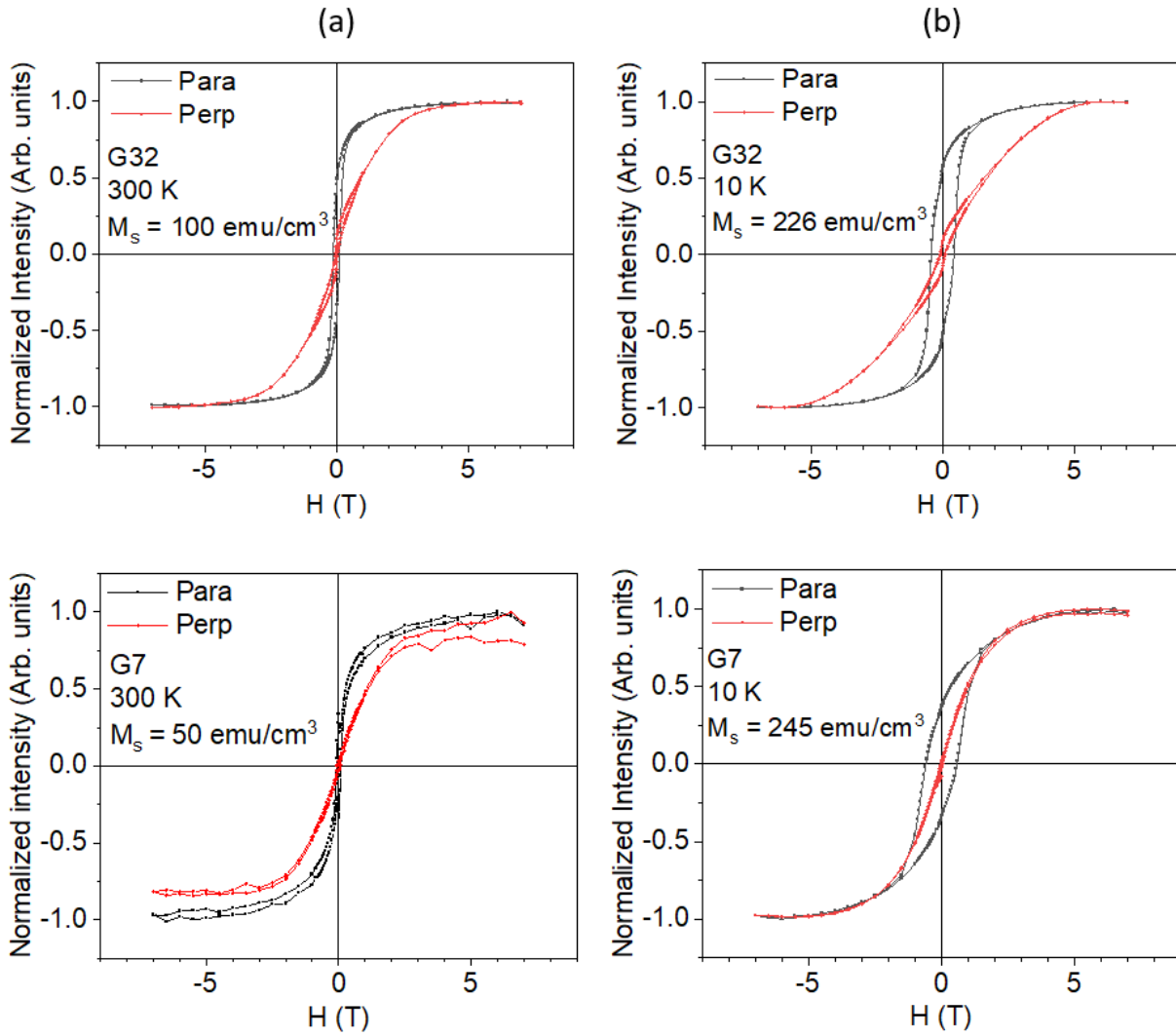


**Fig. 5.4 |** The magnetic hysteresis curves for G32 and G7 samples. (a) At 300 K. (b) At 10 K.

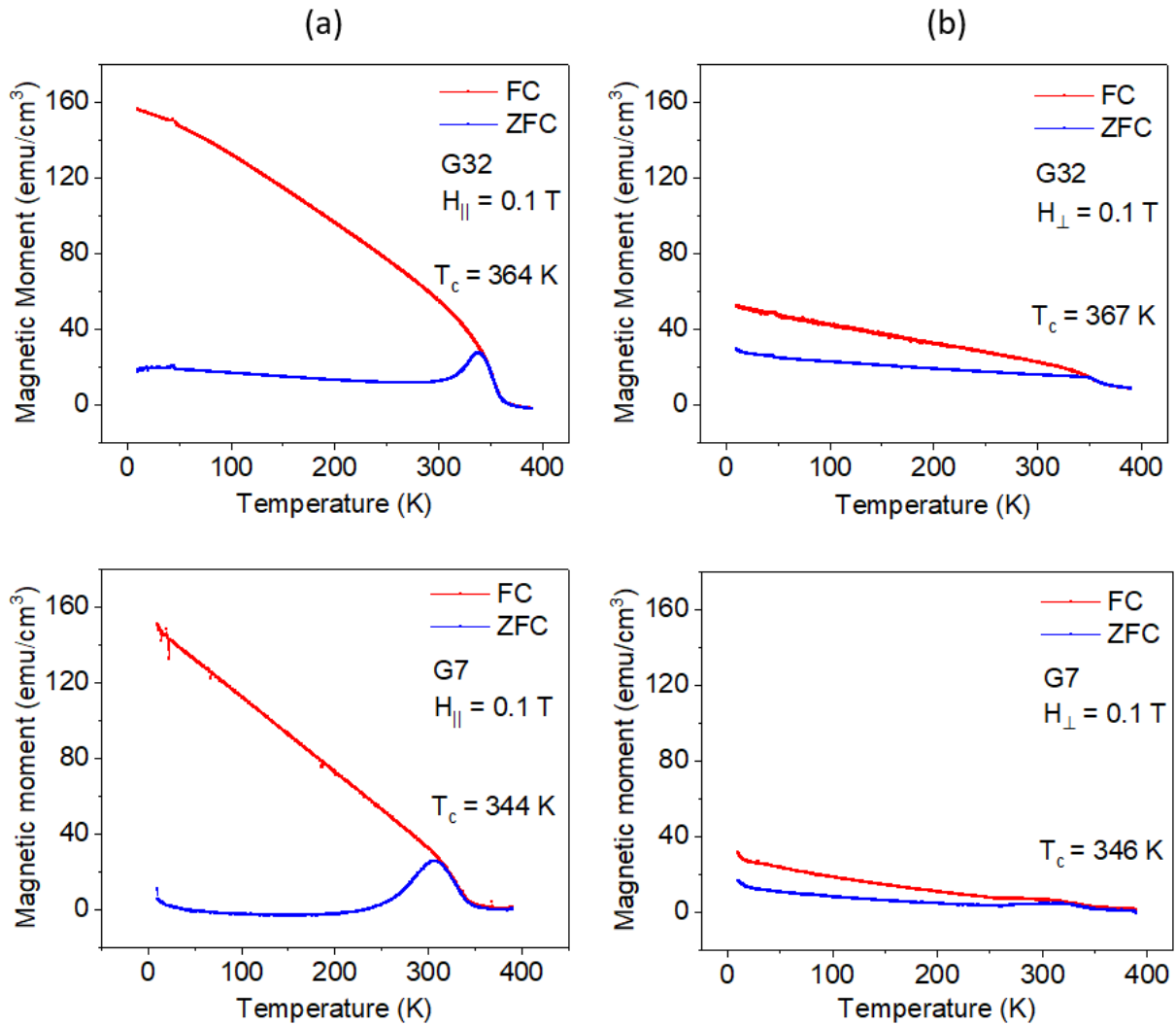


**Fig. 5.5 | The FC/ZFC curves for G32 and G7 samples. (a) In parallel mode. (b) In perpendicular mode.**

After characterizing the structural and magnetic properties of the GFO/Pt samples, we will now investigate the effects of the generation of spin currents in the Pt layer onto the magnetic properties of GFO.

### 5.1.2 Ferromagnetic Resonance (FMR) investigations

One of the premiere techniques to observe spin dynamics in ferromagnetic and ferrimagnetic materials, both in bulk and thin films, is Ferromagnetic Resonance (FMR). In the FMR method, we apply a constant static magnetic field  $H_0$ , and the magnetization dynamics is triggered using

a microwave radiofrequency (RF) in the 3-300 GHz frequency range. This process causes the total magnetization vector to precess around the effective magnetic field 'H<sub>eff</sub>,' as shown in Fig. 5.6 (a). The H<sub>eff</sub> consists of DC magnetic field, RF field component, demagnetization field, and magneto-crystalline anisotropy field. The precession is equivalent to Larmor precession, and the equation of motion for the magnetization vector during precession is described by the Landau-Lifshitz-Gilbert (LLG) equation of motion (see Fig. 5.6 (a)). The green part of the equation gives the precession motion due to field-like-torque experienced by the total magnetic moment, and the Gilbert damping gives the yellow part of the equation.

If the precession frequency equals the microwave RF frequency, resonance occurs in the magnetic material, and the RF frequency can be absorbed. This absorption and its derivative (an example is shown in Fig. 5.6 (b) and its inset) can yield some parameters of the magnetic material, such as the anisotropy constants and damping.

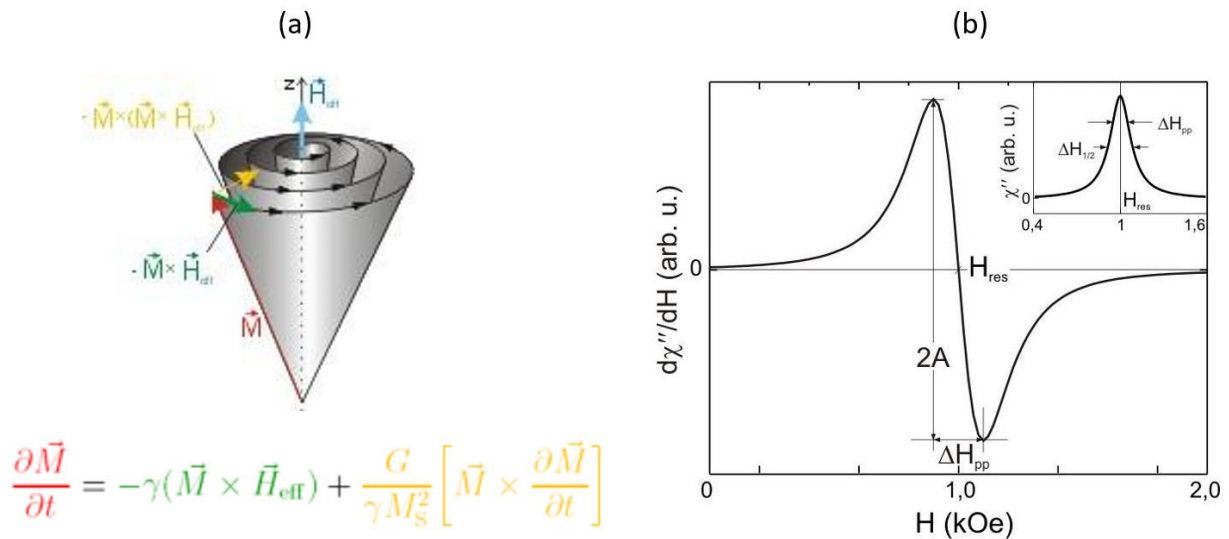


**Fig. 5.6 | The FMR technique.** (a) The schematic for FMR precession motion as described by the LLG equation of motion, (b) A typical derivative of microwave absorption curve shown in the inset. Adapted from ref. [21].

The idea behind studying GFO thin films with the FMR technique was two-fold. The first goal was to determine the anisotropy constants and damping parameters of GFO thin films; the second was to probe the effects of spin current injected from an adjacent Pt thin film on the spin dynamics of GFO in a GFO/Pt heterostructure.

The study has been performed in collaboration with our colleagues of the Institut Jean Lamour in Nancy. Unfortunately, no resonance condition could be found within the experimental limits of the set-up (47 GHz).

A literature review on the FMR studies performed on GFO in various different forms, from bulk to nanoparticles, but not including any thin films, allowed perceiving the stringent requirements of ultra-high frequencies and magnetic fields required to obtain resonance conditions <sup>[22–26]</sup> (Table 6.1). These references attribute the stringent requirement to a relatively high magnetic anisotropy in GFO, as well as to its ferrimagnetic nature. Thin films probably add to the difficulty for FMR measurements with issues such as strain, or shape and surface anisotropies <sup>[27]</sup>.

Compound and year (Approx. stoichiometry)	Type and morphology	Room Temperature Microwave frequency	Room Temperature Anisotropy Field
$\text{Ga}_{0.7}\text{Fe}_{1.3}\text{O}_3$ (1961) <sup>[22]</sup>	Grounded sphere small crystals	55 GHz	17 kOe
$\text{Ga}_{0.85}\text{Fe}_{1.15}\text{O}_3$ (1967) <sup>[23]</sup>	Spherical and small	70 GHz	25 kOe
$\text{Ga}_{0.85}\text{Fe}_{1.15}\text{O}_3$ (1968) <sup>[24]</sup>	Single crystal of parallelepiped shape	37 GHz	13 kOe
$\text{Ga}_{0.61}\text{Fe}_{1.4}\text{O}_3$ (2007) <sup>[25]</sup>	Nano particles sphere	54 GHz	19 kOe
$\text{GaFeO}_3$ (2018) <sup>[26]</sup>	Single Crystal	160 GHz (100 K)	~25 kOe (100 K)

**Table 5.1 | FMR studies of GFO in various stoichiometries and forms, with the experimentally observed resonance frequencies.**

Table 5.1 shows that the excitation of the spin dynamics in GFO requires frequencies which increase with decreasing Fe content within the x range [1.4 – 1], and are around 50 GHz for GFO compositions around  $\text{Ga}_{0.6}\text{Fe}_{1.4}\text{O}_3$  <sup>[28]</sup>. Oriented thin films could exhibit frequencies higher than its bulk counterpart, in the close sub-terahertz regime, due to reasons mentioned earlier. One should note that the Ga free isostructural compound  $\epsilon\text{-Fe}_2\text{O}_3$  exhibits a high-frequency sub-terahertz microwave frequency absorption of 190 GHz for nanoparticles <sup>[29]</sup>.

High-frequency materials are highly desirable in the technological applications of high-speed wireless communication <sup>[29]</sup> or as significant electromagnetic interference (EMI) absorbers for domestic/defense applications <sup>[25]</sup>.

Concerning our goal, since the possibility to observe the FMR dynamics of GFO demanded stringent instrumental criteria that were unfortunately beyond the current potential of the available instruments, we decided to move to other ways of observing the effect of SHE induced spin current from Pt to GFO.

### 5.1.3 Magneto-transport in Pt/GFO heterostructures

In this section, we will explore how magneto-transport phenomena in Pt are affected by an adjacent film of the magnetic insulator GFO. This study is important because Pt at its interface with a magnetic material can have additional exchange interaction combined with a 3d-5d hybridization path, which allows it to satisfy Stoner's criterion and become ferromagnetic in a few layers close to the interface<sup>[30–32]</sup>. Earlier magneto-transport studies in Pt with proximity to some magnetic insulators (MI) were conducted most notably in garnets, with  $\text{Y}_3\text{Fe}_5\text{O}_{12}$  (YIG) /Pt<sup>[33–37]</sup>, followed by spinel ferrites, with  $\text{NiFe}_2\text{O}_4$ /Pt<sup>[36]</sup>,  $\text{Fe}_3\text{O}_4$ /Pt<sup>[36]</sup> and  $\text{CoFe}_2\text{O}_4$ /Pt<sup>[38]</sup>. The recent demonstration of an electric field control of the Hall effect in  $\text{Bi}_{0.9}\text{La}_{0.1}\text{FeO}_3$ /Pt also broadens the systems' types to multiferroic and magneto-electric materials in proximity to Pt<sup>[39]</sup>.

Transport measurements have been performed on single and double Hall bars (Fig 5.7 (a, b)) lithographed on G32 and G7 GFO/Pt bilayers grown on STO(111) substrates. The single Hall bar pattern was used for some preliminary measurements. Double Hall bars were then used to avoid the contact resistance issue associated with the single Hall bar, especially for longitudinal measurements. For the patterned single Hall bar in a 2-probe Hall bar set-up, the longitudinal length ( $L$ ) = 100  $\mu\text{m}$ , width ( $w$ ) = 4  $\mu\text{m}$  and thickness ( $t$ ) = 5 nm, whereas, for the double Hall bar set up,  $L$  = 38  $\mu\text{m}$ ,  $w$  = 10  $\mu\text{m}$  and  $t$  = 5 nm.

The plane of the films is named 'xy', and the normal to the film 'z'.  $H_z$  ( $H_x$ ) refer to the magnetic field applied along the 'z' ('x') direction. The electric current density ' $J_e$ ' may be measured in both 'x' and 'y' directions. The resistivity  $\rho_{xx}$  is evaluated from voltage and current density measurements along the 'x' direction [ $V_x = (+V_L)-(+V_R)$  for double Hall bars and  $V_x = (+V_x)-(-V_x)$  for single Hall bars].  $\rho_{xy}$  is the Hall resistivity, with voltage measured along the 'y' direction and current density  $J_e$  measurements along the 'x' direction [ $V_{xy} = (+V_L)-(-V_L)$  for double Hall bars and  $V_{xy} = (+V_y)-(-V_y)$  for single Hall bars].

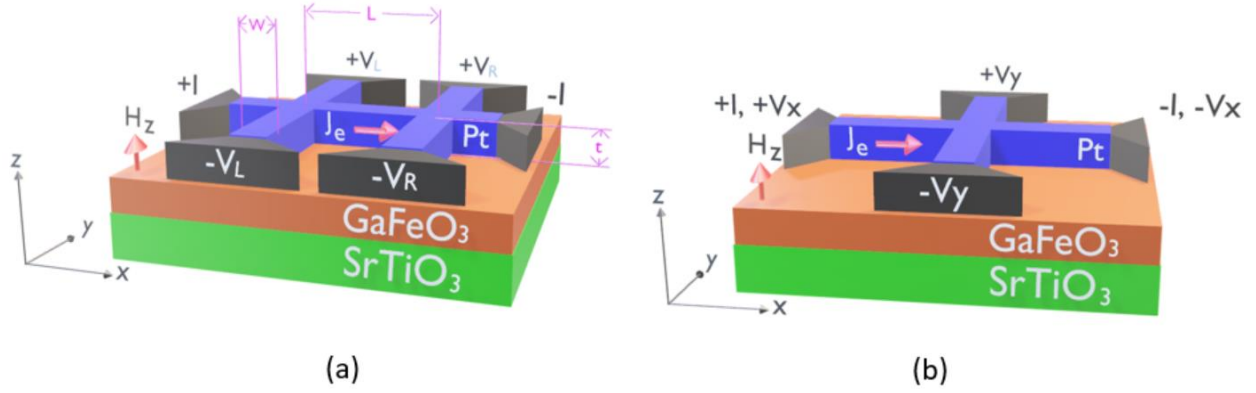


**Fig. 5.7 | 3D models of the lithographed Hall bars on GFO/Pt//STO (111) heterostructures. (a) double Hall bar with markings of length (L) , width (w) and thickness (t) and (b) single Hall bar.**

Magneto-transport in heavy metal (HM) / insulating ferromagnet (FM) heterostructures may be explained according to two different models.

A first one, depicted in Fig. 5.8 (a), implies the existence of some induced interfacial magnetism in the non-magnetic Pt, due to a magnetic proximity effect (MPE). Magneto-transport can then be described as that of traditional metallic ferromagnetic materials by equations 5.1 and 5.2 [37]:

$$\rho_{xx} = \rho_0 + \Delta\rho_{AMR}M_x^2, [M_x^2 \text{ is replaced by } \sin^2 \theta_{xz} \text{ in radial coordinates}] \quad (5.1)$$

$$\rho_{xy} = \Delta\rho_{AMR}M_xM_y + \rho_{AHE}M_z \quad (5.2)$$

where  $M_x$ ,  $M_y$ , and  $M_z$  are the magnetization unit vector components in the 'x,' 'y,' and 'z' directions, respectively.  $\rho_0$  is the intrinsic resistivity of platinum,  $\Delta\rho_{AMR}$  is the anisotropic magneto-resistivity due to the MPE induced anisotropic magnetoresistance (MPE AMR), and  $\rho_{AHE}$  is the anomalous Hall resistivity due to MPE induced anomalous Hall effect (MPE AHE). Theoretically, AMR and AHE contributions depending on the orientation of MPE induced magnetic Pt arises due to extrinsic spin-flip scattering mechanism or/and intrinsic mechanism depending on the band structure of Pt.

A second model, the spin Hall magnetoresistance (SMR) introduced by Nakayama *et al.* [40], depicted in Fig. 5.8 (b), does not necessitate the existence of any MPE. SMR arises only due to the spin Hall effect (SHE) and the inverse spin Hall effect (ISHE). When a charge current flows longitudinally in the nonmagnetic HM, a spin current is produced along the film normal direction by SHE. The spin polarization  $\sigma$  of this spin current is perpendicular to both charge and spin current densities,  $J_e$  and  $J_s$ , respectively, in agreement with  $\vec{J}_s = \theta_{SH} (\vec{\sigma} \times \vec{J}_e)$ , where  $\theta_{SH}$  is the spin Hall angle. The spin current can either be reflected or absorbed by the adjacent FM layer

depending on whether  $\sigma$  is parallel or perpendicular to the magnetization direction of this FM layer, respectively. The reflected spin current will produce an additional charge current through the inverse spin Hall effect (ISHE) which will lead to a decrease of the resistivity. The resistivity of the NM layer will therefore strongly depend upon the orientation of the FM magnetization. This type of magnetoresistance can dominate, in some instances, the resistivities measured in both the longitudinal and transverse modes.

Eq. (5.3) and (5.4) describe the contributions from this spin Hall magnetoresistance, denoted as  $\rho_1$  for the spin Hall induced anisotropic magnetoresistance (SH AMR) and  $\rho_2$  for the spin Hall induced anomalous Hall effect (SH AHE). Both  $\rho_1$  and  $\rho_2$  are negative <sup>[37]</sup>.

$$\rho_{xx} = \rho_0 + \rho_1 M_y^2, [M_y^2 \text{ is replaced by } \sin^2 \theta_{yz} \text{ in radial coordinates}] \quad (5.3)$$

$$\rho_{xy} = -\rho_1 M_x M_y + \rho_2 M_z \quad (5.4)$$

$\rho_{xx}$  is thus lowered by  $\rho_1$  according to the mechanism exposed above. The contribution of the SMR mechanism to  $\rho_{xy}$  is a consequence of the magnetization component in the 'z' direction, which changes the orientation of the SHE-induced spin current and of the resulting reflected spins. This creates a transverse voltage through ISHE, which lowers resistivity by  $\rho_2$ . SMR is thus a pure spin current based effect and is very sensitive to interfacial scattering.

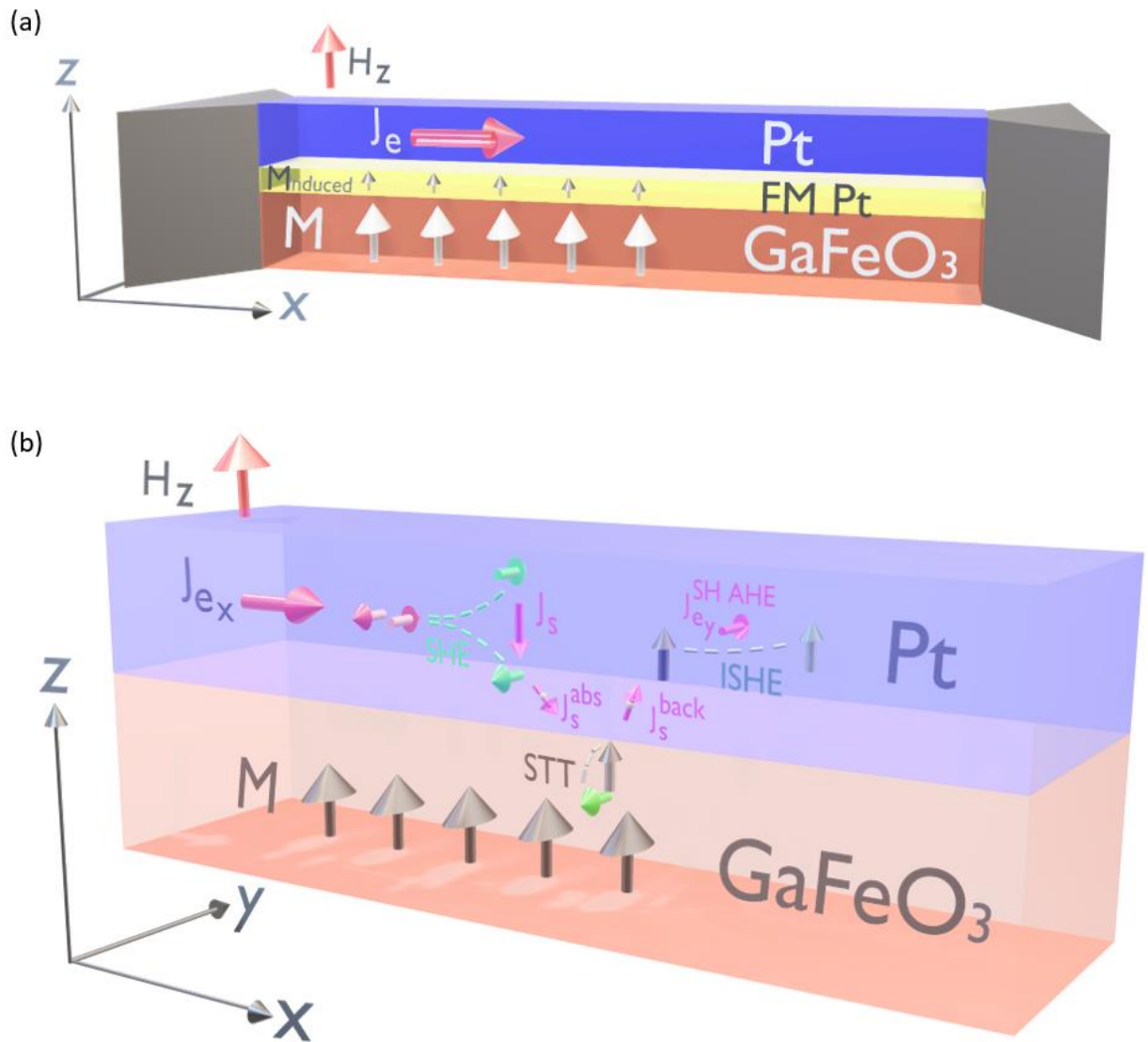


**Fig. 5.8 | 3D models of the Pt/GFO heterostructure in a magnetic field  $H_z$ , allowing to perceive the magneto-transport phenomena.** This can be a result of (a) magnetic proximity effects (MPE) - a magnetic Pt phase can be seen formed at the interface giving rise to magnetoresistance. (b) spin Hall magnetoresistance, with all spin Hall induced contributions for a field applied in the 'z' direction - a change in color indicates a change of direction.

Transport properties measured in G7 and G32 are described in Fig. 5.9 - 5.10 and Fig. 5.11 – 5.13, respectively.

The values of the longitudinal resistivity shown in the plots are extracted from longitudinal resistance values according to Eq. 5.5 and 5.6.

$$R_{xx} = \frac{\rho_{xx}L}{w*t} \quad (5.5), \quad \rho_{xx} = \frac{R_{xx}*w*t}{L} \quad (5.6).$$

For the transverse resistivity, the voltage measured is in the direction perpendicular to the longitudinal current. The current injected in the 'x' direction creates a transverse electric field  $E_{xy}$  in the 'y' direction due to the combination of the ordinary and anomalous Hall effects. This transverse electric field over a distance 'w' (see Fig 5.7) results in a transverse voltage  $V_{xy} = E_{xy} * w = \rho_{xy} * j_{xx} * w$ , with  $j_{xx} = \frac{i_x}{w*t}$ , the current density, which leads to Eq. 5.7 shown below. Magnetoresistance, as described earlier, is the change in the measured resistivity due to an applied magnetic field and is defined by Eq. 5.8.

$$\rho_{xy} = \frac{V_{xy}}{j_{xx}*w} = R_{xy} * t \quad (5.7)$$

$$MR = \frac{\rho_H - \rho(H=0)}{\rho(H=0)} = \frac{\Delta\rho_{xx}}{\rho_{xx}} \quad (5.8)$$

The curves in Fig 5.9 (a)-(b) and Fig 5.9 (c)-(d) are  $\rho_{xx}$  measurements performed on G7 and G32, respectively, for varying magnetic fields applied in the 'z' direction, at high and low temperatures (300 and 20 or 5 K). The MR is small (a few hundredths of percent's) and positive for 300 K, whereas it is more significant (a few tenths of percent's) and reverses its sign, for both G7 and G32, for the low temperatures. The positive high field MR at 300 K is usually attributed to the Lorentz field-induced effect, whereas the negative MR at low temperature is ascribed to the independent moments at the interface which align at high fields, thus reducing the spin scattering, and hence affecting the transport <sup>[41]</sup>.

These first measurements allow establishing the existence of a MR, even if its origin remains to be determined.

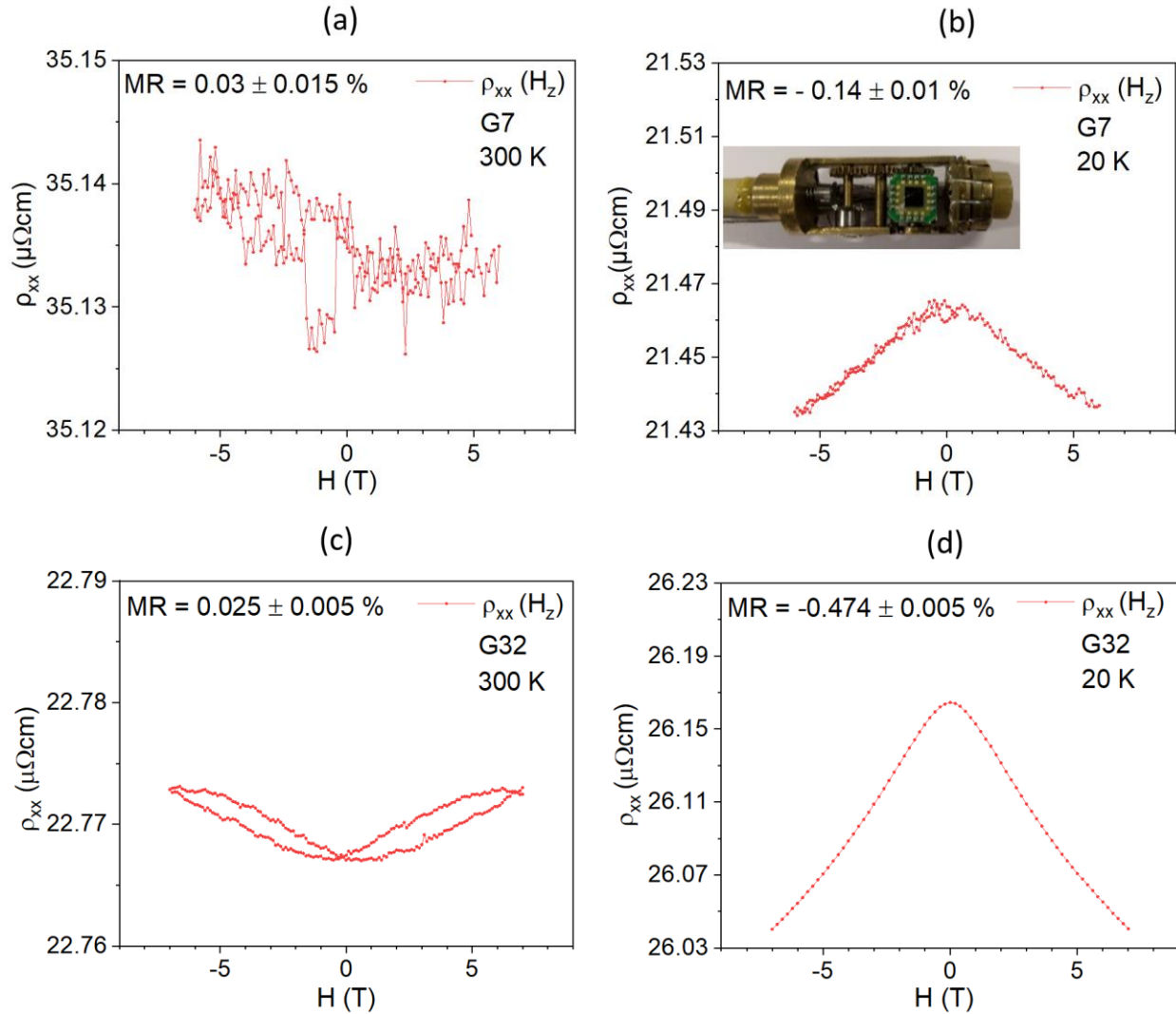


**Fig. 5.9 | Longitudinal resistivity vs.  $H_z$ , measured on a single Hall bar patterned onto G7. For (a) 300 K. (b) 5 K. Inset in (b) shows the experimental set-up of the PPMS used to rotate the sample (changing the relative magnetic field direction).**

**Longitudinal resistivity vs.  $H_z$  measured on a double Hall bar patterned onto G32. For (c) 300 and (d) 5 K.**

In order to determine more precisely the temperature at which the MR sign changes, we perform  $\rho_{xx}$  vs.  $H_z$  measurements in a wide temperature range between 300 and 20 K, for the G32 sample. We complete the set of data by performing the same measurements for the  $H_x$  and  $H_y$  directions, in order to investigate the effect of the magnetic field orientation on the transition temperature. For a better illustration of the results of these experiments, we plot the MR, i.e.  $\Delta\rho_{xx}/\rho_{xx}$  vs.  $H_z$  (and  $H_x$ ,  $H_y$ ) in Fig. 5.10 (a) (and (b), (c)), respectively. We can observe a clear change in the sign

of the MR with temperature, for all  $H_x$ ,  $H_y$ , and  $H_z$  directions. The plot of the evolution of MR at 7 T ( $\Delta\rho_{xx}/\rho_{xx}$  at  $H = 7$  T) with temperature (Fig. 5.10 (d)) shows that its sign reversal transition is within the 100-140 K temperature range for the three axes directions.

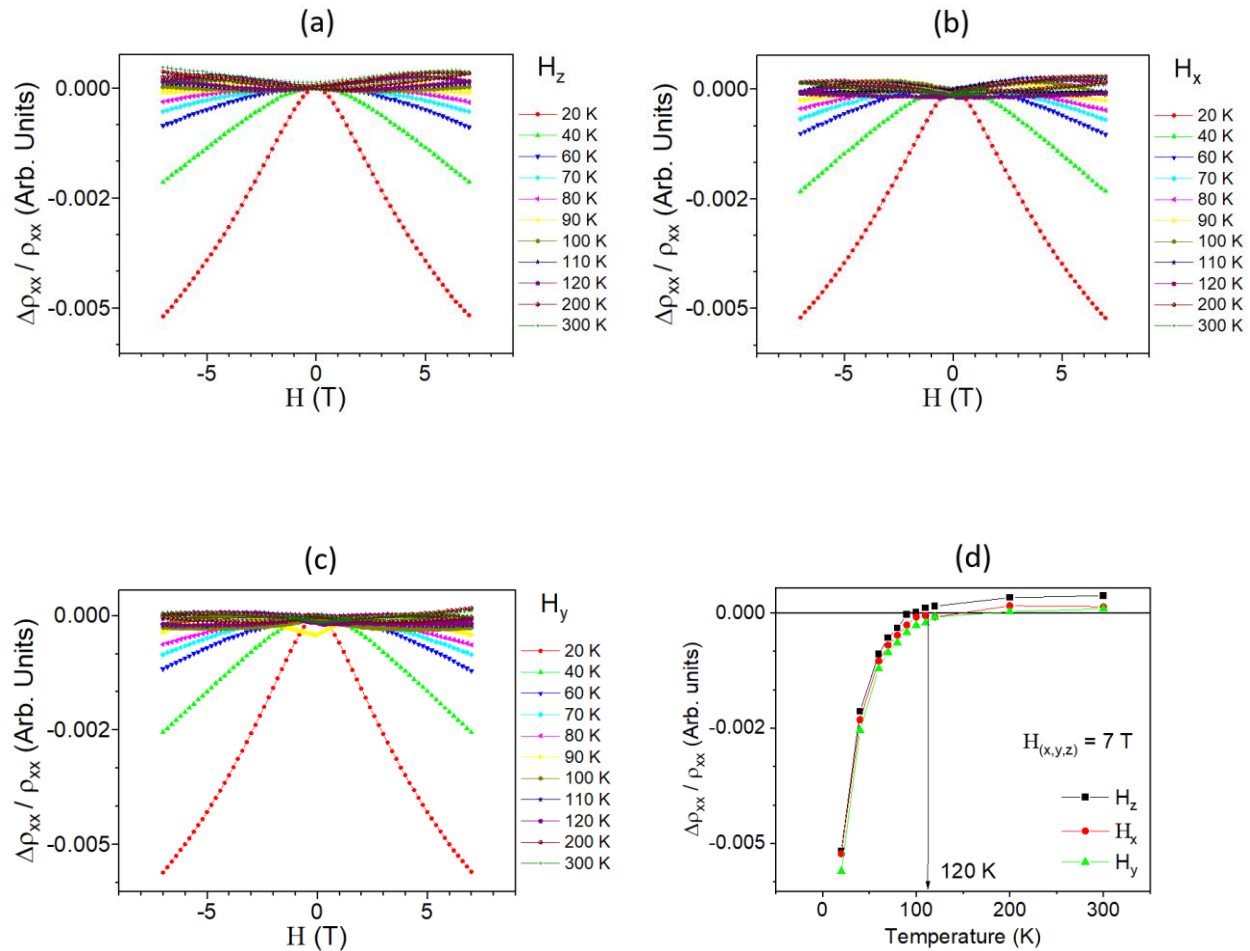


**Fig. 5.10 | Longitudinal MR  $\Delta\rho_{xx}/\rho_{xx}$  measured on a double Hall bar patterned onto G32 at various temperatures.** For external magnetic fields oriented along the (a) z direction. (b) x direction. and (c) y direction. (d) Temperature dependence of the longitudinal MR at 7 T for the various fields orientations  $H_z$ ,  $H_x$ , and  $H_y$ .

The resistivity curves in Fig. 5.9 (a-b) and Fig. 5.10 (a-c), do not saturate even at magnetic fields beyond the magnetic saturation measured by SQUID. This is caused by the independent moments at the interface which do not let the high field MR saturate <sup>[41]</sup>. Another factor is the highly anisotropic nature of magnetism in the GFO films, which induces high anisotropy for the induced magnetic Pt as well through magnetic proximity effect that will inhibit a saturation point even at

high temperatures. Hence, a quantitative MPE-AMR or SH-AMR cannot be computed just from these measurements.

Fig. 5.11 (a) and (c) shows the transverse Hall resistivity  $\rho_{xy}$  vs.  $H_z$  for both the G7 and G32 heterostructures, measured at various temperatures. These measurements are corrected from an offset by fixing  $\rho_{xy} = 0$  for  $H = 0$ . This simply corresponds to the elimination of the ordinary magneto-resistivity (OMR) contribution, due to the temperature variation. Fig 5.12 (a) and Fig. 5.12 (b) show the temperature variations of the longitudinal and transverse resistivities  $\rho_{xx}$  and  $\rho_{xy}$  at  $H = 0$  T, i.e. the OMR contributions for both G7 and G32 heterostructures, respectively. We must also consider the effects of the ordinary Hall resistance (OHR), due to the Lorentz force applied onto the carriers. It gives a contribution which is linear with the applied magnetic field and dominates the curve at high magnetic fields. Fig 5.11 (b) and Fig 5.11 (d) show the transverse Hall resistivity variations with the applied magnetic field, for various temperatures, after subtracting the OHR, for G7 and G32, respectively. The remaining resistivity,  $\rho_{xy-AH}$ , results only from the contribution of the various anomalous Hall effects, and neither from MPE AMR or SH AMR, as indicated by Eq. 5.2 and 5.4. for such a case in which the magnetic field is applied in the  $H_z$  direction (the magnetic unit vector is hence  $M_z$ ).

The  $\rho_{xy-AH}$  curves show hysteresis-like loops, which tends to indicate that the transverse resistivity has a significant contribution from interactions with the magnetic GFO. It has been shown that these hystereses-like  $\rho_{xy-AH}$  curves can not only be explained by the existence of induced magnetic Pt due to MPE-AHE (Fig 5.8 (a)) but also can be explained by SH-AHE contributions (Fig 5.8 (b)) or perhaps a combination of both <sup>[41]</sup>.

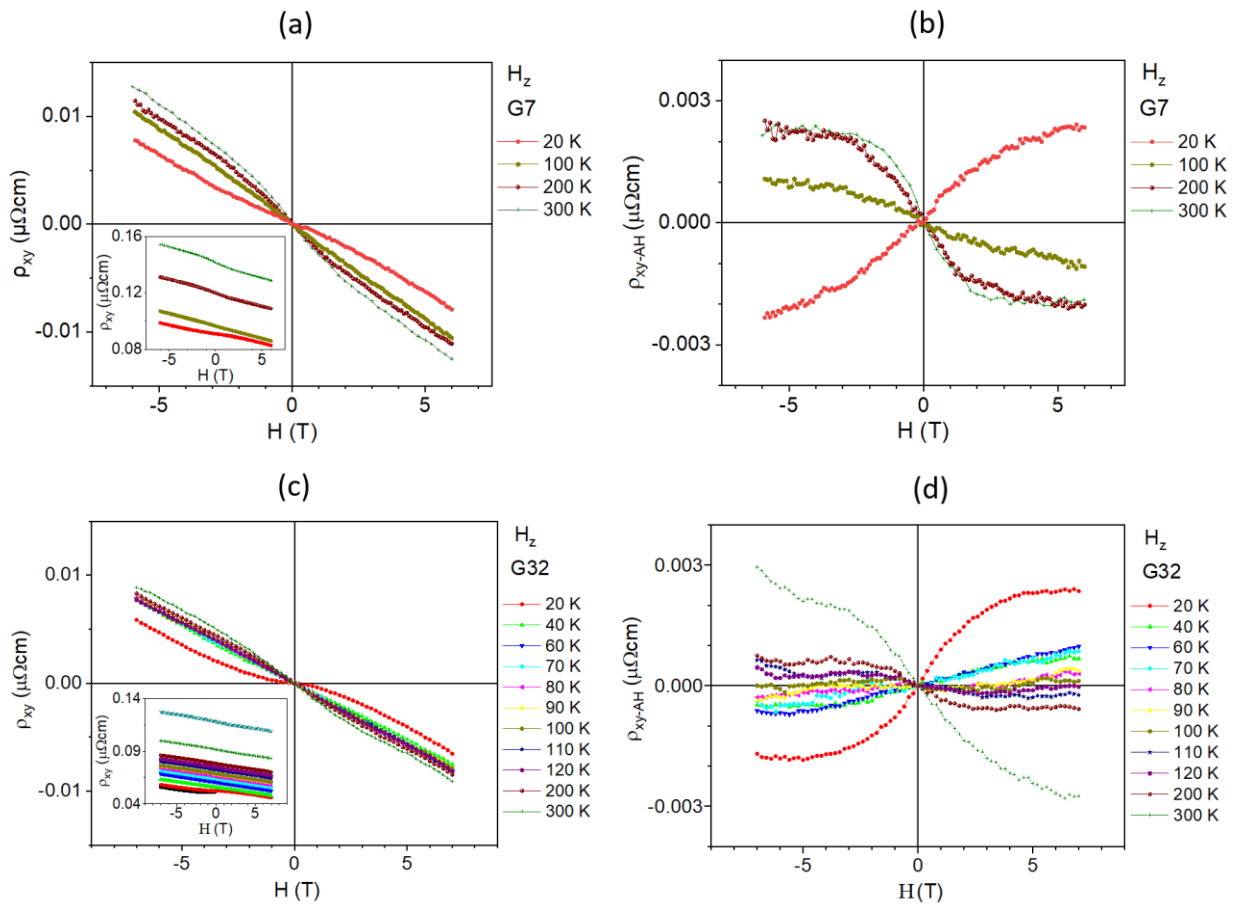


**Fig. 5.11 | Transverse Hall resistivity measurements on a single Hall bar patterned onto G7 for the magnetic field direction  $H_z$ .** (a) The measurements after correcting for ordinary magnetoresistance (OMR). The Inset shows the actual measurements without offset. (b) Contribution of the anomalous Hall effect to the transverse resistivity, as calculated by subtracting the linear contribution of the ordinary Hall effect from the transverse Hall resistivity.

**Transverse Hall resistivity measurements on a double Hall bar patterned onto G32 for the magnetic field direction  $H_z$ .** (c) The measurements after correcting for ordinary magnetoresistance (OMR). The Inset shows the actual measurements without offset. (d) Contribution of the anomalous Hall effect to the transverse resistivity, as calculated by subtracting the linear contribution of the ordinary Hall effect from the transverse Hall resistivity.

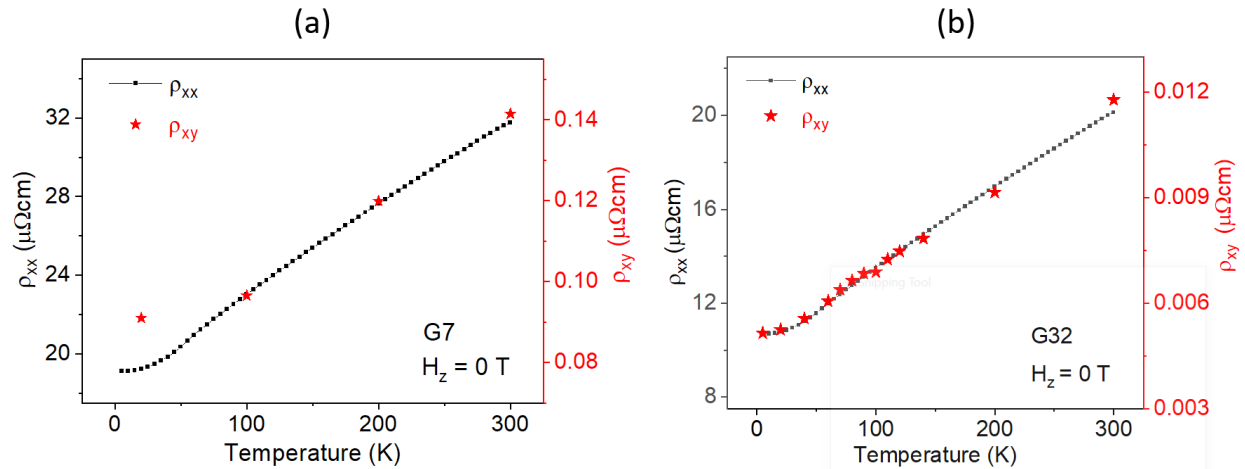


**Fig. 5.12 | Temperature dependence of the longitudinal ( $\rho_{xx}$ ) and transverse ( $\rho_{xy}$ ) resistivities with no applied field. (a) For G7. (b) For G32.**

It is interesting to note that there is a flipping of the anomalous Hall resistivity curves with temperature. Fig. 5.13 (a) and Fig. 5.13 (b) show the temperature evolution of the resistivity value at the magnetic saturation  $\rho_{sat}$  ( $\rho_{sat}$  is calculated as  $\{\rho_{sat}(-7T) - \rho_{sat}(7T)\}/2$ ), for G7 and G32, respectively. In both cases, we observe the sign change of  $\rho_{sat}$ , at around 100 K. Such a flipping has been observed in many other FM/Pt layers and has been explained either by some changes at the Fermi level in the electronic band structure of Pt [42,43] or as a fingerprint of the magnetic monopole in the crystal momentum space of Pt [44,45]. Both explanations rely on the Berry phase formalism and hint that the dominant mechanism for the AHE effects observed here is mostly intrinsic.

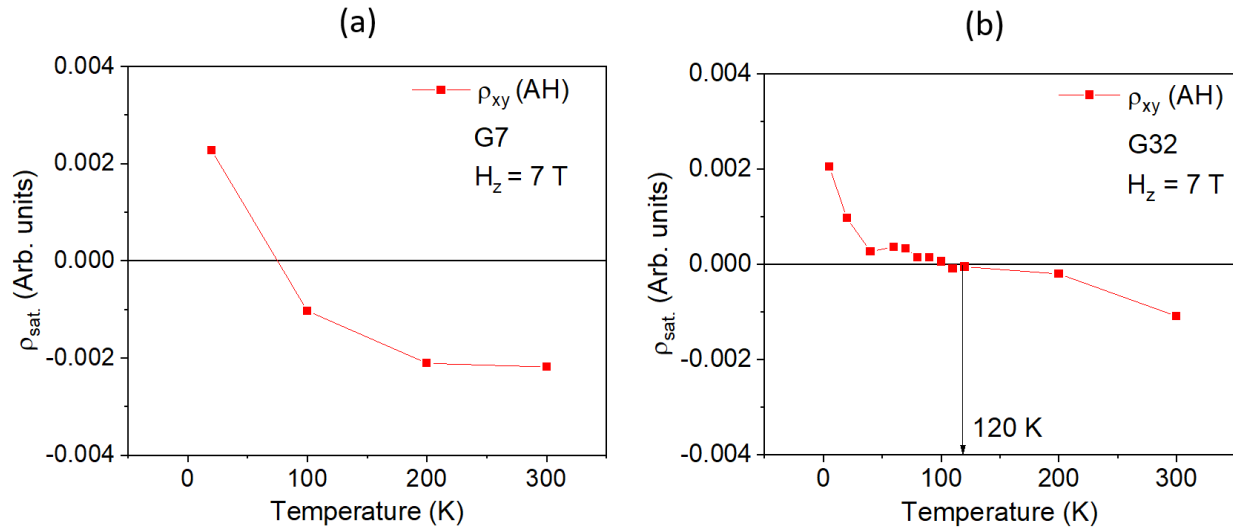


**Fig. 5.13 | Temperature dependence of the transverse resistivity at saturation,  $\rho_{\text{sat}}$ .** (a) As calculated from the values of  $\rho_{xy\text{-AH}}$  [Fig 5.11 (b)] for G7. (b) As calculated from the values of  $\rho_{xy\text{-AH}}$  [Fig 5.11 (d)] for G32.

#### 5.1.4 Differentiating between AMR and SMR

On the grounds of a possible integration of GFO/Pt heterostructures (as other FM/HM) in the next-generation devices, there arises a need to better understand the underlying effects and quantitatively analyze the possible contributions from MPE and SMR and identify the dominant mechanisms. This becomes especially important at low temperatures since the interfacial contributions become more important due to increased mean-free path. It is impossible to distinguish between MPE and SMR phenomena utilizing the measurements shown until now since all measurements are with either  $M_x$  or  $M_z$  unit vector orientation, contributing to both AMR and SMR.

One possible way to distinguish between the MPE and SMR contributions is by inserting a non-magnetic metal like Cu, eliminating the possibility of MPE effects and leaving only SMR effects to be quantified. However, this introduces additional Cu/GFO and Cu/Pt interface issues, which could in turn have some impact on the SMR.

Alternatively, another possible way to separate MPE and SMR contributions is by performing angle-dependent measurements with the magnetic field in either the 'xz' or the 'yz' planes, while the current density  $J_e$  and the measured resistivity  $\rho_{xx}$  are in the 'x' direction <sup>[41]</sup>. This can be understood from Eq. 5.1 and 5.3 : the MPE AMR depends on  $M_x$ , and a rotation in the 'yz' plane will have no effect on it, whereas the SH AMR depends on  $M_y$  and a rotation in the 'xz' plane will have no effect on it. The schematics of the origin of the MPE induced AMR for a magnetic field applied along  $H_x$ , and of the Spin Hall induced AMR for a magnetic field applied along  $H_y$  are depicted in Fig. 5.14 (a, b). The MPE induced AMR shown in Fig. 5.14 (a) originates from the fact

that  $M$  is parallel to the current direction. The SHE induced AMR, shown in Fig. 5.14 (b), originates from the fact that  $M$  is parallel to the spins of the electrons of the spin Hall effect generated spin current, which prevents the spins to be absorbed by the FM and causes them to be reflected into Pt.

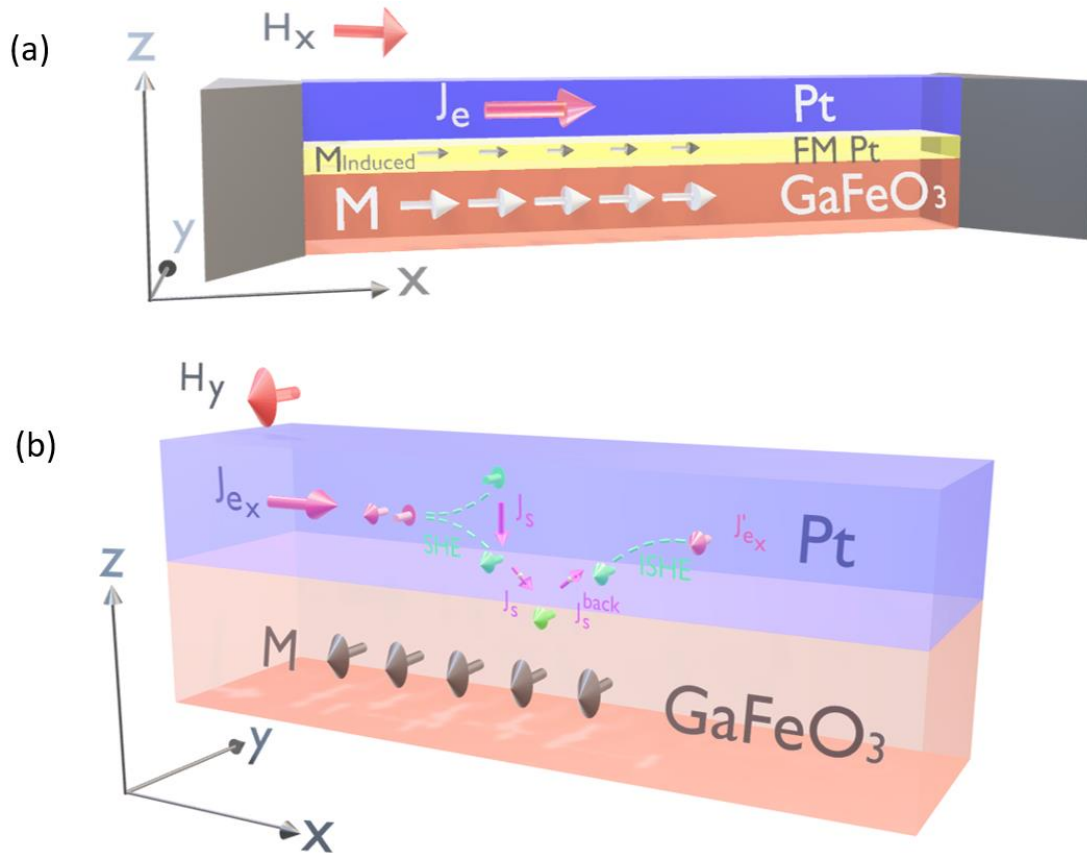


**Fig. 5.14 | Schematic drawings to explain transverse anomalous Hall resistivity measurements.** (a) For the MPE induced AMR due to a partial magnetization of Pt at the interface for a field along  $H_x$ . (b) For the SH induced SMR due to the reflection of the spin current back to Pt for a field along  $H_y$ .

The schematic for angular measurements on STO//GFO/Pt with current density  $j_e$  in the 'x' direction and an  $\alpha$  angle in the plane 'xz' and  $\beta$  angle in the plane 'yz' is shown in Fig. 5.15 below. For the experiments, the  $\alpha$  and  $\beta$  angles were limited to  $90^\circ$  rotation, and conventionally, the 'z' direction is kept as the  $90^\circ$  angle. We measure  $\rho_{xx}$  at  $H = 7$  T while rotating the sample in  $\beta$  and  $\alpha$  angles. These angle-dependent measurements are performed for the G32 sample at various temperatures. We plot the  $\beta$  dependence of  $\frac{\rho(\beta) - \rho_z}{\rho_z}$  and the  $\alpha$  dependence of  $\frac{\rho(\alpha) - \rho_z}{\rho_z}$ , for various

temperatures, as shown in Fig. 5.16 (a, b), respectively. The  $\beta$  measurements show that the resistivity value decreases when going from  $H_z$  to  $H_y$  at all temperatures, and a noticeable change in resistance is observed with a periodic oscillation with a period of  $180^\circ$ . The  $\alpha$  measurements also show that the resistivity value decreases when going from  $H_z$  to  $H_x$  but with a minor change in resistivity, and no unambiguous periodic oscillation is observed, possibly due to the limited range of our measurement. The  $\beta$  measurements profile are well fitted with  $\cos^2 \beta$  and SMR values of  $\frac{\rho_y - \rho_z}{\rho_z}$ , are extracted. Due to the limited angle measurement range, the  $\alpha$  profile could not be fitted with  $\cos^2 \alpha$  and the MPE AMR values of  $\frac{\rho_x - \rho_z}{\rho_z}$  are not directly extracted.

In order to still give an evaluation of the MPE AMR values, we used the  $\frac{\rho(\alpha) - \rho_z}{\rho_z}$  measurements at  $\alpha = 0^\circ$ . We are comforted in that by the fact that the values of  $\frac{\rho_y - \rho_z}{\rho_z}$  (SMR) extracted from the  $\beta$  measurements are same as the values of  $\frac{\rho(\beta) - \rho_z}{\rho_z}$  measured at  $\beta = 0^\circ$ . Hence, assuming that the  $\alpha$  measurements are periodic, we extracted the  $\frac{\rho_x - \rho_z}{\rho_z}$  (or MPE AMR) values from  $\frac{\rho(\alpha) - \rho_z}{\rho_z}$  measurements at  $\alpha = 0^\circ$ .

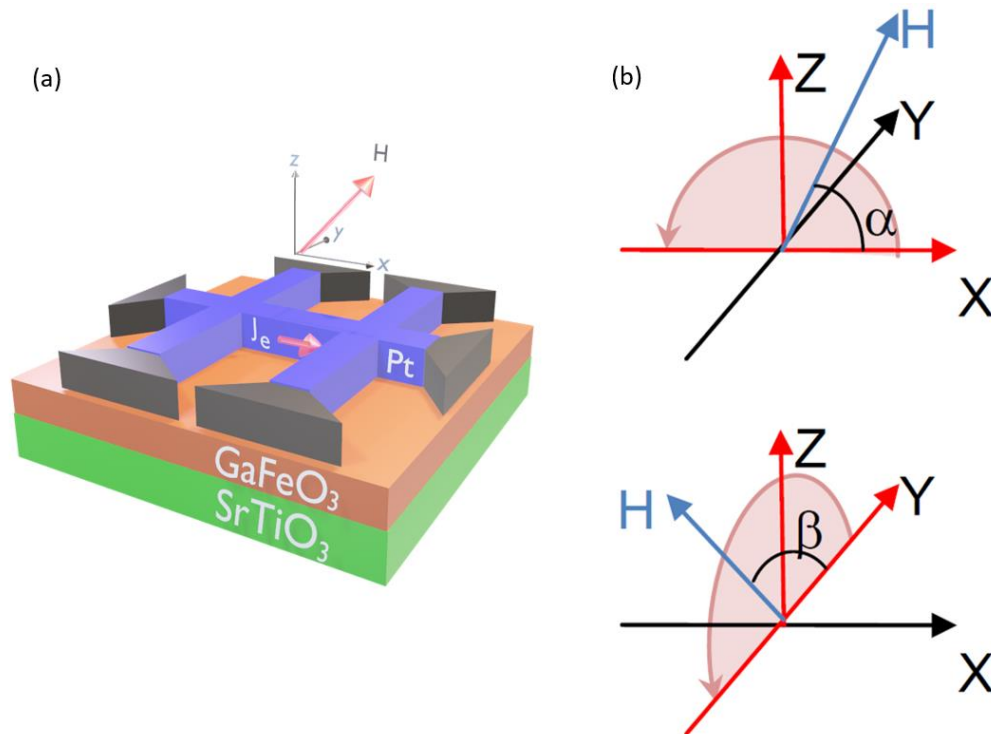


**Fig. 5.15 | Types of angular measurements geometries envisaged.** (a) A schematic for G32. (b) The  $\alpha$  angle measurement in the x-z plane and  $\beta$  angle measurement in the y-z plane. Adapted from ref. [36].

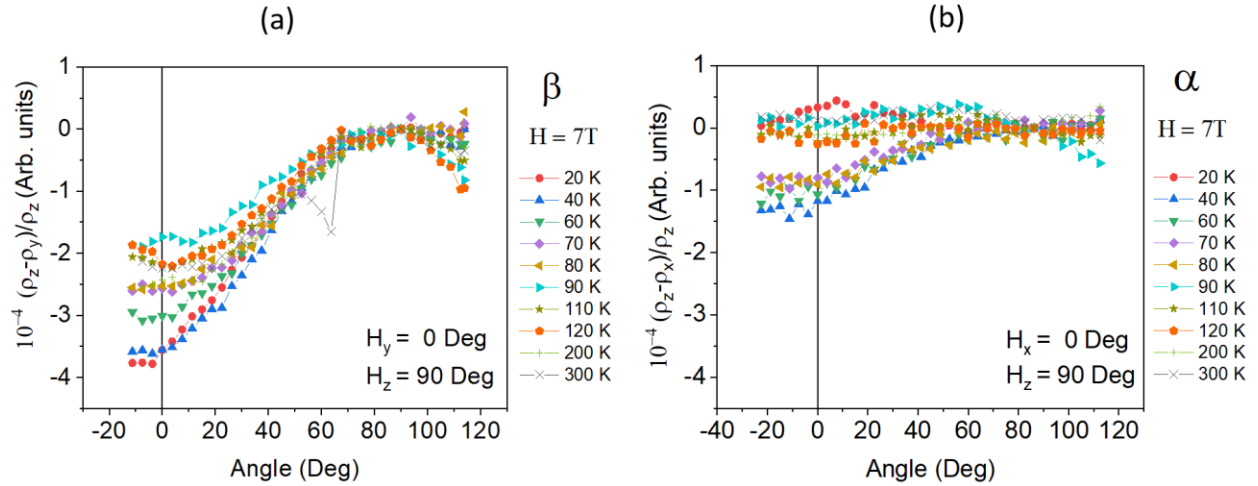


**Fig. 5.16 | Angular measurements at various temperatures for G32.** (a)  $\frac{\rho(\beta) - \rho_z}{\rho_z}$  vs.  $\beta$ . (b)  $\frac{\rho(\alpha) - \rho_z}{\rho_z}$  vs.  $\alpha$ .

This extracted SMR and MPE AMR values are plotted in Fig. 5.17. The SMR contribution is more important than the MPE AMR contribution for our GFO/Pt heterostructures. The MPE AMR contribution, and therefore the proximity effect, is negligible at temperatures higher than approximately 100 K, for which only SMR is present. This phenomenon has also been observed for YIG/Pt and YIG/Pd samples [41].

The SMR value measured for the GFO/Pt heterostructures is about  $2 \cdot 10^{-4}$  at 300 K and  $4.5 \cdot 10^{-4}$  at 20 K. This is identical to what is observed in YIG/Pd heterostructures and only slightly less than what is observed YIG/Pt ( $4 \cdot 10^{-4}$  at 300 K and  $6 \cdot 10^{-4}$  at 20 K) [41]. We notice the existence of a minimum in the SMR measurements in the 90-140 K range. A less pronounced but similar feature is also seen in the MPE AMR temperature profile. Such a variation has also been observed in YIG/Pd and YIG/Pt at a transition temperature of 100 K at low magnetic fields and vanishes for high magnetic field measurements [41]. It has recently been shown theoretically and numerically that the orbital hybridization of the magnetic material plays a role in the magnetoresistance, most probably in relation with spin-orbit coupling [46]. This minimum is thus to be put in perspective with the modification of the spin-orbit coupling observed in GFO near 120 K via our XMCD study. Since both SMR and AMR contributions come from the interaction of charge current flowing in Pt with the magnetic properties (correlated spins) in GFO, it is then possible to hypothesize a link between the non-monotonous change in spin-orbit coupling at 120K with the non-monotonous change in SMR/AMR measurements observed at 90-140K temperature.

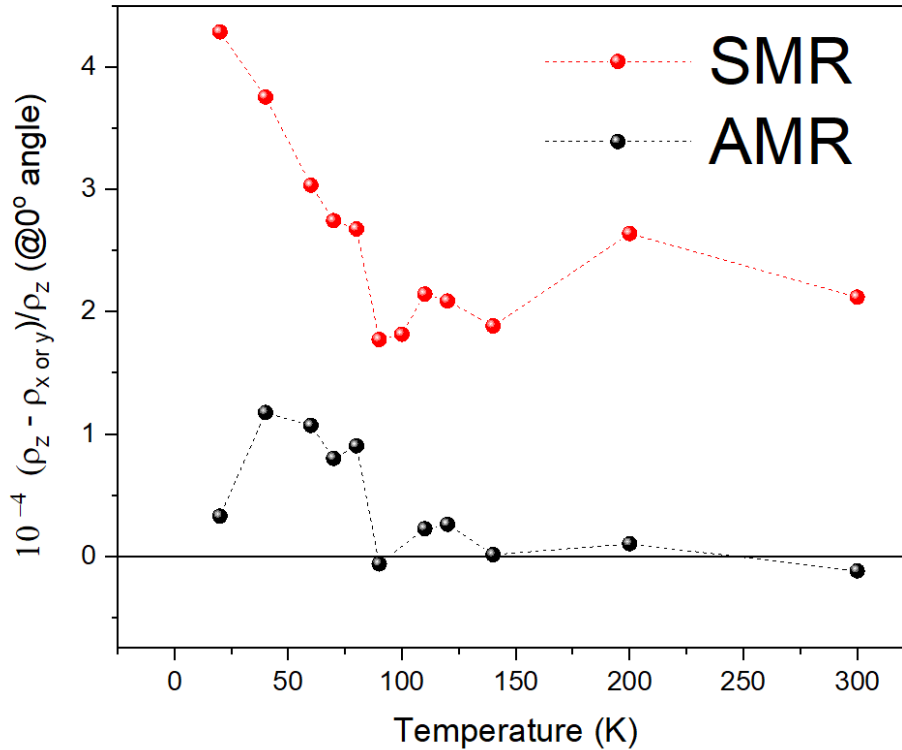


**Fig. 5.17 |** Temperature dependence of the MPE AMR and SMR as deduced from the  $\frac{\rho(\beta) - \rho_z}{\rho_z}$  and  $\frac{\rho(\alpha) - \rho_z}{\rho_z}$  values measured at zero degree angle for both  $\beta$  and  $\alpha$ , respectively.

### 5.1.5 Conclusion

A FM/HM heterostructure with GFO as the FM and Pt as the HM was envisaged for future spin-orbit torque devices with magnetic field-free control. We have demonstrated the highly crystalline and oriented growth of Pt over GFO, with a sharp interface between them, which makes the heterostructure suitable for spin currents transparency. The hard magnetism in GFO probably results in FMR frequencies superior to those we could access to, and it was not possible to observe FMR in GFO. To observe the interactions between the spin current from Pt and the GFO magnetic orientation, we have performed some magneto-transport measurements. The transport mechanisms at the GFO / Pt interface need to be elucidated to optimize the spin-momentum transfer efficiency through the interface. Two main mechanisms were considered : MPE AMR and SMR. We have shown *via* angle-dependent measurements that SMR is the dominant mechanism at all temperatures and is the only mechanism to be considered near room temperature.

Overall, we conclude that this study leads to a better understanding of the spin-current interactions with the magnetization of this important magneto-electric multiferroic GFO.

## 5.2 References

- (1) Atkins, P. W.; Friedman, R. S. *Molecular Quantum Mechanics*; Oxford university press, **2011**.
- (2) Ando, K.; Takahashi, S.; Harii, K.; Sasage, K.; Ieda, J.; Maekawa, S.; Saitoh, E. Electric Manipulation of Spin Relaxation Using the Spin Hall Effect. *Physical review letters* **2008**, *101* (3), 036601.
- (3) Miron, I. M.; Gaudin, G.; Auffret, S.; Rodmacq, B.; Schuhl, A.; Pizzini, S.; Vogel, J.; Gambardella, P. Current-Driven Spin Torque Induced by the Rashba Effect in a Ferromagnetic Metal Layer. *Nature materials* **2010**, *9* (3), 230–234.
- (4) Liu, L.; Pai, C.-F.; Li, Y.; Tseng, H. W.; Ralph, D. C.; Buhrman, R. A. Spin-Torque Switching with the Giant Spin Hall Effect of Tantalum. *Science* **2012**, *336* (6081), 555–558.
- (5) Rojas-Sánchez, J.-C.; Laczkowski, P.; Sampaio, J.; Collin, S.; Bouzehouane, K.; Reyren, N.; Jaffrès, H.; Mougín, A.; George, J.-M. Perpendicular Magnetization Reversal in Pt/[Co/Ni]<sub>3</sub>/Al Multilayers via the Spin Hall Effect of Pt. *Applied Physics Letters* **2016**, *108* (8), 082406.
- (6) Garello, K.; Miron, I. M.; Avci, C. O.; Freimuth, F.; Mokrousov, Y.; Blügel, S.; Auffret, S.; Boule, O.; Gaudin, G.; Gambardella, P. Symmetry and Magnitude of Spin–Orbit Torques in Ferromagnetic Heterostructures. *Nature nanotechnology* **2013**, *8* (8), 587–593.
- (7) Emori, S.; Bauer, U.; Ahn, S.-M.; Martinez, E.; Beach, G. S. Current-Driven Dynamics of Chiral Ferromagnetic Domain Walls. *Nature materials* **2013**, *12* (7), 611–616.
- (8) Fan, X.; Celik, H.; Wu, J.; Ni, C.; Lee, K.-J.; Lorenz, V. O.; Xiao, J. Q. Quantifying Interface and Bulk Contributions to Spin–Orbit Torque in Magnetic Bilayers. *Nature communications* **2014**, *5* (1), 1–8.
- (9) Nguyen, M.-H.; Ralph, D. C.; Buhrman, R. A. Spin Torque Study of the Spin Hall Conductivity and Spin Diffusion Length in Platinum Thin Films with Varying Resistivity. *Physical review letters* **2016**, *116* (12), 126601.
- (10) Fan, X.; Mellnik, A. R.; Wang, W.; Reynolds, N.; Wang, T.; Celik, H.; Lorenz, V. O.; Ralph, D. C.; Xiao, J. Q. All-Optical Vector Measurement of Spin-Orbit-Induced Torques Using Both Polar and Quadratic Magneto-Optic Kerr Effects. *Applied Physics Letters* **2016**, *109* (12), 122406.
- (11) Montazeri, M.; Upadhyaya, P.; Onbasli, M. C.; Yu, G.; Wong, K. L.; Lang, M.; Fan, Y.; Li, X.; Khalili Amiri, P.; Schwartz, R. N.; Ross, C. A.; Wang, K. L. Magneto-Optical Investigation of Spin–Orbit Torques in Metallic and Insulating Magnetic Heterostructures. *Nat Commun* **2015**, *6*.

- (12) Avci, C. O.; Quindeau, A.; Pai, C.-F.; Mann, M.; Caretta, L.; Tang, A. S.; Onbasli, M. C.; Ross, C. A.; Beach, G. S. Current-Induced Switching in a Magnetic Insulator. *Nature materials* **2017**, *16* (3), 309–314.
- (13) Chen, X. Z.; Zarzuela, R.; Zhang, J.; Song, C.; Zhou, X. F.; Shi, G. Y.; Li, F.; Zhou, H. A.; Jiang, W. J.; Pan, F. Antidamping-Torque-Induced Switching in Biaxial Antiferromagnetic Insulators. *Physical review letters* **2018**, *120* (20), 207204.
- (14) Hasegawa, K.; Hibino, Y.; Suzuki, M.; Koyama, T.; Chiba, D. Enhancement of Spin-Orbit Torque by Inserting CoO x Layer into Co/Pt Interface. *Physical Review B* **2018**, *98* (2), 020405.
- (15) Pai, C.-F.; Liu, L.; Li, Y.; Tseng, H. W.; Ralph, D. C.; Buhrman, R. A. Spin Transfer Torque Devices Utilizing the Giant Spin Hall Effect of Tungsten. *Applied Physics Letters* **2012**, *101* (12), 122404.
- (16) Shi, S.; Wang, A.; Wang, Y.; Ramaswamy, R.; Shen, L.; Moon, J.; Zhu, D.; Yu, J.; Oh, S.; Feng, Y. Efficient Charge-Spin Conversion and Magnetization Switching through the Rashba Effect at Topological-Insulator/Ag Interfaces. *Physical Review B* **2018**, *97* (4), 041115.
- (17) Rojas-Sánchez, J.-C.; Oyarzún, S.; Fu, Y.; Marty, A.; Vergnaud, C.; Gambarelli, S.; Vila, L.; Jamet, M.; Ohtsubo, Y.; Taleb-Ibrahimi, A. Spin to Charge Conversion at Room Temperature by Spin Pumping into a New Type of Topological Insulator:  $\alpha$ -Sn Films. *Physical review letters* **2016**, *116* (9), 096602.
- (18) Sánchez, J. R.; Vila, L.; Desfonds, G.; Gambarelli, S.; Attané, J. P.; De Teresa, J. M.; Magén, C.; Fert, A. Spin-to-Charge Conversion Using Rashba Coupling at the Interface between Non-Magnetic Materials. *Nature communications* **2013**, *4* (1), 1–7.
- (19) Guo, C. Y.; Wan, C. H.; Zhao, M. K.; Wu, H.; Fang, C.; Yan, Z. R.; Feng, J. F.; Liu, H. F.; Han, X. F. Spin-Orbit Torque Switching in Perpendicular  $Y_3Fe_5O_{12}/Pt$  Bilayer. *Applied Physics Letters* **2019**, *114* (19), 192409.
- (20) Rojas-Sánchez, J.-C.; Reyren, N.; Laczowski, P.; Savero, W.; Attané, J.-P.; Deranlot, C.; Jamet, M.; George, J.-M.; Vila, L.; Jaffrès, H. Spin Pumping and Inverse Spin Hall Effect in Platinum: The Essential Role of Spin-Memory Loss at Metallic Interfaces. *Physical review letters* **2014**, *112* (10), 106602.
- (21) <https://www.physik.fu-berlin.de/einrichtungen/ag/ag-kuch/research/techniques/fmr/index.html>. Accessed date: **12-09-2020**
- (22) Dymanus, A.; Kaminow, I. P. Ferromagnetic Resonance in Piezoelectric  $Ga_{2-x}Fe_xO_3$ . *Journal of Applied Physics* **1961**, *32* (3), S144–S145.
- (23) Dweck, J. Ferromagnetic Resonance in the Highly Anisotropic Ferrimagnet Gallium Iron Oxide. *Physical Review* **1968**, *168* (2), 602.

- (24) Petrov, M. P.; Kizhaev, S. A.; Smolenskii, G. A. Ferromagnetic Resonance in  $\text{Ga}_{0.85}\text{Fe}_{1.15}\text{O}_3$ . *physica status solidi (b)* **1968**, *30* (2), 871–874.
- (25) Ohkoshi, S.; Kuroki, S.; Sakurai, S.; Matsumoto, K.; Sato, K.; Sasaki, S. A Millimeter-wave Absorber Based on Gallium-substituted E-iron Oxide Nanomagnets. *Angewandte Chemie* **2007**, *119* (44), 8544–8547.
- (26) T. Omi. Observation of nonreciprocal signal in polarized ferromagnetic resonance of polar ferrimagnet  $\text{GaFeO}_3$ , Japan physics conference, **2018**.
- (27) Yalçın, O. *Ferromagnetic Resonance: Theory and Applications*; BoD–Books on Demand, **2013**.
- (28) Nakajima, M.; Namai, A.; Ohkoshi, S.; Suemoto, T. Ultrafast Time Domain Demonstration of Bulk Magnetization Precession at Zero Magnetic Field Ferromagnetic Resonance Induced by Terahertz Magnetic Field. *Optics express* **2010**, *18* (17), 18260–18268.
- (29) Tucek, J.; Zboril, R.; Namai, A.; Ohkoshi, S.  $\epsilon$ - $\text{Fe}_2\text{O}_3$ : An Advanced Nanomaterial Exhibiting Giant Coercive Field, Millimeter-Wave Ferromagnetic Resonance, and Magnetoelectric Coupling. *Chemistry of Materials* **2010**, *22* (24), 6483–6505.
- (30) Grange, W.; Maret, M.; Kappler, J.-P.; Vogel, J.; Fontaine, A.; Petroff, F.; Krill, G.; Rogalev, A.; Goulon, J.; Finazzi, M. Magnetocrystalline Anisotropy in (111)  $\text{CoPt}_3$  Thin Films Probed by x-Ray Magnetic Circular Dichroism. *Physical Review B* **1998**, *58* (10), 6298.
- (31) Wilhelm, F.; Pouloupoulos, P.; Ceballos, G.; Wende, H.; Baberschke, K.; Srivastava, P.; Benea, D.; Ebert, H.; Angelakeris, M.; Flevaris, N. K. Layer-Resolved Magnetic Moments in Ni/Pt Multilayers. *Physical review letters* **2000**, *85* (2), 413.
- (32) Geprägs, S.; Meyer, S.; Altmannshofer, S.; Opel, M.; Wilhelm, F.; Rogalev, A.; Gross, R.; Goennenwein, S. T. Investigation of Induced Pt Magnetic Polarization in  $\text{Pt}/\text{Y}_3\text{Fe}_5\text{O}_{12}$  Bilayers. *Applied Physics Letters* **2012**, *101* (26), 262407.
- (33) Huang, S.-Y.; Fan, X.; Qu, D.; Chen, Y. P.; Wang, W. G.; Wu, J.; Chen, T. Y.; Xiao, J. Q.; Chien, C. L. Transport Magnetic Proximity Effects in Platinum. *Physical review letters* **2012**, *109* (10), 107204.
- (34) Shimizu, S.; Takahashi, K. S.; Hatano, T.; Kawasaki, M.; Tokura, Y.; Iwasa, Y. Electrically Tunable Anomalous Hall Effect in Pt Thin Films. *Physical review letters* **2013**, *111* (21), 216803.
- (35) Vlietstra, N.; Shan, J.; Castel, V.; Ben Youssef, J.; Bauer, G. E. W.; van Wees, B. J. Exchange Magnetic Field Torques in YIG/Pt Bilayers Observed by the Spin-Hall Magnetoresistance. *Appl. Phys. Lett.* **2013**, *103* (3), 032401.
- (36) Althammer, M.; Meyer, S.; Nakayama, H.; Schreier, M.; Altmannshofer, S.; Weiler, M.; Huebl, H.; Geprägs, S.; Opel, M.; Gross, R.; Meier, D.; Klewe, C.; Kuschel, T.; Schmalhorst, J.-M.;

Reiss, G.; Shen, L.; Gupta, A.; Chen, Y.-T.; Bauer, G. E. W.; Saitoh, E.; Goennenwein, S. T. B. Quantitative Study of the Spin Hall Magnetoresistance in Ferromagnetic Insulator/Normal Metal Hybrids. *Phys. Rev. B* **2013**, *87* (22), 224401.

(37) Zhou, X.; Ma, L.; Shi, Z.; Fan, W. J.; Zheng, J.-G.; Evans, R. F. L.; Zhou, S. M. Magnetotransport in Metal/Insulating-Ferromagnet Heterostructures: Spin Hall Magnetoresistance or Magnetic Proximity Effect. *Phys. Rev. B* **2015**, *92* (6), 060402.

(38) Amamou, W.; Pinchuk, I. V.; Trout, A. H.; Williams, R. E. A.; Antolin, N.; Goad, A.; O'Hara, D. J.; Ahmed, A. S.; Windl, W.; McComb, D. W.; Kawakami, R. K. Magnetic Proximity Effect in Pt / CoFe<sub>2</sub>O<sub>4</sub> Bilayers. *Phys. Rev. Materials* **2018**, *2* (1), 011401.

(39) Gao, R.; Fu, C.; Cai, W.; Chen, G.; Deng, X.; Zhang, H.; Sun, J.; Shen, B. Electric Control of the Hall Effect in Pt/Bi<sub>0.9</sub>La<sub>0.1</sub>FeO<sub>3</sub> Bilayers. *Scientific reports* **2016**, *6*, 20330.

(40) Nakayama, H.; Althammer, M.; Chen, Y.-T.; Uchida, K.; Kajiwara, Y.; Kikuchi, D.; Ohtani, T.; Geprägs, S.; Opel, M.; Takahashi, S.; Gross, R.; Bauer, G. E. W.; Goennenwein, S. T. B.; Saitoh, E. Spin Hall Magnetoresistance Induced by a Nonequilibrium Proximity Effect. *Phys. Rev. Lett.* **2013**, *110* (20), 206601.

(41) Lin, T. Magnetic Insulator Thin Films and Induced Magneto-Transport Effect at Normal Metal / Magnetic Insulator Interface, Thesis, UC Riverside, **2013**.

(42) Guo, G. Y.; Murakami, S.; Chen, T.-W.; Nagaosa, N. Intrinsic Spin Hall Effect in Platinum: First-Principles Calculations. *Phys. Rev. Lett.* **2008**, *100* (9), 096401.

(43) Guo, G. Y.; Niu, Q.; Nagaosa, N. Anomalous Nernst and Hall Effects in Magnetized Platinum and Palladium. *Phys. Rev. B* **2014**, *89* (21), 214406.

(44) Fang, Z.; Nagaosa, N.; Takahashi, K. S.; Asamitsu, A.; Mathieu, R.; Ogasawara, T.; Yamada, H.; Kawasaki, M.; Tokura, Y.; Terakura, K. The Anomalous Hall Effect and Magnetic Monopoles in Momentum Space. *Science* **2003**, *302* (5642), 92–95.

(45) Mathieu, R.; Asamitsu, A.; Yamada, H.; Takahashi, K. S.; Kawasaki, M.; Fang, Z.; Nagaosa, N.; Tokura, Y. Scaling of the Anomalous Hall Effect in Sr<sub>1-x</sub>Ca<sub>x</sub>RuO<sub>3</sub>. *Physical review letters* **2004**, *93* (1), 016602.

(46) Ko, H.-W.; Park, H.-J.; Go, G.; Oh, J. H.; Kim, K.-W.; Lee, K.-J. Role of Orbital Hybridization in Anisotropic Magnetoresistance. *Physical Review B* **2020**, *101* (18), 184413.



# General Conclusion and Perspectives

## Conclusions

The objective of this thesis, as part of a wider ANR funded project, was to explore the potential offered by ultra-thin multifunctional oxide films in spintronics applications. In this respect, we focused our interest on a rare single-phased room-temperature magnetoelectric multiferroic oxide, the gallium ferrite  $\text{Ga}_{0.6}\text{Fe}_{1.4}\text{O}_3$  (GFO). We have first optimized its growth in thin films in the ultra-thin regime and investigated the implications of these technologically important rather extreme dimensions on their magnetic and electric properties. Furthermore, with a view to assess the relevance of the use of this oxide in spintronics, we prepared GFO/heavy metal (Pt) heterostructures which give interesting outlooks on the interaction of spin-currents issued from the heavy metal with the GFO layer. Our in-depth study of the various functionalities offered by GFO in the ultra-thin regime actively paves the way towards the last part of the ANR project which will consist in combining spin currents and magnetoelectric effects for engineering a next generation of low power consuming GFO-based spintronics devices.

We have successfully performed the growth of the complex GFO oxide in epitaxial atomically flat thin films by pulsed laser deposition (PLD) on  $\text{SrTiO}_3$  (STO) substrates. The growth shows a 3D to 2D transition above a critical thickness of 4 nm, and then adopts a layer-by-layer mode which allows a control over the deposited thickness down to a resolution of  $1/4^{\text{th}}$  of a unit cell. Atomically resolved electron energy loss spectroscopy (EELS) measurements coupled to high-resolution scanning transmission electron microscopy (HR-STEM) observations unravel the mechanisms at play at the STO/GFO interface. An ionic migration of Ti from the STO substrate into the GFO deposited film was evidenced up to 5 nm in the deposited films. This has led an abrupt electric polarization inversion within these thicknesses, with the presence of tail to tail horizontal polarization domain walls.

The GFO films demonstrate a macroscopically ferromagnetic behaviour, with a room temperature saturation of about  $100 \text{ emu/cm}^3$  and a Curie temperature ( $T_c$ ) of 360 K. While the magnetization is in-plane for the thicker films, it turns out to be out-of-plane for thinner ones (7 nm). The films demonstrate a high, and mainly magnetocrystalline, bulk anisotropy of about  $3 \cdot 10^5 \text{ J/m}^3$  at 10 K. On a microscopic aspect, synchrotron-based X-ray magnetic circular dichroism allowed to measure a non-zero orbital moment on the  $\text{Fe}^{3+}$  cations of the structure. Even if this is surprising for a  $d^5$  element, it has already been previously observed on single crystals, and is probably a clue of the high quality of the films. This non-zero orbital moment originates from a high hybridization level of the Fe 3d orbitals due to distortions of the  $\text{FeO}_6$  octahedra. The hybridization was even shown to extend to the Ga orbitals, since an XMCD signal was also observed on this otherwise non-magnetic element. We have shown that the  $\text{Fe}^{3+}$  orbital moment is highly anisotropic and strongly depends on the direction in which the field is applied. It could vary from an apparent parallel to anti parallel alignment with the spin moment. We attribute this anisotropy to the degree of distortion in the GFO polyhedra, as supported by our study of the film thickness dependence of the orbital moment. These  $\text{FeO}_6$  octahedra distortions can be magnetically driven thanks to an important magneto-structural coupling. The orbital moment interestingly shows a maximum in its temperature variation, for 120 K.

In order to circumvent the usually prevailing artefacts related to the measurements of an electric polarization in rather leaky thin films, we studied the emergence of the electric polarization in our GFO thin films via an original second harmonic generation (SHG) study. This was made possible thanks to a close collaboration with the Laboratory for Multifunctional Ferroic Materials of the ETH, Zürich (Morgan Trassin and Johanna Nordlander), who are experts in this technique. Films as thin as 7 nm were shown to already have an electric polarization through post-deposition *ex situ* measurements. *In situ* SHG monitoring of the early steps of the GFO films growth allowed to obtain completely original information on the sub-unit growth mode of GFO, evidencing a non-obvious symmetry periodicity. The ferroelectric critical temperature  $T_c$  could be established within the 950-1100°C (1223-1373 K) range and the critical thickness for the onset of an electrical polarization was estimated to be between 0.5 and 2 GFO unit cells, which is lower than shown by other ferroelectric materials. This confirms the stiffness of the electric polarization in GFO, and its impressive resistance towards the depolarizing field.

We have then asserted the possibilities of the GFO films in terms of spin-related applications, thanks to a collaboration with the Institut Jean Lamour, Nancy (Carlos Rojas-Sanchez, Sébastien Petit-Watelot, Elodie Martin). We focused our interest on STO//GFO/Pt heterostructures, of which we first optimized the growth. Our study of the magneto-transport properties of GFO was seriously hindered by the experimental impossibility to be in ferromagnetic resonance (FMR) conditions, which we had to face. This is probably due to the strongly anisotropic character of the material which moves the FMR frequencies to values which were not reachable by us. We

therefore performed magneto-transport measurements, which is another way to observe interactions between the spin current issued by Pt and the GFO magnetic orientation. Two main mechanisms were considered: the magnetic proximity effect induced anisotropic magnetoresistance (MPE AMR) and the spin Hall induced anisotropic magnetoresistance (SHE AMR, *a.k.a.* SMR). We have been able to separate their contributions thanks to angle-dependent measurements. This is an important point when aiming at the optimization of the spin-momentum transfer efficiency through the interface. SMR was found to be the dominant mechanism at all temperatures and shows an apparent minimum at 120 K, which could be related to the extremum also observed for the atomic orbital moment at this temperature. It is the only mechanism to be considered near room temperature, with a value of  $2 * 10^{-4}$ . This study constitutes an essential first magneto transport characterization steps towards the use of GFO within spin-related applications, which is the goal of the wider ANR project "MISSION" (end March 2022).

## Perspectives

Across this thesis we have demonstrated the novel multifunctionalities offered by ultra-thin GFO films and evidenced the relevance of GFO in devices in the frame of spintronics. Now we discuss the future perspective that are possible with the use of GFO thin films. The future use of GFO as a magnetoelectric multiferroic in ME-SOT memory or MESO logic architectures for ultra-low power operations is our ultimate goal.

However, I would also suggest some further studies which I could not undertake due to lack of time. For example, I propose to study the interface between the tail-to-tail electric polarization after the first grown 5 nm observed by HR-STEM by conducting tip AFM study to reveal the conducting properties of this interface that could be interesting if highly charged, as I think.

Another point would concern the possibility to study the effect of a gate voltage on the GFO magnetic anisotropy and/or orbital anisotropy, taking advantage of the indirect magneto-electric effect evidenced by XMCD, and of the gate voltage control of the distortions.

A natural follow-up of our SHG investigations would of course be to study a heterostructure of STO//SRO/GFO/SRO *in situ*, *via* ISHG. The idea is to disrupt the charge screening due to the atmospheric adsorbates sitting on the STO//SRO/GFO film by growing a non-conducting single unit-cell SRO on top of the stack. This has been shown to trigger the formation of domains in a single polar domain thin film and would allow determining the ultimate resistance of the GFO cell

towards a depolarizing field. I also propose the use of GFO as ferroelectric tunnel barrier in MFTJ junction due to its ultra-low critical thickness.

Considering the study of the spin-related applications of GFO, I propose to consider a FM1/NM/FM2 tri-layer heterostructure system, where the ferromagnetic material FM1 can be brought into its FMR condition. The magnetic moment of FM1 will then precess and inject a pure spin current in the ferrimagnetic GFO layer FM2 *via* the non-magnetic material NM. We could then assess if a spin-to-charge conversion in the GFO FM2 layer is possible *via* the Inverse spin Hall effect (ISHE). The important spin-orbit coupling observed by XMCD in GFO allow high hopes for a positive result of such an experiment. This would open perspectives of using GFO as a spin-charge convertor.

## **My own contribution to the work**

The work presented in this study has been performed within the frame of a strong collaboration between my affiliation laboratory, the Institut de Chimie des Matériaux de Strasbourg (IPCMS), the Laboratory for Multifunctional Ferroic Materials (Ferroic Lab) in ETH, Zürich, and the Institut Jean Lamour (IJL), in Nancy. I have of course been tutored all along my PhD thesis but I have personally realized all the materials elaboration work (ceramic targets synthesis and PLD films depositions). The electron microscopy study was performed by microscopist colleagues, in both IPCMS and Nancy. I actively took part to the XMCD measurements, which broaded over two weeks, at the synchrotron SOLEIL facility in Paris, and to the data processing, helped in that by the expertise of colleagues in IPCMS. I spent four weeks in the Ferroic Lab in Zürich, during which I was taught the SHG technique and could realize some of the experiments by myself. The data processing was then done with the help of our collaborators in Zürich. I also spent a week in the IJL in Nancy to get familiar with the magnetotransport characterization experiments. Most of the measurements were however performed by Nancy's colleagues. On the other hand, I had a very active part in the data analysis.

# Acknowledgements

I would like to extend my deepest thanks to many truly amazing people for their support in the last three years. It is my great honor to recognize their contributions to this thesis here.

First of all, I would like to thank my advisor, Prof. Dr. Nathalie Viart for introducing me into such an exciting field. I learned a lot from you during the process of the PhD program, not only the scientific insights you gave but also your never-ending passion and enthusiasm for science. The guidance from you helped me solve many puzzles along the journey whenever I needed. I will always be indebted to you as my greatest collaborator, mentor and friend.

I would also like to express my deepest gratitude to Prof. Dr. Kathrin Dörr, Prof. Dr. Wilfrid Prellier, Prof. Dr. Silviu Colis, Dr. Michel Viret, Dr. Morgan Trassin, Dr. Carlos Rojas-Sanchez and Dr. Daniele Preziosi for being on my qualifying exam and dissertation committee and providing important suggestions and comments on my research. Your feedback has been critical to this dissertation.

I would like to give my special thanks to Dr. Daniele Preziosi. Thank you for your support when we both first joined the group and your priceless insights from the endless discussions and arguments, we had during all these years. I am genuinely grateful for all your help and encouragement.

It has been my great honor to work with so many talented colleagues in the Thin Film group at DCMI department. I would like to thank the following present and previous members of the group for your help: To Dr. François Roulland and Dr. Christophe Lefèvre, thank you for mentoring me in my early years of academic career and the close collaborations ever since then; To Dr. Benjamin Meunier, thank you for the physical insights and the new perspective you brought to me during the end phase of my thesis; To Gilles Versini and Sophie Barre, thank you for sharing your valuable experience for thin film deposition; To Dr. Corinne Bouillet and Dr. Xavier Devaux, thank you for the contribution of wonderful TEM studies in this work and to Dr. David Troadec for FIB preparation; To Cédric Leuvrey, thank you for all the SEM characterizations that helped me during this work; To Dr. Guillaume Rogez, Prof. Dr. Silviu Colis and Jerome Robert, thank you very much for all your assistance in the SQUID studies and also for sharing so many intricate ideas regarding the measurement techniques; To Dr. Marc Lenertz, thank you very much for your expertise in XRD characterization; To Prof. Dr. Pierre Rabu and Prof. Dr. Aziz Dinia for their efficient direction at IPCMS and Ecole Doctoral respectively; To administration at IPCMS, notably Catherine Bonnin and Sylvie Maingé for helping me get through all the necessary documents during the thesis; I especially want to thank Laurianne Wendling, Pier Berling, Guillaume Krieger, Dr. Kübra Yasaroglu, Dr. Elodie Martin and Antonio Peña for sharing the same memories of PhD studies at our office 2006 and the support and friendship all these years; A huge thanks to all the members from DCMI department who have continuously supported me all along this thesis. The list would

be incomplete without mentioning my friends at Mau Mitra Mandal from India who have been a great support system for me. Of course, there are many more that I should enlist here: Dr. Nesrine Benamara, Dr. Paula Dueñas, Wissal Belayachi, Alexandre Adam, Frédéric Payet, Dr. Kajal Aggarwal, Dr. Swapneel Pathak, Dr. Sambit Mohapatra, Saeel Momin and Marina Gentle. Thank all of you for your help and support all along the way.

Also, I would like to acknowledge the efforts of the following individuals and groups at various other institutions around the world for the productive collaborations: To Dr. Morgan Trassin, Dr. Johanna Nordlander and Prof. Dr. Manfred Fiebig at Ferroic group in ETH Zürich for their invaluable inputs in measurement and analysis of SHG signal; Dr. Carlos Rojas-Sanchez, Dr. Sebastien Petit-Watelot, Dr. Elodie Martin, Dr. Karine Dumesnil, Dr. Olivier Copie and Dr. Jon Gorchon at IJL Nancy for patterning the devices and help in magneto-resistance measurements and analysis; Dr. Fadi Choueikani and Dr. Phillippe Ohresser for their assistance in XMCD measurements in DEIMOS beamline and Dr. Dominique Thiaudiere for REXS in DiffAbs beamline at Soleil Synchrotron facility.

Last but not the least, I want to express my deepest gratitude to my family. I especially want to thank my parents for their understanding and support to pursue my career in science. Their support has kept me afloat during all the tough times during the thesis. A special thanks to my younger brother whose genuine curiosity about my work and science in general made me look at my thesis in a different perspective beyond all the equations and theories.

The period of working for the thesis has not only been academically and scientifically an interesting one but also from a philosophical point of view, it has been a great journey for me, and I thank everyone who helped me, with utmost sincerity.

# Résumé étendu de la thèse

## Couches ultra-minces d'oxyde multifonctionnel pour des applications en spintronique

### 1. Introduction

Au cours des dernières décennies, la découverte de la magnétorésistance géante dont les dispositifs les plus emblématiques sont les valves de spin a permis un large éventail d'applications qui ont ouvert la voie au nouveau domaine de la spintronique. Un dispositif magnéto-résistif typique est constitué de deux couches magnétiques séparées par une entretoise non magnétique. Sa résistance électrique dépend de l'orientation relative des deux couches magnétiques. Elle sera faible pour une disposition parallèle et élevée pour une disposition antiparallèle. Le fonctionnement des dispositifs spintroniques repose donc sur la possibilité de modifier l'orientation relative des deux couches magnétiques. La recherche dans ce domaine vise actuellement à réduire l'énergie nécessaire au fonctionnement de ces dispositifs en raison de la demande croissante de consommation d'énergie. Dans ce contexte, on attend beaucoup de la prochaine génération de stockage de données basé sur la spintronique, comme les mémoires magnétiques à accès aléatoire (M-RAM), pour fournir ces dispositifs à faible consommation d'énergie. Les dispositifs M-RAM sont actuellement axés sur les techniques basées sur le courant de spin comme le couple de transfert de spin (STT) et le couple d'orbite de spin (SOT) (voir figure 1). Les dispositifs basés sur le SOT sont particulièrement recherchés en raison de leurs faibles besoins en énergie et de leur grande endurance.

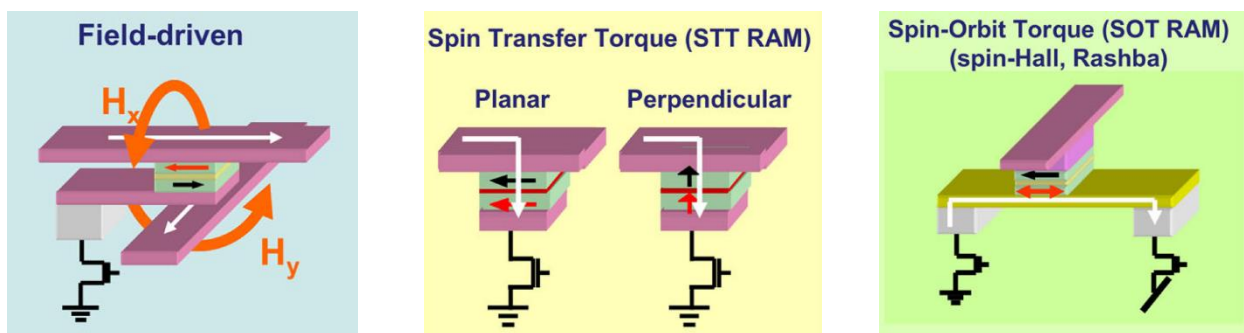


**Fig. 1 | Différentes technologies qui peuvent être incorporées dans l'architecture de la mémoire MRAM.** Ces technologies sont utilisées pour commuter la couche ferromagnétique I et créer une magnétisation parallèle ou antiparallèle par rapport à la couche ferromagnétique II, permettant ainsi des états de résistance faible ou élevée, qui peuvent être définis comme 0 ou 1 bit. Adapté de ref. [1].

Dans les appareils basés sur le SOT, on utilise une hétérostructure ferromagnétique (FM)/métal lourd (HM). Le courant ( $J_c$ ) qui passe à travers le métal lourd génère un courant de spin perpendiculaire ( $J_s$ ) dû à l'effet Hall de spin (SHE). Ce courant de spin est ensuite transféré à la couche ferromagnétique à travers l'interface, ce qui entraîne un couple qui peut être utilisé efficacement pour manipuler sa magnétisation. Les effets sont encore relativement faibles pour l'instant et l'exploration de nouveaux matériaux plus efficaces, plus résistants et aux fonctionnalités enchevêtrées est très recherchée. Une très grande importance est accordée à la qualité des hétérostructures, en particulier aux interfaces telles que la FM/HM mentionnée ci-dessus. La perte de courant de spin due à la dégradation de la surface aux interfaces est en effet un inhibiteur majeur pour l'adoption industrielle à grande échelle de l'effet SOT.

Un autre domaine de recherche sur les dispositifs de mémoire à faible puissance a été l'utilisation de matériaux magnétoélectriques multiferroïques, dans lesquels les ordres électrique et magnétique sont couplés. Cette technique a récemment été considérée avec beaucoup d'enthousiasme comme une solution pour une commutation de l'aimantation à faible puissance (voir figure 2). Dans ce concept, l'aimantation est modulée par l'inversion de sa polarisation électrique couplée sous l'application d'un champ électrique presque gratuit (par rapport à un champ magnétique). L'efficacité de ce contrôle magnétoélectrique de l'aimantation est cependant encore discutable si l'on considère la fiabilité, la rapidité et la production de dispositifs pratiques.

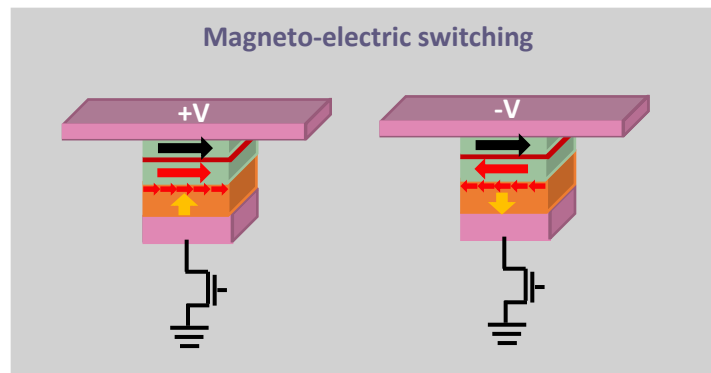


**Fig. 2 | Schéma de la commutation assistée par champ électrique dans un dispositif MTJ.** Un matériau ferroélectrique (FE) et antiferromagnétique (AFM) est couplé magnétiquement à l'une des couches ferromagnétiques (FM) du MTJ. Sa polarisation électrique peut être inversée par un champ électrique. Celui-ci inverse alors l'orientation de son ordre AFM, puis celle de la couche FM.

Les inconvénients présentés par les techniques ME et SOT peuvent être atténués en envisageant un dispositif hybride de couple orbital de rotation magnéto-électrique (ME-SOT) qui réduit l'anisotropie magnétique par une tension de grille rentable qui peut ensuite être commutée par SOT avec un courant  $J_c$  de faible puissance.

Dans cette thèse, nous nous concentrons sur le potentiel offert par la ferrite orthorhombique de gallium  $Ga_{2-x}Fe_xO_3$  (GFO) pour de nouveaux dispositifs multicouches basés sur le courant de spin conçus pour des applications en spintronique. Le GFO se cristallise dans le groupe spatial numéro 33 des Tables internationales de cristallographie, pour lequel deux réglages différents sont couramment utilisés,  $Pc21n$  ou  $Pna21$ . Les paramètres du réseau indiqués dans le réglage  $Pna21$  sont  $a = 5,0806 \pm 0,0002 \text{ \AA}$ ,  $b = 8,7512 \pm 0,0008 \text{ \AA}$  et  $c = 9,3993 \pm 0,0003 \text{ \AA}$ . Dans la structure cristallographique du GFO 1.0 (illustrée à la figure 1.17), les anions  $O^{2-}$  sont disposés dans un double empilement hexagonal ABAC serré le long de l'axe "c". Il existe quatre sites cationiques différents qui peuvent être occupés par les cations  $Ga^{3+}$  et  $Fe^{3+}$ , appelés  $Ga1$ ,  $Fe1$ ,  $Ga2$  et  $Fe2$ , comme le montre la figure 3 (a).  $Ga1$  est un site tétraédrique, et  $Fe1$ ,  $Ga2$  et  $Fe2$  sont des sites octaédriques non équivalents. Bien que les sites  $Fe1$  et  $Fe2$  soient supposés être occupés par des atomes de Fe uniquement et les sites  $Ga1$  et  $Ga2$  par des atomes de Ga uniquement, on observe un certain désordre cationique <sup>[2]</sup>. Le GFO, pour  $x=1,4$  a  $Ga1$  principalement occupé par Ga tandis que  $Ga2$ ,  $Fe1$  et  $Fe2$  sont principalement occupés par Fe (voir figure 3 (b)). À  $x=1,4$ , le GFO est un matériau multiferroïde {ferromagnétique (FM) à température ambiante le long de l'axe a et ferroélectrique (FE) le long de l'axe c} (voir figure 3 (c)) ainsi qu'un matériau magnétoélectrique (ME). Ces fonctionnalités très recherchées existant dans un seul matériau aux conditions ambiantes sont assez rares, ce qui rend ce matériau très intéressant pour les dispositifs multifonctionnels.

Les premiers travaux concernant la croissance des films  $Ga_{2-x}Fe_xO_3$ , avec x différent de 1, se concentrent sur l'étude de l'effet du rapport Fe/Ga sur les caractéristiques structure-propriété. La première croissance de film mince de GFO 1,4 a été signalée sur des substrats YSZ par Trassin et al. en 2009 <sup>[3]</sup>, et la croissance a ensuite été étendue aux substrats STO (111) par Song et al. en 2016 <sup>[4]</sup>. La croissance de GFO 1.0-1.4 (001) sur YSZ (100) conduit à 6 domaines structurels (variantes), alors que sa croissance sur STO (111) conduit à seulement 3 domaines structurels (variantes) <sup>[5,6]</sup>. Pour cette raison, nous avons choisi d'utiliser le substrat STO dans cette thèse.

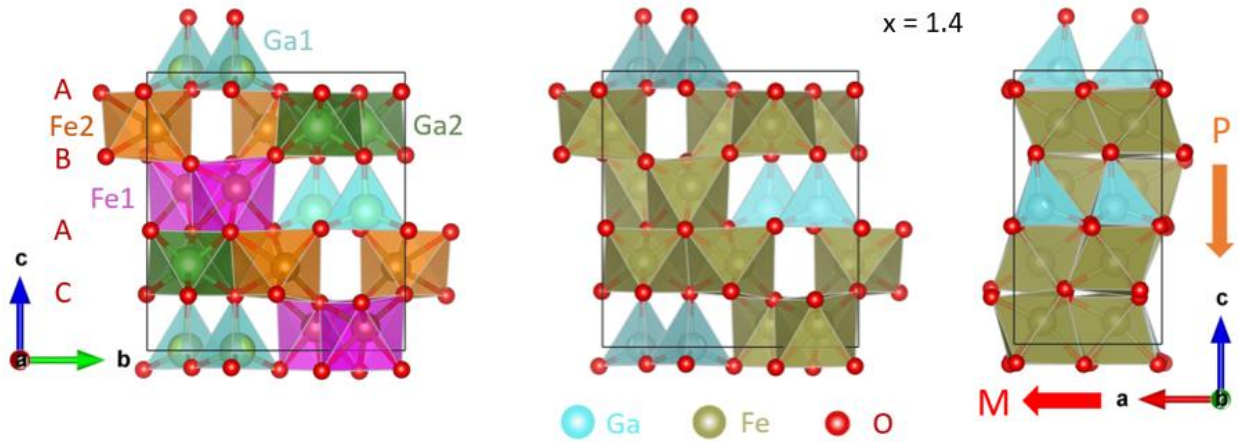


**Fig. 3 | La structure cellulaire de l'unité GaFeO<sub>3</sub> vue depuis les axes des zones "a" et "b" dans le cadre de *Pna2<sub>1</sub>*. Les marques P et M indiquent respectivement la polarisation électrique et l'axe facile de magnétisation.**

Cette thèse s'inscrit dans le cadre plus large d'un projet ANR [MISSION ANR-2018], dont le but est d'explorer la possibilité d'aider les possibilités de commutation de la magnétisation basée sur le SOT avec un effet ME, et ainsi réduire les courants critiques  $J_c$  nécessaires et introduire de nouvelles fonctionnalités également. Le matériau ME choisi pour ce projet ANR est le GFO en raison de ses propriétés ferroélectriques et ferrimagnétiques, avec un moment magnétique résultant non nul, à température ambiante.

Le but de cette thèse était de :

- optimiser les conditions de croissance des couches minces de GFO 1.4 pour obtenir une surface atomiquement lisse, en particulier aux régimes technologiques inférieurs à 10 nm, ce qui est essentiel dans les dispositifs contemporains pour réduire les effets d'interface après intégration dans des hétérostructures. Nous avons réalisé des études détaillées des premières étapes de cette croissance par microscopie électronique à transmission et par des techniques de génération de seconde harmonique.
- d'explorer les propriétés magnétiques et ferroélectriques de ces films GFO, à l'échelle macro et microscopique, et donc les fonctionnalités qu'ils pourraient offrir à des régimes ultra-minces.
- explorer les capacités fonctionnelles des couches minces du GFO 1.4 en effectuant des mesures de magnéto-transport dans les hétérostructures GFO 1.4/Pt envisagées pour l'architecture de mémoire de couple spin-orbite (SOT) dans les dispositifs MRAM (Fig. 4 (a)).

Le but ultime du projet ANR "MISSION" sera, dans le prolongement de cette thèse, la recherche d'une modulation magnéto-électrique de cet effet SOT (Fig. 4 (b)).

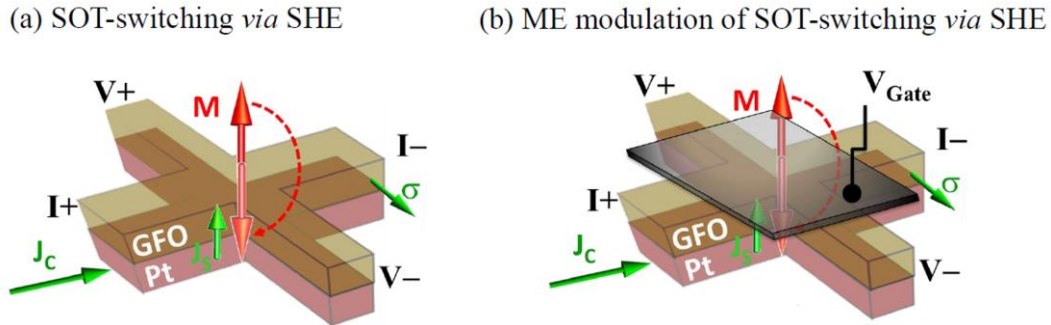


**Fig. 4 | Schéma des fonctionnalités envisagées pour GFO.** (a) Commutation SOT de la magnétisation du GFO par effet Hall de spin (SHE) en Pt. (b) Modulation magnétoélectrique (ME) de la commutation SOT de la magnétisation GFO pour la commutation de faible puissance. Schéma de Carlos-Rojas Sanchez (IJL, Nancy) pour le projet ANR "MISSION".

## 2. Films GFO ultra-minces, lisses et atomiques

Notre premier objectif dans le cadre de ce travail de thèse était de démontrer la croissance de couches minces de  $\text{Ga}_{0.6}\text{Fe}_{1.4}\text{O}_3$  (GFO) sur des substrats de  $\text{SrTiO}_3$  (STO) ayant une surface atomiquement lisse. Comme mentionné dans l'introduction, la croissance d'une surface atomiquement plane est nécessaire pour continuer à construire des interfaces lisses et de haute qualité avec une couche adjacente. L'idée est de favoriser le transfert du moment angulaire de spin dans le GFO à partir d'une couche de Pt adjacente.

Dans cette section, nous rendons donc compte de l'élucidation du mode de croissance des couches minces de GFO par la PLD assistée par le RHEED dès les tout premiers stades de la croissance. Des couches minces de  $\text{Ga}_{0,6}\text{Fe}_{1,4}\text{O}_3$  ont été déposées sur des substrats de titanate de strontium,  $\text{SrTiO}_3$  (STO) (111) (Furuuchi Chemical Corporation, Japon, avec une rugosité efficace inférieure à 0,15 nm) en utilisant un système PLD ayant une pression de base de  $2 \times 10^{-8}$  mbar. Une cible polycristalline de composition stoechiométrique  $\text{Ga}_{0,6}\text{Fe}_{1,4}\text{O}_3$  a été préparée par la méthode céramique<sup>[7]</sup> et ablaté avec un laser excimère KrF de longueur d'onde 248 nm à une fréquence de répétition de 2 Hz dans une atmosphère oxydante avec une pression partielle d' $\text{O}_2$  de 0,1 mbar. La distance cible-substrat était de 5,5 cm et la densité d'énergie du laser sur la cible était de 4 J/cm<sup>2</sup>. La température du substrat a été maintenue à 900 °C pendant la croissance. La croissance a été arrêtée après plusieurs impulsions comprises entre 500 et 24 000 pour produire des échantillons de GFO de différentes épaisseurs. Le RHEED in situ a été utilisé pour surveiller la croissance des couches minces et les propriétés structurales des couches ont été caractérisées par la diffraction des rayons X (XRD), la microscopie à force atomique (AFM) et la microscopie électronique à transmission à résolution atomique (HR TEM). Les propriétés magnétiques ont été étudiées par magnétométrie à interface utilisateur quantique supraconductrice (SQUID) et par dichroïsme circulaire magnétique des rayons X (XMCD). La

polarisation électrique dans nos couches minces a été caractérisée par la génération de second harmonique (SHG).

La surveillance in situ du RHEED pendant la croissance en couche mince de GFO1.4 sur des monocristaux de STO(111) a permis de rendre une transition de 3D à 2D. Afin d'étudier ce phénomène, nous avons étudié des films de différentes épaisseurs. La figure 5 (a) montre certains des motifs du RHEED imagés à la fin du dépôt. Un mode de croissance 3D est observé à 4 nm, comme l'indique le motif RHEED en pointillés. Le motif RHEED présente une transition vers un état avec une caractéristique striée modulée à 7 nm qui devient ensuite complètement striée à 32 nm, indiquant une surface d'échantillon 2D. La transition du mode de croissance 3D au mode de croissance 2D, telle qu'observée par le RHEED, apparaît donc pour une épaisseur d'environ 7 nm. Les images AFM (voir Fig. 5 (b)) montrent également une évolution de la morphologie de la surface à partir d'îles randomisées pour 4 nm, en passant par des îles alignées en rangées, et vers des films atomiquement plats, lorsque les îles finissent par fusionner, dans un processus très similaire à celui signalé pour la croissance de SrRuO<sub>3</sub> sur STO <sup>[8]</sup>. La valeur de rugosité moyenne quadratique (rms) est d'environ 1 nm au début de la croissance et diminue progressivement, avec l'augmentation de l'épaisseur du film, jusqu'à des valeurs comparables à la rugosité moyenne quadratique du substrat avant le dépôt (environ 0,1 nm). La croissance a également été suivie par le RHEED à partir de la variation d'intensité des taches dans la zone Laue d'ordre zéro. La figure 5 (c) couvre le dépôt complet du film GFO1.4 de 7 nm. Le dépôt global a duré 537 s, ce qui donne un taux de dépôt de 0,0130 nm/s. La croissance 2D s'installe environ 108 s après le début de la croissance, et dure 464 s, jusqu'à ce que la croissance soit arrêtée. Elle présente 24 oscillations. Une oscillation du RHEED dure 19,3 s. Elle correspond à un dépôt de 0,25 nm, soit environ 1/4 de cellule unitaire. Une telle croissance de cellule sous-unitaire est rare. Elle avait jusqu'à présent été observée pour la croissance d'autres cellules complexes, comme celles du spinelle ou du grenat <sup>[10]</sup> phases d'oxydes de fer.

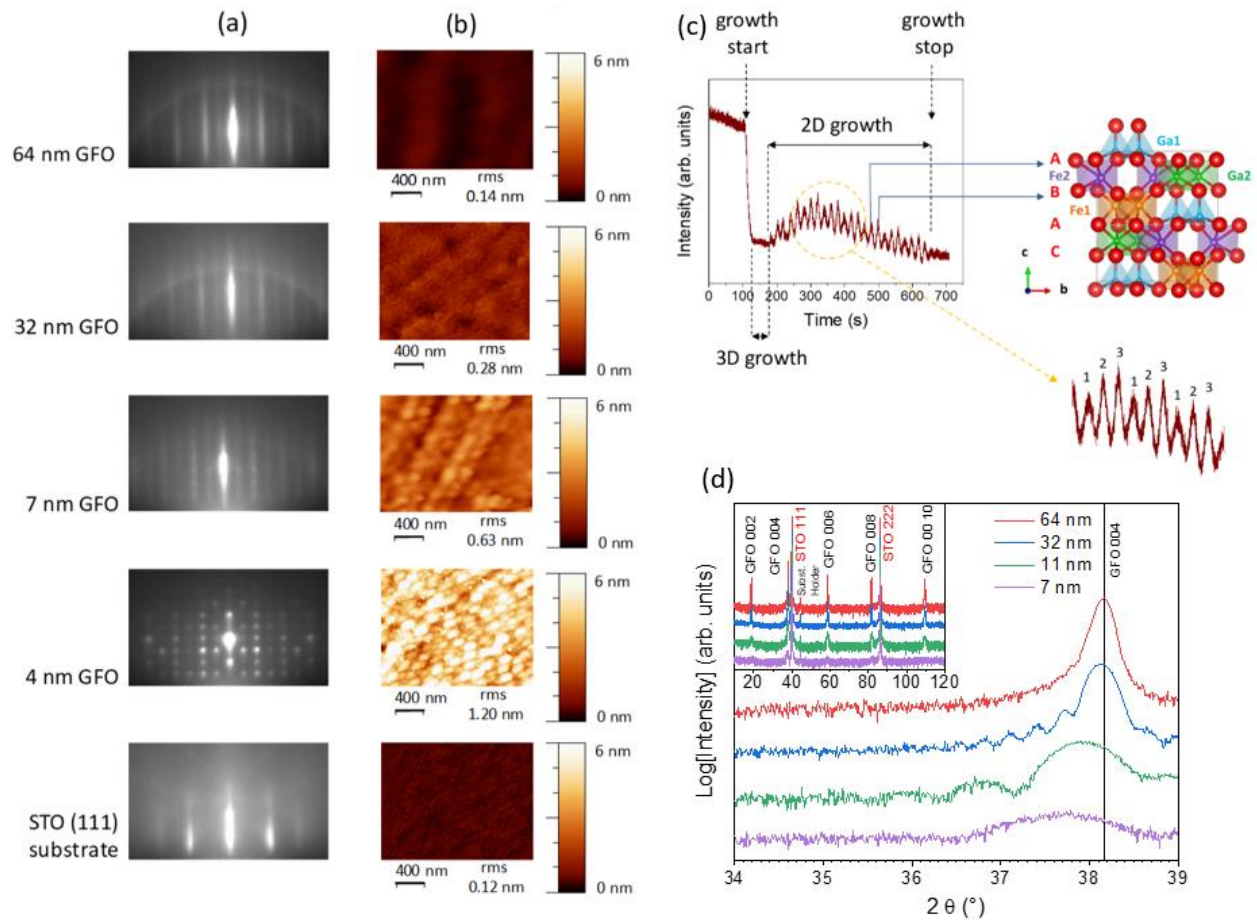


**Fig. 5 | Caractérisation du film GFO à différentes épaisseurs.** (a) Modèles de RHEED in situ observés pendant la croissance du GFO1.4 sur STO (111). (b) Images AFM de la surface des échantillons. (c) La fluctuation de l'intensité d'un spot dans la zone de Laue d'ordre zéro pendant le suivi RHEED de la croissance du film de GFO à 7 nm. (d) Diffractogrammes des rayons X des couches minces de GFO déposées en mode  $\theta$ - $2\theta$ .

Les diagrammes de diffraction des rayons X des films déposés, réalisés en mode  $\theta$ - $2\theta$ , sont présentés dans l'encadré de la figure 5 (d). Ils indiquent que, pour toutes les épaisseurs, les couches minces de GFO sont bien cristallisées, orientées le long de l'axe Pna21 [001], sans aucune trace de phase parasite. L'observation des oscillations de Laue sur les scans zoomés du GFO (004)  $\theta$ - $2\theta$  confirme la haute cristallinité et la faible rugosité des films (voir Fig. 5 (d)). Pour les plus faibles épaisseurs, les pics 00l sont décalés vers des valeurs inférieures à  $2\theta$ . Les relations dans le plan entre la surface STO (111) et la face GFO (ab) sont déterminées à partir de  $\phi$  balayages effectués sur les réflexions STO et GFO. GFO peut adopter trois directions en respectant les relations épitaxiales suivantes avec STO:  $[060]_{\text{GFO}}(001) // [hkl]_{\text{STO}}(111)$  avec  $[hkl]$  égal à  $[2\bar{2}0]$ ,  $[\bar{2}20]$  ou  $[\bar{2}02]$ . Ceci est en parfait accord avec la symétrie du système comme cela a déjà

été observé pour le dépôt de GFO sur le STO (111) [5,11,12]. Les paramètres des cellules  $a$ ,  $b$  et  $c$  ont pu être déterminés à partir de la combinaison des scans  $\theta$ - $2\theta$  et de la cartographie spatiale réciproque des réflexions 206 et 057. Alors que  $c$  diminue avec l'augmentation des épaisseurs (comme déjà observé à partir du pic du GFO (004) dans les scans  $\theta$ - $2\theta$ ),  $a$  et  $b$  restent essentiellement constants. Le paramètre  $c$  hors plan atteint la valeur globale pour les épaisseurs supérieures à 64 nm, après une diminution d'environ 0,2 %. L'expansion hors plan du paramètre  $c$  pour les épaisseurs inférieures n'est donc pas liée à une quelconque déformation dans le plan induite par le substrat, puisqu'il se détend totalement indépendamment des paramètres  $a$  et  $b$ . Le décalage dans cette croissance du GFO (001) sur le système STO (111) est important. Les distances qui doivent être prises en compte sont (i) le long de la  $a_{\text{GFO}}$  direction:  $a_{\text{GFO}} = 0.5088 \text{ nm} \approx 3 d_{\text{STO } 121} = 0.4780 \text{ nm}$  (6.4 % de compression), et (ii) le long de la  $b_{\text{GFO}}$  direction:  $d_{\text{GFO } 060} = 0.1465 \text{ nm} \approx d_{\text{STO } 220} = 0.1380 \text{ nm}$  (6.1 % contrainte de compression). L'énergie élastique relativement élevée introduite par cette grande valeur de déformation explique l'absence d'état de déformation dans le plan dans la structure cristalline du GFO, même pour les plus faibles épaisseurs. Cela pourrait également expliquer la croissance initiale en mode 3D, où des îles GFO totalement détendues fusionnent tandis que le dépôt se poursuit pour obtenir une surface plane. Une telle croissance épitaxiale métamorphique en 3D-2D [13] Le mécanisme a déjà été signalé pour  $\text{SrRuO}_3$  [8] sur STO et pour  $\varepsilon\text{-Fe}_2\text{O}_3$  [14,15] qui est isomorphe au GFO. Dans les deux cas, le mode de croissance 3D initial s'explique par l'important décalage de réseau entre le substrat et la couche mince.

La structure des films GFO a été mieux comprise grâce à HR STEM. La figure 6 présente des images en champ sombre annulaire à grand angle (HAADF) d'une coupe transversale du film GFO de 32 nm. L'interface entre le substrat STO et le film GFO est bien définie et le film montre le schéma cationique attendu pour le GFO dans sa structure de groupe spatial  $Pna2_1$  depuis le début de la croissance. Une zone de contraste plus sombre, indiquant une forte évolution de la composition chimique locale (numéro atomique moyen inférieur), est clairement visible et délimite les cinq premiers nanomètres du reste du film. Il est à noter que les observations d'autres zones de l'échantillon révèlent une légère dispersion dans la position de cette délimitation à des distances comprises entre 2 et 5 nm du substrat. La cartographie de la forme convexe ou concave formée par les quatre sites Fe2 et Ga2 dans une rangée permet de déterminer l'orientation de la polarisation au sein d'une cellule unitaire [11]. De façon surprenante, on observe une inversion de polarisation en s'éloignant de l'interface film/substrat. Cela correspond à la première observation expérimentale de domaines ferroélectriques dans des films GFO ultraminces. La paroi du domaine imagée sur la figure 6 correspond à une configuration de queue à queue nominale chargée. Alors que la formation de domaines ferroélectriques neutres (normaux à la surface) à  $180^\circ$  en régime ultra-mince est attendue en l'absence de filtrage de la charge [16-19] pour les systèmes classiques, la stabilité du type de paroi du domaine queue-à-queue observée ici pourrait être attribuée à la trajectoire de commutation hautement énergétique du GFO. La commutation de polarisation devrait se produire le long du trajet de transition de phase  $Pna2_1$  à  $Pnna$ , avec une énergie d'activation de 0,5-1 eV par unité de formule [12,20,21]. Cette forte énergie

d'activation de commutation entraîne un champ coercitif élevé qui stabiliserait donc les architectures de domaines électrostatiquement défavorables. Des parois de domaines de charge similaires n'ont été observées jusqu'à présent que dans des ferroélectriques inappropriées telles que  $\text{YMnO}_3$ , dans lesquelles le schéma de domaine est défini par un paramètre d'ordre primaire non ferroélectrique [22]. La configuration de la polarisation de queue à queue, avec une limite de domaine à environ 5 nm du substrat, peut être à l'origine du paramètre de cellule hors plan accru, observé pour les faibles épaisseurs. Les domaines de polarisation tail-to-tail devraient en effet se repousser et donc entraîner une augmentation des paramètres globaux de la cellule. Le phénomène sera de moins en moins appréciable avec l'augmentation des épaisseurs de films.

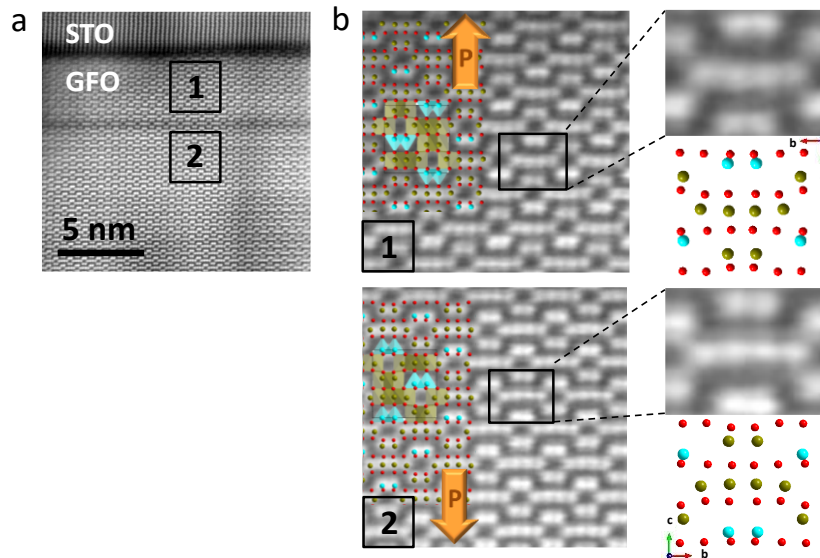


**Fig. 6 | Une étude microscopique de l'interface GFO et STO en utilisant le HAADF HR STEM.** (a) Une coupe transversale du film de GFO (001) de 32 nm déposé sur le STO (111) montrant que le GFO se développe dans sa structure  $Pna21$  prévue dès le début de la croissance. Une ligne sombre délimite une première couche de GFO de 5 nm d'épaisseur par rapport au reste de la couche. (b) Agrandissements de la zone 1, montrant une polarisation pointant vers le substrat, et de la zone 2, montrant une polarisation pointant vers l'extérieur du substrat.

D'importants effets interfaciaux substrat-film sont dévoilés par une étude EELS à résolution atomique (Fig 2.16 ; version complète sur la thèse). Les processus de migration ionique induits par les effets électrostatiques entraînent l'inversion de l'unité GFO-cellule après 5 nm d'épaisseur. La haute qualité épitaxiale et la croissance atomique à plat des couches minces de GFO sont hautement reproductibles, comme le démontre la croissance dans une autre chambre PLD qui suit une dynamique de croissance similaire. La croissance du GFO sur une électrode conductrice telle que le  $\text{SrRuO}_3$  (SRO)-STO tamponné modifie la dynamique de croissance, probablement en raison de la réduction ou de l'absence totale d'insertion de Ti dans les films de

GFO, et la croissance atomique de films lisses est possible même avec une faible épaisseur de cellule unitaire.

La démonstration de la croissance couche par couche hautement épitaxiale du GFO avec une surface atomiquement lisse à un régime d'épaisseur inférieur à 10 nm ouvre des perspectives d'applications pratiques dans les dispositifs de spintronique.

### 3. Propriétés magnétiques des films minces de GFO

Même si les propriétés magnétiques du GFO ont déjà été largement explorées dans la littérature, elles ne sont pas encore complètement comprises. Comme le montre l'introduction, cela est dû aux interactions d'échange complexes entre les ions Fe dans leurs différents environnements sur les quatre sites cationiques. En outre, en raison de l'attrait technologique de ce matériau GFO multifonctionnel, il est nécessaire de mieux comprendre les différents mécanismes à l'œuvre pour régir ses propriétés magnétiques à l'échelle mince/ultra-mince.

Les caractéristiques magnétiques des films minces ont été mesurées à l'aide d'un magnétomètre MPMS SQUID VSM de Quantum Design. Les propriétés magnétiques des films ont été étudiées à température ambiante et à 10 K avec des champs magnétiques allant jusqu'à 7 T appliqués à la fois dans le plan et hors plan. L'aimantation de saturation à température ambiante est d'environ 100 emu/cm<sup>3</sup> pour les échantillons de plus de 11 nm d'épaisseur, comme déjà observé pour les films fins GFO1.4 de forte épaisseur (environ 100 nm) <sup>[23]</sup>. Il diminue à environ 80 emu/cm<sup>3</sup> pour le film de 7 nm. Les boucles d'hystérésis de la magnétisation normalisée en fonction du champ magnétique sont illustrées à la figure 7.

L'axe de magnétisation facile des films dépend fortement de l'épaisseur du film. Il est frappant de constater que si l'aimantation est dans le plan pour les films d'une épaisseur de 11 nm ou plus, elle est hors plan pour l'échantillon de 7 nm d'épaisseur. Ce comportement, observé à température ambiante, est clairement confirmé par des mesures à basse température [Fig. 7 (b)]. Il n'avait jamais été observé auparavant pour les films minces de GFO. Les films présentant une magnétisation hors du plan sont très intéressants pour les applications basées sur la spintronique. Ils répondent en effet au défi actuel de développer des films isolants ferrimagnétiques de haute qualité, d'une épaisseur inférieure à 10 nm, avec une anisotropie magnétique perpendiculaire, qui sont souhaités pour une transmission efficace du courant de spin dans les systèmes ferromagnétiques/à effet Hall à spin plat <sup>[24]</sup>.

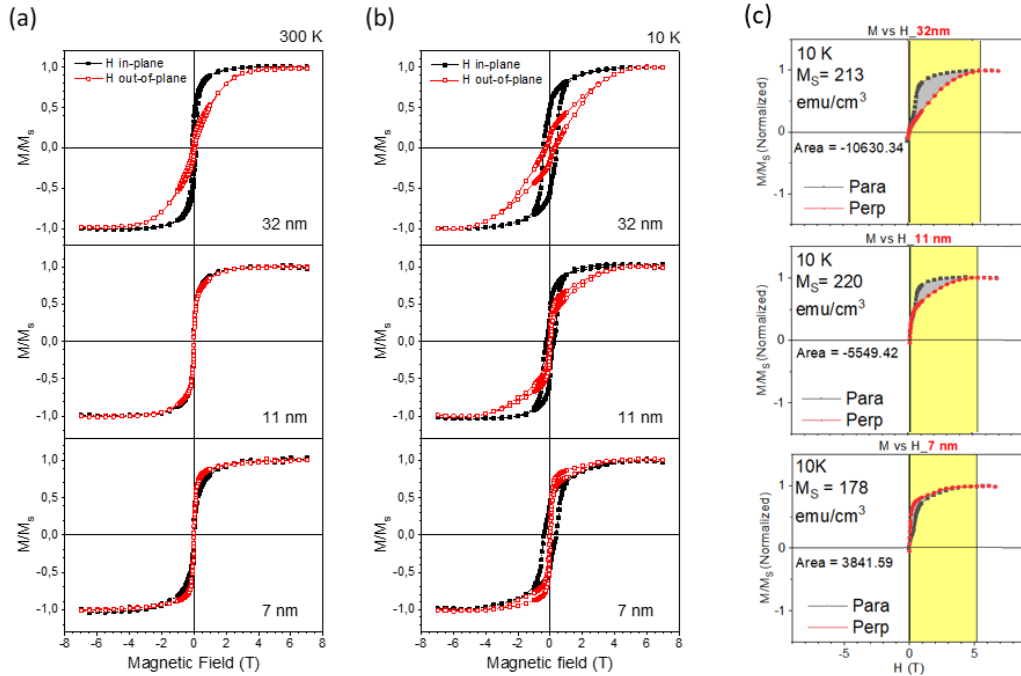


**Fig. 7 | Boucles d'hystérésis mesurées avec un champ magnétique dans le plan et hors plan pour les échantillons de 32 nm, 11 nm et 7 nm d'épaisseur. (a) Température ambiante, (b) 10 K, et (c) Différence de surface entre les courbes anhysterétiques dérivées de mesures parallèles et perpendiculaires à 10 K.**

Pour une manipulation efficace de l'axe magnétique facile, la compréhension de l'anisotropie magnétique est la quintessence. C'est pourquoi nous calculons l'anisotropie effective ( $K_{eff}$ ) qui comprend l'anisotropie magnétocristalline, l'anisotropie de forme, de surface, de contrainte, induite par la croissance et l'anisotropie d'échange. Le  $K_{eff}$  est calculé en utilisant la méthode de l'aire dans laquelle l'aire entre le mode parallèle et le mode perpendiculaire des courbes anisotropiques est mesurée et multipliée par la magnétisation de saturation, comme le montre la figure 7 (c). Puisque, à faible épaisseur, l'anisotropie de surface domine, nous pouvons calculer la constante d'anisotropie de surface ( $K_S$ ) en traçant le graphique  $K_{eff} * t$  en fonction de  $t$  selon la formule suivante  $K_{eff} * t = K_V * t + K_S$ , où " $K_V$ " est l'anisotropie de forme et " $t$ " est l'épaisseur. En ajustant les courbes comme indiqué à la figure 8 (a, b), on obtient  $K_V = -2,637 (63) * 10^5 \text{ J/m}^3$  à 10 K et  $-0,721 (42) * 10^5 \text{ J/m}^3$  à 310 K, comme pente, et  $K_S = 1,21 (37) \text{ mJ/m}^2$  à 10 K et  $0,37 (25) \text{ mJ/m}^2$  à 300 K, comme point d'intersection. L'interception de l'axe des x donne l'épaisseur de réorientation magnétique perpendiculaire  $t_{PMR} = 4,6 \pm 1,5 \text{ nm}$  (10 K) et  $5,13 \pm 3,9 \text{ nm}$  (310 K). Ces valeurs d'anisotropie peuvent être comparées aux valeurs trouvées dans la littérature, et mesurées par Bertaut <sup>[25]</sup> en vrac  $\text{Ga}_{2-x}\text{Fe}_x\text{O}_3$  ( $x = 1.15$ ) sur 20 K ( $K = 4.54 * 10^5 \text{ J/m}^3$ ) et par Katayama <sup>[26]</sup> en couche mince GFO ( $x = 1.4$ ) seulement à 300 K ( $K = 1.1 * 10^5 \text{ J/m}^3$ ). Pour les couches minces de 7 et 11 nm, la  $K_S$  contribution est importante et  $K_V$  ne domine plus. Ce concours explique le taux de changement dans  $K_{eff}$  est plus faible pour le 7 et le 11 nm. Cette

étude forme une base de compréhension de l'anisotropie magnétique dans nos films minces et est essentielle pour la perspective future de modulation de l'anisotropie magnétique à l'aide de la tension de grille.

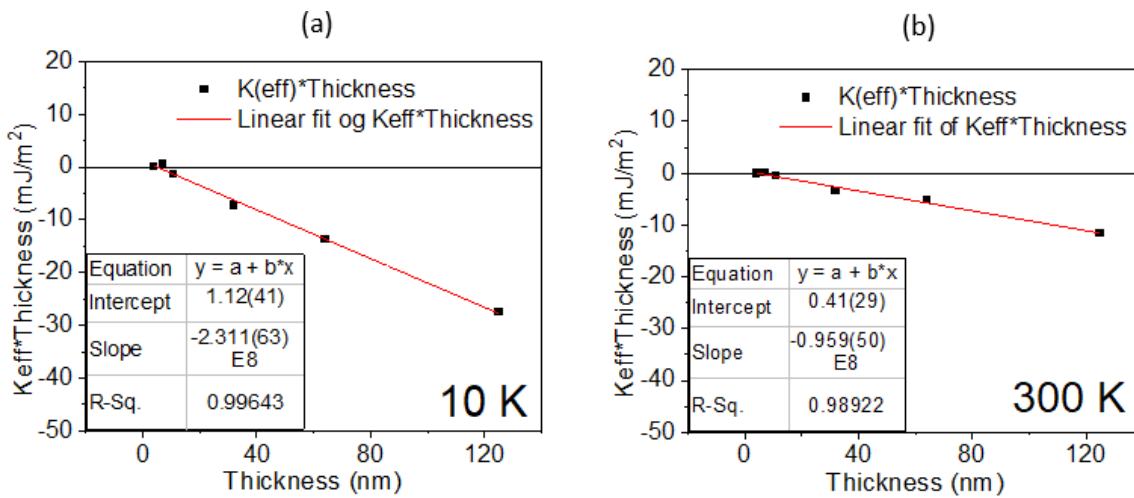


**Fig. 8 | Dépendance de l'épaisseur de  $K_{\text{eff}} * \text{Épaisseur}$ .**  $K_{\text{eff}} = (\text{zone entre les boucles de magnétisation des axes facile et difficile}) * (M_s)$  valeurs obtenues à partir de la figure 7. Pour (a) 10 K. (b) 300 K.

Nous passons maintenant à la mesure magnétique microscopique par dichroïsme circulaire magnétique à rayons X (XMCD). Pour la mesure du XMCD, nous mesurons d'abord les spectres d'absorption des rayons X dus à la transition de l'électron d'un niveau, par exemple Fe 2p, à un autre, par exemple Fe 3d (voir figure 9 (a)). La section transversale d'absorption des rayons X est différente selon l'hélicité circulaire des rayons X et/ou l'orientation de l'aimantation. Le XMCD est la différence entre les spectres XAS mesurés à ces deux hélicités différentes. En intégrant les spectres XAS et XMCD, nous pouvons obtenir le moment orbital et le moment de spin en utilisant les règles de somme élaborées par Thole et Carra (voir Fig. 9 (b, c)). Bien que la validité de ces règles de somme soit examinée dans des matériaux qui ont des sites Fe différents et donc un environnement local différent, nous utiliserons ces données pour obtenir une estimation approximative des valeurs et les comparer avec d'autres mesures.

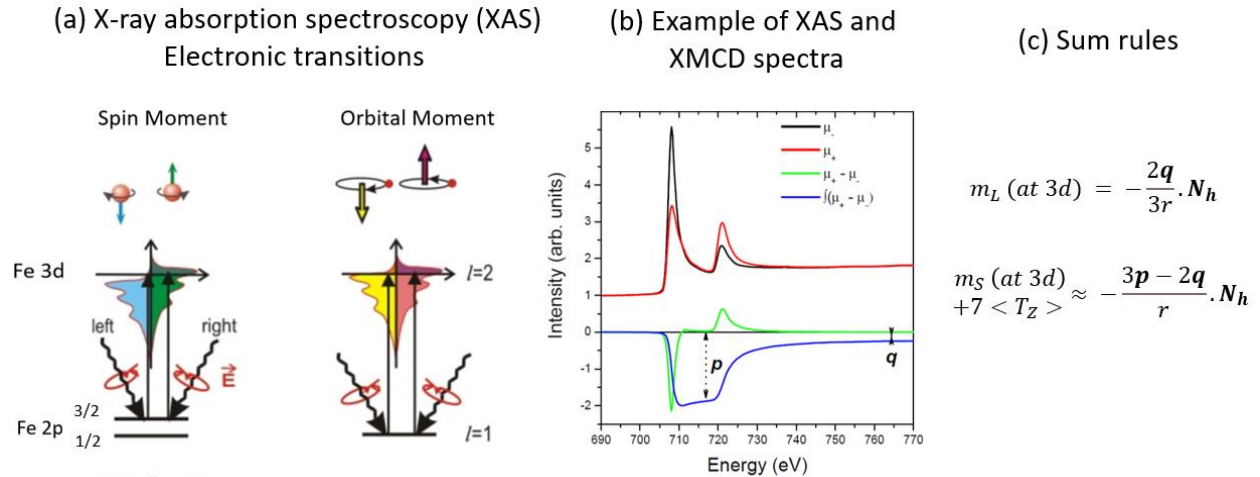


**Fig. 9 | Introduction aux mesures XAS/XMCD.** (a) Schéma des transitions électroniques dues à l'absorption des rayons X dans le modèle à un électron. (b) Un modèle du spectre XAS et XMCD. (c) Règles de somme telles que proposées par Carra et Thole.

Nous allons maintenant nous concentrer sur les spectres XAS et XMCD obtenus au bord du Fe  $L_{2,3}$  pour le film GFO relativement épais de 64 nm d'épaisseur, à 4 K, en géométrie GI, c'est-à-dire pour un champ magnétique appliqué principalement dans le plan. Les spectres sont présentés à la figure 10 (a). L'intégration des données XMCD montre que la valeur négative de "q" n'est pas nulle. Les règles de la somme indiquent que le moment orbital est directement proportionnel à la valeur "q". Le signe du  $m_L$  dépend de son signe. Si q est négatif(/positif),  $m_L$  sera parallèle(/anti-parallèle) à la direction  $m_S$ . Par conséquent, puisque nous observons une valeur négative non nulle de q, cela signifie que Fe dans notre film GFO a un " $m_L$ " fini parallèle à  $m_S$ . Ce résultat est similaire à celui déjà obtenu par Kim *et al.*<sup>[27]</sup> pour les monocristaux de GFO 1.0 à 190 K. Après avoir pris en compte les erreurs des règles d'addition, la valeur expérimentale à basse température de  $m_L = 0.011 \mu_B/Fe$  est mesurée, ce qui est en accord avec le calcul dérivé  $m_L = 0.008 \mu_B/Fe$ <sup>[28–31]</sup>.

Pour explorer l'anisotropie des moments magnétiques portés par le Fe, à la fois  $m_S$  et  $m_L$ , nous devons examiner les mesures XAS et XMCD dans la géométrie GI et NI. Nous avons déjà vu les mesures en mode GI, et nous nous dirigeons maintenant vers les mesures en géométrie NI, toujours pour un film mince de GFO de 64 nm, à 4 K et pour le Fe  $L_{2,3}$  edge. Les spectres XMCD sont présentés à la figure 10. Étonnamment, l'intégrale XMCD présente maintenant une valeur positive non nulle de "q", contrairement à la valeur négative de "q" observée pour la géométrie GI. L'orientation du  $m_L$  par rapport au  $m_S$  change de signe entre les géométries NI et GI puisque le  $m_L$  est antiparallèle au  $m_S$  pour la géométrie NI alors qu'il est parallèle au  $m_S$  pour la géométrie GI. La configuration NI sonde principalement la projection hors plan du moment orbital et celle GI, celle dans le plan. Nous avons donc une indication expérimentale que le moment orbital varie dans l'espace et diffère selon les orientations cristallographiques.

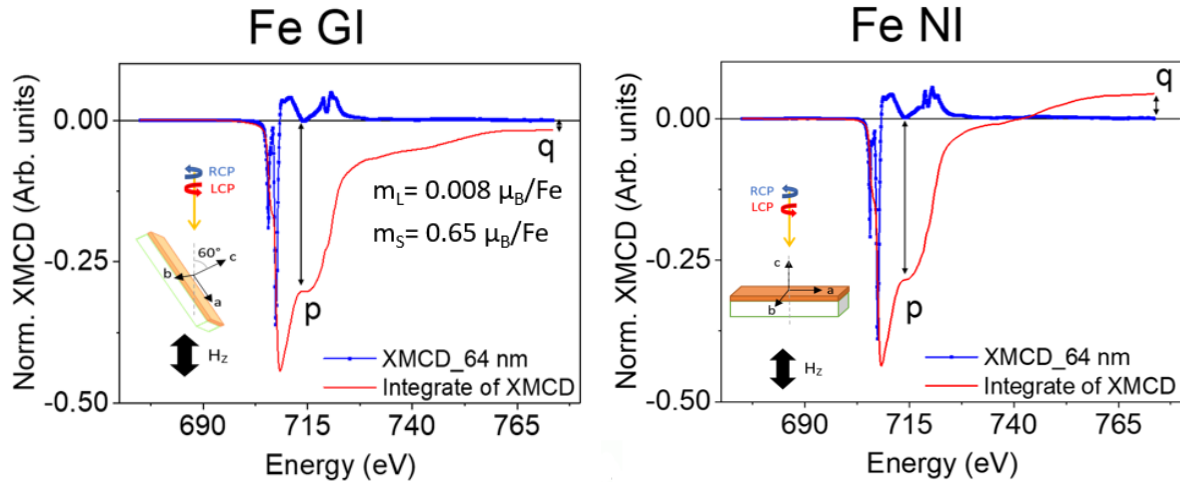


**Fig. 10 | Spectroscopie XMCD à 4K sur le bord Fe  $L_{2,3}$  en mode GI et NI sur un film mince de GFO de 64 nm d'épaisseur.**

Dans une étude précédente Tseng *et al.* [32] a démontré que  $\epsilon\text{-Fe}_2\text{O}_3$ , un composé isostructural au GFO ne contenant que des cations Fe, a également montré un moment orbital non nul, qui avait une dépendance non monotone de la température, avec un minimum en  $m_L$  pour 120 K. Cette caractéristique s'est accompagnée d'une forte diminution du champ coercitif des boucles d'hystérésis de magnétisation du composé. Par conséquent, nous avons d'abord effectué une étude de la dépendance en température du champ coercitif dans nos films GFO, dans des configurations parallèles et perpendiculaires, par SQUID comme le montre la figure 11 (a). Le graphique ne montre aucune anomalie particulière pour la mesure parallèle, pour laquelle l'augmentation attendue de  $H_c$  est observée lors de la baisse de la température, les mesures perpendiculaires montrent un maximum anormal dans la courbe à environ 150 K. Pour explorer le mécanisme microscopique derrière le changement anormal de  $H_c$ , nous concentrons nos mesures microscopiques en géométrie NI puisque l'anomalie a été observée pour les mesures en mode perpendiculaire.

Nous avons observé une valeur "q" positive finie à toutes les températures mesurées, ce qui suggère un alignement antiparallèle de  $m_S$  et de  $m_L$ . Les valeurs  $m_S$  obtenues à partir du XMCD diminuent de façon monotone avec la température et le profil de température est comparable au profil obtenu avec le SQUID pour le même échantillon. On note qu'un comportement non monotone avec la température est observé pour les deux  $m_L$  et  $\frac{m_L}{m_S}$  et se caractérise par un minimum à ca. 120 K. L'évolution de la température de  $\frac{m_L}{m_S}$  est différent pour les différentes épaisseurs d'échantillon comme le montre la figure 11 (b). On observe un déplacement possible de la température minimale de 120 K pour 64 nm à 200 K pour 07 nm, mais il faut davantage de points de données pour vérifier cette affirmation. Bien qu'un comportement clair et non monotone soit observé pour les épaisseurs de 07, 32 et 64 nm, il est intéressant de noter que

l'échantillon de 11 nm ne présente pas de changement significatif dans cette plage de température. Étant donné qu'à 11 nm, la polarisation des 5 premiers nm et celle des 5 nm suivants sont opposées, on peut supposer que le champ électrique intrinsèque des 11 nm est inférieur à celui des échantillons d'autres épaisseurs. Cela pourrait signifier que le champ électrique intrinsèque peut jouer un rôle crucial dans l'anomalie observée à 120 K et est donc une preuve d'un effet magnétoélectrique indirect dans le GFO.

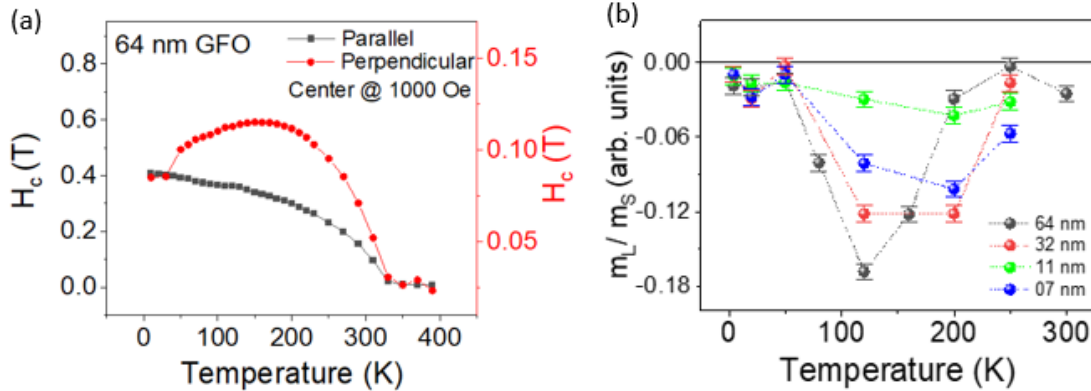


**Fig. 11 | Évolution de la température des valeurs expérimentales extraites de SQUID et XMCD.** (a)  $H_c$  pour 64 nm. (b)  $m_L/m_S$  pour 64 nm en mode NI.

#### 4. Étude de la polarisation électrique dans les couches minces du GFO.

Les techniques de caractérisation électrique utilisées pour sonder la polarisation des oxydes ferroélectriques (FE) en couches minces doivent faire face à des points critiques tels que les courants de fuite ou les problèmes d'interface électrode-ferroélectrique (barrière Schottky, longueur du blindage, etc.). La technique de sondage optique non linéaire basée sur la génération optique de seconde harmonique (SHG) induite par laser est un outil alternatif intéressant pour aborder la caractérisation de la polarisation électrique, même dans les couches minces d'oxydes de FE qui présentent des fuites [33]. Le SHG permettra de générer une lumière ayant une fréquence  $2\omega$ , le double de la fréquence de la lumière incidente, comme le montre la figure 12 (a). Cette fréquence lumineuse  $2\omega$  interagit avec la polarisation  $P$  pour ne donner au SHG que la contribution  $P(2\omega)$  qui est décrite par  $P_i(2\omega) = \epsilon_0 \sum_{j,k} \chi^{(2)}_{ijk} E_j(\omega) E_k(\omega)$ , où la  $ijk$  Les notations précisent les xyz les axes cristallographiques, et  $\chi^{(2)}_{ijk}$  est une composante du tenseur du deuxième ordre  $\chi^{(2)}$  qui caractérise l'état ferroélectrique. L'intensité de la lumière à double fréquence émise par la polarisation induite  $P(2\omega)$  est donnée par  $I_{SHG} \propto |P(2\omega)|^2$ .

Nous rendons compte de l'enquête sur les effets liés aux SHG dans  $\text{Ga}_{0.6}\text{Fe}_{1.4}\text{O}_3$  (GFO) des films minces, qui a été réalisée en collaboration avec ETH, Zürich. Cette étude présente une étude SHG complète des films GFO en mettant l'accent sur les échelles ultra-minces en utilisant à la fois des

méthodologies *ex situ* et *in situ*, qui sont complémentaires les unes des autres et ont leurs propres avantages distincts.

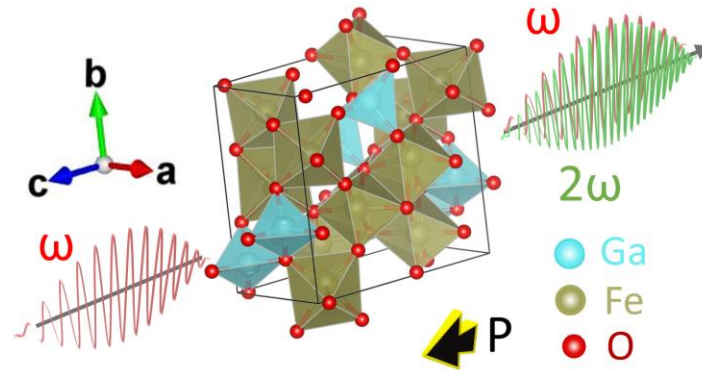


**Fig. 12 | Schéma du doublement de la fréquence des SHG à partir d'un  $\text{Ga}_{0.6}\text{Fe}_{1.4}\text{O}_3$  cellule unitaire avec une polarisation P le long de l'axe c ( $Pna2_1$ ) et la lumière passant à travers la cellule unitaire le long de l'axe c.**

Lors de la mesure *ex situ*, nous avons étudié des couches minces de GFO de différentes épaisseurs (entre 7 et 32 nm) cultivées sur des substrats de STO (111). Pour évaluer l'état polaire du film, nous avons incliné l'échantillon de  $\theta = +30^\circ$  à  $-30^\circ$  par rapport à la normale à la surface. La figure 13 (a, b) montre la dépendance du SHG par rapport à la direction de l'incident et aux polarisations de la lumière détectée pour le film GFO de 32 nm à une inclinaison de  $30^\circ$ . La symétrie des deux lobes principalement dans la direction horizontale (le long de la projection de  $P_s$ ) est en accord avec le groupe de points  $mm2$  moyenné sur les trois variantes cristallographiques, et avec les films massifs et fins précédents <sup>[34]</sup> mesures. Le décalage des lobes par rapport à la direction horizontale est dû à une superposition de la surface du substrat STO SHG avec les contributions OOP-SHG du film. La dépendance de l'épaisseur de la polarisation électrique du GFO a été étudiée en effectuant des mesures SHG dépendantes de l'inclinaison sur un ensemble de films de GFO d'épaisseurs différentes, y compris le substrat STO nu, et en extrayant leur composante OOP respective du signal SHG. Comme le montre la figure 13 (c), l'intensité du SHG augmente globalement en fonction de l'épaisseur du film, et les films d'une épaisseur aussi faible que 7 nm présentent une polarisation finie.

Pour les mesures *in situ*, nous utilisons la technologie de pointe de la deuxième génération d'harmoniques (ISHG) mise au point par nos collègues du Laboratoire des matériaux ferroïques multifonctionnels de l'ETH-Zürich. L'ISHG permet un accès direct à la polarisation spontanée (P) d'une couche mince en temps réel pendant sa croissance et permet à l'utilisateur de suivre l'évolution de la polarisation en fonction de l'épaisseur. Une telle technique qui permet d'étudier la polarisation à chaque étape de la croissance est d'un intérêt particulier, surtout dans un système d'oxyde qui croît de façon épitaxiale avec une précision inférieure à celle d'une

monocouche [35,36]. Un niveau de précision atomique de contrôle des fonctionnalités ferroélectriques (dans ce cas, FE) dans des régimes ultra-minces est à la barre du bateau à succès de la spintronique des oxydes, car un changement de l'épaisseur des cellules des sous-unités peut avoir un impact critique sur la fonctionnalité ferroélectrique [37-41].

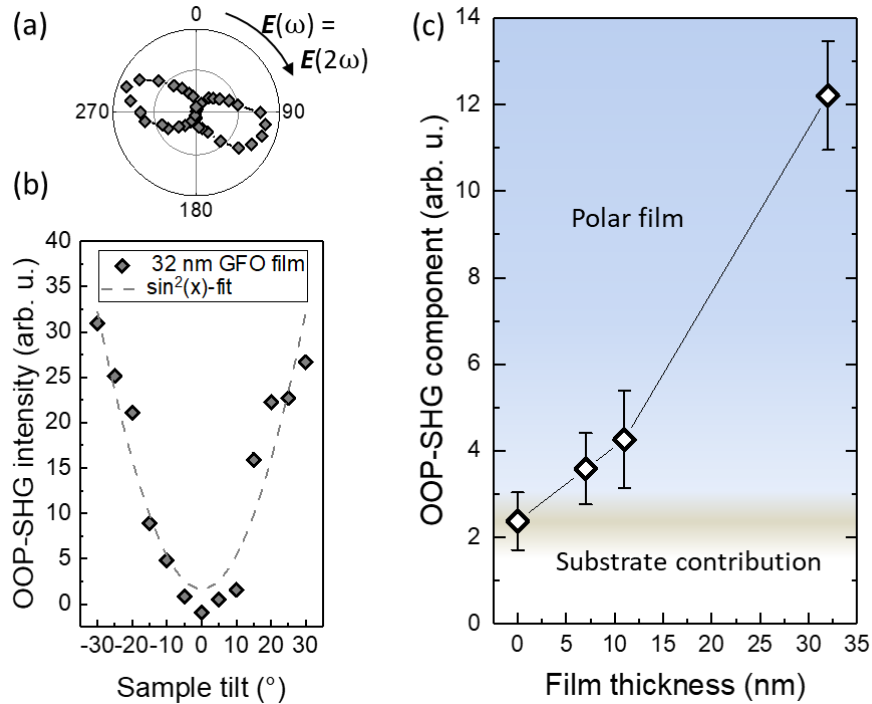


**Fig. 13 | SHG hors avion (OOP) à température ambiante.** (a) Anisotropie OOP-SHG du film GFO 32 nm à une inclinaison de 30°. (b) Dépendance de l'échantillon de la composante OOP SHG indiquée en (a) par rapport à l'inclinaison. La dépendance en  $\sin^2(x)$  confirme l'orientation de la polarisation spontanée dans le matériau. (c) OOP-SHG à température ambiante en fonction de l'épaisseur du film de GFO.

L'évolution du signal ISHG normalisé avec l'épaisseur du film de GFO cultivé sur STO peut être observée sur la figure 14 (a) pour des angles de polarisation/analyse de 30/30. Le signal à 90/90 (voir encadré : carte polaire) correspond à la composante normale à la surface de la polarisation, mais on constate qu'il a une grande contribution liée à la surface, interférant avec le signal de polarisation principal, et donc le signal 30/30 qui a une très petite composante liée à la surface est montré. L'observation d'un signal ISHG croissant à la température de croissance de 800°C démontre expérimentalement l'existence d'une structure non centrosymétrique (qui conduit à la polarisation) dans le GFO au moins jusqu'à 800°C. Comme la croissance est préparée sur un substrat STO, qui est non conducteur, l'effet de champ de dépolérisation devrait conduire à la formation de domaines polaires dans les couches minces du GFO. Mais l'existence d'un signal ISHG fini montre que la polarisation du GFO est robuste et résiste à l'effet de champ de dépolérisation.

Le signal de surface de la Fig 14 (a) montre un comportement oscillatoire au début de la croissance (voir la version zoomée de la Fig 14 (b)), qui est attribué à la sensibilité du signal SHG à une certaine rupture de symétrie d'inversion liée à la croissance d'un quart de cellule de la couche mince de GFO qui a été démontrée par les oscillations RHEED de la Fig 5 (c). La figure 15 (a) montre une cellule de 3\*3\*3 unités (c'est-à-dire 12\*12\*12 sous-unités) projetée perpendiculairement à la direction [110]. Nous divisons cette super-cellule unitaire en 4 parties égales le long de la direction c, chacune contenant 3 sous-cellules unitaires et nous supposons que la croissance de chaque partie conduit à une structure cristalline asymétrique le long de l'axe c. Dans la première partie de l'encadré rouge "3", nous voyons des couches LMLN attribuées à des couches polyédriques de 4 cellules sous-unitaires qui forment une cellule unitaire complète. Dans cette partie, les couches M et N des sous-unités du GFO génèrent une asymétrie qui est contrebalancée par M' et N' en raison de la symétrie de translation entre elles le long de l'axe c, tandis que toutes les couches des cellules L des sous-unités du GFO ont un centre d'inversion dans l'octaèdre. Il est bien établi que la symétrie d'inversion ou la symétrie de translation doit être rompue aux surfaces ou aux interfaces des films pour la génération d'un signal SHG, en raison de l'incomplétude du cristal <sup>[42]</sup>.

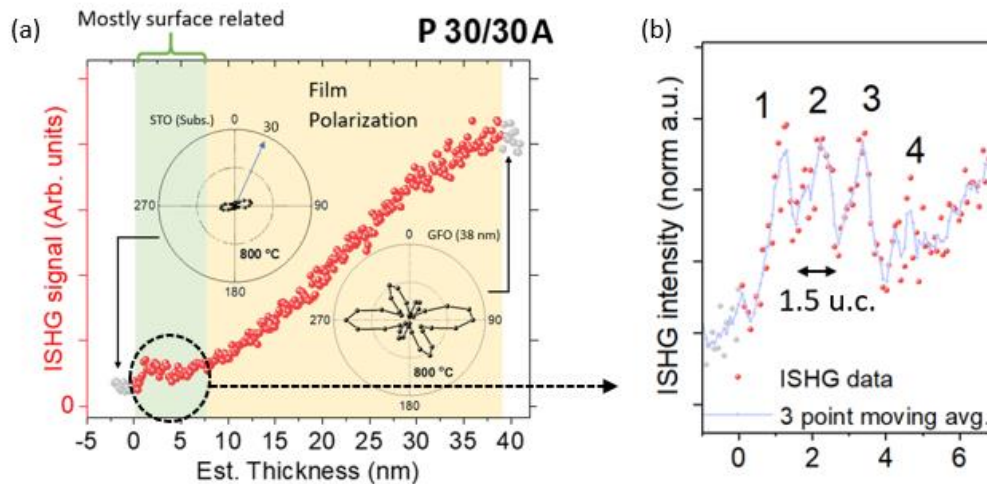


**Fig. 14 | Signal ISHG pour les couches minces de GFO à 800° C.** (a) Aux angles de 30° du polariseur/analyseur, car la contribution de l'STO y est moindre, comme le montre la carte polaire de l'STO insérée. (b) Les données ISHG ont été zoomées de 0 à 7 nm pour se concentrer sur les effets liés à la surface.

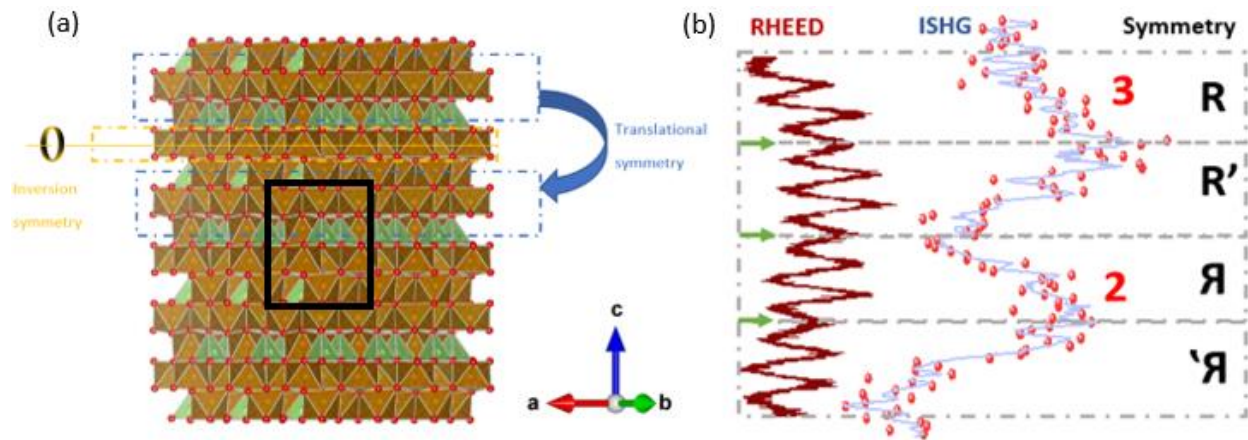


**Fig. 15 | Proposition d'un nouveau modèle basé sur des considérations de symétrie pour expliquer l'oscillation des données ISHG pendant la croissance des premières cellules unitaires.** (a) Schéma de cellules unitaires 3\*3\*3 GFO projetées perpendiculairement à l'axe [110], avec l'axe du vecteur de croissance  $c$  le long de la verticale ( $Pna2_1$ ). (b) Les données du RHEED (de la figure 5 (c)) pour l'échantillon de 7 nm sont présentées ici pour être comparées avec le signal ISHG des oscillations "2" et "3".

En résumé, nous proposons une cellule unitaire étendue  $1*1*3$  comme nouvelle super-unité, chaque oscillation du SHG correspondant à la moitié de celle-ci, soit une super-unité  $1*1*1,5$ . Les données du RHEED sont parfaitement compatibles avec cette analyse SHG, comme le montre le point 15 (b), où chaque pic court est attribué à un changement dans la nature de la symétrie. Le GFO est donc un cas singulier de système d'oxyde où l'on peut non seulement surveiller la croissance du quart de cellule de la sous-unité via le RHEED, mais aussi choisir une terminaison exacte combinant les 3 pics distincts des oscillations du RHEED et les oscillations ISHG associées de la cellule de 6 sous-unités. Un tel contrôle précis et in situ des symétries à des échelles ultrafines est sans précédent et particulièrement intéressant dans un matériau magnéto-électrique multiferroïque comme le GFO.

Nous avons également réalisé des expériences en insérant une électrode SRO conductrice entre le substrat STO et les films GFO, dans des hétérostructures STO//SRO/GFO, afin d'étudier l'effet de l'absence d'un champ de dépolarisation sur la polarisation du GFO. Dans cette configuration, l'impact de la surface sur le signal du SHG s'est avéré beaucoup plus faible que pour la croissance directe sur le STO et une estimation de l'épaisseur critique a été possible. Elle a donné une valeur comprise entre 0,5 et 2 cellules, ce qui est très faible par rapport à d'autres matériaux ferroélectriques (voir la figure 4.14 dans le texte principal de la thèse). Cela confirme la rigidité de la polarisation électrique dans le GFO, et sa résistance impressionnante au champ dépolarisant.

## 5. Fonctionnalité des couches minces de GFO en spintronique

Cette section vise à explorer les fonctionnalités que le GFO pourrait endosser dans les systèmes spintroniques. Nous avons considéré son potentiel dans les hétérostructures ferrimagnétiques (FM) / métaux lourds (HM) pour une manipulation libre de champ magnétique de la magnétisation du FM, où GFO serait la couche FM, et Pt le HM. Dans ces hétérostructures FM/HM, certains courants de spin purs sont créés dans la couche de métal lourd (HM) par effet Hall de spin (SHE), et l'injection de ce courant de spin dans la couche ferrimagnétique (FM) adjacente avec manipulation de son orientation de magnétisation est étudiée.

Nous avons démontré la croissance du GFO (001) atomiquement lisse sur le STO (111) dans les chapitres précédents ; maintenant, nous examinons la croissance du Pt sur une couche de GFO. Nous avons considéré une épaisseur de Pt de 5 nm pour générer des courants de spin, car certaines études détaillées ont suggéré que cette épaisseur était optimale pour les courants de spin induits par SHE après avoir examiné des facteurs tels que la longueur de diffusion du spin ( $\lambda_{sd}$ ), la perte de mémoire de spin (SML) à l'interface <sup>[43]</sup> et l'efficacité du couple de rotation de Hall par unité de champ électrique appliquée <sup>[44]</sup>. Ces films Pt ont été cultivés à température ambiante (27°C) sous vide, *i.e.*, une pression de base de  $5 \cdot 10^{-8}$ , sur un GFO atomiquement lisse, avec une fluence laser de 4 J et une fréquence de répétition de 10 Hz. Nous avons effectué une analyse structurale de surface d'une hétérostructure Pt/GFO//STO telle qu'elle a été développée, en utilisant la microscopie à force atomique (AFM), la diffraction des rayons X et la microscopie électronique à transmission (TEM), comme le montre la figure 16 (a-c). L'AFM est lisse et suit la morphologie de la couche GFO 001. Les données XRD montrent un échantillon propre, sans phase parasite et de haute cristallinité. La preuve de l'interface de haute qualité est corroborée par les images TEM qui montrent une interface nette. La cartographie élémentaire de l'interface ne montre aucune interdiffusion entre le Pt et le GFO.

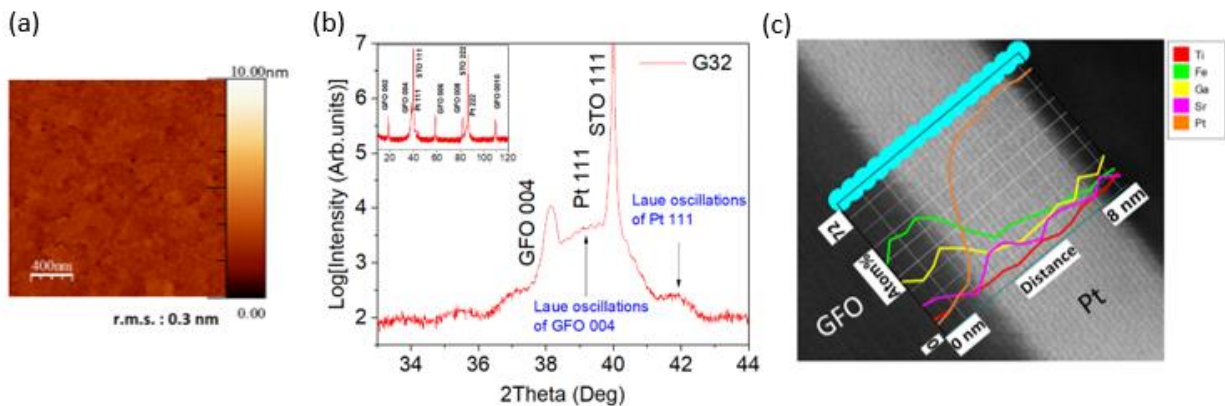


**Fig. 16 | Caractérisation d'un film Pt (111)/GFO (001)// (STO 111) de 32 nm d'épaisseur. (a)** Image AFM du film GFO. **(b)**  $\theta$ -2 $\theta$  mesure par rayons X. **(c)** Caractérisation microscopique à l'aide du STEM.

La résonance ferromagnétique (FMR) est l'une des premières techniques permettant d'observer la dynamique du spin dans les matériaux ferromagnétiques et ferrimagnétiques, qu'il s'agisse de films massifs ou minces. Mais, comme la possibilité d'observer la dynamique de la FMR du GFO exigeait des critères instrumentaux stricts qui étaient malheureusement au-delà du potentiel actuel des instruments disponibles, nous avons décidé de passer à d'autres moyens d'observer l'effet du courant de spin induit par la SHE de Pt au GFO. Nous avons choisi d'étudier comment les phénomènes de magnéto-transport du Pt sont affectés par un film adjacent de l'isolant magnétique GFO. Des mesures de transport ont été effectuées sur une double barre de Hall (Fig 17) lithographiée sur des bicouches Pt (5 nm) /GFO (32 nm) cultivées sur des substrats STO (111) (hétérostructure appelée désormais G32).

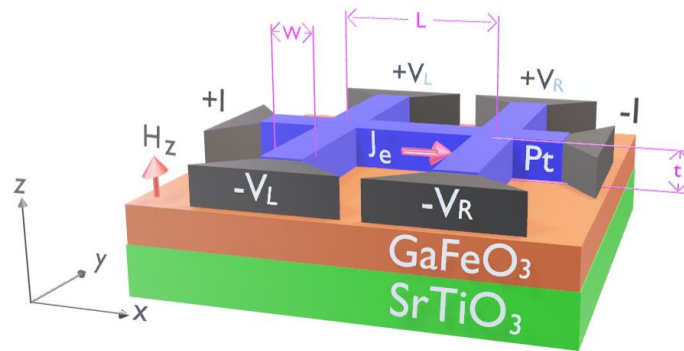


**Fig. 17 | Modèle 3D de la double barre de Hall lithographiée sur des hétérostructures Pt/GFO//STO (111) avec marquages de longueur (L), largeur (w) et épaisseur (t).**

Nous réalisons des études longitudinales  $\rho_{xx}$  vs.  $H_z$  des mesures dans une large gamme de température entre 300 et 20 K pour l'échantillon G32. Pour une meilleure illustration des résultats de ces expériences, nous traçons le graphique de la MR, i.e.  $\Delta\rho_{xx}/\rho_{xx}$  vs.  $H_z$  en Fig. 18 (a). Les courbes de résistivité en Fig. 18 (a), ne saturent pas même aux champs magnétiques au-delà de la saturation magnétique mesurée par le SQUID. Cela est dû aux moments indépendants à l'interface qui ne laissent pas le champ magnétique élevé saturer<sup>[45]</sup>. Nous pouvons observer un changement net du signe du RM avec la température. Le tracé de l'évolution du RM à 7 T ( $\Delta\rho_{xx}/\rho_{xx}$  at  $H = 7$  T) avec la température (Fig. 18 (b)) montre que sa transition d'inversion de signe est proche de la plage de température de 120 K.

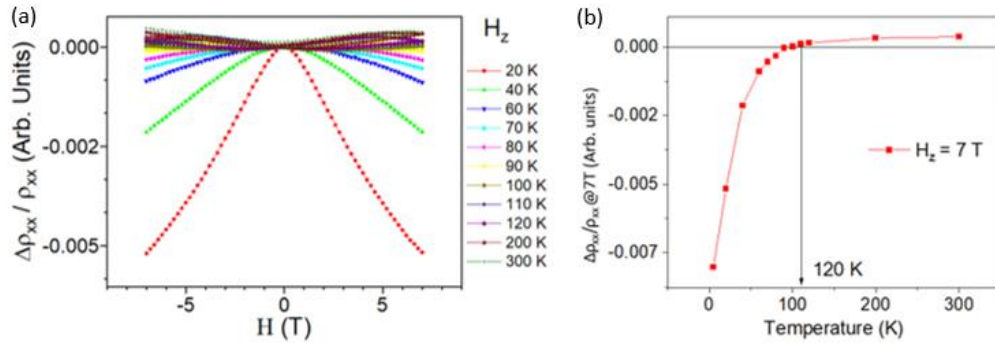


**Fig. 18 | Longitudinal MR  $\Delta\rho_{xx}/\rho_{xx}$  mesuré sur une double barre de Hall, modélisée sur le G32 à différentes températures. (a) Pour les champs magnétiques externes orientés dans la direction z. (b) Dépendance de la température du MR longitudinal à 7 T pour les différentes orientations de champs  $H_z$ .**

Il est intéressant de noter que la résistivité anormale de Hall  $\rho_{xy-AH}$  vs.  $H_z$  (Fig. 19 (a)), dérivée après avoir soustrait la contribution linéaire de l'effet Hall ordinaire de la résistivité Hall transversale montre également une inversion des courbes d'hystérésis en fonction de la température, comme le montre la figure 19 (b). Une telle inversion a été observée dans de nombreuses autres couches FM/Pt et s'explique soit par certains changements au niveau de Fermi dans la structure de la bande électronique du Pt [46,47] ou comme empreinte digitale du monopôle magnétique dans l'espace d'impulsion du cristal de Pt [48,49].

Les hétérostructures magnéto-transport en métal lourd (HM) / ferromagnétique isolant (FM) peuvent s'expliquer selon deux modèles différents. Le premier, illustré à la figure 20 (a), implique l'existence d'un certain magnétisme interfacial induit dans le Pt non magnétique, dû à un effet de proximité magnétique (MPE). Un second modèle, la magnétorésistance de spin Hall (SMR) introduite par Nakayama *et al.* [50], est uniquement due à l'effet Hall de spin (SHE) et à l'effet Hall de spin inverse (ISHE), représentés sur la figure 20 (b). La résistivité de la couche NM dépend donc fortement de l'orientation de la magnétisation FM. En raison d'une éventuelle intégration des hétérostructures GFO/Pt (comme d'autres FM/HM) dans les appareils de la prochaine génération, il est nécessaire de mieux comprendre les effets sous-jacents et d'analyser quantitativement les contributions possibles de l'EMF et de l'ESM et d'identifier les mécanismes dominants.

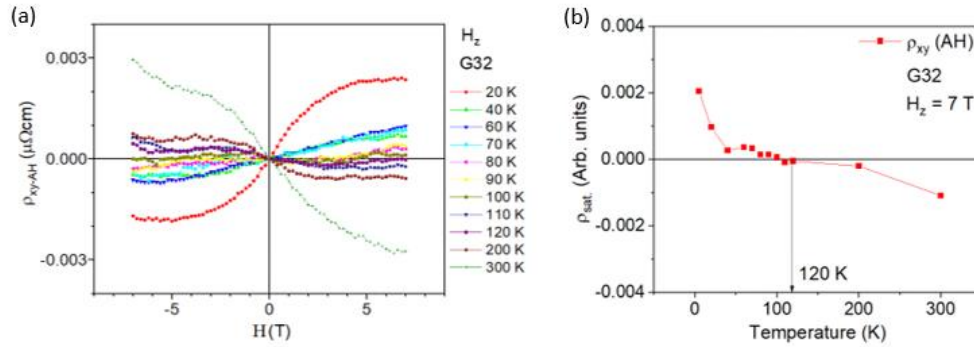


**Fig. 19 | Mesures de la résistivité transversale de Hall sur une double barre de Hall, avec un motif G32 pour la direction du champ magnétique  $H_z$ .** (a) Contribution de l'effet Hall anormal à la résistivité transversale, calculée en soustrayant la contribution linéaire de l'effet Hall ordinaire de la résistivité transversale de Hall. (b) Dépendance de la résistivité transversale à la température de saturation,  $\rho_{\text{sat}}$ .

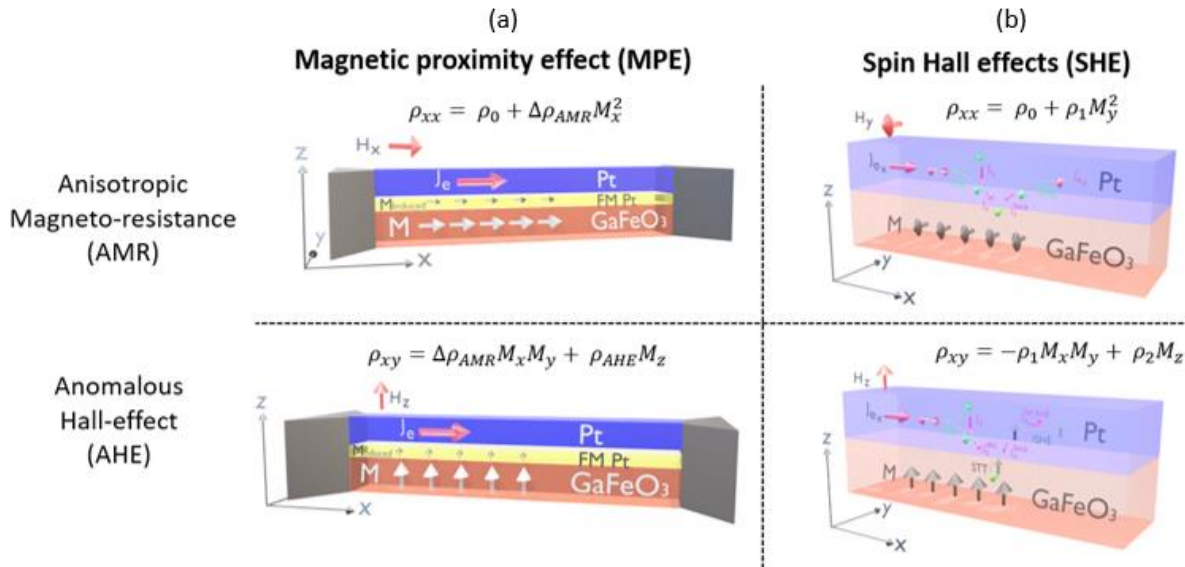


**Fig. 20 | Modèles 3D de l'hétérostructure Pt/GFO dans un champ magnétique  $H_z$ , permettant de percevoir les phénomènes de magnéto-transport à la fois en mode longitudinal (pour la RAM) et transversal (pour l'AHE).** (a) L'effet de proximité magnétique (MPE). (b) Effets induits de Spin Hall (SHE).

Une façon possible de séparer les contributions du MPE et du SMR consiste à effectuer des mesures en fonction de l'angle avec le champ magnétique dans l'un ou l'autre des 'xz' ( $\beta$ ) ou le 'yz' ( $\alpha$ ) comme le montre la figure 21 (a), tandis que la densité de courant  $J_e$  et la résistivité mesurée  $\rho_{xx}$  sont dans la direction 'x' [45]. Nous traçons le  $\beta$  dépendance de  $\frac{\rho(\beta) - \rho_z}{\rho_z}$  et le  $\alpha$  dépendance de  $\frac{\rho(\alpha) - \rho_z}{\rho_z}$ , pour différentes températures, comme le montre la figure 21 (b),

respectivement. Nous extrayons les valeurs SH-AMR et MPE-AMR séparément en prenant les valeurs MR à  $\beta = 0^\circ$  et  $\alpha = 0^\circ$ . Ces valeurs SMR et MPE AMR extraites sont représentées sur la figure 21 (c). La contribution du SMR est plus importante que la contribution du MPE AMR pour nos hétérostructures GFO/Pt. La contribution de la MPE AMR, et donc l'effet de proximité, est négligeable à des températures supérieures à environ 100 K, pour lesquelles seule la SMR est présente.

La valeur du SMR mesurée pour les hétérostructures GFO/Pt est d'environ  $2 \cdot 10^{-4}$  sur 300 K et  $4.5 \cdot 10^{-4}$  sur 20 K. Ceci est identique à ce qui est observé dans les hétérostructures YIG/Pd et seulement légèrement inférieur à ce qui est observé YIG/Pt ( $4 \cdot 10^{-4}$  sur 300 K et  $6 \cdot 10^{-4}$  sur 20 K) [45]. On constate l'existence d'un minimum dans les mesures de SMR dans la gamme 90-140 K. Une caractéristique moins prononcée mais similaire est également observée dans le profil de température de la RMA du MPE. Comme les contributions de la SH-AMR et de la MPE-AMR proviennent de l'interaction du courant de charge circulant dans le Pt avec les propriétés magnétiques (spins corrélés) dans le GFO, il est alors possible d'émettre l'hypothèse d'un lien entre le changement non monotone du couplage spin-orbite à 120 K et le changement non monotone des mesures SMR/AMR observé à la température de 90-140 K. Dans l'ensemble, nous concluons que cette étude permet de mieux comprendre les interactions spin-courant avec l'aimantation de cet important GFO multiferroïque magnéto-électrique.

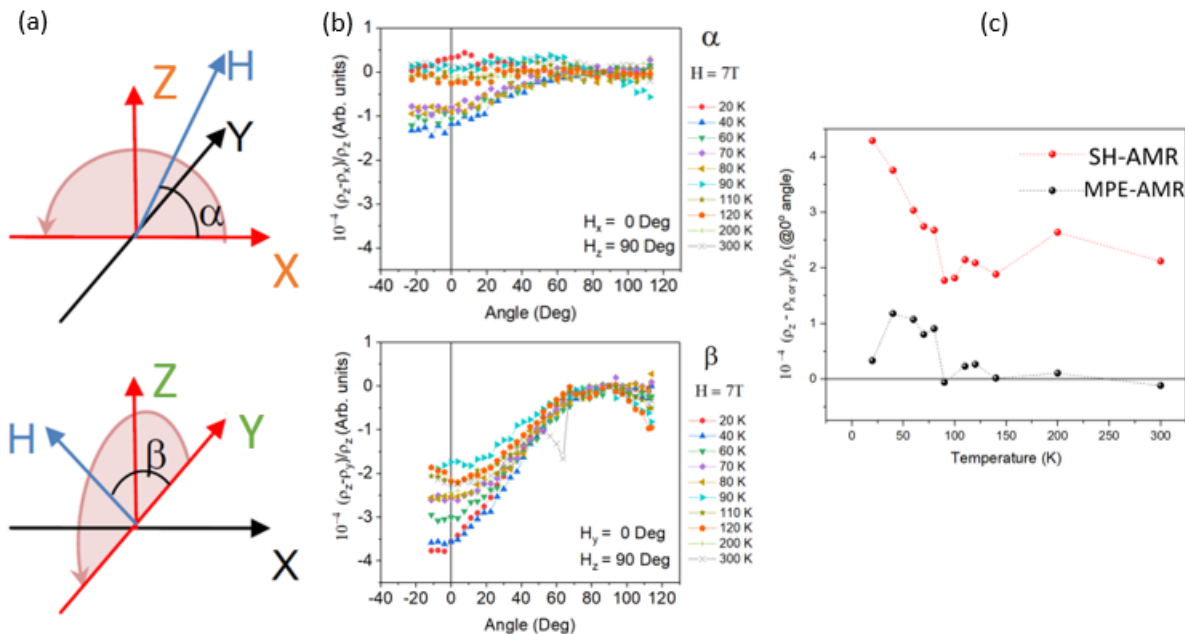


**Fig. 21 | Différenciation entre MPE-AMR et SH-AMR.** (a) Types de géométries de mesures angulaires envisagées. (b) Mesures angulaires à différentes températures pour G32. (c) Dépendance de la température des MPE AMR et SMR telle que déduite de la  $\frac{\rho(\beta) - \rho_z}{\rho_z}$  et  $\frac{\rho(\alpha) - \rho_z}{\rho_z}$  valeurs mesurées à un angle de zéro degré pour  $\beta$  et  $\alpha$ , respectivement.

## Conclusion

En conclusion, nous avons réussi à faire croître l'oxyde de GFO complexe en couches minces atomiques épitaxiales plates par dépôt laser pulsé (PLD) sur des substrats de SrTiO<sub>3</sub> (STO) avec un contrôle de l'épaisseur déposée jusqu'à une résolution de 1/4 de cellule unitaire. Une migration ionique importante du Ti du substrat STO vers le film déposé GFO a été mise en évidence jusqu'à 5 nm dans les films déposés. L'anisotropie magnétique des films a pu être réglée hors du plan, pour les plus minces, et dans le plan pour les plus épais. Contre toute attente dans un matériau à base de Fe<sup>3+</sup> de 3d<sup>5</sup>, le moment orbital du Fe s'est avéré non nul, non monotone, dépendant de la température et fortement anisotrope, indiquant un couplage magnéto-structural important. Les films ont montré une forte polarisation dès le début de la croissance et ne semblent pas être sensibles à un quelconque champ dépolarisant. Des hétérostructures de GFO/Pt ont été produites comme première étape vers le développement de dispositifs spintroniques. Les mesures de magnéto-transport dépendantes de l'angle ont révélé un important effet de magnétorésistance de spin Hall (SMR) et ont donc conforté la pertinence du GFO pour les dispositifs de mémoire à faible consommation d'énergie basés sur l'effet de spin Hall.

## Perspective

Nous discutons maintenant des perspectives d'avenir possibles avec l'utilisation des couches minces GFO. L'utilisation future du GFO comme multiferroic magnétoélectrique dans les mémoires ME-SOT ou les architectures logiques MESO pour des opérations à très faible consommation est notre objectif ultime. Cependant, un point important de préoccupation serait également la possibilité d'étudier l'effet d'une tension de grille sur l'anisotropie magnétique et/ou l'anisotropie orbitale du GFO, en tirant parti de l'effet magnéto-électrique indirect mis en évidence par le XMCD, et du contrôle de la tension de grille des distorsions. Une suite naturelle de nos investigations au SHG serait bien sûr d'étudier une hétérostructure de STO//SRO/GFO/SRO *in situ*, *via* ISHG. Il a été démontré que cela déclenche la formation de domaines dans un film mince à domaine polaire unique et permettrait de déterminer la résistance ultime de la cellule GFO vis-à-vis d'un champ dépolarisant.

Compte tenu de l'étude des applications du GFO liées au spin, je propose d'envisager un système d'hétérostructure tri-couche FM1/NM/FM2, dans lequel le matériau ferromagnétique FM1 peut être amené dans son état FMR. Le moment magnétique de FM1 va alors précontraindre et injecter un courant de spin pur dans la couche ferrimagnétique du GFO FM2 *via* le matériau non magnétique NM. Nous pourrions alors évaluer si une conversion spin/charge dans la couche GFO FM2 est possible via l'effet Hall à spin inverse (ISHE). Cela ouvrirait des perspectives d'utilisation du GFO comme convertisseur spin-charge.

## References:

- (1) Trassin, M. Low Energy Consumption Spintronics Using Multiferroic Heterostructures. *Journal of Physics: Condensed Matter* **2016**, *28* (3), 033001. <https://doi.org/10.1088/0953-8984/28/3/033001>.
- (2) Thomasson, A.; Ibrahim, F.; Lefevre, C.; Autissier, E.; Roulland, F.; Mény, C.; Leuvrey, C.; Choi, S.; Jo, W.; Crégut, O. Effects of Iron Concentration and Cationic Site Disorder on the Optical Properties of Magnetoelectric Gallium Ferrite Thin Films. *RSC advances* **2013**, *3* (9), 3124–3130.
- (3) Trassin, M.; Viart, N.; Versini, G.; Barre, S.; Pourroy, G.; Lee, J.; Jo, W.; Dumesnil, K.; Dufour, C.; Robert, S. Room Temperature Ferrimagnetic Thin Films of the Magnetoelectric  $\text{Ga}_{2-x}\text{Fe}_x\text{O}_3$ . *J. Mater. Chem.* **2009**, *19* (46), 8876–8880. <https://doi.org/10.1039/B913359C>.
- (4) Song, S.; Jang, H. M.; Lee, N.-S.; Son, J. Y.; Gupta, R.; Garg, A.; Ratanapreechachai, J.; Scott, J. F. Ferroelectric Polarization Switching with a Remarkably High Activation Energy in Orthorhombic  $\text{GaFeO}_3$  Thin Films. *NPG Asia Materials* **2016**, *8* (2), e242–e242.
- (5) Demchenko, A. Investigation of the Potential Offered by Gallium Iron Oxide Thin Films in Terms of Multiferroicity, Thesis, University of Strasbourg, 2015.
- (6) Trassin, M. Couches Minces de  $\text{Ga}_{2-x}\text{Fe}_x\text{O}_3$  Par Ablation Laser Pulsée: Vers Un Matériau Magnétoélectrique à Température Ambiante, Strasbourg, 2009.
- (7) Roulland, F.; Lefevre, C.; Thomasson, A.; Viart, N. Study of  $\text{Ga}_{2-x}\text{Fe}_x\text{O}_3$  Solid Solution: Optimisation of the Ceramic Processing. *Journal of the European Ceramic Society* **2013**, *33* (5), 1029–1035. <https://doi.org/10.1016/j.jeurceramsoc.2012.11.014>.
- (8) Sánchez, F.; García-Cuenca, M. V.; Ferrater, C.; Varela, M.; Herranz, G.; Martínez, B.; Fontcuberta, J. Transition from Three- to Two-Dimensional Growth in Strained  $\text{SrRuO}_3$  Films on  $\text{SrTiO}_3(001)$ . *Applied Physics Letters* **2003**, *83* (5), 902. <https://doi.org/10.1063/1.1599040>.
- (9) Ojima, T.; Tainosho, T.; Sharmin, S.; Yanagihara, H. RHEED Oscillations in Spinel Ferrite Epitaxial Films Grown by Conventional Planar Magnetron Sputtering. *AIP Advances* **2018**, *8* (4), 045106. <https://doi.org/10.1063/1.5012133>.
- (10) Krockenberger, Y.; Yun, K.-S.; Hatano, T.; Arisawa, S.; Kawasaki, M.; Tokura, Y. Layer-by-Layer Growth and Magnetic Properties of  $\text{Y}_3\text{Fe}_5\text{O}_{12}$  Thin Films on  $\text{Gd}_3\text{Ga}_5\text{O}_{12}$ . *Journal of Applied Physics* **2009**, *106* (12), 123911. <https://doi.org/10.1063/1.3266004>.
- (11) Lefevre, C.; Demchenko, A.; Bouillet, C.; Luysberg, M.; Devaux, X.; Roulland, F.; Versini, G.; Barre, S.; Wakabayashi, Y.; Boudet, N.; Leuvrey, C.; Acosta, M.; Mény, C.; Martin, E.; Grenier, S.; Favre-Nicolin, V.; Viart, N. Nondestructive Method for the Determination of the Electric Polarization Orientation in Thin Films: Illustration on Gallium Ferrite Thin Films. *Small Methods* **2017**, *1*, 1700234.
- (12) Song, S.; Jang, H. M.; Lee, N.-S.; Son, J. Y.; Gupta, R.; Garg, A.; Ratanapreechachai, J.; Scott, J. F. Ferroelectric Polarization Switching with a Remarkably High Activation Energy in Orthorhombic  $\text{GaFeO}_3$  Thin Films. *NPG Asia Mater* **2016**, *8*, e242. <https://doi.org/10.1038/am.2016.3>.
- (13) Richardson, C. J. K.; Lee, M. L. Metamorphic Epitaxial Materials. *MRS Bulletin* **2016**, *41* (3), 193–198. <https://doi.org/10.1557/mrs.2016.7>.

- (14) Ukleev, V.; Suturen, S.; Nakajima, T.; Arima, T.; Saerbeck, T.; Hanashima, T.; Sitnikova, A.; Kirilenko, D.; Yakovlev, N.; Sokolov, N. Unveiling Structural, Chemical and Magnetic Interfacial Peculiarities in  $\epsilon$ -Fe<sub>2</sub>O<sub>3</sub>/GaN (0001) Epitaxial Films. *Scientific Reports* **2018**, *8* (1), 8741. <https://doi.org/10.1038/s41598-018-25849-z>.
- (15) Gich, M.; Fina, I.; Morelli, A.; Sanchez, F.; Alexe, M.; Gazquez, J.; Fontcuberta, J.; Roig, A. Multiferroic Iron Oxide Thin Films at Room Temperature. *Advanced Materials* **2014**, *26* (27), 4645. <https://doi.org/10.1002/adma.201400990>.
- (16) Fong, D. D.; Stephenson, G. B.; Streiffer, S. K.; Eastman, J. A.; Auciello, O.; Fuoss, P. H.; Thompson, C. Ferroelectricity in Ultrathin Perovskite Films. *Science* **2004**, *304* (5677), 1650–1653. <https://doi.org/10.1126/science.1098252>.
- (17) Lichtensteiger, C.; Dawber, M.; Stucki, N.; Triscone, J.-M.; Hoffman, J.; Yau, J.-B.; Ahn, C. H.; Despont, L.; Aebi, P. Monodomain to Polydomain Transition in Ferroelectric PbTiO<sub>3</sub> Thin Films with La<sub>0.67</sub>Sr<sub>0.33</sub>MnO<sub>3</sub> Electrodes. *Appl. Phys. Lett.* **2007**, *90* (5), 052907. <https://doi.org/10.1063/1.2433757>.
- (18) Dawber, M.; Chandra, P.; Littlewood, P. B.; Scott, J. F. Depolarization Corrections to the Coercive Field in Thin-Film Ferroelectrics. *J. Phys.: Condens. Matter* **2003**, *15* (24), L393–L398. <https://doi.org/10.1088/0953-8984/15/24/L06>.
- (19) Streiffer, S.; Eastman, J.; Fong, D.; Thompson, C.; Munkholm, A.; Murty, R.; Auciello, O.; Bai, G.; Stephenson, G. Observation of Nanoscale 180 ° Stripe Domains in Ferroelectric PbTiO<sub>3</sub> Thin Films. *Physical review letters* **2002**, *89*, 067601. <https://doi.org/10.1103/PhysRevLett.89.067601>.
- (20) Stoeffler, D. First Principles Study of the Electric Polarization and of Its Switching in the Multiferroic GaFeO<sub>3</sub> System. *Journal of Physics-Condensed Matter* **2012**, *24* (18), 185502.
- (21) Stoeffler, D. First Principles Study of the Spontaneous Electric Polarization in Ga<sub>2-x</sub>Fe<sub>x</sub>O<sub>3</sub>. *Thin Solid Films* **2013**, *533*, 93–96. <https://doi.org/10.1016/j.tsf.2012.10.138>.
- (22) Meier, D.; Seidel, J.; Cano, A.; Delaney, K.; Kumagai, Y.; Mostovoy, M.; Spaldin, N. A.; Ramesh, R.; Fiebig, M. Anisotropic Conductance at Improper Ferroelectric Domain Walls. *Nature Materials* **2012**, *11* (4), 284–288. <https://doi.org/10.1038/nmat3249>.
- (23) Thomasson, A.; Cherifi, S.; Lefevre, C.; Roulland, F.; Gautier, B.; Albertini, D.; Meny, C.; Viart, N. Room Temperature Multiferroicity in Ga<sub>0.6</sub>Fe<sub>1.4</sub>O<sub>3</sub>:Mg Thin Films. *J Appl Phys* **2013**, *113* (21), 214101. <https://doi.org/10.1063/1.4808349>.
- (24) Quindeau, A.; Avci, C. O.; Liu, W.; Sun, C.; Mann, M.; Tang, A. S.; Onbasli, M. C.; Bono, D.; Voyles, P. M.; Xu, Y.; Robinson, J.; Beach, G. S. D.; Ross, C. A. Tm<sub>3</sub>Fe<sub>5</sub>O<sub>12</sub>/Pt Heterostructures with Perpendicular Magnetic Anisotropy for Spintronic Applications. *Advanced Electronic Materials* **2017**, *3* (1), 1600376. <https://doi.org/10.1002/aelm.201600376>.
- (25) Bertaut, E. F.; Bassi, G.; Buisson, G.; Chappert, J.; Delapalme, A.; Pauthenet, R.; Rebouillat, H. P.; Aleonard, R. Étude Par Effet Mössbauer, Rayons X, Diffraction Neutronique et Mesures Magnétiques de Fe<sub>1.15</sub>Ga<sub>0.85</sub>O<sub>3</sub>. *Journal de Physique* **1966**, *27* (7–8), 433–448.
- (26) Katayama, T.; Yasui, S.; Hamasaki, Y.; Itoh, M. Control of Crystal-Domain Orientation in Multiferroic Ga<sub>0.6</sub>Fe<sub>1.4</sub>O<sub>3</sub> Epitaxial Thin Films. *Applied Physics Letters* **2017**, *110* (21), 212905. <https://doi.org/10.1063/1.4984211>.
- (27) Kim, J.-Y.; Koo, T. Y.; Park, J.-H. Orbital and Bonding Anisotropy in a Half-Filled GaFeO<sub>3</sub> Magnetolectric Ferrimagnet. *Phys. Rev. Lett.* **2006**, *96* (4), 047205. <https://doi.org/10.1103/PhysRevLett.96.047205>.

- (28) Han, M. J.; Ozaki, T.; Yu, J. Magnetic Ordering and Exchange Interactions in Multiferroic GaFeO<sub>3</sub>. *Physical Review B* **2007**, *75* (6), 060404.
- (29) Roy, A.; Prasad, R.; Auluck, S.; Garg, A. Effect of Site-Disorder on Magnetism and Magneto-Structural Coupling in Gallium Ferrite: A First-Principles Study. *Journal of Applied Physics* **2012**, *111* (4), 043915.
- (30) Ibrahim, F.; Alouani, M. Impact of Excess Iron on the Calculated Electronic and Magnetic Properties of Gallium Ferrite. *Physical Review B* **2012**, *85* (17), 174411.
- (31) Dixit, A.; Stoeffler, D.; Alouani, M. Effect of Site Disorder on the Electronic, Magnetic, and Ferroelectric Properties of Gallium Ferrite. *Physical Review Materials* **2020**, *4* (7), 074406.
- (32) Tseng, Y.-C.; Souza-Neto, N. M.; Haskel, D.; Gich, M.; Frontera, C.; Roig, A.; van Veenendaal, M.; Nogués, J. Nonzero Orbital Moment in High Coercivity  $\epsilon$ -Fe<sub>2</sub>O<sub>3</sub> and Low-Temperature Collapse of the Magnetocrystalline Anisotropy. *Phys. Rev. B* **2009**, *79* (9), 094404. <https://doi.org/10.1103/PhysRevB.79.094404>.
- (33) Denev, S. A.; Lummen, T. T. A.; Barnes, E.; Kumar, A.; Gopalan, V. Probing Ferroelectrics Using Optical Second Harmonic Generation. *Journal of the American Ceramic Society* **2011**, *94* (9), 2699–2727. <https://doi.org/10.1111/j.1551-2916.2011.04740.x>.
- (34) Kundaliya, D. C.; Ogale, S. B.; Dhar, S.; McDonald, K. F.; Knoesel, E.; Osedach, T.; Lofland, S. E.; Shinde, S. R.; Venkatesan, T. Large Second-Harmonic Kerr Rotation in GaFeO<sub>3</sub> Thin Films on YSZ Buffered Silicon. *Journal of Magnetism and Magnetic Materials* **2006**, *299* (2), 307–311.
- (35) Nordlander, J.; De Luca, G.; Strkalj, N.; Fiebig, M.; Trassin, M. Probing Ferroic States in Oxide Thin Films Using Optical Second Harmonic Generation. *Applied Sciences* **2018**, *8* (4), 570. <https://doi.org/10.3390/app8040570>.
- (36) Nordlander, J.; Rossell, M. D.; Campanini, M.; Fiebig, M.; Trassin, M. Inversion-Symmetry Engineering in Sub-Unit-Cell-Layered Oxide Thin Films. *arXiv:2005.09083 [cond-mat, physics:physics]* **2020**.
- (37) Liao, Z.; Huijben, M.; Zhong, Z.; Gauquelin, N.; Macke, S.; Green, R. J.; Van Aert, S.; Verbeeck, J.; Van Tendeloo, G.; Held, K. Controlled Lateral Anisotropy in Correlated Manganite Heterostructures by Interface-Engineered Oxygen Octahedral Coupling. *Nature materials* **2016**, *15* (4), 425–431.
- (38) Lu, H.; Liu, X.; Burton, J. D.; Bark, C.; Wang, Y.; Zhang, Y.; Kim, D. J.; Stamm, A.; Lukashev, P.; Felker, D. A. Enhancement of Ferroelectric Polarization Stability by Interface Engineering. **2012**.
- (39) Fong, D. D.; Stephenson, G. B.; Streiffer, S. K.; Eastman, J. A.; Auciello, O.; Fuoss, P. H.; Thompson, C. Ferroelectricity in Ultrathin Perovskite Films. *Science* **2004**, *304* (5677), 1650–1653.
- (40) Gradauskaite, E.; Campanini, M.; Biswas, B.; Schneider, C. W.; Fiebig, M.; Rossell, M. D.; Trassin, M. Robust In-Plane Ferroelectricity in Ultrathin Epitaxial Aurivillius Films. *Advanced Materials Interfaces* **2020**, 2000202.
- (41) Gao, P.; Zhang, Z.; Li, M.; Ishikawa, R.; Feng, B.; Liu, H.-J.; Huang, Y.-L.; Shibata, N.; Ma, X.; Chen, S. Possible Absence of Critical Thickness and Size Effect in Ultrathin Perovskite Ferroelectric Films. *Nature communications* **2017**, *8* (1), 1–8.
- (42) Bennemann, K. H. *Non-Linear Optics in Metals*; Oxford University Press, 1998.

- (43) Rojas-Sánchez, J.-C.; Reyren, N.; Laczkowski, P.; Savero, W.; Attané, J.-P.; Deranlot, C.; Jamet, M.; George, J.-M.; Vila, L.; Jaffrès, H. Spin Pumping and Inverse Spin Hall Effect in Platinum: The Essential Role of Spin-Memory Loss at Metallic Interfaces. *Physical review letters* **2014**, *112* (10), 106602.
- (44) Nguyen, M.-H.; Ralph, D. C.; Buhrman, R. A. Spin Torque Study of the Spin Hall Conductivity and Spin Diffusion Length in Platinum Thin Films with Varying Resistivity. *Physical review letters* **2016**, *116* (12), 126601.
- (45) Lin, T. Magnetic Insulator Thin Films and Induced Magneto-Transport Effect at Normal Metal / Magnetic Insulator Interface, UC Riverside, 2013.
- (46) Guo, G. Y.; Murakami, S.; Chen, T.-W.; Nagaosa, N. Intrinsic Spin Hall Effect in Platinum: First-Principles Calculations. *Phys. Rev. Lett.* **2008**, *100* (9), 096401. <https://doi.org/10.1103/PhysRevLett.100.096401>.
- (47) Guo, G. Y.; Niu, Q.; Nagaosa, N. Anomalous Nernst and Hall Effects in Magnetized Platinum and Palladium. *Phys. Rev. B* **2014**, *89* (21), 214406. <https://doi.org/10.1103/PhysRevB.89.214406>.
- (48) Fang, Z.; Nagaosa, N.; Takahashi, K. S.; Asamitsu, A.; Mathieu, R.; Ogasawara, T.; Yamada, H.; Kawasaki, M.; Tokura, Y.; Terakura, K. The Anomalous Hall Effect and Magnetic Monopoles in Momentum Space. *Science* **2003**, *302* (5642), 92–95.
- (49) Mathieu, R.; Asamitsu, A.; Yamada, H.; Takahashi, K. S.; Kawasaki, M.; Fang, Z.; Nagaosa, N.; Tokura, Y. Scaling of the Anomalous Hall Effect in  $\text{Sr}_{1-x}\text{Ca}_x\text{RuO}_3$ . *Physical review letters* **2004**, *93* (1), 016602.
- (50) Nakayama, H.; Althammer, M.; Chen, Y.-T.; Uchida, K.; Kajiwara, Y.; Kikuchi, D.; Ohtani, T.; Geprägs, S.; Opel, M.; Takahashi, S.; Gross, R.; Bauer, G. E. W.; Goennenwein, S. T. B.; Saitoh, E. Spin Hall Magnetoresistance Induced by a Nonequilibrium Proximity Effect. *Phys. Rev. Lett.* **2013**, *110* (20), 206601. <https://doi.org/10.1103/PhysRevLett.110.206601>.

# Ultra-thin multifunctional oxide layers for spintronics applications

## Résumé

Le contexte de ce travail est le développement de dispositifs de spintronique à faible consommation d'énergie. Le projet vise à explorer les possibilités de contrôle de l'aimantation d'un oxyde multiferroïque et magnétoélectrique à température ambiante, le  $\text{Ga}_{0.6}\text{Fe}_{1.4}\text{O}_3$  (GFO), sans champ magnétique, en associant des mécanismes de retournement magnétoélectrique à ceux dûs à un couple spin-orbite. Cet objectif nécessite l'utilisation de couches ultra-minces de GFO, dont l'étude n'avait jamais été faite auparavant. Dans un premier temps, nous avons étudié les propriétés structurales, magnétiques et électriques de couches minces de GFO épitaxiées sur des substrats de  $\text{SrTiO}_3$  (STO) dans le régime ultra-mince. L'épaisseur des films a pu être contrôlée jusqu'à un quart de maille. Un effet de diffusion à l'interface substrat-film conduit à une inversion abrupte de l'état de polarisation du film qui a pu être mise en évidence dans les cinq premiers nanomètres de la couche. Les films ont montré une forte polarisation dès le début de leur croissance et ne semblent pas être sensibles à un quelconque champ dépolarisant. L'anisotropie magnétique des films a pu être ajustée de façon à ce qu'elle soit hors plan pour les plus minces et dans le plan pour les plus épais. Contre toute attente pour un matériau à base de  $\text{Fe}^{3+} 3d^5$ , le moment orbital du Fe s'est avéré non nul, non-monotone en fonction de la température et fortement anisotrope, indiquant un couplage magnéto-structural important. Des hétérostructures de GFO/Pt ont été produites comme première étape vers le développement de dispositifs spintroniques basés sur le GFO. Des mesures de magnéto-transport en angle ont révélé un important effet de magnétorésistance de Hall de spin (SMR) et ont donc conforté la pertinence de GFO pour des dispositifs de mémoire à faible consommation d'énergie basés sur l'effet de Hall de spin.

## Résumé en anglais

The context of this work is the development of low power consuming spintronics-based devices. The project aims to explore the magnetic-field-free control of the magnetization of a room temperature multiferroic and magnetoelectric oxide,  $\text{Ga}_{0.6}\text{Fe}_{1.4}\text{O}_3$  (GFO), by coupling magneto-electric and spin-orbit torque switching mechanisms. This objective requires the use of ultra-thin layers of GFO, the study of which had never been done before. In a first move, we have investigated the structural, magnetic and electric properties of epitaxially grown atomically flat GFO thin films on  $\text{SrTiO}_3$  (STO) substrates at ultra-thin regimes. The thickness of the films could be controlled down to one fourth of a unit cell. A substrate-film interface diffusion effect which leads to an abrupt reversal of the polarization state of the film could be evidenced within the first five nanometers. The films showed a stout polarization from the very early growth and do not seem to be sensitive to any depolarizing field. The magnetic anisotropy of the films could be tuned from out-of-plane, for the thinnest ones, to in-plane for the thicker ones. Against all odds in such a  $3d^5 \text{Fe}^{3+}$  based material, the orbital moment of Fe was found to be non-zero, non-monotonously temperature dependent, and strongly anisotropic, indicating an important magneto-structural coupling. Heterostructures of GFO/Pt were produced as a first step towards the development of spintronics devices based on GFO. Angle-dependent magneto-transport measurements unveiled an important spin Hall magnetoresistance effect (SMR) and therefore comforted the relevance of GFO for spin-Hall-effect-based low power consuming memory devices.